November 2017

Arctic and North Atlantic paleo-environmental reconstructions from lake sediments

Gregory A. de Wet
Department of Geosciences

Arctic and North Atlantic paleo-environmental reconstructions from lake sediments

A Dissertation presented

by

GREGORY A. DE WET

Submitted to the Graduate School of the University of Massachusetts Amherst
in partial fulfillment of the requirements for the degree of

DOCTOR OF PHILOSOPHY

September, 2017

Department of Geosciences

Arctic and North Atlantic paleo-environmental reconstructions from lake sediments

A Dissertation presented

by

GREGORY A. DE WET

Approved as to style and content by:

_____
Raymond S. Bradley, Co-Chair

_____
Isla Castañeda, Co-Chair

_____
Julie Brigham-Grette, Member

_____
Jostein Bakke, Member

_____
James Holden, Member

_____
Julie Brigham-Grette, Department Head
Geosciences Department

DEDICATION

To my parents, Carol and Andy – thank you for all your love and support.

ACKNOWLEDGMENTS

I would like to thank my co-advisors, Ray Bradley and Isla Castañeda, for all their support and guidance throughout my time at the University of Massachusetts. Working with Ray opened up a world of experiences and opportunities for which I am eternally grateful. Isla is an amazing researcher who opened my eyes to the world of biomarkers and made me a much better scientist and writer. I thank them both for their patience and understanding as I navigated multiple projects and many challenges. I would also like to thank the members of my dissertation committee, Julie Brigham-Grette, Jostein Bakke, and James Holden for their insights and suggestions. It has been a privilege to discuss science with you all.

I would also like to thank the many people who contributed ideas, data, field and/or lab assistance, and insight to the work presented here. In particular I would like to thank Drs. Nicholas Balascio and William D'Andrea, who I consider secondary advisors and have contributed a great deal both to the following chapters and to my own development as a scientist. I would also like to thank Dr. Jeff Salacup for his assistance and patience in the biogeochem lab. Thanks also to Dr. Sheila Seaman, a wonderful person to collaborate with, who allowed me to use the FTIRS whenever I wished. Many thanks also to the numerous undergraduate students who have contributed to this work; Tom Barrasso, Geoff Small, Annie Kandel, and Adam Kassirer.

None of this would have been possible without the support of my family. Thank you, Mom and Dad, (Carol and Andy) for everything you have done for me. Both in science and life I have tried to follow the excellent example set by you both. Thank you also to my sister, Emily, and my brother, Cameron. Spending time with you during graduate school was both a wonderful escape and an impetus to continue forward. A monumental thanks to Erika, for your love, support, and understanding. Your calmness and grace has steadied me on many occasions, and your kindness and empathy is always inspirational.

Sincere and heartfelt thanks to the Department of Geosciences faculty, fellow students, and staff. My six years here in Amherst have been incredibly rewarding and enjoyable thanks to you all. I could not have asked for a better environment to learn and study. Thank you especially to my officemates in the climate center for the good humor and conversations.

This research was funded by several sources, including the National Science Foundation, the Geological Society of America, National Geographic, the Svalbard Science Forum, the Norwegian Research Council, Experiment.com, and the University of Massachusetts, Amherst Department of Geosciences.

ABSTRACT

ARCTIC AND NORTH ATLANTIC PALEO-ENVIRONMENTAL RECONSTRUCTIONS FROM LAKE SEDIMENTS

SEPTEMBER 2017

GREGORY A. DE WET, B.Sc., BATES COLLEGE

M.Sc., UNIVERSITY OF MASSSCHUSETTS, AMHERST

Ph.D., UNIVERSITY OF MASSACHUSETTS, AMHERST

Directed by: Drs. Raymond S. Bradley and Isla S. Castañeda

There are few fields in the discipline of Earth Science that hold more relevancy in 2017 than studies of earth's climate. Called the "perfect problem" considering its complexity and magnitude, climate change will continue to be one of the greatest challenges humanity will face in the 21st century. And while numerical models provide valuable information on conditions in the future, the results from these simulations must be contextualized by the past. Climate reconstructions from paleo-environmental archives, even from periods colder or different from what we are experiencing today, provide that context. Every piece of information gleaned from these studies informs our collective knowledge of the climate system. In some cases, environmental reconstructions may include proxies for anthropogenic as well as climatological information, directly addressing one of the most important questions in climate science: how does changing climate affect humans?

The following chapters of this dissertation are exercises in trying to understand climate change in one of the most climatically sensitive regions on earth – the high northern latitudes. While my doctoral studies cover a wide range of timescales, it is broadly unified by the focus on the Arctic. In some cases, my research spans multiple glacial/interglacial cycles, in others the concentration is on the past few thousand years. In all cases, however, the goal is to utilize lacustrine sedimentary archives to inform our knowledge of climatic change in this important region.

One of the most rewarding aspects of this Ph.D. has been the creativity I have been afforded in working towards that goal. Chapter One of this dissertation involves the analysis of organic molecules, specifically bacterial membrane lipids called branched glycerol dialkyl glycerol tetraethers (brGDGTs), to sediments from Lake El'gygytgyn. These biomarkers allow for a quantitative reconstruction of temperature from multiple interglacial periods over a million years ago. Our data suggests that "super interglacial" Marine Isotope Stage 31 may have in fact lasted much longer than previously thought in the Arctic, with implications for Antarctic ice sheet extent and CO_2 concentrations highly relevant to our future. Though the extraction and analysis of these biomarkers is expensive and time-consuming, the data is highly valuable and informative.

Conversely in some cases more "quick and dirty" techniques are sufficient to reconstruct important processes or factors back through time (e.g. the presence of a glacier within a lake catchment) at relatively low cost, and therefore are highly useful. The chapters dealing with Lake Gjøavatnet in Svalbard (Chapter Two) or the application of Fourier Transform Infrared (FTIR) spectroscopy to lake sediments (Chapter Five) exhibit how such techniques can also be highly informative. In Chapter Two, using a combination of core-scanning data and relatively simple destructive analyses (%loss-on-ignition, bulk carbon isotopes), we reconstructed past fluctuations in glacier extent over the Holocene, as well as identified intervals that may have been related to freshwater pulses in Fram Strait. Chapter Five is focused mainly on expanding and confirming the use of FTIR spectroscopy to Arctic lake sediments to reconstruct biogenic silica and organic matter concentrations through time. Though potentially a less direct climate proxy than paleotemperature from brGDGTs, this new technique allows for more rapid analyses using less sediment than previous methods, a valuable advance.

Chapters Three and Four are in many ways the confluence of these earlier stages of my Ph.D., where we apply a wide range of proxies to answer questions related to climate and human population dynamics. The use of biomarkers is expanded in these projects, where a broad suite of

organic molecules are used to reconstruct both climate and other paleo-environmental conditions, including vegetation changes, variations in pH, and potentially anthropogenic influences. Coupled with some of the more "basic" techniques described above, we characterize an environmental disturbance in the Faroe Islands ~2200 years ago that may be evidence for the first appearance of humans in the archipelago (Chapter Three). In Chapter Four, we explore the application of brGDGTs (among other proxies) to reconstruct temperature change in southwest Greenland during the period of Norse settlement and subsequent abandonment. This work is part of an ongoing investigation into the efficacy and calibration of this promising proxy in a locale where climate change likely had a dramatic impact on the fragile communities living there.

In summary, I have not attempted to unify these chapters into a single climatological context (though some of my work, such as in the Faroes and Greenland, is highly related). Instead I present them as they are, individual projects that each have their own goals and merits within the broad framework of paleoclimatology. As I mentioned above, one of my favorite things about this field is the creativity we are afforded in our attempts to answer questions about the past. This Ph.D. has been an exercise in that creativity, focused in the high northern latitudes, and centered around the archive of lake sediments.

PREFACE

Chapter 1

Chapter one was published in *Earth and Planetary Science Research Letters* (2016) and is therefore written in the first person plural with co-authors Isla Castaneda, Robert DeConto, and Julie Brigham-Grette. No changes have been made to the published manuscript, which reconstructs paleo-temperatures from Lake El'gygytgyn over "super interglacial" Marine Isotope Stage 31.

Chapter 2

Chapter two has been accepted for publication by *Quaternary Science Reviews* in April, 2017. This chapter is also written in the first person plural with co-authors Nicholas Balascio, William D'Andrea, Jostein Bakke, Raymond Bradley, and Bianca Perren. No changes have been made to the accepted manuscript, which documents the Holocene paleo-environmental history of a proglacial lake in NW Svalbard.

Chapter 3

Chapter three contains a prepared manuscript written in collaboration with Geoffrey Small, Isla Castañeda, Raymond Bradley, Nicholas Balascio, William D'Andrea, and Lorelei Curtin. It therefore contains third person plural pronouns. The chapter deals with a paleo-environmental reconstruction from a lake record from the Faroe Islands over the Holocene, including the possible first appearance of humans in the archipelago. This manuscript has not been submitted for publication at the time of dissertation completion.

Chapter 4

Chapter four contains a prepared manuscript written in collaboration with Thomas Barrasso, Isla Castaneda, Boyang Zhao, and Raymond Bradley. It therefore contains third person

plural pronouns. This project entails reconstructions of human occupancy and paleoclimate from lakes in SW Greenland, with particular emphasis on biomarker temperature reconstructions over the interval of Norse settlement in the region. This manuscript has not been submitted for publication at the time of dissertation completion.

Chapter 5

Chapter five contains a prepared manuscript written in collaboration with Samuel Davin, Stephen Giguere, Darby Dyer, Sheila Seaman, and Raymond Bradley. It therefore contains third person plural pronouns. This chapter deals with the use of Fourier Transform Infrared Spectroscopy (FTIRS) to determine the biogenic silica and organic matter concentrations of Arctic lake sediments. This manuscript has not been submitted for publication at the time of dissertation completion.

TABLE OF CONTENTS

Page

ACKNOWLEDGMENTS v

ABSTRACT vii

PREFACE x

LIST OF TABLES xvi

LIST OF FIGURES xvii

CHAPTER

1. A HIGH RESOLUTION MID-PLEISTOCENE TEMPERATURE RECORD FROM ARCTIC LAKE EL'GYGYTGYN; A 50 KYR SUPER INTERGLACIAL FROM MIS 33-31? 1

1.1 Introduction 1
1.2 Site Description 2
1.3 Methods 5
1.4 Results 7
1.5 Discussion 8
1.5.1 brGDGT temperature reconstruction 8
1.5.2 Super Interglacial MIS 31 at Lake El'gygytgyn 10
1.5.3 Global Signature of MIS 33-31 12

1.6 Conclusions 16

2. HOLOCENE GLACIER ACTIVITY RECONSTRUCTED FROM PROGLACIAL LAKE GJØAVATNET ON AMSTERDAMØYA, NW SVALBARD 25

2.1 Introduction 25
2.2 Regional Setting 27
2.3 Methods 28
2.3.1 Fieldwork and Lake Coring 28
2.3.2 Composite sediment record 29
2.3.3 Laboratory Analyses 29
2.3.4 Statistical and Multivariate Analyses 30

2.4 Results and Interpretations 31

2.4.1 Chronology 31
2.4.2 Multivariate Analysis 32
2.4.3 Stratigraphy and Interpretation of Stratigraphic Units 32
2.4.4 Unit A: Base of core (206.5 cm) – 11.1 cal kyr BP (162.5 cm) - Glacial Till 33
2.4.5 Unit B: 11.1cal kyr BP (162.5 cm) – 8.4 cal kyr BP (136.5 cm) - Deglaciation of Gjøavatnet Catchment 35
2.4.6 Unit C: 8.4 cal kyr BP (136.5 cm) – 1.0 cal kyr BP (16.5 cm) -Non-glacial sedimentation in Gjøavatnet 37
2.4.7 Unit D: 1.0 cal kyr BP (16.5 cm) to present - Re-advance of Annabreen 39

2.5 Regional Paleoclimate Context of Gjøavatnet Record 40
2.5.1 Early Holocene: Deglaciation of Amsterdamøya 41
2.5.2 Middle Holocene – Sea ice and freshwater influences on Amsterdamøya climate 42
2.5.3 Late Holocene advance of Annabreen glacier 45

2.6 Conclusions 46

3. A MAJOR ENVIRONMENTAL DISTUBANCE IN THE FAROE ISLANDS 2200 YEARS AGO: POTENTIAL EVIDENCE FOR EARLY HUMAN SETTLEMENT? 63

3.1 Introduction 63
3.2 Site Description 67
3.3 Methods 68
3.3.1 Fieldwork and Coring 68
3.3.2 Laboratory Analyses 69
3.3.3 Paleoenvironmental Reconstructions 71

3.4 Results 72
3.4.1 Composite Sediment Record 72
3.4.2 Chronology 72
3.4.3 Proxy Results 73
3.4.4 Biomarker Data 76

3.5 Discussion 79
3.5.1 Nature of disturbance in Eiðisvatn 80
3.5.2 Mass movement deposit? 82
3.5.3 Climatically induced event? 82
3.5.4 An anthropogenic event? 86

4. RECONSTRUCTION OF ENVIRONMENTAL CONDITIONS AND HUMAN OCCUPANCY IN SW GREENLAND 102
4.1 Introduction 102
4.2 Background 102
4.3 Study Site 103
4.4 Methods 104
4.4.1 Laboratory Analyses 104
4.4.2 Paleoenvironmental Reconstructions 106
4.5 Results 107
4.5.1 Chronology 107
4.5.2 Core-scanning results 107
4.5.3 Laboratory Results 109
4.5.4 Biomarker Results 110
4.5.5 brGDGT Results 110
4.5.6 Leaf wax n-alkane data 111
4.5.7 Primary productivity compounds 111
4.6 Discussion of Preliminary Results 112
4.7 Ongoing Research 114
5. CONFIRMATION OF THE USE OF FTIR SPECTROSCOPY TO DETERMINE BIOGENIC SILICA AND ORGANIC MATTER CONTENT OF ARCTIC LAKE SEDIMENTS: A POWERFUL TOOL FOR HIGH-RESOLUTION PALEOCLIMATE RECONSTRUCTIONS 129
5.1 Introduction 129
5.2 Study Area 131
5.3 Methods 131
5.3.1 Conventional biogenic silica measurements 131
5.3.2 Conventional total organic carbon measurements 132
5.3.3 Fourier Transform Infrared Spectroscopy analyses 132
5.3.4 Numerical Analyses 133
5.3.5 Normalization of spectral data 133
5.3.6 Calibration models 134
5.4 Results 136
5.4.1 Biogenic silica linear regression calibration model results 136

5.4.2 Biogenic silica calibration model results – All spectrum models 136
5.4.3 Biogenic silica PLS calibration model results – Specific spectral region models 136
5.4.4 BAS and BSS model predictions downcore from Nanerersarpik record 137
5.4.5 Total organic carbon linear regression calibration model results 137
5.4.6 Total organic carbon calibration model results – All spectrum models 138
5.4.7 Total organic carbon calibration model results – Specific spectral region models 138
5.4.8 TAS and TSS model predictions downcore from Nanerersarpik record 138

5.5 Discussion 139
5.5.1 Biogenic silica estimates using FTIRS 139
5.5.2 Progressive addition of traditionally measured values to biogenic silica calibration dataset 140
5.5.3 Total organic carbon concentration estimates using FTIRS 140
5.5.4 Progressive addition of traditionally measured values to organic carbon calibration dataset 141
5.5.5 Applicability of created PLS models to other lacustrine systems 142

5.6 Conclusions 142

REFERENCES 161

LIST OF TABLES

Table Page

Table 1.1: Average reconstructed temperatures from MIS 33-31 18

Table 2.1: Sediment cores collected from Gjøavatnet 48

Table 2.2: Radiocarbon results from macrofossils taken from GJP-01-14 core 48

Table 2.3: Correlation coefficients for variables used in PCA analysis 49

Table 2.4: Results from PCA analysis with 8 principal components 49

Table 2.5: Relevant proxy data for sedimentary units identified in Gjøavatnet record 50

Table 3.1: Sediment cores collected from Eiðisvatn 88

Table 3.2: Radiocarbon + Tephra dates from Eiðisvatn 88

Table 4.1: Radiocarbon dates on Eriksvatnet A core. 116

Table 5.1: Results of conventional biogenic silica analyses used as calibration dataset for FTIRS BSi models 144

Table 5.2: Results of conventional organic carbon measurements used as calibration dataset for FTIRS TOC models 144

Table 5.3: Calibration model results for BAS and BSS partial least squares regression models 145

Table 5.4: Predicted biogenic silica downcore from BAS and BSS models 145

Table 5.5: Calibration model results for TAS and TSS organic carbon PLS models 146

Table 5.6: Predicted total organic carbon downcore from TAS and TSS models 147

Table 5.7: Model information for BAS 17.1 (22 calibration samples), 17.2 (30 calibration samples), and 14.2 (35 calibration samples) 147

Table 5.8: Downcore model information for TAS models incorporating increasing numbers of calibration samples 148

LIST OF FIGURES

Figure Page

Figure 1.1 - Approximate location of Lake El'gygytgyn in NE Siberia and other locations relevant to this study. Background image source: NASA's Earth Observatory. 19

Figure 1.2 - brGDGT results from MIS 35-29 at Lake El'gygytgyn: a) concentrations of total brGDGTs relative to grams sediment extracted; b) MBT, c) CBT, and d) pH values calculated using equation of Weijers et al., (2007); e) MBT/CBT based temperatures calculated using equation of Sun et al. (2011). Pink shading denotes period from start of MIS 33 (1114 kyr BP) to end of MIS 31 (1062 kyr BP), dashed lines denote duration of MIS 31. 20

Figure 1.3 - Compilation of proxy data from Lake El'gygytgyn: a) brGDGT based temperatures (blue) (this study); pollen based mean temperature of the warmest month (MTWM) estimates (purple) (Melles et al., 2012); b) % tree and shrub pollen at the lake (green) (Melles et al., 2012); c) ratio of silica to titanium (Si/Ti) (gray), interpreted as a proxy for primary productivity. d) Red bars in bottom panel denote presence of interglacial (red) or super interglacial (dark red) facies (Melles et al., 2012). Long dashed line at 10ºC indicates modern mean July temperature. Maximum brGDGT temperature estimates from other Pleistocene interglacials and modern mean July temperatures indicated with shorter dashed lines (data from Brigham-Grette and Nolan, 2007; Habicht et al., in prep; Castañeda et al., in prep). Light pink shading denotes entire period from MIS 33-31 (1114-1062 kyr BP), darker pink shading denotes tranditional definition of MIS 31 (1082-1062 kyr BP) (Lisiecki and Raymo, 2005). 21

Figure 1.4 - a) Insolation values for 65°N (dashed red line) and 65°S (gray line) (Berger and Loutre, 1991); b) LR04 benthic stack (Lisiecki and Raymo, 2005); c) MBT/CBT temperature values from Lake El'gygytgyn (this study); d) and accumulation rate of IRD (ice-rafted detritus) from Site 1090 in South Atlantic (Teitler et al., 2015). Pink shading denotes period from start of MIS 33 (1114kyr BP) to end of MIS 31 (1062 kyr BP), dashed lines indicate traditional defintion of MIS 31 (1082-1062 kyr BP) (Lisiecki and Raymo, 2005). 22

Figure 1.5 - Compilation of existing paleotemperature records of sufficient resolution to be relevant spanning MIS 31. Upper panel (Sites 772- 1123) depicts records where magnitude of cooling during MIS 32 appears reduced relative to other Early Pleistocene glacial periods: a) Site 772 (16°N, Herbert et al., 2010), b) Site 871 (5°N, Dyez et al., 2014), c) Site 847 (0°N, Medina-Elizalde et al., 2008), d) Site 849 (0°N, McClymont and Rosell-Melé, 2005), e) Site 846 (3°S, Herbert et al., 2010), f) Site MD06-301 (23°S, Russon et al., 2011), g) Site 1123 (41°S, Crundwell et al., 2008). Middle panel depicts h) biomarker based temperatures from Lake El'gygytgyn (this study) and i) the LR04 benthic stack (Lisiecki and Raymo, 2005) along with labels denoting marine isotope stages. Lower panel shows locations (Sites 306-1090) where, while cold "glacial" temperatures are recorded during MIS 32, the duration of cooling during appears abbreviated: j) Site 306-U1313 (41°N, Naafs et al., 2013), k) Site 1146 (19°N, Herbert et al., 2010), l) Site 1143 (9°N, Li et al., 2011), m) Site 1087 (31°S, McClymont et al., 2005b), n) Site 1090 (42°S, Martinez-Garcia et al., 2010). 24

Figure 2.1 - A) Map of Svalbard and surrounding surface currents as well as locations of marine sediment cores MSM5/5-723-2 and MSM5/5-712-2 (Werner et al., 2013; 2015); B)

Aerial image of island of Amsterdamøya with Annabreen glacier and Gjøavatnet lake (this study) and Halkuytuvatnet lake (Gjerde et al., in press) labeled. Blue polygons represent the approximate locations of marble outcrops (Ohta et al., 2007). Dashed white line denotes approximate catchment of Gjøavatnet. 51

Figure 2.2 - Bathymetric map of Gjøavatnet with coring sites noted by red circles. Our investigation focused mainly on core GJP-01-14 from eastern basin. 52

Figure 2.3 - Line-scan images and x-radiographs of all cores collected from Gjøavatnet. GJP-01-14 was the focus of this investigation. Depth of radiocarbon dates are denoted with white rectangles. Dashed black lines represent existing core that could not be imaged. Lighter shades in x-radiographs represent denser material. Note that color difference in lowest portion of GJP-01-14 (section from ~170-180 cm) is due to simply to different lighting during imaging. 53

Figure 2.4 - Age depth relationship for GJP-01-14 core created in using the Clam modeling package (Blaauw, 2010) for software R (v. 3.0.1; R Development Core Team, 2013) with 95% confidence intervals for individual radiocarbon dates in blue. 54

Figure 2.5 - Ordination diagram showing 1st (80.6% of variance) and 2nd (10.72% of variance) principal components of PCA. 55

Figure 2.6 - Downcore scores of 1st principal component from PCA analysis (blue line) plotted on age scale with Itrax elemental data for Ti (gray), K (dark red) and Ca (cyan) for core GJP-01-14. Note different scale for Ca data relative to Ti and K. 56

Figure 2.7 - Downcore proxy results for GJP-01-14. Shaded background colors denote different sedimentary units (Units A-D). a) Sediment accumulation rates based on smooth spline interpolation (light green) and linear interpolation (dark blue) between radiocarbon dates; b) Itrax elemental data showing Ti (gray) and Ca (cyan) (note different scales); c) Loss-on-ignition (dark green), bulk $\delta^{13}C$ (purple) and dry bulk density values (dark blue); d) location of diatom taxonomy samples (black dashed lines); e) normal image and f) X-ray image of GJP-01-14 core. Light/white shades in f) denote denser material. 57

Figure 2.8 - Percent abundance of diatom taxa throughout the early evolutionary history of Gjøavatnet. Note sedimentary unit delineations (labels and background shaded colors) that correspond with Figure 2.7. 58

Figure 2.9 - Relationship between % Loss-on-ignition (LOI) and Ti counts from Itrax. Data from sedimentary units when Annabreen glacier is interpreted to be present are shown in blue shades (Unit A, B, D); data from units when Annabreen interpreted to be absent are shown in green shades (Unit C, C1, C2, C3). 59

Figure 2.10 - Holocene glacial activity reconstructions from Svalbard: a) June insolation values at 79°N over the Holocene (Laskar et al., 2004); schematic depiction of glacier activity in Svalbard based on published reconstructions: a) and b) proglacial lake reconstructions from Mitrahalvøya peninsula (Røthe et al., 2015; van der Bilt et al., 2015); c) proglacial paleosol and vegetation study (Humlum et al., 2005); d) & e) proglacial lake records from Linnévatnet (Svendsen and Mangerud, 1997; Snyder et al., 2000); f) %LOI and titanium counts from Gjøavatnet (this study). Blue boxes represent periods of glacial activity (dark blue = enhanced glacial activity), red boxes suggest no glacier was present

in the catchment or glacial activity was greatly reduced; gray boxes indicate periods of reduced organic matter accumulation (Gjøavatnet) or increased laminations (Snyder et al., 2000) that are not interpreted as glacial activity. 60

Figure 2.11 - Compilation of relevant paleoclimate data from NW Svalbard, Fram Strait, and Davis Strait: a) Alkenone based sea-surface temperatures from NW Icelandic shelf (Moossen et al., 2015); b) % hematite stained grains from core VM29-191 as a proxy for drift ice, w/ Bond Event #4 labeled (Bond et al., 2001); c) sub-surface (~100m depth) foram-based temperatures from core MSM5/5-712-2 (Werner et al., 2013); d) IRD counts and e) IP_{25} concentrations from core MSM5/5-712-2 (cyan/blue square data points) (Werner et al., 2013) and MSM5/5-723-2 (purple circle data points) (Werner et al., 2015) from Fram Strait; f) % loss-on-ignition data (green) from Gjøavatnet lake. Background shaded colors refer to sedimentary units from Gjøavatnet record (Figure 7). 62

Figure 3.1 - Map of the North Atlantic depicting Norse expansion during the late 1st millennium AD with the Faroe Islands labeled (modified from: vinland-map.brandeis.edu/assets/images/lightbox/Viking_voyage.jpeg) 89

Figure 3.2 - A): Map of the Faroe Islands with lakes cored in the summer of 2015 labeled. Gray shaded area represents suitable land for farming activities (modified from Arge et al., 2005). B): Oblique Google Earth image of Eiðisvatn and the nearby town of Eidi. C): Composite panorama image of Eiðisvatn taken during fieldwork in 2015. 90

Figure 3.3 - Timeline depicting published evidence for settlement of the Faroes (black boxes) and date of possible anthropogenic disturbance in Eiðisvatn (blue) (this study). 91

Figure 3.4 - Images and X-radiographs of EI-D-01-15 and EI-P-01-15. Both the disturbance associated with lake damming in the 1980s and the potential earlier settlement disturbance are outlined in dashed black lines. 92

Figure 3.5 - "EidiAll" age model, created in Bacon using all available radiocarbon dates from Eiðisvatn (blue symbols) and 3 identified tephra layers (green lines). Disturbance interval is outlined in orange. 93

Figure 3.6 - "EidiBest" age model created without 3 stratigraphically old dates from disturbance interval, and sediment accumulation rates in cm/yr (bottom panel). Disturbance interval is outlined in orange. 94

Figure 3.7 - % Loss-on-ignition (%LOI) and dry bulk density values (DBD) for both surface core EI-D-01-15 (green) and piston core EI-P-01-15 (blue). Note scale break in DBD y-axis. Disturbance interval is outlined in orange. 95

Figure 3.8 - Selected elemental counts from Itrax XRF core scanning for composite Eiðisvatn record. Disturbance interval is outlined in orange. 96

Figure 3.9 - Selected elemental ratios from Itrax XRF core scanning for composite Eiðisvatn record. 97

Figure 3.10 - brGDGT results from Eiðisvatn. Disturbance interval is outlined in orange. 98

Figure 3.11 - Leaf wax n-alkane results from Eiðisvatn. Disturbance interval is outlined in orange..... 99

Figure 3.12 - Concentrations of primary productivity biomarkers in Eiðisvatn. Disturbance interval is outlined in orange..... 100

Figure 3.13 - Mn/Fe ratio (purple) from XRF core-scanning and accumulation rate (black) from Eiðisvatn over the Holocene. The ratio of Mn/Fe is indicative of bottom water oxygen levels (Naeher et al., 2013), and high values during the disturbance interval suggest relatively higher levels of oxygenation during that time. 101

Figure 4.1 – Modified map of Norse Eastern Settlement region with known Norse sites marked (black circles) and the locations of studied lakes (modified from Bichet et al., 2013). 117

Figure 4.2 – Oblique air photograph of Eriksvatnet lake and nearby settlemtent of Brattahlíð (known as Qassiarsuk today). 118

Figure 4.3 – Preliminary age/depth model for Eriksvatnet A core based on 8 radiocarbon dates. 118

Figure 4.4 – Results from Itrax XRF core-scanning of Eriksvatnet A core. 119

Figure 4.5 – Selected ratios of elemental data from Itrax XRF core-scanning from Eriksvatnet. 120

Figure 4.6 – Sediment density and magnetic susceptibility results from the Geotek MSCL core-logging system for the Eriksvatnet A core. 121

Figure 4.7 – Loss-on-ignition and dry bulk density results for the Eriksvatnet A core. 122

Figure 4.8 – Biomarker concentrations from Eriksvatn A core. 123

Figure 4.9 – brGDGT results from Eriksvatnet A core. pH and temperature were reconstructed using the equations of Sun et al., 2011. 124

Figure 4.10 – Preliminary leaf wax n-alkane results from the Eriksvatnet A core. 125

Figure 4.11 – Preliminary sterol and stanol biomarker concentration data from the Eriksvatnet A core..... 126

Figure 4.12 – Relative abundances of brGDGTs from both lake surface sediment samples (left panel) and soil samples (right panel) from throughout the Eastern Settlement region. 127

Figure 4.13 – Preliminary Eriksvatnet brGDGT based paleotemperatures on AD/BC age depth scale with approximate interval of Norse settlement outlined (red box). 128

Figure 5.1 - Location of study area in SE Greenland (Nanerersarpik and Lower Sermilik used in this study). 149

Figure 5.2 – Characteristic FTIRS absorbance spectra. Light blue circle denotes spectral region used for BSS models, light green circle for TSS models. Gold box outlines regions used in BSS linear regression model..... 150

Figure 5.3 – BAS 14.2, BSS 13.1, linear regression calibrations model results compared against traditionally determined values (red rectangles). Error bars associated with wet chemistry values are inferred from Conley (1998). 151

Figure 5.4 – Unrealistically high downcore predictions from BAS 13.1 (blue) compared to linear regression model (gray) and conventionally measured values (red)..... 152

Figure 5.5 – Downcore BSi predictions from the best performing BAS model (14.2) and BSS model (13.1). Lower panel shows the most recent 4kyr of the record, where sampling resolution for FTIRS analysis was every centimeter. 153

Figure 5.6 – TAS 10.1 and TSS 3.1 calibration model results compared against traditionally determined values (red rectangles). 154

Figure 5.7 – Unrealistically high downcore predictions for PLS model TAS 8.1 (green) compared against predictions from linear regression model (gray) and traditionally measured values (red). 155

Figure 5.8 – Downcore TOC predictions from the best performing TAS model (10.1) and TSS model (3.1). Lower panel shows the most 4 kyr of the record, where sampling resolution for FTIRS analyses was every centimeter..... 156

Figure 5.9 – PLS model loading plots for biogenic silica model BAS 14.2. 157

Figure 5.10 – Positive relationship between predicted total organic carbon (TOC) and biogenic silica (BSi) in Nanerersarpik record. 158

Figure 5.11 – Biogenic silica predictions downcore in Nanerersarpik record using best performing PLS models. Lower panel depicts past 4 kyr. 159

Figure 5.12 – PLS model loading plot for organic carbon PLS model TAS 10.1 160

CHAPTER 1

A HIGH RESOLUTION MID-PLEISTOCENE TEMPERATURE RECORD FROM ARCTIC LAKE EL'GYGYTGYN; A 50 KYR SUPER INTERGLACIAL FROM MIS 33-31?

1.1 Introduction

Placing predicted future climate change into a broader context necessitates detailed paleoclimate reconstructions that extend beyond the last glacial period, especially from high latitudes where such changes are expected to be the largest (Stocker et al., 2013). The term "super interglacial" has been used to describe periods in the past that appear to have been characterized by exceptionally warm conditions (DeConto et al., 2012; Melles et al., 2012; Pollard and DeConto, 2009), and as such are of great interest when searching for analogues of future climate. One such period is Marine Isotope Stage (MIS) 31, defined as 1.082-1.062 million years before present (Ma BP) by Lisiecki and Raymo (2005) (NB: in this study we refer to MIS boundaries as defined by the LR04 stack). Paleoclimate records from this period are desirable because MIS 31 falls beyond the current temporal range of the Antarctic ice cores, yet occurred during the Pleistocene, when the climate system and oceanographic gateways were generally similar to today.

MIS 31 was characterized by the highest summer insolation receipts at high latitudes of the past 1.2 Ma (Laskar et al., 2004), as well as some of the lowest oxygen isotopic values in the composite LR04 benthic stack (Lisiecki and Raymo, 2005). It has been identified as a period of extreme warmth in the southern high latitudes (e.g. Maiorano et al., 2009; Teitler et al., 2015) and is also the last time strong proxy evidence is available for a collapse of the West Antarctic Ice Sheet (WAIS) (McKay et al., 2012; Naish et al., 2009; Villa et al., 2012). In the Northern Hemisphere (NH), the vast majority of paleoclimate reconstructions that cover this period are marine sediment records, with notable exceptions being sediments from Lake Baikal (Khursevich

et al., 2005) and the Chinese loess archives (Sun et al., 2010). However, no high-resolution terrestrial paleotemperature reconstructions from MIS 31 currently exist.

Here we present data from the Lake El'gygytgyn (northeast Russia) sediment record, which provides continuous coverage of MIS 31 (Melles et al., 2012). Our high-resolution brGDGT-based paleotemperature reconstruction spans MIS 33-31 (~1114 – 1050 kyr BP) at a time step of approximately 500 years. We find that MIS 31 in the Arctic experienced some of the warmest temperatures of the Pleistocene, but that peak warmth occurred out of phase with local summer insolation. Additionally, it appears that glacial conditions preceding this interval, during glacial stage 32, were short-lived in the Arctic. This finding partially echoes recent evidence from the Southern Hemisphere (Teitler et al., 2015), where it was suggested that MIS 32 was warm at southern high latitudes and should be relegated to a stadial period instead of a glacial stage. The global signature of MIS 33-31 is discussed and potential teleconnections that could link changes in Antarctica and Lake El'gygytgyn are explored.

1.2 Site Description

The composite sediment core from Lake El'gygytgyn is exceptional in that it provides an archive of terrestrial paleoclimate covering the past 3.6 Ma (million years) from within the Arctic Circle (**Figure 1.1**) (Brigham-Grette et al., 2013). This site has already provided numerous insights into high latitude climate over the Plio-Pleistocene (Brigham-Grette et al., 2013; Melles et al., 2012; Climate of the Past Special Issue: Initial results from lake El'gygytgyn, western Beringia: first time-continuous Pliocene-Pleistocene terrestrial record from the Arctic), and MIS 31 has been identified as one of over a dozen "super interglacials" within this record. Warm conditions during this interval have been identified in other proxy reconstructions from Lake El'gygytgyn, such as pollen-based paleotemperatures, total organic carbon and biogenic silica concentrations, and elemental ratios (Melles et al., 2012).

Lake El'gygytgyn is located approximately 100 km north of the Arctic Circle in northeastern Siberia (67.5°N, 172°E) (**Figure 1.1**) and was created 3.58±0.25 Ma by a meteorite impact (Layer, 2000). The lake has a diameter of 12 km, with a total surface area of 110 km^2, and is 170 m deep. Today, the continental Arctic climate leads to tundra vegetation occupying the surrounding catchment and ice cover on the lake for 10 months of the year (Nolan and Brigham-Grette, 2007). The lake is classified as oligotrophic to ultra-oligotrophic, with full overturning occurring during the summer leading to an oxygenated water column throughout the year (Melles et al., 2012; Nolan and Brigham-Grette, 2007). Measurements from a thermistor string deployed in the lake indicates water temperatures vary from 0-4°C (Nolan and Brigham-Grette, 2007). Measured air temperatures at the lake over the calendar year 2002 indicate a mean annual air temperature (MAAT) of -10.3°C, with a maximum temperature of 26°C and a minimum of -40°C. Average temperatures in July were ~10°C, which was shown to be representative of the broader region (Nolan and Brigham-Grette, 2007).

The lake was drilled during the winter of 2008/2009, resulting in a composite sediment sequence of ~320 m. The age model for the core is based primarily on magnetostratigraphy and tuning of paleo-productivity proxies to the benthic oxygen isotope stack and insolation curves (Haltia and Nowaczyk, 2014; Nowaczyk et al., 2013). Age uncertainty during the MIS 31 section of the core is, therefore, related to uncertainties in the LR04 stack (estimated to be up to 6 kyr from 1 to 3 Ma), but Nowaczyk et al. (2013) note that "relative age assignments to the reference records should have a precision of ~500 yr since many (3rd order) tie points were derived from the insolation reference record, which has a higher temporal resolution". Identification of MIS 31 in the composite sequence is aided by the presence of the Jaramillo paleomagnetic reversal (0.991-1.073 Ma) (Haltia and Nowaczyk, 2014). For further details the reader is referred to Nowaczyk et al. (2013). Sedimentation rates were relatively high during the Pliocene (~50 cm kyr^{-1}), and then decreased during the Pleistocene (~4-5 cm kyr^{-1}), with brief intervals of much

higher sedimentation (Supplementary Materials) (Melles et al., 2012). During the MIS 35-29 study interval, the sedimentation rate varies from ~5-30 cm kyr^{-1} (Supplementary Materials). The MIS 31 section of the core spans approximately 100 cm.

For this study 143 sediment samples (~1-8 g dry mass) were taken spanning MIS 29-35 (approx. 1010-1145 kyr BP). The majority of samples from MIS 33-31 were taken at centimeter increments, resulting in a sample resolution of ~500 years per sample. The sediment was freeze-dried and homogenized using a mortar and pestle before lipid extraction.

A total lipid extract (TLE) was obtained using a Dionex accelerated solvent extractor (ASE 200). Samples were extracted with a dichloromethane (DCM)/methanol (9:1, v/v) mixture at 100°C. The TLE was then separated into two fractions, apolar (9:1 DCM:hexane, v/v) and polar (1:1 DCM:methanol), using alumina oxide column chromatography. Polar fractions were filtered in 99:1 hexane:isopropanol using a 0.45μm PTFE syringe filter. A C_{46} GDGT internal standard was added to all polar fractions prior to analysis.

BrGDGTs were identified and quantified via high performance liquid chromatography - mass spectrometry using an Agilent 1260 HPLC coupled to an Agilent 6120 MSD following the methods of Hopmans et al. (2000) with minor modifications (Schouten et al., 2007). For compound separation a Prevail Cyano column (150 x 2.1mm, 3 μm) was used. Two solvent mixtures were used as eluents: mixture A) 100% hexane; mixture B) 90% hexane, 10% isopropanol (v/v). Samples were eluted with 10% mixture B for 5 minutes, which was then linearly increased to 18% mixture B from minutes 5-39, and finally increased to 100% mixture B for one minute. Scanning was performed in selected ion monitoring (SIM) mode. Concentrations were calculated by comparing brGDGT HPLC-MS chromatogram peak areas with peak areas of a known concentration (C_{46} GDGT standard added to every sample run). These values were then normalized to the mass of sediment extracted.

Further paleoenvironmental conditions were reconstructed using two indices based on brGDGT concentrations as originally defined by Weijers et al. (2007). The first is the cyclisation ratio of branched tetraethers (CBT) (Eq. 1). This index measures the relative amount of cyclopentyl moieties in the branched GDGTs, which Weijers et al. (2007) found to be correlated to pH. The second index, the Methylation of Branched Tetraethers (MBT), measures the presence of methyl branches at the C-5 and C-5' positions and was found to be positively correlated to MAAT, and to a lesser extent, negatively correlated to pH (Eq. 2). By combining these two indices, Weijers et al. (2007) were able to produce a robust paleotemperature proxy for soil-derived brGDGTs. In recent years this MBT/CBT relationship has been expanded to include lake sediment samples, yielding numerous lake specific calibrations (e.g. (Loomis et al., 2012; Pearson et al., 2011; Sun et al., 2011; Tierney et al., 2010). For this study the calibration of Sun et al. (2011) (Eq. 3) was applied to reconstruct temperature. In equations 1 and 2 the roman numerals and letters denote the different brGDGT structures as shown in Figure A1, Appendix A in Weijers et al. (2007).

Eq. 1: $\mathbf{CBT} = \frac{[\mathbf{Ib}]+[\mathbf{IIb}]}{[\mathbf{I}]+[\mathbf{II}]}$ (Weijers et al., 2007)

Eq. 2: $\mathbf{MBT} = \frac{[\mathbf{I+Ib+Ic}]}{[\mathbf{I+Ib+Ic}]+[\mathbf{II+IIb+IIc}]+[\mathbf{III+IIIb+IIIc}]}$ (Weijers et al., 2007)

Eq. 3: $\boldsymbol{T = 6.803 - 7.602 \times CBT + 37.090 \times MBT}$ (Sun et al., 2011)

1.3 Methods

For this study 143 sediment samples (~1-8 g dry mass) were taken spanning MIS 29-35 (approx. 1010-1145 kyr BP). The majority of samples from MIS 33-31 were taken at centimeter increments, resulting in a sample resolution of ~500 years per sample. The sediment was freeze-dried and homogenized using a mortar and pestle before lipid extraction.

A total lipid extract (TLE) was obtained using a Dionex accelerated solvent extractor (ASE 200). Samples were extracted with a dichloromethane (DCM)/methanol (9:1, v/v) mixture at 100°C. The TLE was then separated into two fractions, apolar (9:1 DCM:hexane, v/v) and polar (1:1 DCM:methanol), using alumina oxide column chromatography. Polar fractions were filtered in 99:1 hexane:isopropanol using a 0.45μm PTFE syringe filter. A C_{46} GDGT internal standard was added to all polar fractions prior to analysis.

BrGDGTs were identified and quantified via high performance liquid chromatography - mass spectrometry using an Agilent 1260 HPLC coupled to an Agilent 6120 MSD following the methods of Hopmans et al. (2000) with minor modifications (Schouten et al., 2007). For compound separation a Prevail Cyano column (150 x 2.1mm, 3 μm) was used. Two solvent mixtures were used as eluents: mixture A) 100% hexane; mixture B) 90% hexane, 10% isopropanol (v/v). Samples were eluted with 10% mixture B for 5 minutes, which was then linearly increased to 18% mixture B from minutes 5-39, and finally increased to 100% mixture B for one minute. Scanning was performed in selected ion monitoring (SIM) mode. Concentrations were calculated by comparing brGDGT HPLC-MS chromatogram peak areas with peak areas of a known concentration (C_{46} GDGT standard added to every sample run). These values were then normalized to the mass of sediment extracted.

Further paleoenvironmental conditions were reconstructed using two indices based on brGDGT concentrations as originally defined by Weijers et al. (2007). The first is the cyclisation ratio of branched tetraethers (CBT) (Eq. 1). This index measures the relative amount of cyclopentyl moieties in the branched GDGTs, which Weijers et al. (2007) found to be correlated to pH. The second index, the Methylation of Branched Tetraethers (MBT), measures the presence of methyl branches at the C-5 and C-5’ positions and was found to be positively correlated to MAAT, and to a lesser extent, negatively correlated to pH (Eq. 2). By combining these two indices, Weijers et al. (2007) were able to produce a robust paleotemperature proxy for soil-

derived brGDGTs. In recent years this MBT/CBT relationship has been expanded to include lake sediment samples, yielding numerous lake specific calibrations (e.g. (Loomis et al., 2012; Pearson et al., 2011; Sun et al., 2011; Tierney et al., 2010). For this study the calibration of Sun et al. (2011) (Eq. 3) was applied to reconstruct temperature. In equations 1 and 2 the roman numerals and letters denote the different brGDGT structures as shown in Figure A1, Appendix A in Weijers et al. (2007).

Eq. 1: $\mathbf{CBT} = \frac{[\mathbf{Ib}]+[\mathbf{IIb}]}{[\mathbf{I}]+[\mathbf{II}]}$ (Weijers et al., 2007)

Eq. 2: $\mathbf{MBT} = \frac{[\mathbf{I+Ib+Ic}]}{[\mathbf{I+Ib+Ic}]+[\mathbf{II+IIb+IIc}]+[\mathbf{III+IIIb+IIIc}]}$ (Weijers et al., 2007)

Eq. 3: $\boldsymbol{T = 6.803 - 7.602 \times CBT + 37.090 \times MBT}$ (Sun et al., 2011)

1.4 Results

Branched GDGT results from this study are plotted in **Figure 1.2**. brGDGTs are present in all samples analyzed in this study. Total brGDGT concentrations vary from 0.0039 μg/g sediment to 1.039 μg/g sediment, with a mean concentration of 0.23 μg/g sediment. Generally, concentrations are higher during inferred interglacial periods, with the notable exception of ~1100-1110 kyr BP, when the highest concentrations of the studied interval occur briefly during glacial MIS 32. Values for the MBT Index range from 0.075 to 0.36, with a mean of 0.22. The CBT Index ranges from 0.084 to 1.37 with a mean of 0.48.

Reconstructed temperatures based on the MBT/CBT index vary from between 17.3 and 4.0°C, with a mean value of 11.8°C using the calibration of Sun et al. (2011). Twenty eight samples were run in duplicate, with a standard error of 0.1°C. Temperatures rise from 6-8°C during MIS 34 to ~14-17°C during MIS 33 (**Figure 1.2**). Temperatures then decrease relatively rapidly to between 4 and 8°C at the start of MIS 32. This cooling is short-lived, however, with temperatures rising to ~13°C after only a few thousand years. Temperatures remain generally

warm but variable until ~1088 kyr BP, when an increase of 4.5°C is observed. This extreme warmth during MIS 32, reaching 17.5°C, is supported by 4 samples representing ~2,000 years. Temperatures then rapidly decrease back to around 13°C. They slowly rise during the traditional definition of the beginning of MIS 31 to ~16°C before declining into glacial MIS 30, punctuated by numerous episodes of abrupt temperature change (4-5°C over less than a thousand years).

Reconstructed pH using the calibration of Sun et al. (2011) yields a maximum of 8.8 and a minimum pH of 7.3 (mean of 8.2). While reconstructed pH does generally seem to covary with reconstructed temperature, there are periods when large changes in pH are not accompanied by a major temperature change (e.g. ~1093-1092 kyr BP) and vice versa (1108-1107 kyr BP) (**Figure 1.2**).

1.5 Discussion

1.5.1 brGDGT temperature reconstruction

Our paleotemperature reconstructions are based on concentrations of brGDGTs extracted from sediments. These compounds are bacterial membrane lipids that differ in the number of methyl branches and cyclopentane groups in their structures (Hopmans et al., 2004). The distribution of these methyl branches and cyclopentyl moieties was originally shown to be related to temperature and, to a lesser extent, pH, in soils and peat (Weijers et al., 2007). This relationship has since been observed in lake sediments as well, with increasing evidence for autochthonous production of brGDGTs in the water column (e.g. Loomis et al., 2014; Tierney et al., 2010). Modern calibration studies are used to derive pH and air temperature estimates from brGDGT distributions back through time (e.g (Loomis et al., 2012; Pearson et al., 2011; Tierney et al., 2010).

In this study, temperature reconstructions using the CBT and MBT indices were calculated based on the calibration of Sun et al. (2011) (Eq. 3). This decision was based mainly

on the fact that this calibration is in agreement with reconstructed mean temperature of the warmest month (MTWM) estimates from pollen data over the same interval (purple line, **Figure 1.3**). It also incorporates lake-derived data from China and Nepal, the spatially closest sites to Lake El'gygytgyn. We note that applying other lake-specific MBT/CBT calibrations (e.g Loomis et al., 2012; Tierney et al., 2010; Yang et al., 2014) produces a wide range of absolute temperatures (differences of up to 6°C for the same sample). However, relative temperature changes are similar regardless of which MBT/CBT calibration is applied. We have also applied brGDGT fractional abundance calibrations (e.g. Loomis et al., 2012; Pearson et al., 2011; Tierney et al., 2010), but those resulted in numerous unrealistic (>30°C) temperatures at certain periods in the record. We also note recent research suggesting the dependence of MBT on pH is related to incomplete separation of 6-methyl isomers on all penta- and hexa-methylated brGDGTs using current methods (De Jonge et al., 2013, 2014). While we are aware of this new methodology to separate these isomers, the majority of our analyses were carried out prior to the publication of this method.

We suggest that the majority of brGDGTs that have accumulated in Lake El'gygytgyn sediments were not sourced from catchment soils and likely come from *in-situ* production in the water column. While we cannot entirely rule out production in the sediments themselves, numerous studies have shown that the majority of brGDGTs are being produced in the upper water column (e.g. Buckles et al., 2014; Loomis et al., 2014). Because the catchment of Lake El'gygytgyn is roughly circular and bounded by the crater walls formed from the meteorite impact, the basin (15km in diameter) drains a small area relative to the size of the lake (12km in diameter). The lake is also surrounded by continuous permafrost (Nolan and Brigham-Grette, 2007), and a preliminary analysis of a soil core collected from within the catchment was essentially bereft of brGDGTs (Bischoff, pers. comm. 2014). Additionally the bottom water temperature of Lake El'gygytgyn remains a nearly constant 4°C throughout the year (Nolan and

Brigham-Grette, 2007), inconsistent with the large variations seen in MBT values and reconstructed temperature.

We also assume that our reconstruction represents summer temperature. Studies from mid to high latitude lakes have noted the strongest relationship between brGDGT indicies and summer/warm months temperature (Pearson et al., 2011; Shanahan et al., 2013; Sun et al., 2011). Shanahan et al. (2013) note that this warm season bias is likely due to increased biological productivity during the summer months (higher temperatures, lakes are ice-free, greatest number of daylight hours). Lake El'gygytgyn is currently only ice free for approximately two months during July and August (Nolan and Brigham-Grette, 2007), and it is likely that the majority of primary production at/in the lake occurs during this period. Mean summer temperatures at the lake today are ~10°C, which compares favorably with our reconstructions based on the Sun et al. (2011) calibration (**Figure 1.3**). We note, however, that without a site-specific calibration, or at least more knowledge of local sources of GDGT production, absolute temperature reconstructions using any external calibration should be regarded with caution. In spite of this uncertainty, we expect relative temperature changes reconstructed using the MBT/CBT proxy to be robust, as supported by temperature reconstructions from pollen assemblage data, and these changes form the basis for the majority of our conclusions.

1.5.2 Super Interglacial MIS 31 at Lake El'gygytgyn

While we hesitate to draw conclusions on the absolute temperature values reached during the studied interval due to the calibration issues mentioned above, numerous interesting features are apparent based on relative temperature changes. The first is the apparent warm nature of glacial MIS 32 at Lake El'gygytgyn (**Figure 1.3**). Average brGDGT based temperatures for MIS 33-31 are shown in Table 1. Mean temperatures during MIS 32 (1081-1104 kyr) are only ~0.5°C lower than MIS 31, and only 0.1°C lower than MIS 33 (similar regardless of MBT/CBT

calibration chosen). Cold conditions are recorded only briefly for ~2 kyr centered around 1102 kyr BP (**Figure 1.3**). This warming pattern shows a dramatic departure from both boreal summer insolation and the LR04 stack, suggesting that other factors were influencing climate at Lake El'gygytgyn during this time.

Other published proxies from the lake provide limited insight on this observation (**Figure 1.3**) (Melles et al., 2012). Mean temperature of the warmest month (MTWM) estimates based on pollen reconstructions, which agree well with our brGDGT data during most of MIS 31, deviate in the early part of MIS 31/late 32 (where only 3 data points exist). The % of tree and shrub pollen in the lake shows a dramatic increase between 1091.5 kyr and 1086 kyr BP, well before peak NH insolation, but low sample resolution, along with the potential influence of precipitation on vegetation, precludes robust conclusions. The accumulation of biogenic silica (based on Si/Ti ratios) steadily increases from a minima ~1101 kyr BP (the same time the lowest brGDGT temperatures for MIS 32 are recorded) to a maximum ~1072 kyr BP. While it does not display the dramatic fluctuations seen in the MBT/CBT data, it does appear that the low productivity seen around 1100 kyr BP was short lived during MIS 32. Perhaps most notable is the presence of the characteristic "super interglacial" sediment facies during MIS 32 at Lake El'gygytgyn (Melles et al., 2012) (**Figure 1.3**), suggesting extremely warm conditions at the lake prior to the traditional definition for the onset of MIS 31.

Also worth noting is the presence of abrupt episodes of both warming and cooling throughout the high-resolution section of our record. Perhaps most notable is the relatively abrupt warming event just prior to the onset of MIS 31 (ca. 1087-1084 kyr BP), which is defined by multiple data points. This event is close in timing to a small peak noted in the global benthic $\delta^{18}O$ record within the MIS 31 interval (**Figure 1.4**) and considering uncertainties in both age models, may be coincident. While this event has not yet been resolved in other marine or terrestrial records lacking the resolution of the Lake El'gygytgyn core, it may have been global, given similarities in timing to the excursion in the benthic $\delta^{18}O$ record.

In summary, our record demonstrates considerable high-frequency variability in temperature during this time interval. It also suggests that the entire period encompassing MIS 33-31 was generally warm in the Arctic. Existing proxies from Lake El'gygytgyn either suggest that warm conditions prevailed at the lake prior to the traditional definition of MIS 31, or are of insufficient resolution to rule out this possibility. Further analyses, including higher resolution pollen sampling and the determination of the deuterium isotopic composition of leaf waxes, will help confirm this assertion.

1.5.3 Global Signature of MIS 33-31

The observation that Lake El'gygytgyn appears warm during MIS 32 echoes recent findings from high southern latitudes (Teitler et al., 2015), where the majority of research pertaining to MIS 31 explicitly has been carried out to date (DeConto et al., 2012; Maiorano et al., 2009; McKay et al., 2012; Villa et al., 2008, 2012). Results from the ANDRILL project (McKay et al., 2012; Naish et al., 2009; Scherer et al., 2008; Villa et al., 2012) noted the presence of diatomite and presumed open water conditions at the coring site in the Ross Sea (**Figure 1.1**), implying a dramatically reduced West Antarctic Ice Sheet (WAIS) during this time. A large-scale reduction in WAIS is further supported by the modeling studies of Pollard and DeConto (2009) and DeConto et al. (2012). The authors also found reduced sea ice concentrations around the entire continent. Elsewhere around the Antarctic margin, Villa et al. (2008) found evidence for a major shift in dominant circulation patterns in the form of a decrease or disappearance of the Polar Front (indicated by increases in warm water nannofossil assemblages) at Sites 1165 and 1167 (Prydz Bay, East Antarctica) (**Figure 1.1**). This finding was echoed further from the Antarctic continent, with evidence for a southward migration of the Subtropical Front at Site 1090 (Maiorano et al., 2009) (**Figure 1.1**).

Although MIS 31 has been identified as an exceptional event in the SH, the exact timing of warmth is still a subject of debate. The majority of the studies mentioned above ascribed peak interglacial conditions to ~1080 kyr BP, when austral summer insolation was at a maximum (~10 kyr earlier than the boreal summer insolation peak during MIS 31 ~1070 kyr) (**Figure 1.4**). However, a recent study by Teitler et al. (2015) revisited the age models of the ANDRILL, CRP-1 (Cape Roberts), Site 1165 and Site 1090 records and concluded that a secondary interpretation may be that warm conditions actually began earlier, during MIS 33. The authors also analyzed iceberg rafted detritus (IRD) and found minimal accumulation of IRD across the entirety of MIS 33-31 at Site 1090 (Teitler et al., 2015). The timing of the decrease in IRD agrees strongly with our reconstructed warm temperatures at Lake El'gygytgyn (**Figure 1.4**). In summary, Teitler et al. (2015) suggest that glacial MIS 32 be relegated from a glacial stage to a stadial and that MIS 31 be reclassified as a longer interglacial more akin to later post Mid-Pleistocene Transition interglacials, lasting closer to 50 kyr BP instead of the ~20 kyr as it is currently defined. The authors point to another SH austral insolation peak at the beginning of MIS 33 as the potential catalyst for the beginning of this long interglacial.

The apparent strong linkage between Lake El'gygytgyn and records from the Antarctic margin has been highlighted previously (Melles et al., 2012; Brigham-Grette et al. 2013). The authors suggest that dramatic warming in the SH (reduction of WAIS, less sea ice) would lead to reduced Antarctic Bottom Water (AABW) production during this time (e.g. McKay et al., 2012). Less AABW production could lead to decreased northward flow of deep water into the North Pacific, subsequently reducing upwelling and increasing water column stratification (Melles et al., 2012). The resulting increase in sea surface temperature might then lead to changes in air temperature at Lake El'gygytgyn, although this has not been supported by modeling efforts to date (Melles et al., 2012). Possible evidence for this mechanism operating during MIS 31 comes in the form of lower concentrations of sortable silt off the coast of New Zealand (Hall et al.,

2001) as well as low rates of biogenic silica accumulation at Site 882 in the North Pacific (Haug et al., 1999) (**Figure 1.1**).

Previously this reduction of AABW and subsequent changes in ocean circulation has been suggested as a mechanism for the warmth of MIS 31 proper. However, existing proxy records have not been of sufficient resolution to investigate more intricate timing and relationships with insolation or other global climate records such as the benthic oxygen isotope stack (Lisiecki and Raymo, 2005). In light of our temperature reconstruction, however, it could be interpreted as a mechanism that can explain the warmth during MIS 32 (when SH insolation was high, prior the NH peak) (**Figure 1.4**). A recent study by Hao et al. (2015) also pointed to changes in Antarctic ice volume driving prolonged interglacial conditions in the NH during MIS 15-13. More research is required to substantiate this interhemispheric linkage, but it does provide a plausible explanation for the apparent connection between SH records and the warming seen in western Beringia.

Looking beyond the poles, paleotemperature reconstructions that cover this period in sufficient resolution to be meaningful are generally limited to sea surface temperature (SST) records (**Figure 1.5**). While a limited number of terrestrial archives do span MIS 31, existing data are mainly limited to indirect climate proxies: biogenic silica from Lake Baikal (Khursevich et al., 2005), magnetic susceptibility and grain size from Chinese loess (Sun et al., 2010). However, these proxies more closely track local summer insolation values. Of the SST data plotted here, the majority are part of longer time-series, and as such have not been interpreted in relation to MIS 31 specifically. Interestingly, however, the majority of data suggest that MIS 32 was either reduced in duration or magnitude, similar to our Lake El'gygytgyn data. The upper part of Figure 5 (Sites 722-1123) depicts SST records where MIS 32 appears to be a relatively "weak" glacial compared to other cold periods. Cooling within the shaded area (MIS 33-31) does not seem to reach the low temperatures of MIS 34 or 30, for example. The lower section of **Figure 1.5** (Sites 882-1090) alternatively suggests that although cooling may have reached a similar magnitude as

other mid-Pleistocene glacial periods, the duration appears abbreviated (only a few kyr). Closer analysis of the LR04 benthic stack also indicates that MIS 32 was a weaker glacial period compared to 34 and 30. It also suggests, however, that at least some return to glacial conditions must have occurred (high $\delta^{18}O$ values around 1100 kyr BP).

More widely distributed high-resolution records are required to provide a definitive answer on the glacial versus stadial nature of MIS 32 globally. The highest resolution ocean SST records presented here have a resolution of 1-2 kyr (Herbert et al., 2010), and in many cases the "glacial" temperatures representing MIS 32 (**Figure 1.5**) are represented by only one or two data points. Alternatively other records spanning this interval may be missing the coldest periods of MIS 32. However, based on the available evidence from the Beringian Arctic, high southern latitudes, and existing SST records, it seems that MIS 32 was reduced in magnitude and/or duration relative to other glacial intervals of the Pleistocene.

The underlying cause of the protracted warmth around MIS 31 remains elusive. The unique nature of this super interglacial is thought to have occurred largely in response to summer insolation during this time (DeConto et al., 2012), which was anomalously high (especially at the poles) due to the concurrence of high obliquity and high eccentricity. Insolation values at 65°N in July for instance, were nearly 30 Wm^{-2} higher during peak MIS 31 than our current interglacial (Laskar et al., 2004). In the NH, however, peak boreal insolation occurs ~1070 kyr BP, significantly after peak temperatures are recorded at Lake El'gygytgyn (**Figure 1.4**). SH austral summer insolation is highest one half a precession cycle earlier (~1080 kyr BP), but again this is too late to explain the warming suggesting by Teitler et al. (2015), and our temperature record beginning at MIS 33 (~1114 kyr BP). In relation to our temperature reconstruction, it is plausible that the alternating insolation peaks between hemispheres, separated by half a precession cycle, could register as a continued period of warmth at Lake El'gygytgyn, through oceanic teleconnections linked to Antarctic ice volume. It seems unlikely, however, that insolation alone triggered a substantial WAIS retreat at the beginning of MIS 33 (when maximum austral

insolation values reached only ~511 Wm^{-2} at the end of the interglacial (Laskar et al., 2004) (**Figure 1.4**).

While greenhouse gas concentrations likely played a role, their relative contribution remains unresolved. High concentrations of CO_2 have been explored as a possible forcing in model simulations during MIS 31 (DeConto et al., 2012), but current proxy reconstructions are of insufficient resolution and/or fidelity to be definitive. While there may be a relative peak in CO_2 concentrations in the reconstruction of Honisch et al. (2009) ~1 Ma BP it is only supported by 2-3 data points. Generally, existing CO_2 reconstructions do not suggest dramatically higher concentrations relative to other Pleistocene interglacials (Honisch et al., 2009; Tripati et al., 2011).

More research is needed to definitively characterize MIS 32 at Lake El'gygytgyn. Lower "glacial" temperatures are recorded during MIS 32 in our brGDGT data, albeit briefly, and the question of glacial stage versus stadial could change depending on whether duration or intensity is deemed more important. Extension of pollen analyses back to MIS 33 and planned deuterium istotopic analyses of leaf waxes will provide further independent reconstructions to compare to our brGDGT temperatures. More global high-resolution records will similarly be of great use in determining the true nature of this period.

1.6 Conclusions

BrGDGTs are present in the Lake El'gygytgyn sediment record throughout the interval surrounding MIS 31, and reconstructed temperatures are in agreement with pollen based summer temperature estimates from the same interval. While we acknowledge the absolute reconstructed temperatures using this methodology are reliant on the calibration chosen and should be treated with caution, relative temperature changes revealed by the brGDGT record nevertheless provides insight into the pattern of temperature variability, duration and intensity of super interglacial MIS

31 in the terrestrial Arctic. Our high-resolution reconstruction displays numerous abrupt temperature changes on the order of 4-6°C over a few thousand years or less. Additionally it appears that apart from a brief period ~1104 kyr BP, conditions at Lake El'gygytgyn were relatively warm during glacial Stage MIS 32. While this finding echoes recent results from the SH, more research is needed to determine whether the entire period of MIS 33-31 should be reclassified as one long interglacial. Should this prove true, it would add to the complexity surrounding the Mid-Pleistocene Transition.

Table 1.1: Average reconstructed temperatures from MIS 33-31

Marine Isotope Stage	Average MBT/CBT Temperature (°C)	Minimum Temperature (°C)	Maximum Temperature (°C)
31	12.8	8.6	16.0
32	12.2	5.6	17.3
33	12.3	11.6	17.2

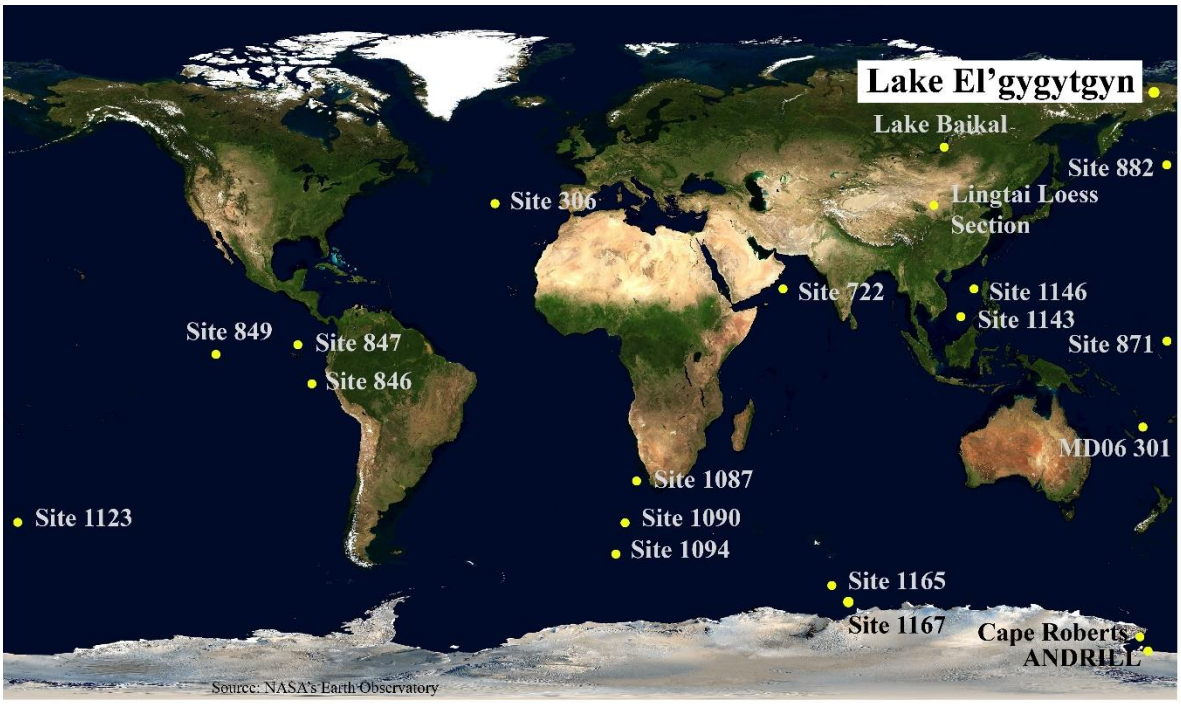

Figure 1.1 - Approximate location of Lake El'gygytgyn in NE Siberia and other locations relevant to this study. Background image source: NASA's Earth Observatory.

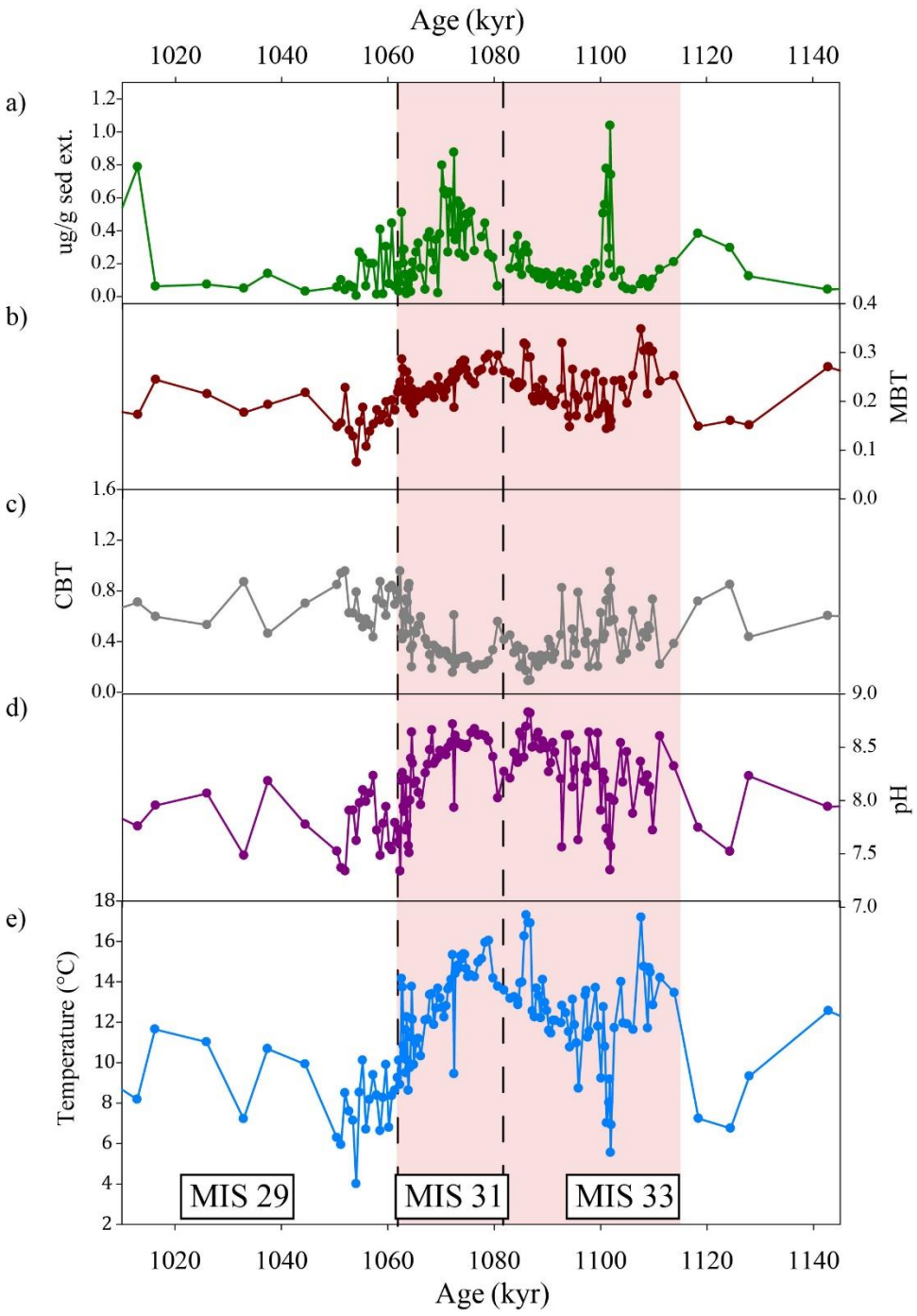

Figure 1.2 - brGDGT results from MIS 35-29 at Lake El'gygytgyn: a) concentrations of total brGDGTs relative to grams sediment extracted; b) MBT, c) CBT, and d) pH values calculated using equation of Weijers et al., (2007); e) MBT/CBT based temperatures calculated using equation of Sun et al. (2011). Pink shading denotes period from start of MIS 33 (1114 kyr BP) to end of MIS 31 (1062 kyr BP), dashed lines denote duration of MIS 31.

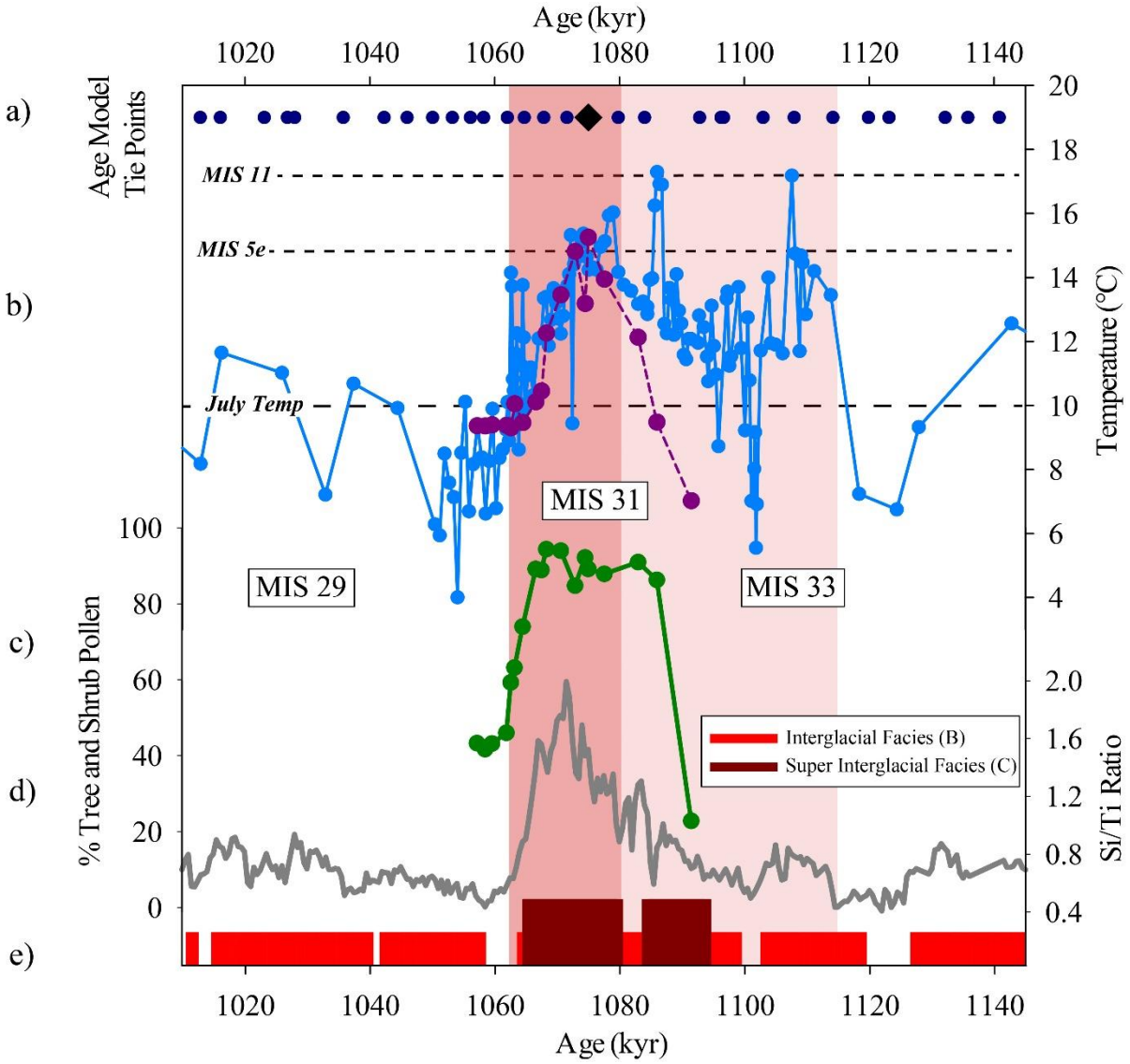

Figure 1.3 - Compilation of proxy data from Lake El'gygytgyn: a) brGDGT based temperatures (blue) (this study); pollen based mean temperature of the warmest month (MTWM) estimates (purple) (Melles et al., 2012); b) % tree and shrub pollen at the lake (green) (Melles et al., 2012); c) ratio of silica to titanium (Si/Ti) (gray), interpreted as a proxy for primary productivity. d) Red bars in bottom panel denote presence of interglacial (red) or super interglacial (dark red) facies (Melles et al., 2012). Long dashed line at 10ºC indicates modern mean July temperature. Maximum brGDGT temperature estimates from other Pleistocene interglacials and modern mean July temperatures indicated with shorter dashed lines (data from Brigham-Grette and Nolan, 2007; Habicht et al., in prep; Castañeda et al., in prep). Light pink shading denotes entire period from MIS 33-31 (1114-1062 kyr BP), darker pink shading denotes tranditional definition of MIS 31 (1082-1062 kyr BP) (Lisiecki and Raymo, 2005).

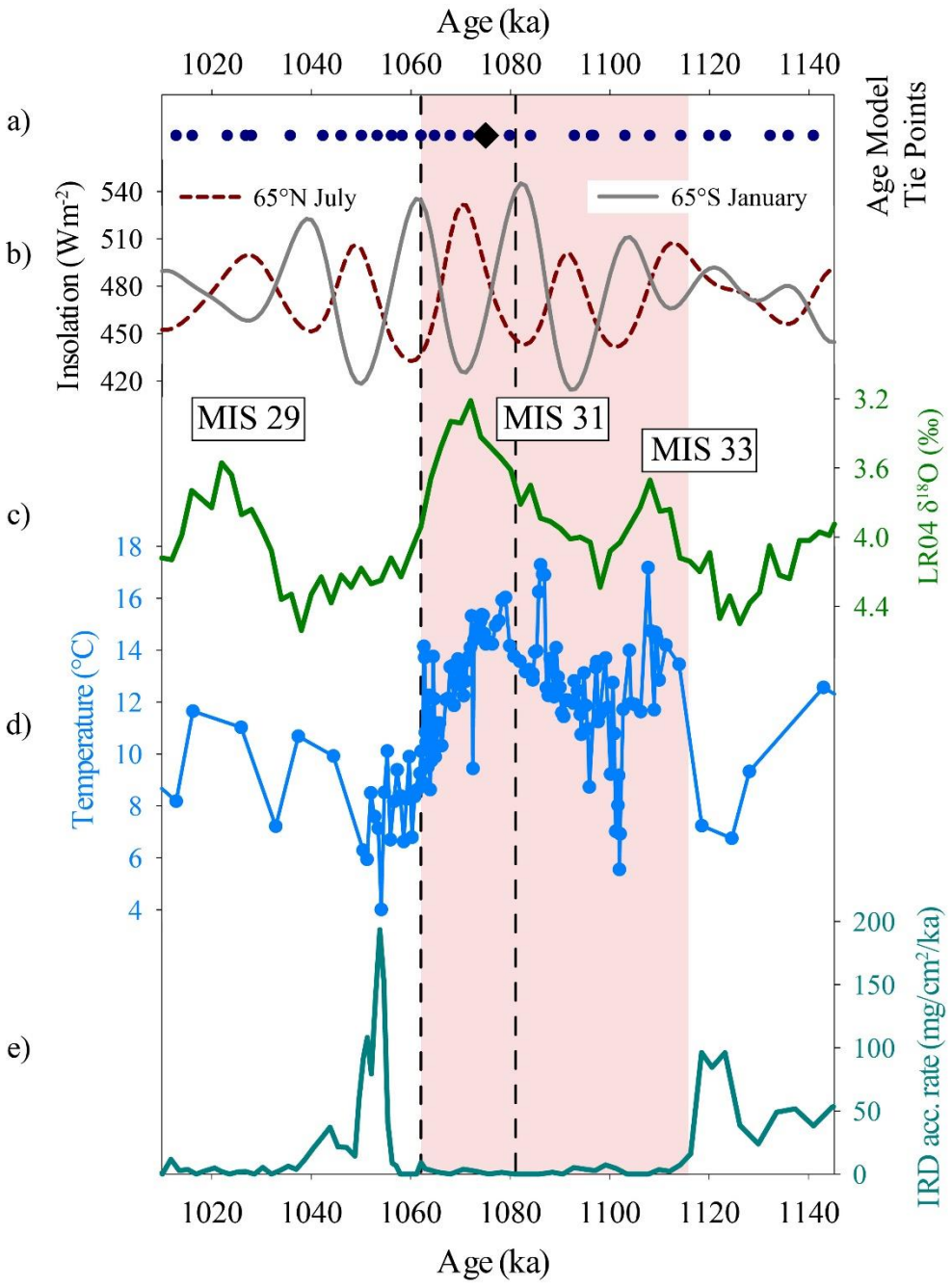

Figure 1.4 - a) Insolation values for 65°N (dashed red line) and 65°S (gray line) (Berger and Loutre, 1991); b) LR04 benthic stack (Lisiecki and Raymo, 2005); c) MBT/CBT temperature values from Lake El'gygytgyn (this study); d) and accumulation rate of IRD (ice-rafted detritus) from Site 1090 in South Atlantic (Teitler et al., 2015). Pink shading denotes period from start of MIS 33 (1114kyr BP) to end of MIS 31 (1062 kyr BP), dashed lines indicate traditional defintion of MIS 31 (1082-1062 kyr BP) (Lisiecki and Raymo, 2005).

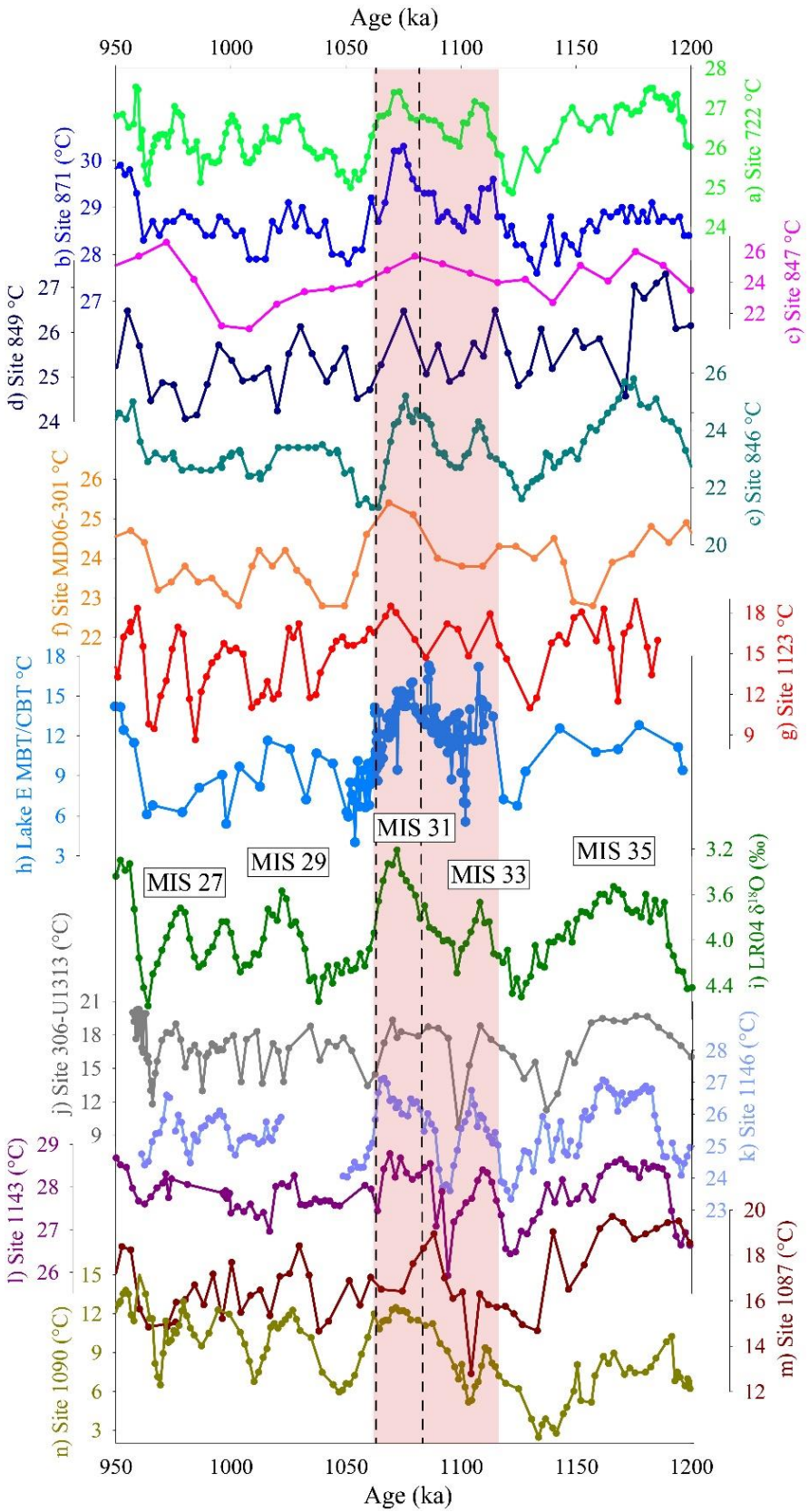
Age (ka)
950
1000
1050
1100
1150
1200
a) Site 722 °C
b) Site 871 (°C)
c) Site 847 °C
d) Site 849 °C
e) Site 846 °C
f) Site MD06-301 °C
g) Site 1123 °C
h) Lake E MBT/CBT °C
i) LR04 δ18O (‰)
j) Site 306-U1313 (°C)
k) Site 1146 (°C)
l) Site 1143 (°C)
m) Site 1087 (°C)
n) Site 1090 (°C)
MIS 27
MIS 29
MIS 31
MIS 33
MIS 35

Figure 1.5 - Compilation of existing paleotemperature records of sufficient resolution to be relevant spanning MIS 31. Upper panel (Sites 772- 1123) depicts records where magnitude of cooling during MIS 32 appears reduced relative to other Early Pleistocene glacial periods: a) Site 772 (16°N, Herbert et al., 2010), b) Site 871 (5°N, Dyez et al., 2014), c) Site 847 (0°N, Medina-Elizalde et al., 2008), d) Site 849 (0°N, McClymont and Rosell-Melé, 2005), e) Site 846 (3°S, Herbert et al., 2010), f) Site MD06-301 (23°S, Russon et al., 2011), g) Site 1123 (41°S, Crundwell et al., 2008). Middle panel depicts h) biomarker based temperatures from Lake El'gygytgyn (this study) and i) the LR04 benthic stack (Lisiecki and Raymo, 2005) along with labels denoting marine isotope stages. Lower panel shows locations (Sites 306-1090) where, while cold "glacial" temperatures are recorded during MIS 32, the duration of cooling during appears abbreviated: j) Site 306-U1313 (41°N, Naafs et al., 2013), k) Site 1146 (19°N, Herbert et al., 2010), l) Site 1143 (9°N, Li et al., 2011), m) Site 1087 (31°S, McClymont et al., 2005b), n) Site 1090 (42°S, Martinez-Garcia et al., 2010).

CHAPTER 2

HOLOCENE GLACIER ACTIVITY RECONSTRUCTED FROM PROGLACIAL LAKE GJØAVATNET ON AMSTERDAMØYA, NW SVALBARD

2.1 Introduction

Reliable and highly resolved paleoclimate reconstructions are necessary in order to better contextualize recent and predicted climate change (Kaplan and Wolfe, 2006), especially from high latitudes where these changes are expected to be greatest (Callaghan et al., 2010; Serreze and Barry, 2011; Stocker et al., 2013). Glaciers and small ice caps respond rapidly to climate variations, but direct evidence for past changes in ice extent in remote areas is temporally and spatially limited. The Holocene Epoch (past ~11.7 thousand calendar years before present (cal kyr BP)) provides important context to understand Arctic climate dynamics because atmospheric and ocean circulation patterns were similar to their current configuration and natural insolation forcing caused widespread environmental change without the overprint of significant anthropogenic influence (until recent decades) (Johnsen et al., 2001; Kaufman et al., 2004; Mayewski et al., 2004). Broad scale Arctic climate throughout this interval is understood to have been characterized by early Holocene warmth that progressively transitioned toward a colder late Holocene (i.e., the Neoglacial), driven mainly by declining high latitude summer insolation (Laskar et al., 2004; Miller et al., 2010; Briner et al., 2016). Superimposed on this trend are spatial heterogeneities linked to the decaying Northern Hemisphere ice sheets and associated meltwater pulses (e.g. Sejrup et al., 2016). High-resolution paleoclimate records are important to better examine the timing, expression, and magnitude of Holocene climate change throughout the Arctic.

The Svalbard archipelago is uniquely situated at the intersection between the northern North Atlantic and the Arctic Ocean basins (**Figure 2.1**). Near Svalbard, warm Atlantic Water transported via the West Spitsbergen Current (WSC) mixes with cold, less saline water from the

Arctic Ocean. Atmospheric conditions are influenced by the relative influence of cold, polar-derived air masses from the north and east and warmer subpolar maritime air masses from the south and south west (Førland et al., 2011). The relative locations of these important boundaries, along with associated sea ice feedbacks, has been shown to vary throughout the Holocene and influence climate in Svalbard (Müller et al., 2012; Rasmussen et al., 2014; Werner et al., 2013, 2015).

Broadly, evidence from marine records near Svalbard and in the northern North Atlantic suggests a warm early Holocene period (~11-8 kyr BP), characterized by an increased flux of Atlantic water to high latitudes (Aagaard-Sørensen et al., 2014; Forwick and Vorren, 2009; Hald et al., 2004, 2007; Müller et al., 2012; Rasmussen et al., 2014; Risebrobakken et al., 2011; Sarnthein et al., 2003; Skirbekk et al., 2010; Ślubowska et al., 2005; Werner et al., 2013, 2015). The transition to cooler (Neoglacial) conditions during the middle Holocene is not well constrained, with some records suggesting cooling began as early 8.8 cal kyr BP (e.g. Hald et al., 2004), while others point to cooling beginning ~6 kyr BP (e.g. Rasmussen et al., 2014). Oceanic conditions near Svalbard during the late Holocene are generally characterized by cold temperatures overprinted by fluctuations linked to changes in the advection of warm Atlantic Water in the WSC (e.g. Aagaard-Sørensen et al., 2014; Berben et al., 2014; Ślubowska et al., 2005; Werner et al., 2013).

While there has been an increase in the number of terrestrial Holocene paleoclimate studies from Svalbard in recent years (e.g. D'Andrea et al., 2012; Reusche et al., 2014; Røthe et al., 2015; van der Bilt et al., 2015; van der Bilt et al., 2016; Gjerde et al., *in press*; Balascio et al., *in press*), this region generally lacks continuous, well-dated paleoenvironmental reconstructions. Retreat of the Barents Sea ice sheet had begun during the end of the Pleistocene (~20-14 cal kyr BP) (Gjermundsen et al., 2013; Hormes et al., 2013; Ingólfsson and Landvik, 2013), and numerous records suggest many smaller glaciers in Svalbard retreated or completely melted during the early Holocene (Reusche et al., 2014; Røthe et al., 2015; Snyder et al., 2000; Svendsen

and Mangerud, 1997; van der Bilt et al., 2015). The timing of late-Holocene glacial re-advance however, remains poorly constrained; some studies suggest glaciers advanced ~3-4 cal kyr BP (Reusche et al., 2014; Røthe et al., 2015; Svendsen and Mangerud, 1997), while others point to a later advance closer to 1 cal kyr BP (Humlum et al., 2005; Snyder et al., 2000; van der Bilt et al., 2015).

Here we present a glaicer reconstruction from proglacial lake Gjøavatnet on the island of Amsterdamøya in NW Svalbard spanning the Holocene (**Figure 2.1**). The objective of this study is to reconstruct the history of the upstream Annabreen glacier (**Figure 2.1**) towards a better understanding of Holocene climate change in the region. The maritime climate of Amsterdamoya, and the presence of a glacier in the Gjoavatnet catchment, makes this record valuable for addressing questions about past climate variations in the High Arctic North Atlantic. Our record suggests that Annabreen disappeared or was dramatically reduced in size by ~8.4 cal kyr BP. During the interval 8.4 – 1 cal kyr BP, sedimentation in the lake was marked by higher amounts of organic material accumulation, but was punctuated by multi-centennial-length periods with relatively lower organic matter content. A return to minerogenic sedimentation at 1 cal kyr BP is interpreted to represent the re-advance of Annabreen at that time.

2.2 Regional Setting

Svalbard's climate is characterized by highly variable temperatures and low average annual precipitation. A meteorological station at Ny-Ålesund, ~95 km south of Amsterdamøya, recorded average annual temperatures of -5.2°C over the period 1981-2010, though average temperatures of individual years ranged from -12°C to 3.8°C (Førland et al., 2011). The average annual precipitation at Ny-Ålesund is 427 mm (Førland et al., 2011), with the majority of moisture sourced from the south/southwest and occurring during the fall and winter months (Førland et al., 2011). The dry nature of this environment suggests that relatively small changes in

the precipitation budget could play a large role in the mass balance of local glaciers. There is a positive relationship between temperature and precipitation in all seasons (Førland et al., 2011).

Lake Gjøavatnet (79°46'00"N, 10°51'45"E, 2 m a.s.l.) is a small proglacial lake on the eastern coast of Amsterdamøya, Svalbard (**Figure 2.1**). The lake catchment contains a steep-sided cirque (area of ~2.8 km^2), marked by the presence of the Annabreen glacier (surface area of 0.87 km^2), which currently terminates in the southwest corner of the lake. The limited vegetation in the catchment is characterized as northern Arctic tundra (Birks et al., 2004). Gjøavatnet itself has an area of ~0.52 km^2 and has a maximum depth of ~15m. The lake is separated from the ocean by a narrow (~30 m wide) strip of bedrock (Hjelle and Ohta, 1974; Ohta et al., 2007), which is currently covered with large numbers of smoothed boulders and driftwood (**Figure 2.1**). There has been no net postglacial uplift relative to sea level in the immediate region during the Holocene (Forman, 1990; Landvik et al., 1998; 2003). The surrounding bedrock is comprised mainly of Mesoproterozoic banded gneiss and migmatite of the Smeerenburgfjorden Complex containing small outcrops of marble with skarn mineralization in the northwestern part of the catchment (blue outlines in **Figure 2.1**) (Hjelle and Ohta, 1974; Ohta et al., 2007).

2.3 Methods

2.3.1 Fieldwork and Lake Coring

Prior to coring, Gjøavatnet was surveyed using ground penetrating radar (GPR) as well as a Lowrance sonar bathymetric device to determine lake bottom bathymetry and soft sediment distribution (**Figure 2.2**). GPR profiles were collected using a Mala RAMAC GPR unit with a 50 MHZ antenna.

Five sediment cores were collected from Gjøavatnet in the summer of 2014; 2 piston cores (GJP-01-14; 210 cm in length, and GJP-02-14; 82 cm), and 3 gravity/surface cores (GJD-01-14; 39 cm, GJD-02-14; 46 cm, and GJD-03-14; 42 cm) (**Table 2.1**) (see **Figure 2.2** for coring

locations). Surface cores were collected using a Uwitec surface corer. Piston cores were collected using a percussion piston coring device and were hammered until refusal to ensure maximum sediment recovery. GJP-01-14 was cut into two sections in the field (1 of 2: 135.5 cm long, 2 of 2: 71 cm long) to allow for transport. The sediment cores were then shipped back to the University of Bergen for splitting and analysis.

2.3.2 Composite sediment record

A composite sediment record was created based mainly on piston core GJP-01-14, which was collected from the deepest part of the lake (**Figure 2.2**) and is the longest core retrieved from Gjøavatnet (**Figure 2.3**). Comparison of both visual stratigraphy and proxy data between piston core GJP-01-14 and surface cores GJD-01-14 and GJD-02-14 (recovered from the same basin) reveal that only 2.5 cm of sediment were lost from the upper part of the GJP-01-14 during piston coring. The basal sediment in both piston cores (GJP-01-14 and GJP-02-14) is comprised of diamict, interpreted as glacial till, suggesting the entire Holocene record was recovered (**Figure 2.3**). To achieve the highest resolution record possible we focused our investigation on the GJP-01-14 core (206.5 cm length). Results from this core form the basis of most of our interpretations.

2.3.3 Laboratory Analyses

Cores were split and imaged at the University of Bergen prior to analyses. All five cores were analyzed for surface magnetic susceptilibity (MS) at 0.5 cm resolution using a Bartington MS2E point sensor. The cores were also analyzed using an ITRAX X-ray fluorescence (XRF) core scanner located at EARTHLAB, University of Bergen, to determine elemental concentrations. Scans were carried out using a molybdenum (Mo) tube with a downcore resolution of 200 µm. The voltage and current were set to 30kV and 45mA respectively, with an

XRF count time of 10 seconds. For GJP-01-14, Itrax core scanning data were not collected below 167cm depth because the sediment surface was too uneven for the instrument to accommodate.

GJP-01-14 was sub-sampled at 0.5 cm intervals for weight loss-on-ignition (LOI), dry bulk density (DBD), and water content (WC) (*n*=335) (after Dean, 1974; Heiri et al., 2001). A syringe was used to ensure a constant 1 cm^3 of sediment was removed. The sediment below ~167cm in GJP-01-14 was either too stiff to properly remove the necessary volume of sediment for accurate LOI and DBD analysis or was simply composed of large clasts, making the analyses impossible. Accordingly, the majority of our proxy data (and associated figures) do not include data from the bottom ~40 cm of the GJP-01-14 core.

Macrofossils for radiocarbon dating were removed and sent to the Poznan Radiocarbon Laboratory in Poland for analysis (**Table 2.2**). $\delta^{13}C$ values of bulk sediment (*n*=50) were measured at the Lamont Doherty Earth Observatory using a Costech elemental combustion system (EA) coupled to a Delta V Plus IRMS (Thermo). A two-point isotope calibration curve was constructed using standards USGS40 and USGS41 to place measured values on the VPDB scale. A third standard (USGS24) was run during the period of data acquisition to evaluate the accuracy of measurement.

Eight samples were chosen for diatom taxonomic analysis from 121.5, 135.5, 137, 149.5, 161.5, 163.5, 164.5, and 165.5 cm composite depth in GJP-01-14 to evaluate the possibility of early Holocene marine incursions and to characterize lacustrine conditions. Diatoms were isolated from the sediments using standard oxidative techniques modified from Renberg (1990) and mounted on glass coverslips using Naphrax mounting medium. At least 300 diatom samples were identified from each slide at 1000x under oil immersion and identified using predominantly Arctic diatom floras (e.g. Antoniades et al., 2008).

2.3.4 Statistical and Multivariate Analyses

Principal component analysis (PCA) and computation of correlation coefficients were carried out on 10 measured proxies using Matlab software for Windows. This included 9 geochemical element counts (Ti, K, Ca, Rb, Sr, Fe, Mn, Si, Al) from the Itrax core scanner as well as %LOI. These elements were selected based on their high signal response on the Itrax (counts per second generally >100), their prevalence in siliclastic sediments, and previous studies that have identified them as useful for reconstructing minerogenic input from bedrock erosion (Bakke et al., 2013; Balascio et al., 2015; Røthe et al., 2015). Itrax data were smoothed using a 24pt running mean and resampled at 0.5cm intervals to achieve comparable resolution to the LOI data. All datasets were also log-transformed prior to analysis.

2.4 Results and Interpretations

2.4.1 Chronology

The chronology of the composite sedimentary record is based on 13 radiocarbon dates of organic macrofossils taken from the GJP-01-14 core (**Table 2.2**). An age model was created using the Clam age modeling package (Blaauw, 2010) for the open-source software R (v. 3.0.1; R Development Core Team, 2013) (**Figure 2.4**). A smooth spline function was used to create the age model, with a default smoothing value of 0.3 applied. Radiocarbon dates were calibrated using the terrestrial northern hemisphere Intcal13.14C curve (Reimer et al., 2013). Calculated sedimentation rates in Gjøavatnet using this age model vary from a maximum of ~29.8 cm/kyr to a minimum of ~8.6 cm/kyr with an average value of 14.7 cm/kyr. We also created an age model using the same parameters but with a linear interpolation between data points instead of a smooth spline. We only use the linear interpolation-based age model as an illustrative tool to highlight differences in sedimentation rate throughout the core, and do not use it for any of our paleoclimate interpretations. We note that age estimates below a depth of 162.5 cm (11,140 cal yr BP calibrated age) are based on extrapolation of the age model and therefore have unconstrained

uncertainty. This impacts only a small portion of our proxy data, which extends to ~167 cm, but does affect our ability to accurately date the onset of lacustrine sedimentation in Gjøavatnet.

2.4.2 Multivariate Analysis

Calculated correlation coefficients for each of XRF-based elemental abundance datasets reveal that most of the geochemical elements are highly positively correlated with each other and negatively correlated with LOI (**Table 2.3)**. The exception to this pattern is Ca, which is only weakly positively correlated with the other elements (but still negatively correlated with LOI). Principal component analysis yielded 2 components responsible for 91% of the observed variance in the dataset (**Table 2.4**). Most of the geochemical elements align with PC1, responsible for 80.6% of the variance (**Table 2.3**, **Figure 2.5**). As suggested by their correlation coefficients, most of the geochemical elements are positively correlated with PC1, while LOI is inversely correlated. Accordingly, the downcore scores for PC1 look broadly similar to elemental counts from the Itrax **(Figure 2.6)**. PC2 (10.7% of variance) shows weak correlations with most elements and LOI, but is highly positively correlated with the element Ca. We recognize that PC1 is an extension of the elemental data and we utilize the principal component analysis to highlight the similar behavior of these elements over the length of our record, and as justification for interpreting each as a record of bedrock erosion (and therefore glacial activity). In the ensuing discussion, we will consider Ti elemental abundances as a proxy for glacially derived sediment input to Gjøavatnet; however, the use of PC1 or of a different element (apart from Ca, see below) would not change any of our interpretations or conclusions.

2.4.3 Stratigraphy and Interpretation of Stratigraphic Units

The composite Gjøavatnet sedimentary sequence was separated into 4 major units: A, B, C, and D, and Unit C was further divided into 3 distinct subunits **(Figure 2.7)**. This determination

was made based on major density transitions apparent in x-radiograph data and corresponding visual transitions between gray, silty sediment and brown, organic rich sediment (**Figure 2.3**). Proxy data (Itrax elemental data, diatom analyses, and LOI and DBD values) were then used to inform/confirm these definitions (**Table 2.5**) (see below).

2.4.4 Unit A: Base of core (206.5 cm) – 11.1 cal kyr BP (162.5 cm) - Glacial Till

The basal sedimentary unit, Unit A, consists of dark to light gray diamict (206.5 cm - ~170 cm), which transitions to dense silty sand (170 – 162.5 cm). The diamict in the lower portion of this unit is massive and poorly sorted, with individual clasts up to 5 cm in diameter. The x-radiograph of the upper section shows some faint evidence for horizontal bedding structures, but lacks the distinct laminations of later units. The unit broadly is characterized by low LOI values, ranging from 1.8% at ~11.6 cal kyr BP to ~8% at 11.2 cal kyr BP with a mean value of 3.9%. The highest dry bulk density values of the entire record are found in Unit A, with a mean value of 0.71 g/cm^3. Values decrease steadily from a maximum of 1.15 g/cm^3 at a depth of 167 cm (lowest sample) to 0.41 g/cm^3 at the top of the unit (**Table 2.5, Figure 2.7**). Unit A has the 2nd highest average Ti counts of the entire record (1622 cps), with relatively little variation about the mean. Ca counts during the majority of this interval are the highest of any unit by nearly two orders of magnitude. They reach a maximum value of 50,014 cps and are above 30,000 cps for most of the unit (mean of 24,466 cps) (**Table 2.5**) before declining to ~1500 cps before the end of Unit A. $\delta^{13}C$ values range from -22.2‰ to -23.7‰, with an average of -23.1‰ (n = 5). Diatom species were analyzed in 3 samples from Unit A (dashed lines in **Figure 2.7**). Assemblages were dominated by *Pinnularia lenticular* and *Stauroneis anceps family (cf. gracilis, vandevijveri),* which are characteristic of a silty, shallow freshwater environment (Perren et al., 2012; Wojtal et al., 2014) (**Figure 2.8**).

One of the most interesting aspects of Unit A is the high Ca abundance during in this interval. High Ca counts are also observed in the other piston core collected from Gjøavatnet

(GJP-02-14), confirming that it is a persistent feature of the sediments across the lake basin. One possible interpretation of the calcium signal is that it represents a period when the lake basin was subject to marine influence. Diatom analysis, however, has revealed that all species present at the time were freshwater-dwelling, ruling out the possibility of a marine influence. We note here that despite the abundant driftwood on the narrow strip of land separating Gjøavatnet from the ocean today, we see no evidence in our proxy data to suggest sustained or meaningful marine influence on the lacustrine sediment record.

We interpret the high Ca abundance as a signal of bedrock erosion from the marble units within the Gjøavatnet catchment. Although the majority of the underlying bedrock consists of banded gneiss of the Smeerenburgfjorden Complex (Hjelle and Ohta, 1974; Ohta et al., 2007).), there are two small outcrops of marble that would have resulted in glacial flour with elevated Ca content in the northwest part of the catchment (blue outlines in **Figure 2.1**). The exposed marble units are not being eroded by the Annabreen glacier today, but would have been subject to glacial erosion if the glacier advanced across the outcrops. We suggest that the large decrease in XRF-inferred Ca deposition to the lake c. 11.5 cal kyr BP represents the retreat of Annabreen up-valley from the marble outcrops. If this interpretation is correct, the abrupt decline in sedimentary Ca abundance ~11.4 cal kyr BP represents a threshold response as the glaciers retreated beyond the marble outcrops, and as such, we do not consider the large change in Ca abundance in our assignment of stratigraphic units.

The carbon isotopic signature of this section is also intriguing, suggesting at face value a variable but perhaps predominantly marine source (values ranging from -22.2 to -23.7‰) (Meyers, 1997). Again, however, diatom analysis has ruled out this possibility. An alternative explanation may be found in the weathering of silicate rocks and limited recycling of carbon within the catchment immediately following deglaciation (Hammarlund, 1993). Glacial activity would have resulted in a large amount of freshly weathered siliciclastic material on the landscape following deglaciation. The weathering of this material could have resulted in bicarbonate

delivery to the lake water, leading to ^{13}C enrichment (i.e. more positive $\delta^{13}C$ values) of dissolved inorganic carbon and, therefore, of autochthonous organic material in the lake (Hammarlund, 1993).

We interpret Unit A to represent a period when Annabreen was terminating at or near the coring site during deglaciation of the catchment. Due to the extrapolated nature of our age model, we cannot place a definitive date on the onset of sedimentation in Gjøavatnet. The highest dry DBD and lowest LOI percentages are recorded during this interval, along with the presence of large individual clasts in the sediment, all of which suggest substantial glacial presence proximal to the coring site. The lowermost ~30cm of GJP-01-14 is comprised of glacial till/diamict, which was likely deposited when the glacier was directly adjacent to (or overriding) the coring site. We speculate that the remainder of Unit A (~167 – 162.5 cm), when DBD values were still relatively high, represents a period when Annabreen was likely terminating within the lake.

The boundary between Unit A and Unit B at ~11.1 cal kyr BP is primarily defined by DBD values, a shift in diatom species, and a major density change seen in the x-radiograph data (**Figure 2.3**). The diatom samples below the transition represent a silt-dominated environment (e.g Perren et al., 2012), as would be expected if Annabreen was terminating within the lake or was contributing a significant amount of meltwater to the lake system, whereas the samples above (in Unit B) are more diverse and point to a reduction of suspended silt in the water column. Together, these proxies suggest that while Annabreen was still active during the deposition of Unit B (see below), it was reduced in size and/or influence compared to Unit A.

2.4.5 Unit B: 11.1cal kyr BP (162.5 cm) – 8.4 cal kyr BP (136.5 cm) - Deglaciation of Gjøavatnet Catchment

Unit B consists of a mixture of gray, laminated, clayey silt interbedded with relatively organic rich brown material. It is characterized by generally low but variable LOI values ranging from 8.1 – 19% (mean of 13.0%) (**Figure 2.7**). DBD values (0.14 – 0.36 g/cm^3; mean of 0.22

g/cm^3) are relatively high during this unit, though much lower than in preceding Unit A. Ti counts are higher in the lower portion of this unit than Unit A, increasing to a maximum of 3034 counts at ~10.8 cal kyr BP before decreasing to ~800-1,000 cps for the majority of the Unit B. Ca counts in Unit B are significantly lower than in Unit A, decreasing from ~1,500 counts at the base of Unit B to ~300 cps (average value of 655 cps). $\delta^{13}C$ values are the most enriched in this section of the core, rising from ~ -23.5‰ at 162.5 cm to a value of ~ -21‰ (average of -22.2‰, n = 13).

Three samples from Unit B were analyzed for diatom taxonomy. Assemblages in the lowermost two samples are dominated by *Navicula (Genkalia) digitulus* and *Pseudostaurosira pseudoconstruens* and also contain the first appearance of *Navicula schmassmannii* in the sediment record **(Figure 2.8).** These species are characteristic of a deeper lake with less suspended silt than the species from Unit A (Perren et al., 2012). The third sample, taken at a depth of 137 cm (approx. 8.6 cal kyr BP), is characterized by a more diverse assemblage including *Stauroforma exiguiformis, Hyropetra balfouriana*, and *Aulacoseira distans*.

We interpret Unit B to represent an interval when Annabreen was still present within the catchment, but likely not terminating within the lake. The two oldest diatom samples from this interval (~11 and 9.7 cal kyr BP) (**Figure 2.7, Figure 2.8**) are characteristic of a deeper lake with lesser suspended silt load than during the deposition of Unit A. Elemental abundance data **(Figures 2.6, 2.7)** suggest a broad decrease in the influence of Annabreen on the sediment record across this interval, although reductions in elemental counts occur stepwise (cf., Ti counts). The LOI trend across Unit B is also non-linear and is quite variable at multi-centennial timescales (**Figure 2.7**), suggesting the glacier may have been fluctuating dynamically during this time and/or that sedimentation was influenced by glaciofluvial dynamics in the glacier forefield as ice retreated. The third diatom sample from this section (just prior to 8.4 cal kyr BP) (**Figure 2.8**) reveals a more diverse assemblage than the two older samples from Unit B, including planktonic taxa. Again, this assemblage suggests Annabreen's influence on sedimentation in the lake waned throughout this period.

Bulk organic carbon isotope values in Unit B are the most positive of the record, with a mean of -22.2‰. Such a value is generally associated with marine algae (Meyers, 1997), however, only freshwater diatom species are found in the Gjøavatnet sediment record, precluding a marine source for the relatively ^{13}C-enriched carbon isotope values. As discussed above, a possible explanation is the weathering of glacial flour derived from silicate rocks during this time that could have increased the $\delta^{13}C$ value of DIC (dissolved inorganic carbon) in Gjøavatnet (Hammarlund, 1993).

The boundary between Unit B and Unit C at ~8.4 cal kyr BP is marked by an increase in LOI, an abrupt decrease in Ti abundance, and a concomitant shift in $\delta^{13}C$ values (**Figures 2.6, 2.7, 2.8**). It is apparent that the nature of sedimentation in Gjøavatnet changed dramatically at this point. The most likely explanation is the disappearance, or the dramatic reduction in size, of the Annabreen glacier at ~8.4 cal kyr BP.

2.4.6 Unit C: 8.4 cal kyr BP (136.5 cm) – 1.0 cal kyr BP (16.5 cm) -Non-glacial sedimentation in Gjøavatnet

Unit C comprises the majority of the sediment record from Gjøavatnet (120 cm of ~206 total) and is composed of laminated brown organic rich sediment with interbedded gray minerogenic layers. The highest LOI values of the entire core are recorded in Unit C, and generally follow a linear increasing trend from ~18% to 35% (average of 25.5%) **(Figure 2.7).** This linear trend is interrupted by at least three distinct multicentennial-scale intervals characterized by abrupt shifts to relatively lower LOI values, higher Ti and DBD values, and decreases in sedimentation rate. These subunits are defined as C1 (81-89.5 cm, ~5.0 – 5.9 cal kyr BP); C2 (42-48.5cm, 2.2 – 2.7 cal kyr BP); and C3 (27-32cm, 1.5-1.7 cal kyr BP). Proxy data for these three subunits are compared to average values from the remainder of Unit C, and presented in **Table 2.5,** to examine the differences between these subunits and Unit C in general. DBD values for Unit C generally follow the inverse trend of LOI, beginning at ~0.15 g/cm^3 and

declining to a minimum of 0.03 g/cm^3 near the top of the section. Ti counts are generally low throughout this portion of the record, ranging from 88 – 661 cps with an average value of 372 cps. Ca counts are extremely low in Unit C, averaging 231 counts (max of 305 cps, min of 69 cps), with little variation. During the deposition of this sedimentary unit we interpret Ti abundances to reflect catchment dynamics unrelated to glacier activity (e.g., such as changes in runoff), or by changes in dilution by organic matter deposition.

Carbon isotope values in Unit C increased from ~ -25.5‰ to -24‰ at 7.6 cal kyr BP and then steadily decreased to -28.5‰ (average value of -27.1‰). Two samples analyzed for diatoms from the base of this unit, at ~ 8.1 (135.5 cm depth) and 7.6 cal kyr BP (121.5 cm depth), show similar assemblages to the uppermost sample from Unit B (**Figure 2.8**), revealing a diverse community including planktonic diatoms living in the upper water column

We interpret Unit C to represent a phase during the Holocene when the Annabreen glacier either completely melted or was too small to influence sedimentation in the lake. Ti counts and DBD are at their lowest during this period (**Table 2.5, Figure 2.7**). Bulk δ^{13}C values during this period average -27.1‰, likely reflecting a lacustrine algal source (-25 to -30‰) (Meyers, 1997). LOI values increase from ~20% at ~8.0 cal kyr BP to nearly 40% near the transition to Unit D at 1.0 cal kyr BP. An increasing trend in % organic matter during the Holocene has also been observed in other Svalbard lakes (e.g. Gjerde et al., *in press*; van der Bilt et al., 2015) and is attributed to lake and catchment ontogeny and greater nutrient recycling. The trend may have also have been influenced by increasing preservation of organic matter, as declining summer insolation potentially shortened the ice-free season resulting in greater bottom water anoxia or hypoxia (Laskar et al., 2004).

Unit C is punctuated by abrupt transitions between brown, organic-rich sediment and gray, more minerogenic sediments (the latter defined as subunits C1-C3; **Figure 2.7**). These transitions are apparent in LOI, visual stratigraphy, x-radiograph images, and DBD values. As evidenced by the visual stratigraphy, core images, and x-radiograph, these units appear massive,

with few laminations. Subunits C1-C3 could represent: (i) short-lived advances of the Annabreen glacier, (ii) slump activity (e.g. turbidites), or (iii) periods of reduced organic matter accumulation. We suggest that advances of Annabreen are not likely to have caused these changes because sediment characteristics during subunits C1, C2, and C3 are not consistent with other intervals associated with glacial erosion in the catchment (Units A, B, D). Ti counts are much lower in the Unit C subunits, for example (**Figure 2.7**). Additionally, the relationship between Ti and %LOI is broadly similar across Unit C and subunits C1-C3 relative to Units A, B and D, inferred to represent a glacial signature (**Figure 2.9**). Furthermore, the timing of Unit C1 corresponds with the interval when nearby lake Hakluytvatnet completely dried out, likely in response to dry conditions (c. 7.7-5.0 cal kyr BP), suggesting the precipitation regime was not favorable for the regrowth of Annabreen (Gjerde et al., *in press;* Balascio et al., *in press*). It is also unlikely that these subunits were the result of slump events. Radiocarbon dates from either side of both units C1 and C2 were used to quantify sedimentation rates across each interval using a linear interpolation between data points (**Figure 2.7**), and indicate that sedimentation rates slowed during deposition of these subunits. Mass wasting events, such as slumping, would lead to an increase, not a decrease in sedimentation rate.

We therefore interpret subunits C1, C2, and C3 as intervals of reduced organic productivity, most likely driven by periods of prolonged summer lake ice cover and/or drier and colder conditions on Amsterdamøya. Sediment was likely delivered to the lake during a short period of reduced ice cover during the summer, which have been potentially limited to a moat around the lake edge.

2.4.7 Unit D: 1.0 cal kyr BP (16.5 cm) to present - Re-advance of Annabreen

The uppermost stratigraphic unit, Unit D, is characterized by an abrupt shift to gray, minerogenic sediment with faint laminations and a small number of sand sized grains (visually identified from the split core). Unit D is characterized by low LOI values (mean of 6.9%) and

high DBD (mean of 0.43 g/cm^3) (**Table 2.5**). The dense nature of Unit D is also evident from the X-radiograph (**Figure 2.7**). Ca counts increase in this unit relative to Unit B (average of 785 vs. 231), but remain nearly two orders of magnitude lower than Unit A at the base of the core. Bulk $\delta^{13}C$ values increase from -28.9‰ to -26.7‰ across the three samples representing this section. Ti counts in Unit D are the highest of the entire record (mean of 2,127 cps).

We interpret Unit D to represent the reemergence of the Annabreen glacier, though this could also represent the transition from residual cold-based ice to a polythermal glacier. The youngest radiocarbon date from the Gjøavatnet record was taken just below this transition, allowing confident age assignment to the boundary. Although there are only three $\delta^{13}C$ samples from this interval, we note that they increase from -28.9‰ to -26.7‰, a change similar in magnitude to the pattern seen at the beginning of Unit B, which is likely related to increased glacial erosion and delivery of relatively ^{13}C-enriched material to the lake (Hammarlund et al., 1993).

The sedimentary units described here represent the broad phases of environmental change within the Gjøavatnet catchment. Unit A represents the period when Annabreen was likely larger than today and much of the catchment covered by ice. We infer that the glacier was terminating within the lake during this time. The transition to Unit B at ~11.1 cal kyr BP likely marks the time when Annabreen retreated from the lake basin. We propose that the glacier was present in the Gjøavatnet catchment until ~8.4 cal kyr BP. From ~8.4-1.0 cal kyr BP the glacier was absent or had become dramatically diminished in size, and variations in sediment properties were likely controlled primarily by changes in summer temperature and/or the duration of the summer ice free season. At ~1 cal kyr BP the local ELA lowered enough to allow Annabreen to reform, and the glacier has been terminating in the lake since that time.

2.5 Regional Paleoclimate Context of Gjøavatnet Record

2.5.1 Early Holocene: Deglaciation of Amsterdamøya

During the Last Glacial Maximum, ice extended all the way to the shelf edge in NW Svalbard, ~8 km offshore (Ingólfsson and Landvik, 2013). During this time it is likely that the majority of the Gjøavatnet catchment was covered by ice, although the >300 m high plateaus on the island have been ice free for at least 80 cal kyr BP (Landvik et al., 2003). Ice began to retreat from the shelf edge sometime prior to 14 cal kyr BP, reaching the coast of NW Svalbard by ~13.8 cal kyr BP (Ingólfsson and Landvik, 2013). The deglaciation of the nearby Hakluytvatnet catchment at ~12.8 cal kyr BP suggests some small cirques on the island were largely ice-free by this time (Gjerde et al., *in press*). However, Annabreen was still terminating near the coring site in Gjøavatnet for another ~1.7 kyr until it retreated out of the lake basin at ~11.1 cal kyr BP and then disappeared, or at least greatly diminished in size, at 8.4 cal kyr BP.

Proglacial lake records from the nearby Mitrahalvøya peninsula also point to a complex deglacial history in western Svalbard, with the catchment of Lake Kløsa deglaciating ~9.2 cal kyr BP (Røthe et al., 2015), while glacial ice persisted in the catchment of Lake Hajeren until ~7.4-6.7 cal kyr BP (van der Bilt et al., 2015) (**Figure 2.10**). Further south in the Linné valley, the Linnébreen glacier and another small cirque glacier in the same area are believed to have melted away during the early Holocene (Svendsen and Mangerud, 1997; Snyder et al., 2000; Reusche et al., 2014). Lacustrine alkenone-based temperature reconstructions from Amsterdamøya and the Mitrahalvoya peninsula also point to warm conditions before ~8 kyr BP (van der Bilt et al., 2016).

The proposed final deglaciation of the Gjøavatnet catchment (~8.4 cal kyr BP) occurred during a prolonged period of warm surface water conditions in Fram Strait (Müller et al., 2012; Werner et al., 2013; 2015; Rasmussen et al., 2014). Aagaard-Sorensen et al. (2014) found the warmest Mg/Ca based temperatures in their record from core MSM5/5-712-2 from ~10.5-7.9 kyr BP. IP_{25} concentrations (a biomarker indicative of diatoms associated with sea ice) (Belt et al., 2007) from the same core also suggest the region experienced “significantly reduced ice cover”

between 8.2 and 7.8 cal kyr BP (Müller et al., 2012). IP_{25} concentrations in the nearby MSM5/5-723-2 core also suggested warm temperatures and low concentrations of sea ice from the period ~11-7 kyr BP (Werner et al., 2015). Foram-based temperatures also suggest increased advection of warm Atlantic water into this part of the Fram Strait during this time (Werner et al., 2013). While we acknowledge the possibility that Annabreen was dramatically reduced in size during the mid-Holocene (or became a cold-based glacier with little erosive power), we point to warming trends seen in marine records, along with evidence that many other glaciers in Svalbard melted away during this time (**Figure 2.10**), as strong evidence for our interpretations.

Warmer conditions following deglaciation generally define the early Holocene climate of this region, although periodic cooling events have been identified in the North Atlantic and attributed to freshwater forcing (Sejrup et al., 2016). The "8.2" event (Alley et al., 1997) is the most prominent of these, although we do not see it expressed in the Gjøavatnet record, a finding that echoes another similar study from Svalbard (van der Bilt et al., 2015). It may be that dry conditions during this time (Rohling and Pälike, 2005), coupled with its brief duration (Thomas et al., 2007), prevented Annabreen from re-growing sufficiently to impact the sediment in Gjøavatnet.

2.5.2 Middle Holocene – Sea ice and freshwater influences on Amsterdamøya climate

During the middle Holocene period on Amsterdamøya (~8-1 cal kyr BP), we propose that Annabreen was absent from the catchment. This period is generally marked by the absence of a glacier in the Gjøavatnet catchment and punctuated by periodic decreases in organic matter accumulation in the lake (subunits C1-C3). We hypothesize that the most likely mechanism for these intervals is an abrupt change in temperature and/or precipitation (we note these two parameters are positively correlated today (Førland et al., 2011)), which at this maritime location would most likely be driven by offshore oceanographic conditions. Periodic increases in freshwater input and the presence of a surface freshwater layer (and likely accompanying sea ice)

could dramatically lower both temperature and precipitation near Gjøavatnet, leading to the reduction in organic matter accumulation seen during the subunits. Interestingly, Unit C1 occurs during a period of increased deposition of discrete laminae in Linnévatnet (Snyder et al., 2000) (grey shaded area in **Figure 2.10**). The deposition of Unit C1 also occurs during a hiatus in sedimentation in nearby Haklutuyvatnet (Gjerde et al., *in press*), suggesting dry conditions on Amsterdamøya during this time. Numerous authors have suggested the presence of a freshwater cap or lens near Svalbard (Rasmussen et al., 2013; Werner et al., 2013, 2015), although the exact timing and magnitude of this oceanographic feature remains somewhat ambiguous. With respect to the most prominent of the subunits, C1, there does appear to be complimentary evidence for oceanographic changes during the period ~6-5 cal kyr BP.

Multiple marine records from near Svalbard and in the Fram Strait have found evidence for an increased flux of cold water from the Arctic around 6 cal kyr BP. Ślubowska et al. (2005, 2007) found increases in the concentrations of the benthic foraminifera *E. excavatum*, characteristic of Arctic ocean water, ~6.8 and 6 cal kyr BP north of Svalbard. Ebbesen et al. (2007) cite a shift in $\delta^{18}O$ values of foraminiferal tests at 6 cal kyr BP as evidence for a change in the relative contributions of water masses off western Svalbard. Numerous studies have also shown that the thermophilious mollusk, *Mytulis edulis*, likely died out in northern Svalbard around 6-5 cal kyr BP (Blake, 2006; Salvigsen, 2002). Evidence from a proglacial fjord record in Nordauslandet points to the rapid deposition of a glacial diamict between 5.8 and 5.7 cal kyr BP (Kubischta et al., 2011). These reconstructions point to cooling conditions occurring during the hiatus in Haklutuyvatnet and the deposition of Unit C1 in Gjøavatnet.

Interestingly, several proxy reconstructions from the Fram Strait, just west of Amsterdamoya (**Figure 2.1**), suggest there was warm and saline water in the *subsurface* ocean (~depth of 100 m) during this time (Müller et al., 2012; Werner et al., 2013; 2015; Aagaard-Sorensen et al., 2014). Two proxies for sub-surface seawater temperature from core MSM5/5-712-2 depict warm temperatures from 6.1 to 5.2 ka (Werner et al., 2013; Aagard-Sorensen et al.,

2014) (**Figure 2.11**). The warm, saline water is presumed to be Atlantic-sourced water carried by the WSC. Werner et al. (2013) attribute the subsurface temperature increase to insulation by meltwater that limited heat loss to the atmosphere; if correct, these hydrographic conditions suggest an increased amount of cold, fresh meltwater (and also associated sea ice) near Amsterdamøya during this time. The subsurface warmth is not a feature of all temperature records from the Fram Strait, however. The foram-based subsurface temperature reconstruction from nearby core MSM5/5-723-2 (Werner et al., 2015) instead suggests that a broad cooling trend began around 6 kyr BP. 6 kyr BP also marks the beginning of a decline in both the concentration of subpolar planktic forams and reconstructed subsurface (75m depth) temperatures in the Kongsfjorden Trough (Rasmussen et al., 2014).

Local sea ice reconstructions also do not support the notion of dramatic increases in sea ice in eastern Fram Strait from ~6-5 kyr BP. IP_{25} concentrations from cores MSM5/5-723-2 and MSM5/5-712-2 are broadly stable during this time, as are IRD concentrations (**Figure 2.11**) (Müller et al., 2012; Werner et al., 2013, 2015). Interestingly, however, relatively high IP_{25} concentrations are found on the East Greenland Shelf from ~6.5-5.6 kyr BP, the only extended period of high IP_{25} accumulation until ~1.0 cal kyr BP (Müller et al., 2012). Funder et al. (2011) also inferred increased export of multiyear sea ice out of the Fram Strait after 6 kyr BP, based on driftwood deposits on the coast of East Greenland.

Further afield, numerous marine records from the north of Iceland also suggest dramatic changes were occurring ~6-5 cal kyr BP. Castañeda et al. (2004) and Knudsen et al. (2004) both cite cooling trends beginning at 6.2 and 6.0 cal kyr BP respectively, while the alkenone based SST record of Moosen et al. (2015) shows a similar cooling trend beginning at this time (**Figure 2.11**). There is also evidence for an increase in sea ice concentrations north of Iceland beginning at 6.2 cal kyr BP(Cabedo-Sanz et al., 2016). Risebrobrakken et al. (2011) cite 6 cal kyr BP as the end of the Holocene Thermal Maximum in the North Atlantic, based on 6 cores from the Nordic and Barents Seas. Further south in the Atlantic basin Hoogakker et al. (2011) suggest 6.5 cal kyr

BP was the start of a major reorganization of water masses associated with deep ocean circulation. Our C1 subunit also aligns with the largest so-called Bond Event of the Holocene (Bond Event #4) identified in a marine record in the North Atlantic (Bond, 2001) (**Figure 2.11**).

Although there is not a clear relationship between these offshore records and the timing of subunits C2 (c. 2.7-2.2 kyr BP) and C3 (c. 1.7-1.5 kyr BP), the IP_{25} concentration record of Müller et al. 2012, shows the highest accumulation rates of IP_{25} in the entire record during subunit C3 (**Figure 2.11**). A minor dip in LOI concentrations in Gjøavatnet at ~3.2 cal kyr BP, which is one of the most pronounced in the Hakluytvatnet record (Gjerde et al., *in press*), does appear contemporaneous with a spike in IRD in the record of Werner et al., (2013) as well. Similar to the 6-5 cal kyr BP interval, many of the marine records from the Fram Strait suggest a warming of subsurface waters and an increase in meridional overturning circulation after 3 ka (e.g. Berben et al., 2014; Rasmussen et al., 2013; Sarnthein et al., 2003; Werner et al., 2015) while simultaneously suggesting increased sea ice cover at the surface (Müller et al., 2009; 2012; Werner et al., 2015).

In summary, it appears there is evidence for greater subsurface warming and increased Atlantic advection around 6-5 kyr BP (Werner et al., 2013; 2015; Aagaard-Sorensen et al., 2014), as well as increased sea ice concentrations in the western part of the Fram Strait (Müller et al., 2012, Funder et al., 2011), when we infer cold conditions on Amsterdamøya. The agreement between the end of unit C1 in Gjøavatnet and the resumption of sedimentation in nearby Haklutuyvatnet also points to a wider forcing beyond the lake catchment itself. We propose similar oceanographic conditions may have existed during the deposition of subunits C2 and C3.

2.5.3 Late Holocene advance of Annabreen glacier

The sediment record from Gjøavatnet clearly indicates that input of minerogenic material, formed by bedrock erosion by the Annabreen glacier, abruptly began again ~1.0 cal kyr BP, and that this input has continued up to the present day. Other terrestrial records also suggest glaciers

began to regrow around Svalbard around this time (Humlum et al., 2005; Snyder et al., 2000; van der Bilt et al., 2015), although Karlbreen on Mitrahalvøya appears to have begun to re-advance earlier (~3.5 cal kyr BP) (Røthe et al., 2015). Linnebreen also began to regrow much earlier in the Holocene (~4-5 cal kyr BP), but is believed to have reached its maximum Holocene extent during the 18-19th centuries (Svendsen and Mangerud, 1997). Offshore marine records also suggest broad cooling conditions ~1.0 cal kyr BP. Werner et al. (2015) posit that elevated advection of North Atlantic waters into the eastern Fram Strait region likely ended around 1.0 kyr BP. Evidence for seasonal sea ice and unstable oceanographic conditions was found south of Svalbard in the western Barents Sea after 1.1 kyr BP (Berben et al., 2014) and Hald et al. (2004) point to a peak in IRD off western Svalbard at 0.8 cal kyr BP.

It remains unclear whether colder summer temperatures or increased wintertime precipitation led to the reemergence of Annabreen. Temperature reconstructions from Kongressvatnet (D'Andrea et al., 2012), as well as from Lake Skardtjørna (Velle et al., 2011), both on western Svalbard, suggest that summer temperatures were relatively stable during the past 1800 years, prior to recent anthropogenic warming.

2.6 Conclusions

This paper reports a Holocene reconstruction of the Annabreen glacier from Lake Gjøavatnet on Amsterdamøya, NW Svalbard. We show that sedimentation was dominated by glacial activity in the catchment during the early and late Holocene and likely responded to regional-scale oceanographic changes in the intervening period. The early Holocene interval in Gjøavatnet is characterized by a two -phase sedimentation history, with Annabreen retreating out of the lake catchment ~11.1 kyr BP and shrinking to its minimum Holocene extent by ~8.4 kyr BP. During the period from ~8.4-1.0 cal kyr BP it seems likely there was no glacial influence on sedimentation in Gjøavatnet. The organic-rich sediments deposited during this time are interrupted by at least three intervals of lower organic matter content (c. 5.9-5.0 kyr BP, 2.6 – 2.2

kyr BP, and 1.7 – 1.5 kyr BP). We interpret the reductions in organic carbon content as periods of more extensive summer lake ice cover (due to colder summer conditions) related to changing oceanographic conditions in Fram Strait. At c. 1.0 cal kyr BP Annabreen re-advanced to the extent that it dominated sedimentation in the lake.

Maritime lakes in places like Svalbard provide the opportunity to capture both local glacier fluctuations along with offshore oceanographic conditions. Marine records are generally lower resolution than their lacustrine counterparts, and incorporate information from the entire water column, potentially complicating the detection of short-lived oceanographic events. Ocean based reconstructions over the Holocene near Svalbard suggest a complex and variable water mass and climate history, which we propose can be informed by the high-resolution lacustrine record from Gjøavatnet. While more research from both the terrestrial and marine realms would help confirm the climate patterns identified here, this study provides a unique record of both local glacial fluctuations and offshore oceanographic conditions spanning the Holocene.

Table 2.1: Sediment cores collected from Gjøavatnet

Core Name	GJP-01-14	GJP-02-14	GJD-01-14	GJD-02-14	GJD-03-14
Core Type	Piston	Piston	Surface/Gravity	Surface/Gravity	Surface/Gravity
Core Length (cm)	206.5	95	30	43	42

Table 2.2: Radiocarbon results from macrofossils taken from GJP-01-14 core

Core	Composite Depth (cm)	Sample Material	Sample Mass (mg)	^{14}C Age	Error +/- (1σ)	Calibrated Age ±2 sigma	Δ^{13}C ‰ VPDB
GJP-01-14 1of2	16	Plant Remains	4.2	1125	30	960 - 1172	-23
GJP-01-14 1of2	32	Plant Remains	9.1	1795	35	1619 - 1819	-22.4
GJP-01-14 1of2	44.5	Plant Remains	4.4	2175	35	2066 - 2312	-20.5
GJP-01-14 1of2	48.5	Plant Remains	7.8	2685	30	2753 - 2846	-24
GJP-01-14 1of2	66	Plant Remains	11.6	3530	35	3702 - 3895	-22.8
GJP-01-14 1of2	80.5	Plant Remains	2.2	4230	40	4628 - 4861	-24.1
GJP-01-14 1of2	88	Plant Remains	6.9	5350	50	6002 - 6084	-24.4
GJP-01-14 1of2	102	Plant Remains	8.7	5860	40	6563 - 6778	-27.7
GJP-01-14 1of2	114	Plant Remains	6.2	6520	50	7323 - 7556	-22.4
GJP-01-14 1of2	129	Plant Remains	14.2	7060	50	7789 - 7976	-25.5
GJP-01-14 2of2	138.5	Plant Remains	3.9	7590	40	8343 - 8448	-26.8
GJP-01-14 2of2	146.5	Plant Remains	3.6	8550	30	9494 - 9547	-26.1
GJP-01-14 2of2	162.5	Plant Remains	2.9	9690	40	10827 - 11217	Not Reported

Table 2.3: Correlation coefficients for variables used in PCA analysis

Correlation Coefficients	Ti	Al	Si	K	Ca	Mn	Fe	Rb	Sr	LOI
Ti	1.00									
Al	0.81	1.00								
Si	0.87	0.75	1.00							
K	0.97	0.81	0.95	1.00						
Ca	0.78	0.61	0.50	0.66	1.00					
Mn	0.83	0.77	0.85	0.88	0.39	1.00				
Fe	0.84	0.72	0.90	0.90	0.34	0.94	1.00			
Rb	0.95	0.71	0.88	0.95	0.69	0.77	0.83	1.00		
Sr	0.91	0.69	0.82	0.90	0.80	0.65	0.68	0.94	1.00	
LOI	-0.91	-0.67	-0.69	-0.82	-0.85	-0.63	-0.64	-0.86	-0.85	1.00

Table 2.4: Results from PCA analysis with 8 principal components

Principal Component #	Eigenvalue of Cov (x)	% Variance Captured this PC	Cumulative Variance Captured
1	8.08	80.6	80.6
2	1.08	10.72	91.32
3	0.39	3.87	95.19
4	0.21	2.09	97.28
5	0.11	1.05	98.33
6	0.08	0.84	99.17
7	0.05	0.48	99.64
8	0.02	0.19	99.83

Table 2.5: Relevant proxy data for sedimentary units identified in Gjøavatnet record

Unit	Depth Range (cm)	Approx. Age Range (cal kyr BP)	Avg. Ca cps	Avg. Ti cps	Avg. DBD (g/cm^3)	Avg. LOI	Avg. Acc. Rate (cm/kyr)	Avg. $\delta^{13}C$ (‰)
Unit A	209.5 -162.5	Base – 11.1	24466†	1623†	0.71† *n* = 9	3.9† *n* = 9	9.8	-23.0 *n* = 5
Unit B	162.5 – 136.5	11.1– 8.4	655	1174	0.22 *n* = 56	13.0 *n* = 56	9.7	-22.2 *n* = 13
Unit C	136.5 – 16.5	8.4 – 1.0	231	372	0.09 *n* = 198	25.5 *n* = 198	18.4	-27.1 *n* = 24
Unit C1	89.5 – 81	5.9 – 5.0	253	489	0.15 *n* = 18	16.5 *n* = 18	10.1	-27.3 *n* = 2
Unit C2	48.5 – 42	2.7 – 2.2	199	341	0.10 *n* = 14	24.0 *n* = 14	15.7	-27.6 *n* = 2
Unit C3	32 – 27	1.7 – 1.5	174	279	0.08 *n* = 11	28.2 *n* = 11	21.6	-28.5 *n* = 1
Unit D	16.5 – 0	1.0 - present	785	2157	0.43 *n* = 29	6.9 *n* = 29	15.7	-27.7 *n* = 3

† Data collected down to a depth of ~167 cm

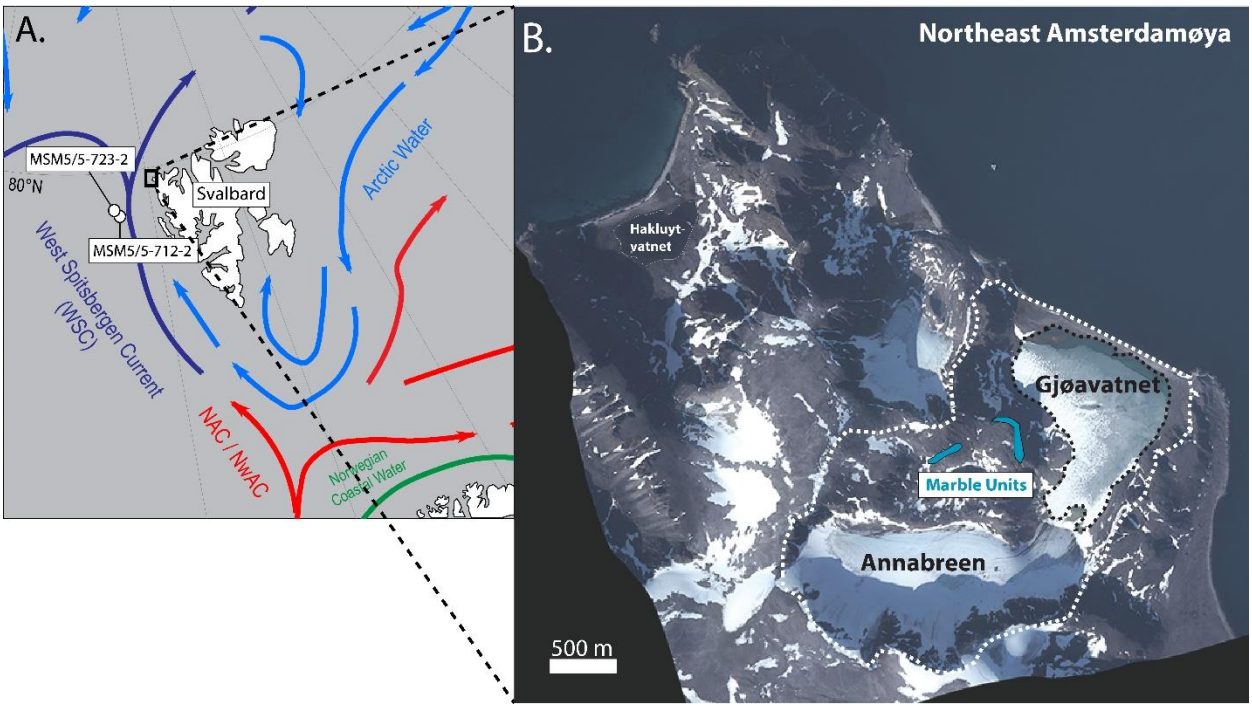

Figure 2.1 - A) Map of Svalbard and surrounding surface currents as well as locations of marine sediment cores MSM5/5-723-2 and MSM5/5-712-2 (Werner et al., 2013; 2015); B) Aerial image of island of Amsterdamøya with Annabreen glacier and Gjøavatnet lake (this study) and Halkuytuvatnet lake (Gjerde et al., *in press*) labeled. Blue polygons represent the approximate locations of marble outcrops (Ohta et al., 2007). Dashed white line denotes approximate catchment of Gjøavatnet.

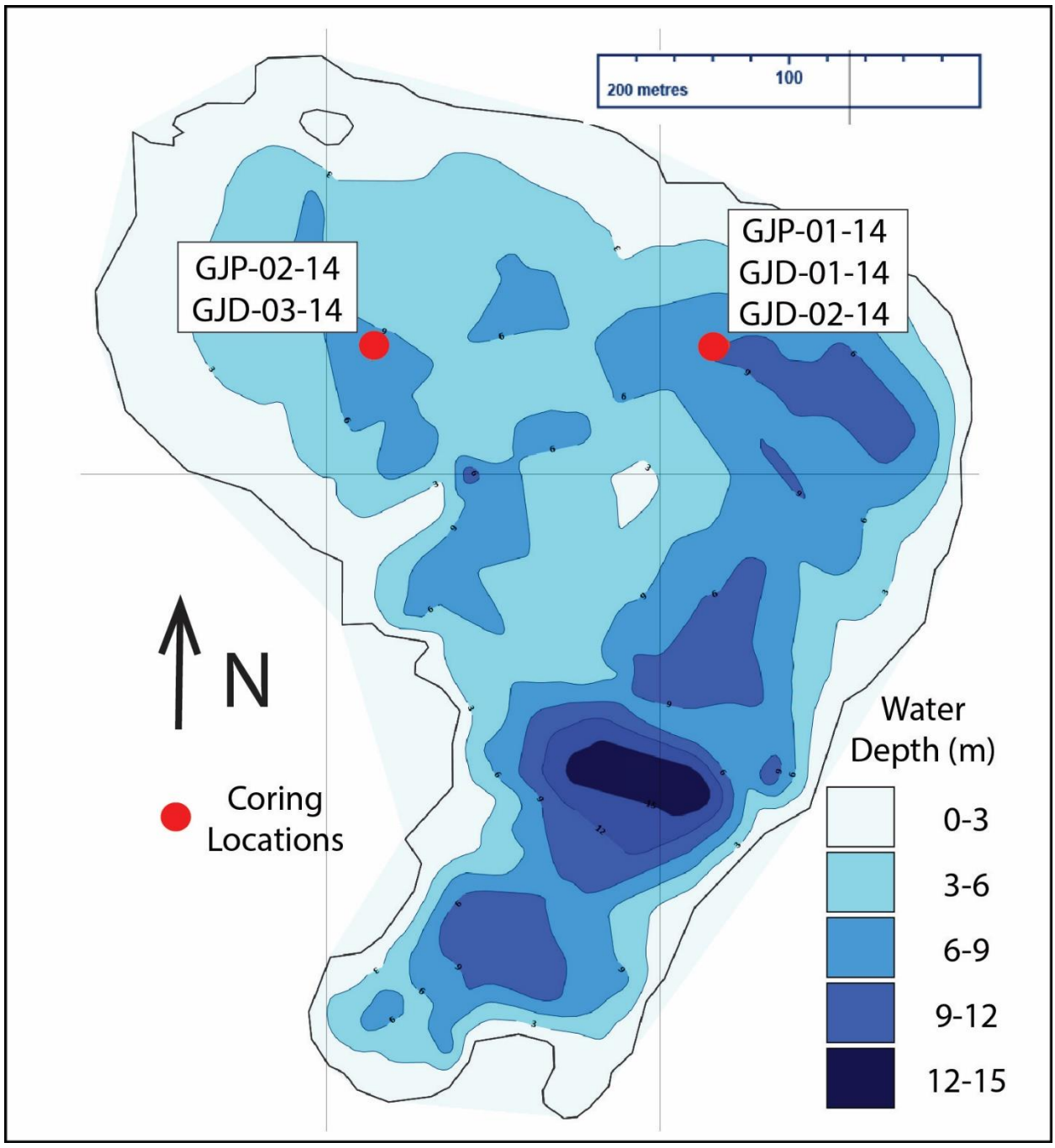

Figure 2.2 - Bathymetric map of Gjøavatnet with coring sites noted by red circles. Our investigation focused mainly on core GJP-01-14 from eastern basin.

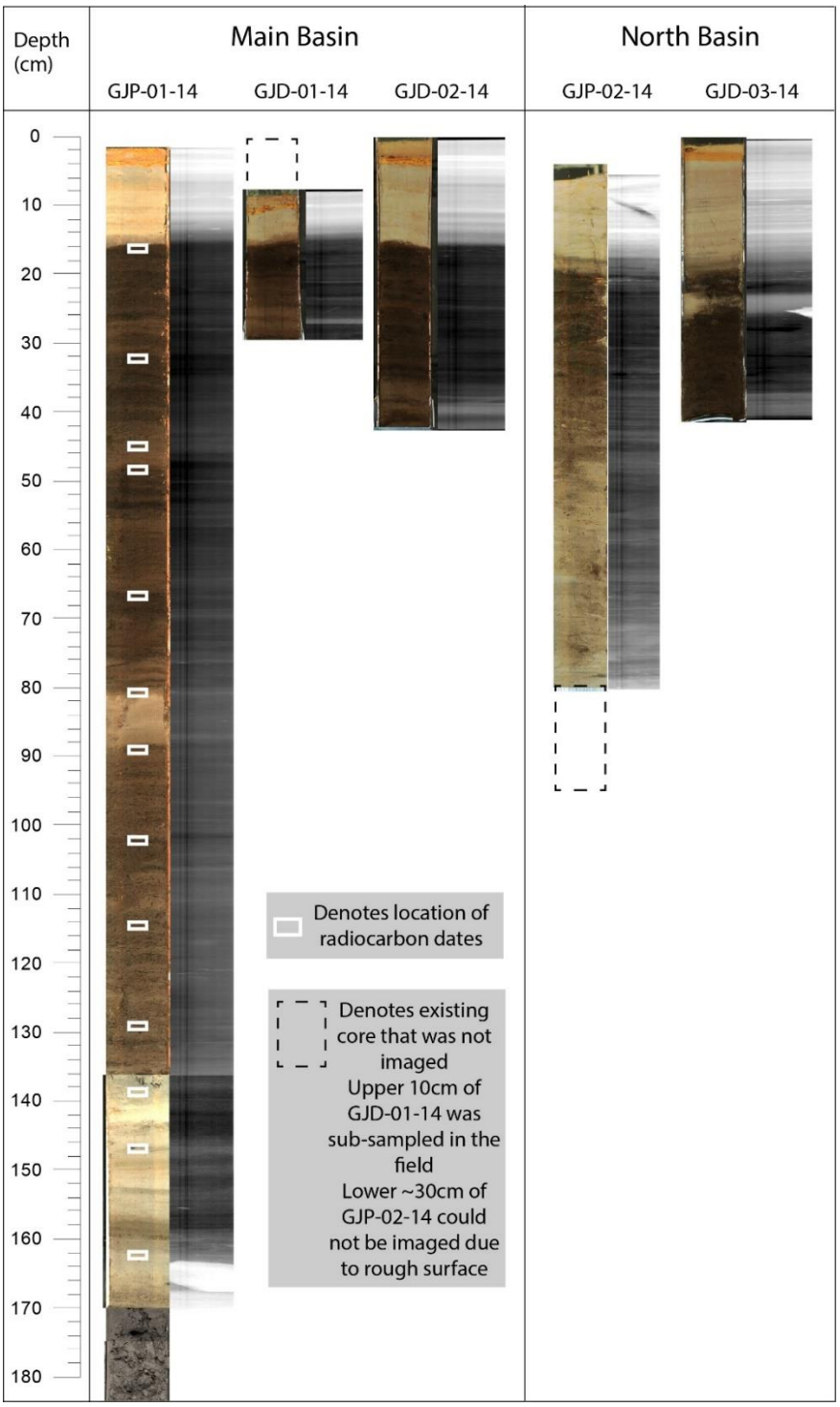

Figure 2.3 - Line-scan images and x-radiographs of all cores collected from Gjøavatnet. GJP-01-14 was the focus of this investigation. Depth of radiocarbon dates are denoted with white rectangles. Dashed black lines represent existing core that could not be imaged. Lighter shades in x-radiographs represent denser material. Note that color difference in lowest portion of GJP-01-14 (section from ~170-180 cm) is due to simply to different lighting during imaging.

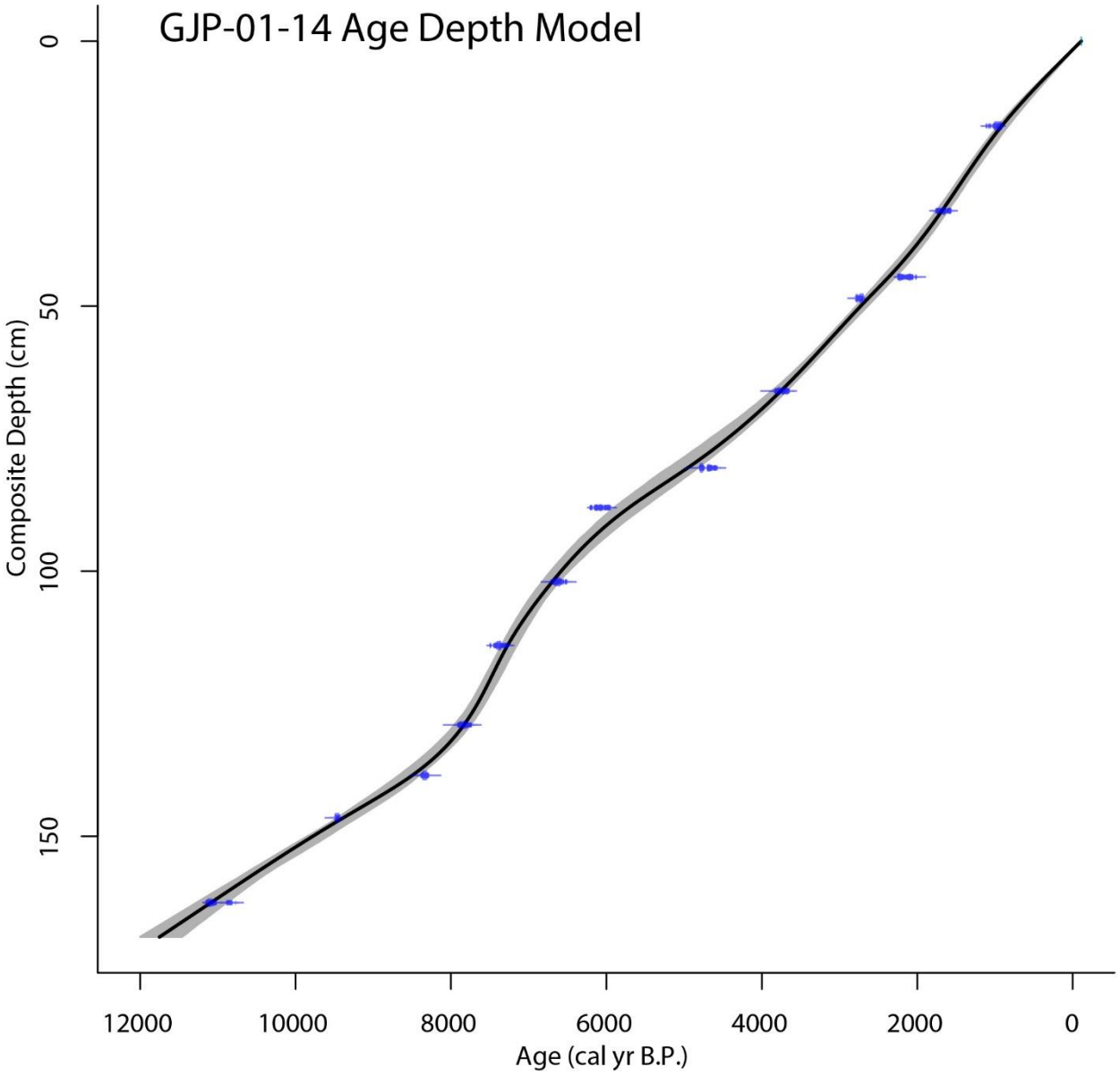

Figure 2.4 - Age depth relationship for GJP-01-14 core created in using the Clam modeling package (Blaauw, 2010) for software R (v. 3.0.1; R Development Core Team, 2013) with 95% confidence intervals for individual radiocarbon dates in blue.

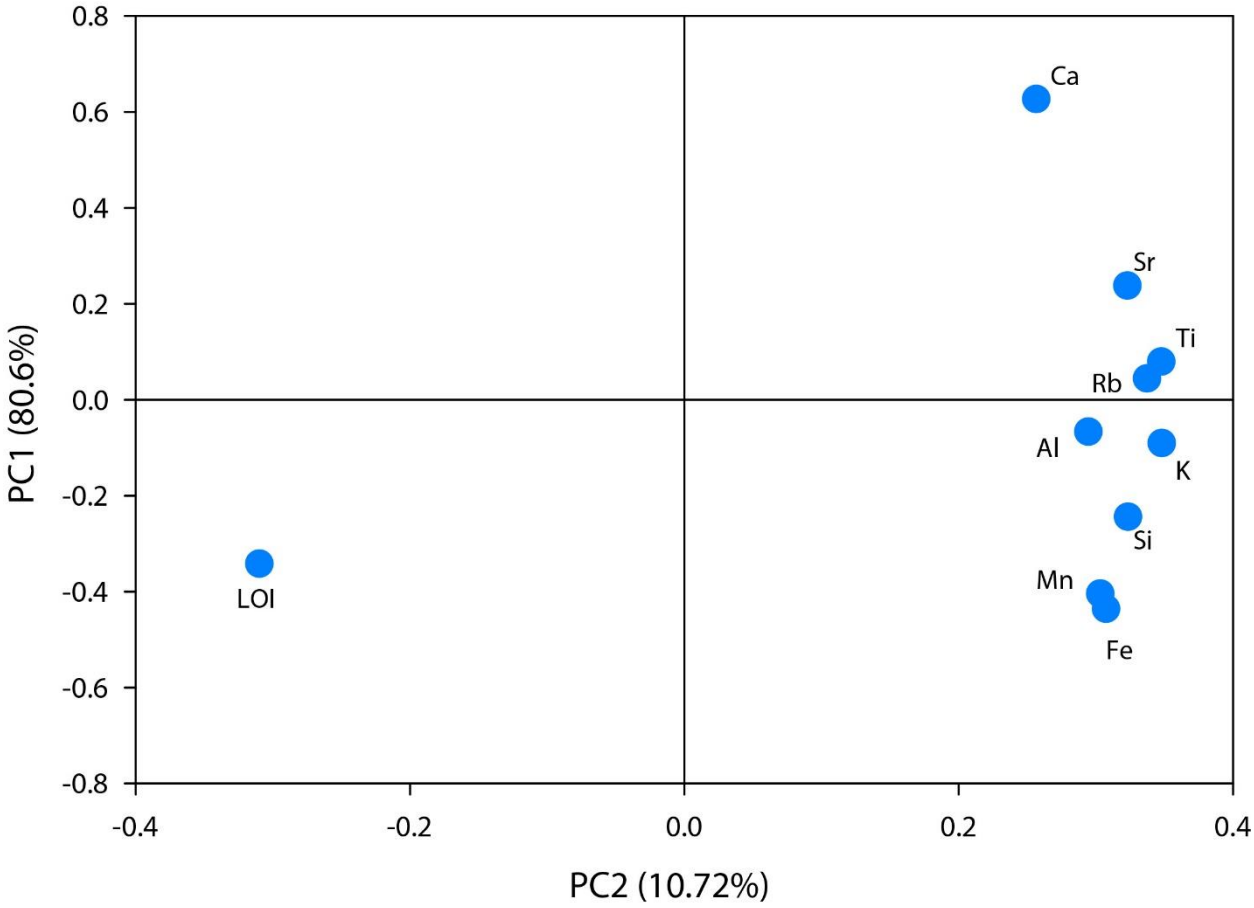

Figure 2.5 - Ordination diagram showing 1st (80.6% of variance) and 2nd (10.72% of variance) principal components of PCA.

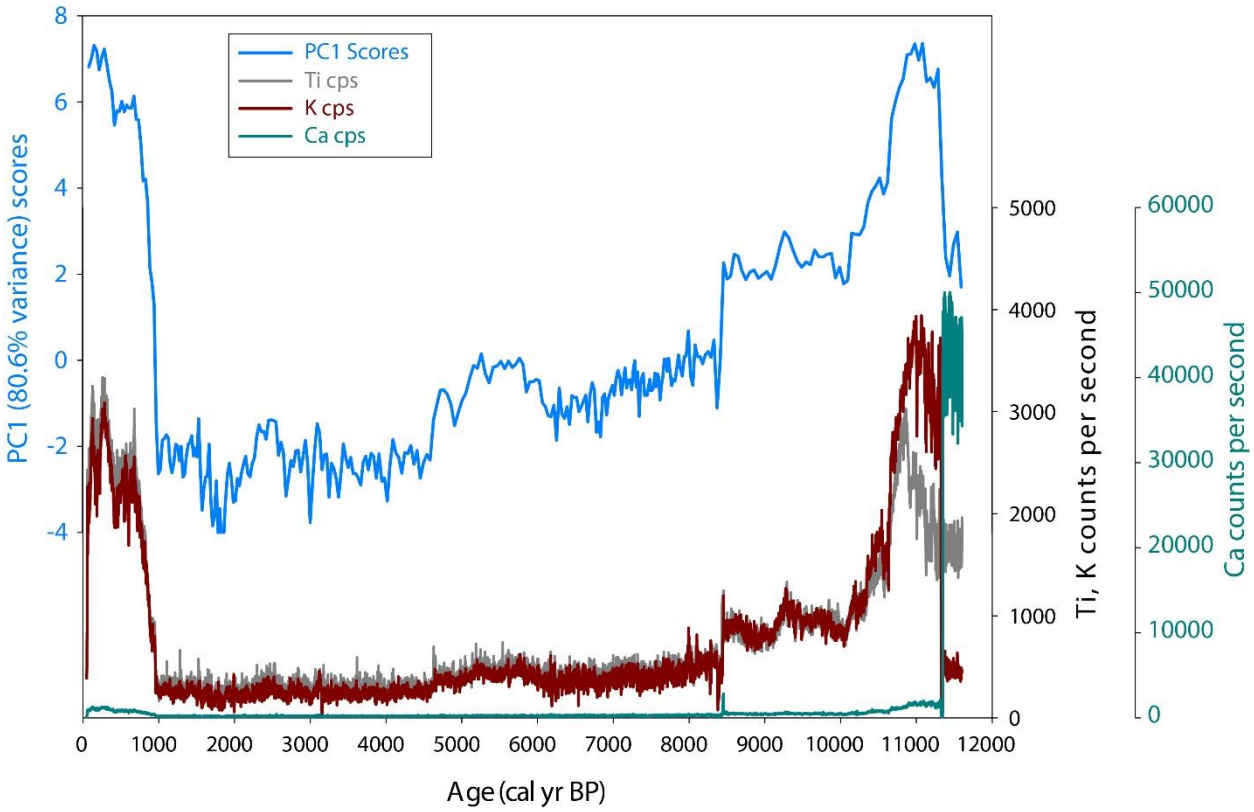

Figure 2.6 - Downcore scores of 1st principal component from PCA analysis (blue line) plotted on age scale with Itrax elemental data for Ti (gray), K (dark red) and Ca (cyan) for core GJP-01-14. Note different scale for Ca data relative to Ti and K.

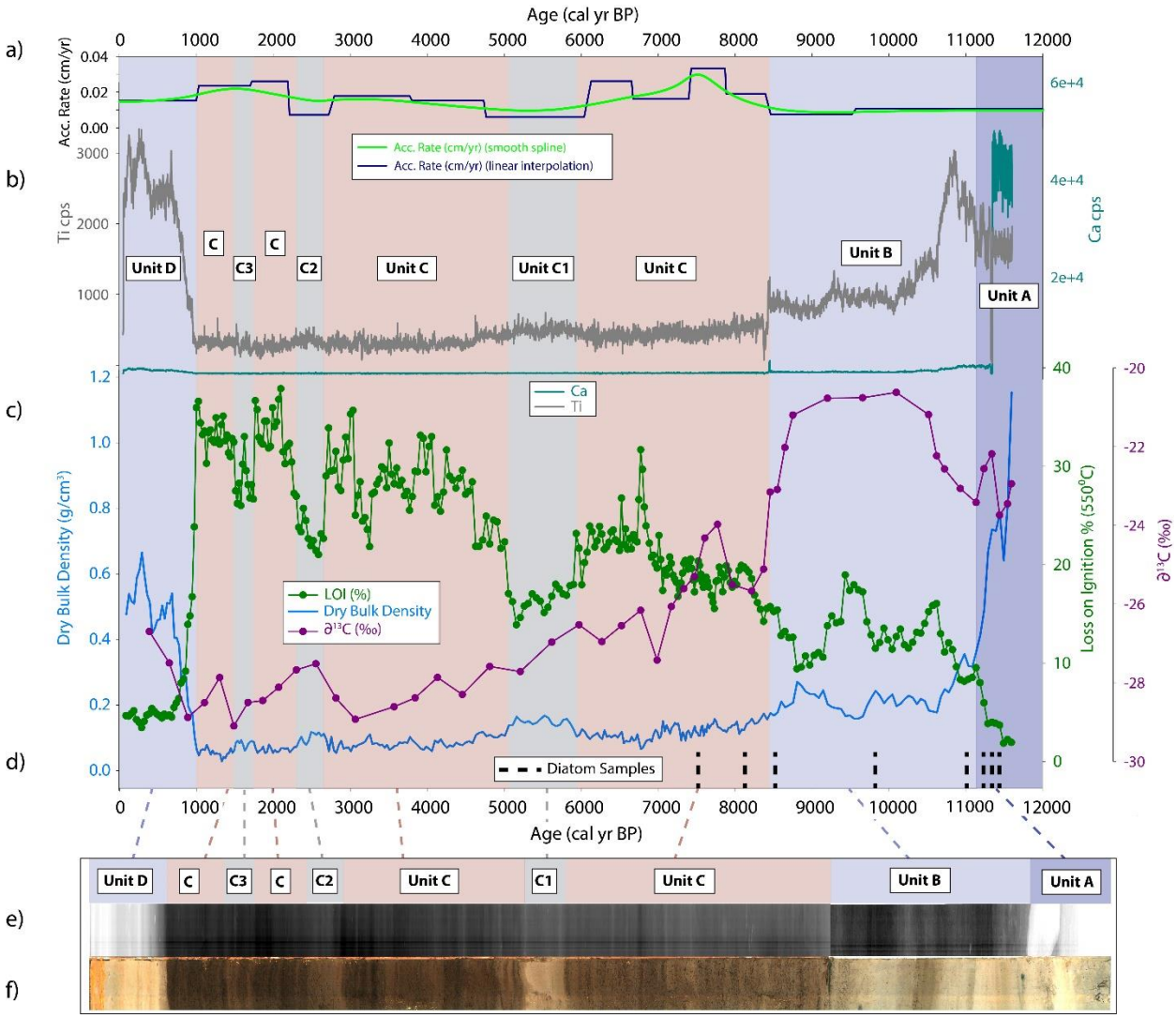

Figure 2.7 - Downcore proxy results for GJP-01-14. Shaded background colors denote different sedimentary units (Units A-D). a) Sediment accumulation rates based on smooth spline interpolation (light green) and linear interpolation (dark blue) between radiocarbon dates; b) Itrax elemental data showing Ti (gray) and Ca (cyan) (note different scales); c) Loss-on-ignition (dark green), bulk $\delta^{13}C$ (purple) and dry bulk density values (dark blue); d) location of diatom taxonomy samples (black dashed lines); e) normal image and f) X-ray image of GJP-01-14 core. Light/white shades in f) denote denser material.

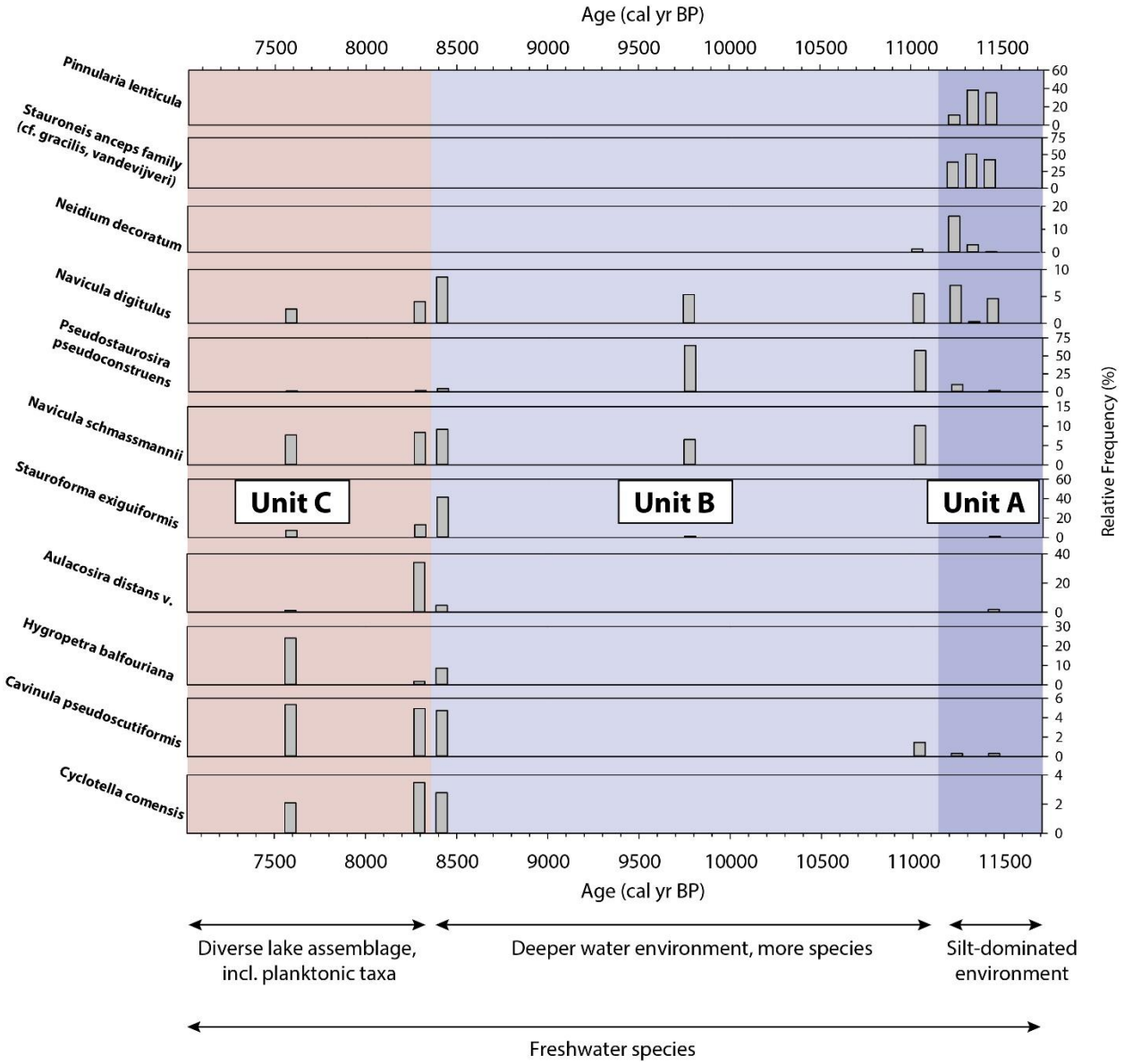

Figure 2.8 - Percent abundance of diatom taxa throughout the early evolutionary history of Gjøavatnet. Note sedimentary unit delineations (labels and background shaded colors) that correspond with **Figure 2.7**.

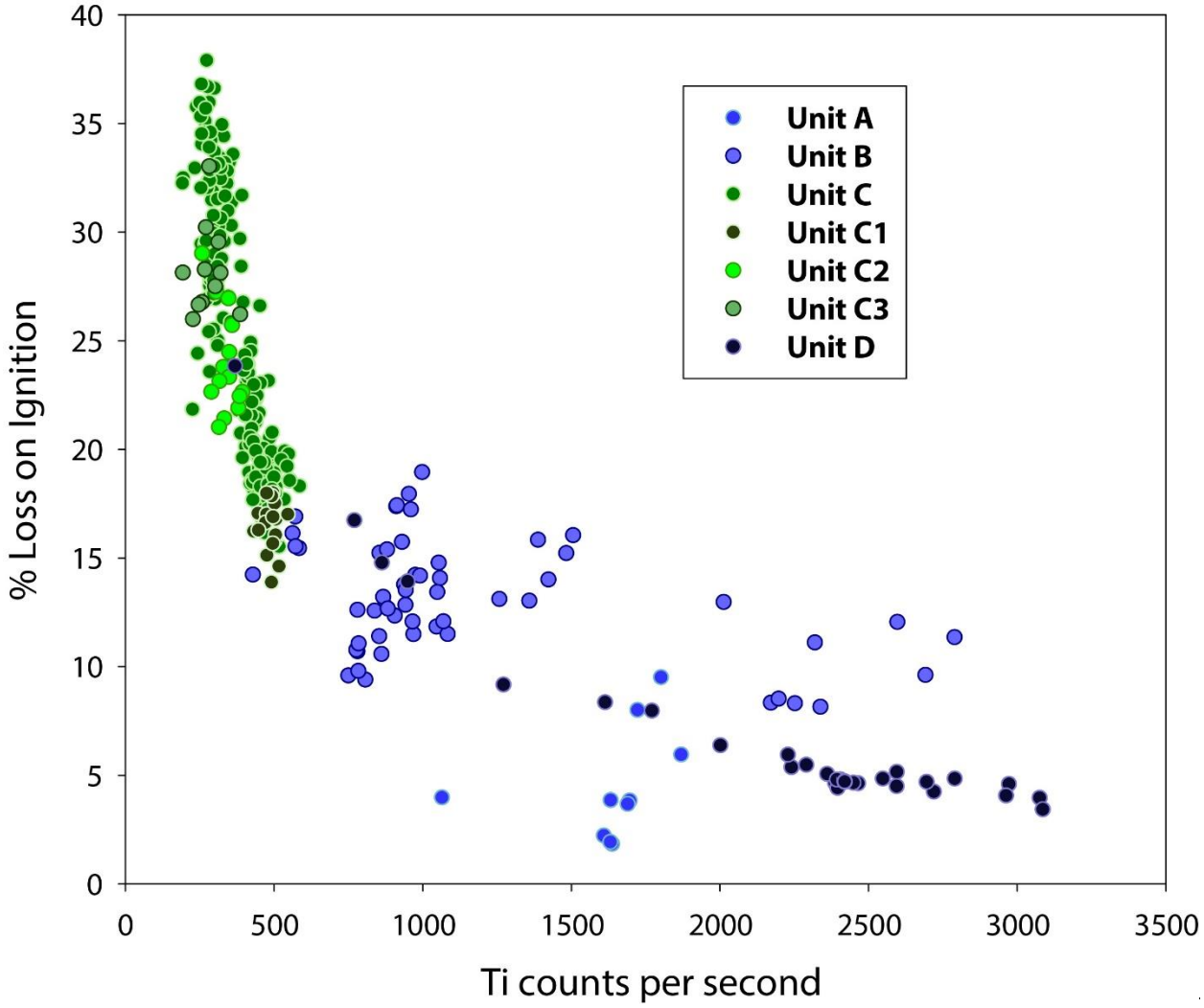

Figure 2.9 - Relationship between % Loss-on-ignition (LOI) and Ti counts from Itrax. Data from sedimentary units when Annabreen glacier is interpreted to be present are shown in blue shades (Unit A, B, D); data from units when Annabreen interpreted to be absent are shown in green shades (Unit C, C1, C2, C3).

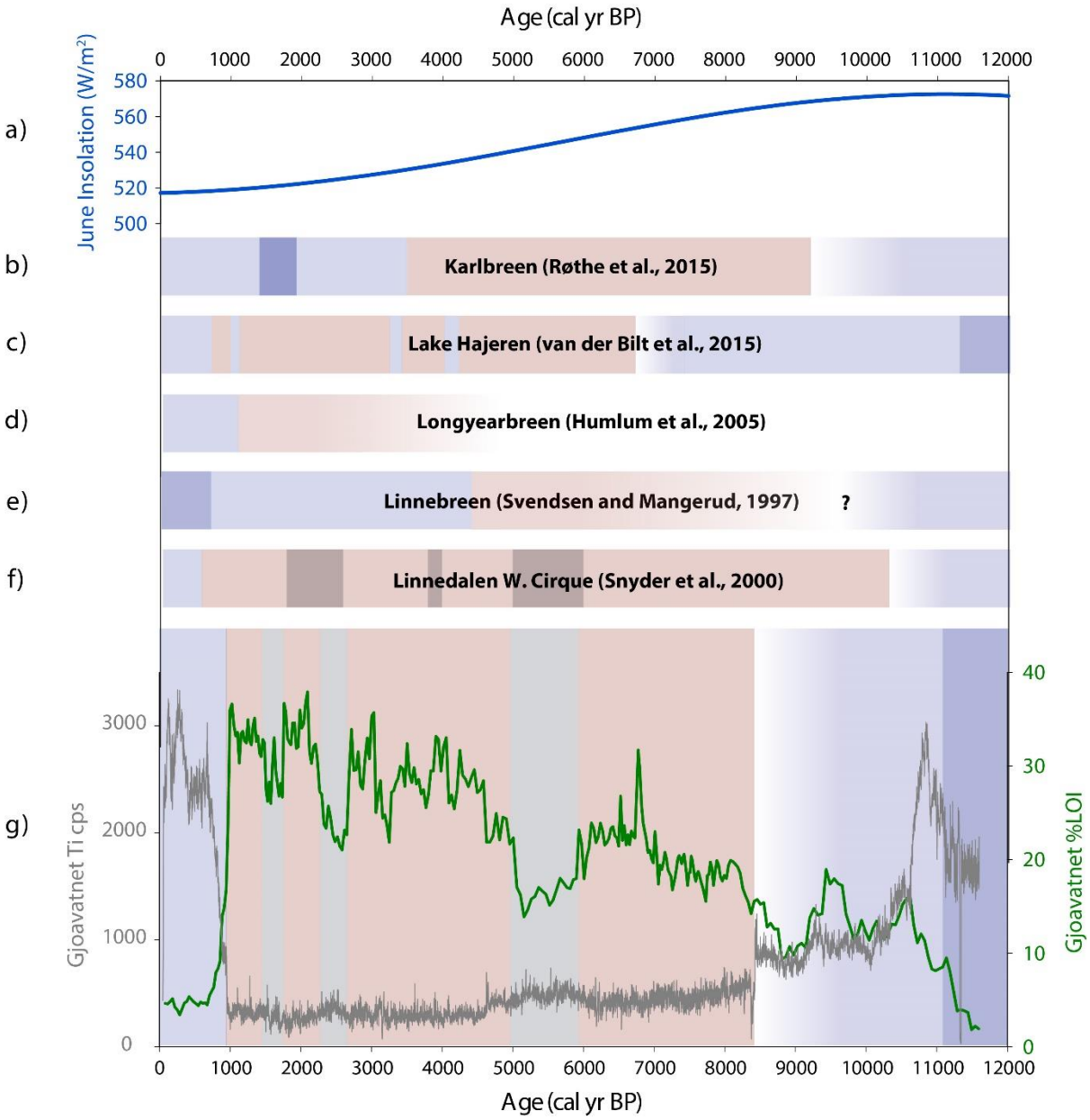

Figure 2.10 - Holocene glacial activity reconstructions from Svalbard: a) June insolation values at 79°N over the Holocene (Laskar et al., 2004); schematic depiction of glacier activity in Svalbard based on published reconstructions: a) and b) proglacial lake reconstructions from Mitrahalvøya peninsula (Røthe et al., 2015; van der Bilt et al., 2015); c) proglacial paleosol and vegetation study (Humlum et al., 2005); d) & e) proglacial lake records from Linnévatnet (Svendsen and Mangerud, 1997; Snyder et al., 2000); f) %LOI and titanium counts from Gjøavatnet (this study). Blue boxes represent periods of glacial activity (dark blue = enhanced glacial activity), red boxes suggest no glacier was present in the catchment or glacial activity was greatly reduced; gray boxes indicate periods of reduced organic matter accumulation (Gjøavatnet) or increased laminations (Snyder et al., 2000) that are not interpreted as glacial activity.

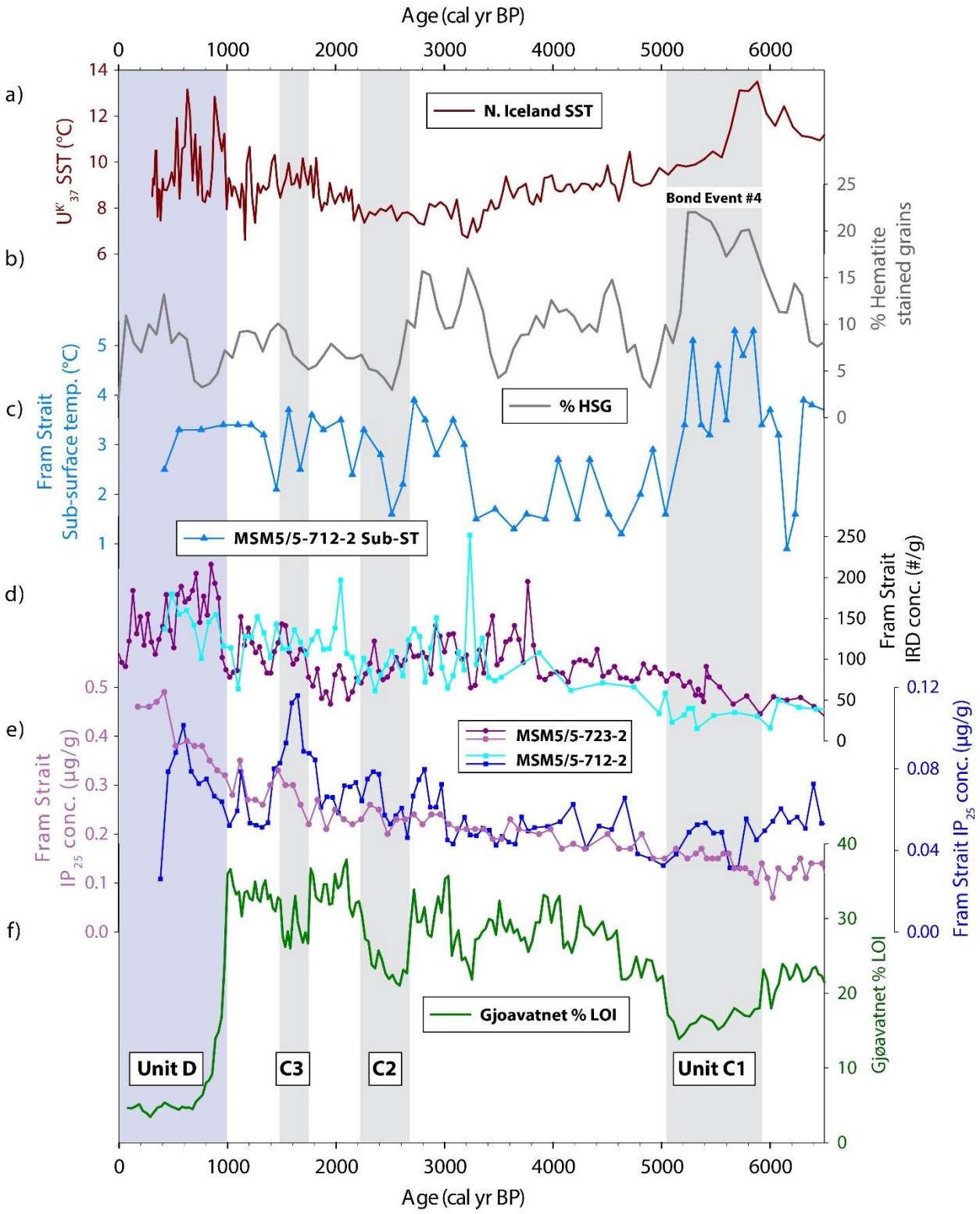
Age (cal yr BP)
0
1000
2000
3000
4000
5000
6000
a)
b)
c)
d)
e)
f)
N. Iceland SST
$U^{K'}_{37}$ SST (°C)
Bond Event #4
% Hematite stained grains
% HSG
Fram Strait Sub-surface temp. (°C)
MSM5/5-712-2 Sub-ST
Fram Strait IRD conc. (#/g)
MSM5/5-723-2
MSM5/5-712-2
Fram Strait IP_{25} conc. (µg/g)
Fram Strait IP_{25} conc. (µg/g)
Gjoavatnet % LOI
Gjøavatnet % LOI
Unit D
C3
C2
Unit C1

Figure 2.11 - Compilation of relevant paleoclimate data from NW Svalbard, Fram Strait, and Davis Strait: a) Alkenone based sea-surface temperatures from NW Icelandic shelf (Moossen et al., 2015); b) % hematite stained grains from core VM29-191 as a proxy for drift ice, w/ Bond Event #4 labeled (Bond et al., 2001); c) sub-surface (~100m depth) foram-based temperatures from core MSM5/5-712-2 (Werner et al., 2013); d) IRD counts and e) IP_{25} concentrations from core MSM5/5-712-2 (cyan/blue square data points) (Werner et al., 2013) and MSM5/5-723-2 (purple circle data points) (Werner et al., 2015) from Fram Strait; f) % loss-on-ignition data (green) from Gjøavatnet lake. Background shaded colors refer to sedimentary units from Gjøavatnet record (**Figure 7**).

CHAPTER 3

A MAJOR ENVIRONMENTAL DISTUBANCE IN THE FAROE ISLANDS 2200 YEARS AGO: POTENTIAL EVIDENCE FOR EARLY HUMAN SETTLEMENT?

3.1 Introduction

The Faroe Islands, located ~300 km northwest of the Shetland islands and ~400 km east of Iceland, have been seen as an important "stepping stone" for the colonization of the North Atlantic by the Norse during the latter stages of the first millennium AD (Arge, 1991, 2014) (**Figure 3.1**). Though the narrative of intrepid 'Vikings' exploring and colonizing this archipelago is compelling, the intellectual community has long been at odds over when this *landám,* or first settlement, actually occurred (Arge, 2014). Archaeologists generally have favored a later, Norse *landám* ~800 AD (Arge, 2014), while paleo-ecologists argued that much earlier vegetation changes could have been caused by humans (e.g. Hannon et al., 1998, 2005; Hannon and Bradshaw, 2000; Jóhansen, 1989, 1985). Beyond the intriguing debate regarding first settlement, the archipelago's unique position straddling the boundary of warmer, Atlantic Ocean water from the south and cold Norwegian Sea overflow water makes paleoclimate records from this location potentially useful to reconstruct changes in ocean circulation back through time (e.g. Humlum and Christiansen, 1998; McGowan et al., 2008). Paleoclimate and paleo-environmental reconstructions from the Faroe Islands are therefore useful in that they have the potential to record both climatic and anthropogenic changes over the Holocene Epoch (past ~11,700 calendar years before present (cal yr BP)). Here we present a well-dated, multi-proxy record from Eiðisvatn (vatn = lake) on the Faroe Islands (**Figure 3.2**), where a marked disturbance in the sediments suggests humans may have reached the archipelago ~200 BC (2200 cal yr BP), much earlier than currently thought. This research is part of a larger project involving numerous lake sediment records from throughout the Faroes that attempts to reconstruct both when humans reached the Faroes and how climate has changed in the region over the Holocene.

The longstanding tradition regarding the first settlement of the Faroe Islands suggests that the archipelago was first settled by Norse colonizers from Norway, which is based on numerous historical texts collectively known as the *Færeyinga Saga*. The vast majority of archaeological evidence supports this notion of a Norse arrival and *landnám* around the start of the 9th century (Arge et al., 2005; Arge 2014).

A tantalizing piece of literary evidence does exist, however, that potentially challenges this supposition. A manuscript written by a monk named Dicuil describes a group of islands to the north of Shetland. The text reads: "There are many other islands in the North British sea. They can be reached from the northern islands of Britain by sailing for two days and two nights on a straight course under full sail if the wind is favorable the whole time. A devout priest has told me that he navigated this route in two summer days and the intervening night, in a small boat with two thwarts, and landed on one of the islands. These islands are for the most part small, and there are mostly narrow sounds between them, and in these islands hermits, come from Ireland by boat, have lived for almost a hundred years. But as they have always been uninhabited from the beginning of the world, so have Norwegian Vikings caused them to be devoid of monks, but sheep are abundant and there are different kinds of seabirds. I have never seen these islands mentioned in the books of other authors" Dicuil (Irish Clergyman) A.D. 825: *De Mensuris Orbis Terrae (The Dimensions of the Earth) [translation by Tierney, 1967*]. Due to the fact that Dicuil mentions he actually spoke to someone who had been to these islands, and that he writes about monks living there for "almost 100 years", it has been suggested that this represents evidence for an earlier, non-Norse settlement of the Faroes. This suggestion has generated much debate, however (e.g. Debes, 1993; Arge, 1991, 1993). Some dispute that the text even refers to the Faroes, others question Dicuil's sources, and most importantly there is considerable skepticism about the inferred date of settlement.

Interestingly, there is further evidence beyond this intriguing passage for earlier settlement date. The proposed dates for initial human settlement of the Faroes are compiled in

Figure 3.3. The pioneering Johaness Jóhansen, working in the 1970s and 1980s, chronicled environmental change on the islands throughout the Holocene, mainly through the analysis of pollen grains preserved in lake and bog sediments (Jóhansen, 1985; 1989). He noted the first appearance of the plant *plantago lanceolata* (ribwort plantain), which is often associated with the settlement of humans, as early as 2300 BC (4300 cal yr BP). While this very early settlement date remains highly contentious (Arge, 1991), more recent research has suggested that people likely arrived well before the Norse in 800 AD (Hannon et al., 1998, 2005; Hannon and Bradshaw, 2000). These paleo-environmental studies on lake and bog sediments suggest, based on increased erosion, the appearance new plants species, etc., that humans (likely Irish or Celtic monks) arrived in the Faroes by 500-700 AD (1500-1300 cal yr BP). This notion was further supported by archaeological evidence in the form of charred barley grains dating from 300-500 AD on Suderoy in the southern part of the archipelago (Church et al., 2013).

The use of paleo-environmental archives such a lake sediments to answer historical questions is advantageous in many ways, as lake watersheds collect a wealth of information that is eventually transferred to the sediment record. Conversely, archaeological evidence is hampered by availability and access issues, and, in localities like the Faroes where desirable land is in short supply, new buildings were often constructed directly on top of older ones (e.g. Arge, 2014). In theory, a landscape devoid of both humans and grazing mammals would undergo marked change when these forces were introduced (Church et al., 2005; Gathorne-Hardy et al., 2007). In practice however, separating and properly identifying anthropogenic signals from climate-forced signatures in sedimentary records is complicated. Indeed, many other researchers have found evidence for widespread “landscape degradation” in the Faroes beginning earlier during the Holocene (e.g. Andresen et al., 2006; Gathorne-Hardy et al., 2007; Lawson et al., 2005; McGowan et al., 2008; Olsen et al., 2010). In most cases, the authors attribute these changes to “climate deterioration”, i.e. wetter and cooler conditions, and not human influence. Many of these records are poorly dated however, with only a few radiocarbon dates in some places, rendering

the timing of some of these changes suspect. It is obviously important, therefore, to understand how climate has varied in the past, along with the signature of those climatic changes in the sediment record, when attempting to ascribe an observed paleo-environmental change to human influence.

The very early Holocene (> 10200 cal yr BP) in the Faroes was characterized by an open landscape with gravely and rocky soil cover (Jóhansen, 1985). By 10000 cal yr BP the climate is thought to have become more mild and oceanic, with grasses and sedges colonizing the islands (Hannon et al., 2010; Jessen et al., 2008; Jóhansen, 1985). Warmer temperatures, in the form of a climatic optimum centered on 8400 cal yr BP (Andresen et al., 2006; Roncaglia, 2004), gave way to cooling conditions beginning ~7000 cal yr BP (Jóhansen, 1985; Olsen et al., 2010). Peat development on the islands is thought to have occurred throughout the Holocene, with basal peat dates spanning the past 9000 years (Humlum and Christiansen, 1998; Lawson et al., 2007a). Landscape erosion rates appear to have increased ~5000 cal yr BP (Andresen et al., 2006; Lawson et al., 2007b; Olsen et al., 2010), with further increases noted at some sites beginning at 1700 cal yr BP (McGowan et al., 2008), and 1360 cal yr BP (Olsen et al., 2010). In both cases the authors *assume* a settlement date of ~ 1150 cal yr BP (800 AD), and therefore rule out an anthropogenic cause for these changes. By the late Holocene the landscape vegetation was apparently similar to what is seen today, composed primarily of grasses and shrubs, with only minor contributions of trees like juniper and birch (Arge, 2014; Lawson et al., 2005). At some sites the period of human settlement is accompanied by an increase in erosion and terrestrial input (Hannon et al., 2005; Hannon and Bradshaw, 2000; Olsen et al., 2010), though at others this signal is weaker and less dramatic (Gathorne-Hardy et al., 2007; Lawson et al., 2005). Broadly, the literature suggests conditions on the Faroes were cooler and wetter heading into the late Holocene, with any anthropogenic impacts occurring against a backdrop of increased erosion and landscape degradation.

In summary, it is apparent that significant uncertainty remains regarding; a) the settlement date of the Faroe Islands, and b) the nature of climate changes during the settlement period. To answer these questions we analyzed %loss-on-ignition, geochemical elemental abundances, and a suite of biomarkers (branched glycerol dialkyl glycerol tetraethers – brGDGTs, leaf wax *n*-alkanes, and sterol & stanol compounds indicative of primary productivity) from a ~3m long sediment core from Eiðisvatn lake on the Island of Streymoy in the Faroes (**Figure 3.2**). Our results suggest a major environmental disturbance occurred ~2200 cal yr BP (approx. 220 yrs BC) that seem unlikely to be forced by climatic variations. Reconstructed changes in productivity and organic matter composition, indicative of increased delivery of nutrients and terrestrial organic matter to the lake system, fit well with a narrative of landscape change caused by the introduction of grazing animals to a watershed. If confirmed to be anthropogenic in nature, our results would shift the date of human settlement of the Faroes Islands earlier by ~600 years.

3.2 Site Description

The Faroe Islands are located between 61°19’ and 62°22’ N and 7°38’ and 6°15’ W and constitute 18 hilly islands with numerous fjords and small islets. The archipelago is 113 km from north to south and 75 km from east to west (**Figure 3.2**). The islands are composed primarily of Tertiary flood basalts erupted nearly 60 million years ago prior to the opening of the North Atlantic ocean basin (Rasmussen et al., 1970). The Faroes were heavily glaciated in the past, with the youngest glacial activity suggested to be Younger Dryas in age (Humlum et al., 1996).

Today, the climate is generally mild and windy, with mean temperatures in January of ~3°C and ~10°C in August (1961-1990) (Cappelen and Laursen, 1998). Precipitation is variable across the islands, with an average annual rainfall of ~800 mm in the south and 3300 mm in the north (Cappelen and Laursen, 1998). The highest peak in the islands is 882 m a.s.l., and ~70% of the archipelago is above 200 m in elevation. Much of the landscape today is covered by peat and the vegetation is primarily grass heath (McGowan et al., 2008). Of the ~800 lakes and ponds

(area >300m^2) on the Faroes, only those at high elevations experience any lake ice in the winter (McGowan et al., 2008).

Eiðisvatn, the location investigated in this study, is a relatively large lake situated at approx. 130 m a.s.l. (**Figure 3.2**). It is roughly 1 km wide and 1.2 km long, and is surrounded by low-relief peat/heathland with higher peaks (>600 m) present within the catchment to the northeast and east (**Figure 3.2**). The lake is situated just upslope from the village of Eiði and the lake Heimavatn, which was investigated by Hannon et al. (2005).

The straight southern and western boundaries of the lake today are the result of lake damming activities in the late 1980s (Arge, 2014), which expanded the surface area of Eiðisvatn. Prior to damming of the lake, an archaeological site named Argisbrekka was situated just adjacent to Eiðisvatn. Thought to be a "sheiling", or summer dwelling for sheep herders and farmers, the remains of more than 21 buildings have been found there, dating primarily to the Viking age (800-1000 AD) (Mahler, 2007; Arge, 1991; 2014). Interestingly, the name element "ærgi" or "argi" is of Celtic origin and is thought to have entered the Norse language during the 9th century (Matras, 1956), potentially suggesting an older, Celtic origin for this site.

3.3 Methods

3.3.1 Fieldwork and Coring

Fieldwork was conducted in August of 2015, and five lakes were cored in total (Eiðisvatn, Lenynavatn, Sandsvatn, Storavatn, and Grothusvatn – **Figure 3.2**). Three sediment cores were collected from Eiðisvatn; 2 gravity/surface cores (EI-D-01-15; 83.7cm in length, and EI-D-02-15; 100.7cm), and 1 piston core (EI-P-01-15; 281.5 cm) (**Table 3.1**). Gravity cores were collected using a Uwitec surface corer and cores were only retained if the sediment/water interface was undisturbed. The piston core was collected using a percussion piston coring device and was hammered until refusal to ensure maximum sediment recovery. The upper 10 cm of EI-

D-01-15 was sub-sampled in the field before being packed for shipment. The EI-P-01-15 core was cut into two sections (1 of 2: 139.6cm, 2 of 2: 141.9 cm) to allow for transport and core scanning. The sediment cores were then shipped back to the University of Massachusetts, Amherst for splitting and analysis.

3.3.2 Laboratory Analyses

Cores were split and imaged at the University of Massachusetts, Amherst prior to analysis. EI-D-01-15 and both core sections of EI-P-01-15 were analyzed using an ITRAX X-ray fluorescence (XRF) core scanner to determine elemental abundances. Scans were carried out using a molybdenum (Mo) tube with a downcore resolution of 200 µm. The voltage and current were set to 30kV and 55mA respectively, with an XRF count time of 10 seconds.

Both EI-D-01-15 and EI-P-01-15 were sub-sampled at 1 cm intervals for weight loss-on-ignition (LOI), dry bulk density (DBD), and water content (WC) (n=335) (after Dean, 1974; Heiri et al., 2001). A syringe was used to ensure a constant 1 cm^3 of sediment was removed.

Macrofossils for radiocarbon dating were sampled from both the piston and EI-D-01-15 cores. Analyses were carried out at the Woods Hole NOSAMS facility and the University of California, Irvine AMS facilities.

A total of 68 samples were chosen for biomarker extraction and analysis. 47 samples were selected from the EI-D-01-15 surface core and 21 from the EI-P-01-15 piston core. The sediment was freeze-dried and homogenized before lipid extraction.

A total lipid extract (TLE) was obtained using a Dionex accelerated solvent extractor (ASE 200). Samples were extracted with a dichloromethane (DCM)/methanol (9:1, v/v) mixture at 100ºC. The TLE was then saponified to separate the lipid extract into a neutral and fatty acid fraction (after Birk et al., 2012). The neutral fraction was then further separated into three fractions, apolar (9:1 DCM:hexane, v/v), ketone (1:1 DCM:Hexane, v/v) and polar (1:1 DCM:methanol, v/v), using alumina oxide column chromatography.

One half of the polar fraction was filtered in 99:1 hexane:isopropanol using a 0.45μm PTFE syringe filter prior to analysis by high performance liquid chromatography (HPLC) to identify and quantify brGDGTs. A C_{46} GDGT internal standard was added to all polar fractions prior to analysis. BrGDGTs were identified and quantified via high performance liquid chromatography - mass spectrometry using an Agilent 1260 HPLC coupled to an Agilent 6120 MSD following the methods of Hopmans et al. (2000) with minor modifications (Schouten et al., 2007). For compound separation a Prevail Cyano column (150 x 2.1mm, 3 μm) was used. Two solvent mixtures were used as eluents: mixture A) 100% hexane; mixture B) 90% hexane, 10% isopropanol (v/v). Samples were eluted with 10% mixture B for 5 minutes, which was then linearly increased to 18% mixture B from minutes 5-39, and finally increased to 100% mixture B for one minute. Scanning was performed in selected ion monitoring (SIM) mode. Concentrations were calculated by comparing brGDGT HPLC-MS chromatogram peak areas with peak areas of a known concentration (C_{46} GDGT standard added to every sample run). These values were then normalized to the mass of sediment extracted.

The other half of the split polar fraction was derivatized using BSTFA before injection on either a gas chromatograph – mass spectrometer (for compound identification) or gas chromatograph – flame ionization detector (GC-FID), for compound quantification. Individual compound peaks were compared against published mass spectra. Compound peak areas were related to a squalene calibration curve of known concentrations run within two weeks of analysis.

Plant leaf waxes (*n*-alkanes) form the waxy surface of terres-trial plant leaves, and can be short- (e.g. C_{17}–C_{21}, characteristic of aquatic organisms) or long-chained (C_{27}–C_{33}, characteristic of terrestrial higher plants) (Eglinton and Hamilton, 1967). For *n*-alkane analyses, apolar fractions were first injected on a Agilent 7890A dual gas chromatograph-flame ionization detector (GC-FID) with an Agilent 7693 autosampler equipped with a 5% phenyl methyl siloxane column (HP-5, 60 m ×0.32 mm×0.25 μm). The oven program ramped from 70°C to 130°C at a rate of 10°Cmin^{-1}, then from 130°C to 320°C at a rate of 4°Cmin^{-1}, and held the final temperature for 10

min. Quantification was achieved by an external calibration curve of squalane ranging in concentration from 1 ng/µl to 100 ng/µl. The *n*-alkanes were identified by a Hewlett Packard 6890 gas chromatograph coupled to an Agilent 5973 Mass Selec-tive Detector equipped with a 5% phenyl methyl siloxane column (HP-5MS, 60 m ×0.25 mm×0.25 µm), with an identical oven pro-gram to the GC-FID.

3.3.3 Paleoenvironmental Reconstructions

Paleotemperatures and paleo-pH were reconstructed from brGDGT distributions using two indices as originally defined by Weijers et al. (2007). The first is the cyclisation ratio of branched tetraethers (CBT) (Eq. 1). This index describes the relative amount of cyclopentyl moieties in the branched GDGTs, which Weijers et al. (2007) found to be correlated to pH. The second index, the Methylation of Branched Tetraethers (MBT), describes the presence of methyl branches at the C-5 and C-5' positions and was found to be positively correlated to MAAT, and to a lesser extent, negatively correlated to pH (Eq. 2). By combining these two indices, Weijers et al. (2007) were able to produce a robust paleotemperature proxy for soil-derived brGDGTs. In recent years this MBT/CBT relationship has been expanded to include lake sediment samples, yielding numerous lake specific calibrations (e.g. (Loomis et al., 2012; Pearson et al., 2011; Sun et al., 2011; Tierney et al., 2010). For this study the calibration of Sun et al. (2011) (Eq. 3) was applied to reconstruct temperature. In equations 1 and 2 the roman numerals and letters denote the different brGDGT structures as shown in Figure A1, Appendix A in Weijers et al. (2007).

Eq. 1: $\mathbf{CBT} = \frac{[\mathbf{Ib}]+[\mathbf{IIb}]}{[\mathbf{I}]+[\mathbf{II}]}$ (Weijers et al., 2007)

Eq. 2: $\mathbf{MBT} = \frac{[\mathbf{I+Ib+Ic}]}{[\mathbf{I+Ib+Ic}]+[\mathbf{II+IIb+IIc}]+[\mathbf{III+IIIb+IIIc}]}$ (Weijers et al., 2007)

Eq. 3: $\boldsymbol{T = 6.803 - 7.602 \times CBT + 37.090 \times MBT}$ (Sun et al., 2011)

Eq. 4: $\boldsymbol{ACL = \sum_{n=21}^{33} n * f(C_n)}$

3.4 Results

3.4.1 Composite Sediment Record

A composite sediment record was created based on aligning proxy data and visual stratigraphy from the EI-D-01-15 surface core with the EI-P-01-15 core (NB: due to the fact that the upper 10cm of the EI-D-01-15 core was sub-sampled in the field, core scanning and LOI data is not available from that section of the core). Based on these comparisons, it is apparent that ~20cm of sediment was lost from the upper part of EI-P-01-15 during coring (**Figure 3.4**) (note that top 10cm of EI-D-01-15 is missing from image). We assign an offset of 20.36 cm based on matching of elemental counts from Itrax data. This results in a ~300 cm composite record. As noted above, Eiðisvatn was dammed and expanded in the 1980s. This operation likely caused the smaller disturbance near the top of EI-D-01-15 (**Figure 3.4**). A 'modern' (post 1950) radiocarbon sample was taken just below this disturbance, at a composite depth of 18.5cm. We assign that depth an age of zero (1950) for our age depth model (see below).

For the purposes of this investigation, where we wish to search for the first presence of humans in the landscape and mid-late Holocene climate evolution, we focus mainly on the upper ~200 cm of the core, though we contextualize changes in the upper part of the core with the entire Holocene. The climate record over the entire Holocene at Eiðisvatn (and specifically related to differences with Eemian climate) is being investigate by colleagues at Lamont Doherty Earth Observatory (Curtin et al. *in prep*).

3.4.2 Chronology

At the time of writing, the chronology of the composite Eiðisvatn sediment record is based on 16 radiocarbon dates and three identified tephra layers (**Table 3.2**). Tephra isolation, analysis, and identification was conducted by N. Balascio at the College of William & Mary and are discussed in a companion publication (Balascio et al., *in prep*). In the coming months we

expect to supplement this age model with ^{137}Cs and ^{210}Pb data along with further cryptotephra horizons. As evident from **Table 3.2**, at least three radiocarbon dates appear to be "too old" stratigraphically. These ages likely result from old organic matter preserved on the landscape being washed in to the lake (see discussion below). To account for this possibility two different age/depth models were created using the Bayesian framework calibration software code 'Bacon' (v. 2.2; Blauw and Christen, 2011), run in 'R' (v. 3.2.2). The first, termed "EidiAll" (**Figure 3.5**) utilizes all available radiocarbon ages and allows Bacon to determine which are true outliers. The second, termed "EidiBest" excludes the three reversed dates (**Figure 3.6**), and we use this age model to plot all proxy data in this manuscript. Radiocarbon ages are reportedly mainly in calibrated years before present (cal yr BP; BP = 1950) according to IntCal13 (Reimer et al., 2013). Importantly, the modern radiocarbon date at 18.5 cm composite depth is interpreted to represent the base of the disturbance caused by the damming of the lake in the 1980s.

Accumulation rates in the lake (based on the EidiBest age model) vary between ~ 0.01 cm/yr to a maximum of 0.14 cm/yr **(Figure 3.6)**. Highest sedimentation rates are recorded between ~70-160 cm, and are generally lowest during the deeper half of the core (<0.05 cm/yr).

3.4.3 Proxy Results

% Loss-on-ignition (%LOI) and dry bulk density (DBD) data for both the piston core (EI-P-01-15) and the surface core EI-D-01-15 are presented in **Figure 3.7**. The lowest %LOI (and highest DBD) values are recorded at the base of the core (~10400 cal yr BP), with <1% organic matter content. LOI concentrations broadly increase over the next few thousand years, reaching nearly 20 %LOI by 4870 cal yr BP. From this point to ~2400 cal yr BP, LOI concentrations fluctuate between ~12-21%, with a fair amount of short term variability. Beginning around 2400 cal yr BP, organic matter concentrations increase rapidly, peaking at over 40% in EI-P-01-15. %LOI remains high (>30% in the piston core) until ~1000 cal yr BP when concentrations decline to ~ 15%.

Dry bulk density variations are generally the inverse of the %LOI record, with the highest values recorded in the base of the core (note scale break) and the lowest values in both the piston and surface cores recorded in the 2200 -1000 cal yr BP interval (**Figure 3.7**).

Relevant elemental counts from Itrax core scanning are presented in **Figure 3.8** and elemental ratios are presented in **Figure 3.9**. For brevity, only the elements Ti, Ca, K, Si, Mn, and Fe are presented in **Figure 3.8**. The elements Ti and Ca can be related to minerogenic input from erosion and weathering of rocks within a lake catchment (e.g. Balascio et al., 2015; Kylander et al., 2011). These elements have generally similar profiles in Eiðisvatn over the Holocene, with the highest counts recorded in the basal Saksunarvatn ash layer ~10400 cal yr BP (gray bars in **Figures 3.8** and 3.**9**). A period of elevated Ti and Ca counts occurs from ~8700 – 8000 cal yr BP. During the rest of the Holocene peaks in Ti (and to a lesser extent Ca) occur at approx. 7340, 6710, 5780, 4900, 4370, 3500, and 800 cal yr BP. The lowest Ti counts of the entire Holocene are recorded from ~2200 – 1100 cal yr BP. Trends in Ti raw counts are similar to the ratio of Ti counts against Incoh/Coh scattering (**Figure 3.9**), which has been suggested by some researchers as a preferable way to interpret XRF core-scanning data (Kylander et al., 2012).

Raw K counts can be related to both to minerogenic input as well as the presence of tephra particles in lake sediments (Kylander et al., 2011, 2012). In the early Holocene portion of the Eiðisvatn record, K counts display similar variability to Ti and Ca. After ~6000 years BP however, this relationship breaks down somewhat, and the major K peaks at ~3750 cal yr BP (tephra from the Hekla-Selsund eruption) and 4260 cal yr BP (tephra layer from the Hekla 4 eruption) (Balascio et al., *in prep*) (**Figure 3.8**), are not associated with major changes in Ca or Ti counts. Normalizing K counts against Ti has been suggested as a method for isolating tephra layers in lake sediments (**Figure 3.9**) (Kylander et al., 2012). In Eiðisvatn, the Hekla-Selsund and Helka-4 eruptions are easily identified in the K/Ti ratio, but the basal Saksunarvatn tephra registers as only a slight increase. The co-variance of Ca, Ti, and K in the early Holocene and divergence later in the record may be due to differing chemical compositions of erupted tephras.

Si counts may be related to diatom production of biogenic silica, or conversely may also be a measure of input from silicate minerals, though generally this parameter is normalized against other elements like Ti (Si/Ti ratio in **Figure 3.9**) (Brigham-Grette et al., 2013; Kylander et al., 2011; Liu et al., 2013). In Eiðisvatn, both raw Si counts and the Si/Ti ratio exhibit a broadly declining trend over the course of the Holocene, with some short-term variability (**Figure 3.9**). Differences between the Si/Ti ratio and %LOI and the ratio of incoherent to coherent scattering (Incoh/Coh) (see below), both proxies for organic matter concentration, suggest Si/Ti is not capturing primary productivity as a whole in Eiðisvatn. It is possible that the declining trend represents a long-term decline in diatom productivity over the course of the Holocene, but other data (e.g. independent biogenic silica measurements) are needed to confirm this hypothesis. Another possible interpretation is that clastic input broadly declined over this period.

Mn and Fe are both redox sensitive elements, and the ratio of Mn/Fe (**Figure 3.9**) has been shown to vary in response to redox conditions in lake sediments (Koinig et al., 2003; Kylander et al., 2011; Loizeau et al., 2001; Naeher et al., 2013; Wennrich et al., 2014). In these systems, lower values of Mn/Fe are indicative of lower O_2 concentrations in the water column. Under anoxic conditions Mn undergoes more rapid reduction than Fe, leading to a preferential Mn release into the lake water and lower Mn/Fe ratios in sediments (Naeher et al., 2013). In Eiðisvatn, the Mn/Fe ratio is relatively low (<.012), with low amplitude variability, from the start of the record to ~7900 cal yr BP (**Figure 3.9**). From this point until approx. 4730 cal yr BP the ratio displays high amplitude variability, with values reaching up to 0.019. From ~4730 to ~1950 cal yr BP, the Mn/Fe displays generally lower values and lower amplitude variability (apart from a peak at ~4260, likely caused by the Hekla 4 tephra). Mn/Fe ratios begin to increase ~1950 cal yr BP, and for much of the disturbance interval (~1670 cal yr BP - 1000 cal yr BP), values are consistently high. Lower amplitude variability is observed from ~1000 – 300 cal yr BP before the Mn/Fe ratio increases near the top of the core. The data suggests Eiðisvatn experienced relatively

more oxic sediments and bottom waters for two consistent intervals: from ~7900 – 4730 cal yr BP and then again during the disturbance interval, from ~2200 – 1000 cal yr BP.

The ratio of incoherent (Compton) over coherent (Rayleigh) scattering (Incoh/Coh) relates to the average atomic number of the sample material (Chawchai et al., 2016). Material with low average atomic numbers, such as organic rich sediment, generate high Compton (incoherent) scattering and low Rayleigh (coherent) scattering values (Guyard et al., 2007; Chawchai et al., 2016) and the Incoh/Coh ratio of sediments has been applied as a proxy for organic matter content in a wide range of locations (Guyard et al., 2007; Kylander et al., 2011; Chawchai et al., 2016). In Eiðisvatn, the similarities between the Incoh/Coh ratio (**Figure 3.9**) and %LOI (**Figure 3.7**) support this assertion. The lowest values of this ratio are found at the bottom of the core in the Saksunarvatn ash layer. The Incoh/Coh ratio is broadly stable (~4.6) for much of the rest of the Holocene (without the generally increasing trend present in %LOI) until the disturbance interval. At ~2200 the ratio gradually starts to increase, reaching a maximum of ~5.7 approx. 1560 cal yr BP. It then declines steadily until ~650 cal yr BP, where it increases towards the top of the core.

3.4.4 Biomarker Data

Organic compounds were extracted and identified from 68 samples spanning both the EI-D-01-15 surface core and EI-P-01-15 piston. Sampling was concentrated around peak LOI values seen in **Figure 3.7** (composite depth ~32-55 cm, ~2200 – 1000 cal yr BP), with the deepest sample extracted from a composite depth of 200 cm (approx. 5,760 cal yr BP).

BrGDGT results, along with the mass of the total lipid extract (TLE) for each sample, are plotted in **Figure 3.10**. TLE masses ((A) in Figure 8) are relatively low and consistent throughout the deeper part of the record, with only one sample above 0.08 grams older than 2200 cal yr BP. Beginning at this time, however, concentrations increase markedly, reaching a maxima of ~0.16g

at 2145 cal yr BP. Masses remain generally high, but variable, until ~1024 cal yr BP, when they decline to 0.05 g. TLE masses remain below this value through the rest of the Holocene.

Concentrations of brGDGTs (B), are generally ~200 ng for the early part of the record before increasing markedly ~2200 cal yr BP, reaching a maximum of almost 1000 ng by 2104 cal yr BP. Concentrations then decline, reaching ~560 ng by 1055 cal yr BP and 365 ng by 100 years ago.

The BIT Index is a ratio that compares the relative contributions of isoprenoid vs. branched GDGTs and was originally interpreted as a measure of the relative input from aquatic (isoprenoid) versus supposed terrestrial (branched) GDGTs, with values closer to one representing a purely branched source, and values closer to 0 representing isoprenoid (aquatic) production (Hopmans et al., 2004). Subsequent research has provided compelling evidence for the production of brGDGTs within the water column of lakes (e.g. Buckles et al., 2014; Loomis et al., 2014), rendering the previous aquatic/terrestrial interpretation dubious. Interestingly however, we do see meaningful changes in the BIT Index in Eiðisvatn, with values averaging ~0.983 throughout much of the lower part of the record up to ~2510 cal yr BP. At this time, BIT values increase to 0.990 by 2484 cal yr BP, then decline slightly to 0.987 at 2319 cal yr BP. Here the BIT Index rises markedly, with values reaching 0.995 by 2200 cal yr BP. High BIT values persist until ~1055 cal yr BP. The uppermost three samples have BIT values ~0.991.

Reconstructed pH (using the equation of Sun et al., 2011) also displays interesting changes around this 2200 cal yr BP boundary (**Figure 3.10**). pH values for the lower part of the core are relatively constant ~7.5 from ~5350 cal yr BP to ~4000 cal yr BP. They then slowly decline to ~7.2 pH units by 2300 cal yr BP. Reconstructed pH then drops rapidly to a minimum of 6.6 pH units by 2150 cal yr BP.

Reconstructed temperatures (using the calibration of Sun et al., 2011) display relatively high variability over the course of the record, with a broadly declining trend from ~5,000 to 2,800 cal yr BP. At this point temperatures increase from 11.7°C to 13.3°C by 2280 cal yr BP. Over the

centuries, reconstructed temperatures decrease rapidly, reaching a minimum of 11.4°C by 2050 cal yr BP. Values then rise to 13.1°C by ~430 cal yr BP before declining to ~12.1°C in the uppermost sample (**Figure 3.10**).

Leaf wax *n*-alkanes are long chain carbon compounds that make up the waxy outer coating of plant leaves and stems. Short chain lengths (e.g. C_{17}-C_{21}) are broadly characteristic of aquatic plants, while longer chain lengths (C_{27}-C_{33}) are thought to be generally sourced from terrestrial higher plants (Eglinton and Hamilton, 1967). *n*-alkane results from Eiðisvatn are presented in **Figure 3.11**. Average chain length (ACL) values are based on the equation of Poynter and Eglinton (1990) (Eq 4.) ACL values are generally stable at ~28.5 for the early part of the record until 2760 cal yr BP, when they start to decline, reaching a mimima of 27.0 by 2380 cal yr BP. The index then increases rapidly over the next 10 cm, to a maxima of ~29.2 by 2150 cal yr BP. Chain lengths then broadly decrease, with some variability, through the end of the Holocene, with a value of ~27.4 by 100 cal yr BP.

n-alkane concentrations display relatively little variation over the early part of the record, with all values below 100 ng/g sed. extracted until ~2200 cal yr BP. At this point concentrations of all chain lengths increase, with the most marked increases in C_{31} and C_{33} (**Figure 3.11**). Concentrations remain relatively high until ~1000 cal yr BP, when they decline to similar values seen in the early part of the record.

The concentrations of six primary productivity biomarkers are shown in **Figure 3.12**. Concentrations are plotted in raw ng, relative to grams sediment extracted (ng/g sed extracted), and relative to the mass of the total lipid extract for that sample (ng/g TLE). Of the six compounds identified here, only cholesterol is not produced by plants. Campersterol, campestanol, stigmasterol, β-Sitosterol, and sitostanol are all plant phytosterols. They are structurally similar to cholesterol, with varying carbon side chains and number and location of double bonds.

From 5800 cal yr BP to ~2200 cal yr BP, concentrations of all six compounds remain below 500 ng/ g sed extracted (**Figure 3.12**). At this time, concentrations of these biomarkers increase markedly. β-Sitosterol, for instance, increases from an average of ~130 ng/g sed extracted in both the piston and surface cores to maxima of 2,000 ng/g sed ext. Concentrations decline somewhat, but remain relatively high, until approx. 1000 cal yr BP. After this time, they decline to similar values seen in the lower part of the core.

When compared relative to ng/g TLE (total lipid extract), a different pattern is apparent (lower panel in Figure 3.12). In this case, concentrations of these primary productivity biomarkers decrease relative to the overall TLE mass at the 2200 cal yr BP boundary. This suggests that other compounds (beyond the six identified here) may have increased in concentration relative to the over total lipid extract at this time, likely in a way that was unprecedented over the past 6,000 years. While some of this increase may come from higher abundances of leaf wax n-alkanes as noted above, further analysis of the total lipid extract, and the polar fraction in particular, will help elucidate what other compounds may be responsible for this pattern.

3.5 Discussion

The most striking interval from our Eiðisvatn composite sediment record is the abrupt change in nearly all analyzed proxies ~2200 cal yr BP (~200 BC). Are these unprecedented changes the result of humans entering the landscape? A settlement date of 200 BC is much earlier than has been proposed by nearly all researchers who have studied the Faroes, apart from Johansen's first appearance of *plantago lanceolota* ~2300 BC (Jóhansen, 1989). To properly answer this question, we first define the nature of this event in Eiðisvatn based on our proxy results. We then address the other possible causes for this disturbance beyond anthropogenic influence, and compare the timing and signature of this disturbance with other records from the Faroes.

3.5.1 Nature of disturbance in Eiðisvatn

The disturbance interval in Eiðisvatn sediments spans roughly 30-50 cm composite depth in the core, or ~1000 – 2200 cal yr BP (1000 AD – 200 BC) (**Figure 3.4**) It is characterized by abrupt and dramatic increases in numerous proxies for organic matter; %LOI, TLE mass, overall concentrations of brGDGTs, primary productivity biomarkers, and *n*-alkanes, which all reach values unprecedented relative to the rest of the Holocene. What drove these changes? Did the entire ecosystem become more productive at this time? Or were greater amounts of terrestrially derived organic matter delivered to the lake while autochthonous productivity remained constant?

Interestingly, proxies typically associated with increased erosion, such as Ti elemental counts and bulk density, decrease during this period. The interval also shows up as relatively less dense than most of the rest of the core in the X-radiograph (**Figure 3.4**). In other settings, declining Ti and DBD values would likely represent decreased levels of bedrock erosion and terrestrial input. That interpretation is potentially complicated here by the expansive peat formations throughout the catchment. Peat generally has a very high organic matter content and a low bulk density, so at this site the Ti and DBD values could be reflecting *increased* transport of terrestrial organic material to the lake. Additional proxy evidence also suggests that peat may be contributing to this change. Peat is generally relatively acidic, with pH values ~4.5. Reconstructed pH (based on our brGDGT data), declines abruptly just prior to this interval, from ~7.2 pH units at ~2300 cal yr BP to a minimum of 6.6 at 2150 cal yr BP (**Figure 3.10**).

This hypothesis is further informed by changes in the BIT Index, which increases markedly across this boundary, suggesting a higher input of brGDGTs relative to isoprenoid GDGTs. While brGDGTs are produced by bacteria living in both soils and the water column, the archaea who produce isoprenoid GDGTs are exclusively aquatic (Schouten et al., 2013). The observed BIT Index changes suggest an increase in relative brGDGT concentrations in the sediments, which could be the result of higher amounts of terrestrial organic matter input to Eiðisvatn.

Leaf wax n-alkanes are also potentially informative, with major changes in both the ACL and P(aq) ratios across this transition. ACL values increase by nearly an entire integer at 2200 cal yr BP, and P(aq) drops from over 0.3 to 0.17, both of which suggest increased terrestrial input at this time. While concentrations of all chain lengths increase across this interval, the most pronounced increases are of C_{31} *n*-alkanes, followed by C_{33}. Higher concentrations of C_{31} have been related to increased preponderance of grasses in certain catchments (Cranwell et al., 1987; Maffei, 1996), but this relationship does not hold everywhere (Bush and McInerney, 2013). C_{31} n-alkanes have also been shown to be highly abundant in non-sphagnum plants growing in bog/peat settings (Nichols et al., 2006; Nott et al., 2000), and the increased concentrations at this time may therefore represent increased peat delivery to the lake. In either case, however, the n-alkane chain length data suggest an increase in the delivery of terrestrially derived organic matter (grasses and/or peat) to the lake at this time.

While the evidence appears to clearly point to increased organic matter concentrations from terrestrial sources over the disturbance interval, a potential complication to this interpretation are the apparently lower sedimentation rates that occur during this time (**Figure 3.6**). If much higher amounts of peat were entering the lake through erosive processes (whether climatic or anthropogenic), one would expect sedimentation rates to increase. The answer to this conundrum may lie in the oxic conditions of the lake bottom water and sediments. The ratio of Mn/Fe, a proxy for relative bottom water oxygenation, is plotted alongside inferred sedimentation rate in **Figure 3.13**. There appears to be a strong negative relationship between Mn/Fe values and sedimentation rate in Eiðisvatn, especially over the disturbance interval. This might suggest that more oxygenated bottom waters (and subsequent higher rates of consumption of organic matter) are the likely cause for the lower sedimentation rate during the disturbance interval, even during a period of increased delivery of terrestrial organic matter. More research is needed to properly characterize this relationship however.

In summary, our proxy data indicates this interval likely represents a sustained period of increased delivery of terrestrial organic matter (likely peat) to the lake. There are three possible explanations for the cause of this interval in the Eiðisvatn sediment record: 1) a natural instantaneous mass movement event (a slump or turbidite); 2) a climatically induced increase in catchment productivity/peat development; or 3) an anthropogenic forcing related to the arrival of humans and/or grazing animals in the landscape. Each possibility will be discussed in turn below.

3.5.2 Mass movement deposit?

While this interval is characterized by increased delivery of terrestrial organic matter to Eiðisvatn, it does not appear to be the result of an instantaneous mass movement event. The transition to this interval at ~2200 cal yr BP, though abrupt in some of our lower-resolution proxy records, appears more gradual in the high-resolution Itrax data, and is visually recorded in the sediments as a relatively diffuse transition to darker brown gytjja/organic rich-sediment (**Figure 3.4**). We do not see a strong erosive boundary, nor visual evidence for a 'fining upward' grain size sequence in the sediments. While multiple radiocarbon dates from this interval provide stratigraphically "too old" dates (**Table 3.2** and **Figure 3.5**), the fact that the old dates do not cluster around a single age suggests this was not a single package of sediment delivered to the lake all at once. Indeed, the EidiBest age model suggests this interval was broadly a period of lower accumulation relative to the middle Holocene (**Figure 3.6**). The structure in many of our proxy reconstructions throughout this interval (e.g. pH and BIT Index) also suggest this interval was not an instantaneous event. We therefore conclude that the disturbance is not the result of a mass movement deposit.

3.5.3 Climatically induced event?

The unprecedented response of most analyzed proxies across this interval suggests that if the cause of these changes was a climatic event, it would have been the most dramatic change that occurred over the course of the Holocene. Generally, such dramatic increases in organic matter concentrations would be interpreted to result from a warming event. Conversely, it has been argued in some publications from the Faroes that cooling temperatures might cause increases in organic matter accumulation, though these suppositions are somewhat speculative (Gathorne-Hardy et al., 2007; McGowan et al., 2008). Gathorne-Hardy et al. (2007) argue, for instance, that a decline in temperature during the Little Ice Age may have driven an increase in lake productivity in Grothusvatn, on the southern island of Sandoy. The authors suggest "Colder weather tends to reduce the growth rate of plants, so a LIA temperature decline might well have reduced their ability to recover from grazing, allowing the landscape to become more open, and nutrients to be washed into the lake" (Gathorne-Hardy et al., 2007). In either case, whether the increases are from a warming or cooling event, the unprecedented nature of the response in the sediments suggests that this climate event would have been quite significant.

There is little evidence, however, to suggest climate changed dramatically ~2200 cal yr BP in the Faroe Islands. The majority of available research suggests that temperatures were decreasing from the mid- to late Holocene (Roncaglia, 2004; Andresen et al., 2006; McGowan et al., 2008; Olsen et al., 2010; Rasmussen and Thomsen, 2010;), though much of this evidence is based on indirect climate proxies. Olsen et al. (2010) for example, studied three lakes also on the island of Streymoy, to the southeast of Eiðisvatn. The authors point to higher titanium counts and magnetic susceptibility in their records, beginning ~7400 cal yr BP, with further increases at 4190 and 3000 cal yr BP, as evidence for cooling temperatures (higher frequency of freeze/thaw events, greater delivery of minerogenic material to the lakes). McGowan et al. (2008) also suggest climate became cooler and wetter throughout the course of the Holocene. Olsen et al. (2010) do suggest a brief "warm and wet" interval occurred ~1800 cal yr BP, which the authors

link with other lake records from the Faroes (Lawson et al., 2007; 2008), though this connection is somewhat tenuous.

Marine records from the Faroes shelf also seem to generally confirm a broad cooling trend from the mid to late Holocene. Roncaglia (2004) studied dinoflagellate cyst and acritarch assemblages from a marine sediment core taken in Skalafjord, located less than 20 km east of Eiðisvatn. The author found evidence for broadly cooler temperatures from ~7300 to 2210 cal yr BP, when a mild warming trend is observed that lasted until ~860 cal yr BP (Roncaglia, 2004). Though the timing of this change is somewhat synchronous with the start of the disturbance interval in Eiðisvatn, the inflection is relatively gradual and the relative temperature change is much less than events at the start of the Holocene and ~4100 cal yr BP in this record. Rasmussen and Thomsen (2010), analyzed benthic and planktic foraminifera from Faroe-Shetland channel and similarly found a broad cooling trend from 4000 – 400 cal yr BP. It therefore seems that little evidence exists from other paleoclimate records from the Faroes for a dramatic climatic change ~2200 cal yr BP.

Returning to Eiðisvatn specifically, preliminary low-resolution δD analyses of leaf waxes spanning the entire Holocene exhibit the largest variations during the early Holocene (~9000-10000 cal yr BP), although there is a coherent shift in both short (C_{25} and C_{27}) and long chain (C_{29}, C_{31}, and C_{33}) δD just prior to 2200 cal yr BP by ~10-15‰ (Curtin et al., *in prep*). While the data broadly seem to support the notion that the Faroes became progressively wetter throughout the Holocene (e.g. Lawson et al., 2005; McGowan et al., 2008), there is little evidence for an unprecedented climate shift around the time of the disturbance (Curtin et al., *in prep*). brGDGT based paleotemperatures from Eiðisvatn (this study) display significant variability over the mid Holocene (~5500 – 2500 cal yr BP), with both warming and cooling fluctuations of >1.5°C, without a comparable response in %LOI or organic matter concentrations.

A final consideration when attempting to address climatic responses to the observed disturbance in Eiðisvatn is the *sudden* appearance/formation of peat deposits within the

catchment. This mechanism has been used to explain marked organic matter increases in other records from the Faroes (e.g. McGowan et al., 2008; Olsen et al., 2010), but this explanation seems unlikely at Eiðisvatn. Lawson et al. (2007) addressed the timing of peat expansion in the Faroes explicitly in their 2007 study, which showed that the initiation of peat formation across the islands occurred at variable times throughout the Holocene, with perhaps some indication of higher activity from 6000 - 4000 cal yr BP (Figure 6 in Lawson et al., 2007). Based on more than 30 estimates for the initiation of peat lands across the archipelago, the authors conclude "there is, at present, no strong evidence to suggest that climatic changes have played a role in the timing of peat initiation in the Faroes". Johansen (1989) has suggested that peat initiation occurred at the Argisbrekka site ~6000-4000 cal yr BP, much earlier than the date of the disturbance seen in the Eiðisvatn record. The initiation of peat development in the Eiðisvatn catchment may be captured in our reconstructed pH values, which begin to decline ~3400 cal yr BP, similar in timing to the suggested date of 6000-4000 cal yr BP, before that decline accelerates rapidly at ~2300 cal yr BP. Based on the available evidence, it seems unlikely that sudden peat formation caused the disturbance seen in Eiðisvatn, especially in light of the fact that basal peat dates from Argisbrekka suggest peat formation began much earlier (Jóhansen, 1989).

In summary, there appears to be little evidence for a singular climatic event (either a warming or cooling) of sufficient magnitude to drive the changes seen in the Eiðisvatn sediment record at 2200 cal yr BP. Climate was likely getting progressively cooler and wetter from ~7400 cal yr BP up through the late Holocene, but this trend does not explain the disturbance at 2200 cal yr BP. While we cannot explicitly rule out the expansion of peat lands in the Eiðisvatn catchment at this time, it appears that peat formation had started adjacent to the lake between 6000-4000 cal yr BP, much earlier than the date of disturbance. We are therefore left with the need for a mechanism to drive the apparent increase in delivery of terrestrial organic matter to Eiðisvatn over a sustained period of 1000+ years. Though a *landnám* date of 2200 cal yr BP is much earlier than suggested almost anywhere else in the Faroes (the 4300 cal yr BP date of Johansen (1989)

notwithstanding), human influence seems to be the most likely explanation for the disturbance at Eiðisvatn.

3.5.4 An anthropogenic event?

While we do not have unequivocal proof that the cause of this disturbance was anthropogenic, the arrival of humans (or at least, the arrival of grazing animals) seems to be the most logical explanation. People had occupied the Shetland Islands, ~300 km to the southeast of the Faroes, by 4540 cal yr BP (Bennett et al., 1992; Melton and Nicholson, 2004). If we are to believe the supposed settlement date of 800 AD (1150 cal yr BP) (Arge et al., 1991), that would leave nearly 3500 years between the occupation of Shetland and the Faroe Islands. The sudden introduction of grazing animals certainly has the potential to produce the response seen in the Eiðisvatn sediments. The potential erosive power of sheep in a landscape that has previously been devoid of land mammals could lead to the large increase in terrestrial organic matter delivery to the lake. Increases in lake productivity associated with human settlement have been noted in other lakes records in Faroes, as noted by Lawson et al. (2005): "…an increase in lake productivity accompanied the settlement, perhaps due to mobilization of nutrients by grazing and manuring, or to soil erosion". Human presence in a watershed has been shown to drive increasing in bottom water oxygenation at certain locations (Fritz, 1989; Scully et al., 2000), as could be the case at Eiðisvatn.

There are obviously numerous caveats to this hypothesis, and further research is needed to definitively determine if this disturbance was anthropogenic. Though our age model is more robust than many previously published records from the Faroes (some of which have only two or three radiocarbon dates), the damming of the lake in the 1980s, along with the preponderance of "too old" radiocarbon dates in the disturbance interval, means our suggested date of 2200 cal yr BP must be treated with some caution. We plan to pursue further dating methods to address this

potential issue, and even if the date is revised, it seems highly unlikely to approach 800 AD (1150 cal yr BP).

In summary, the data presented here describes a major environmental disturbance/change in the nature of sedimentation in Eiðisvatn ~2200 cal yr BP. While we cannot definitively ascribe this change to an anthropogenic forcing at this time, it seems to be the most likely possibility based on our research and comparison with other records from the Faroes. Ongoing/future work will be geared towards further characterizing this disturbance interval, with ancient sedimentary DNA and charcoal analysis underway.

Table 3.1: Sediment cores collected from Eiðisvatn

Core Identifier	EI-D-01-15	EI-D-02-15	EI-P-01-15
Core Type	Surface/Gravity	Surface/Gravity	Piston
Core Length (cm)	83.7	100.7	281.5

Table 3.2: Radiocarbon + Tephra dates from Eiðisvatn

Core Name	Composite Depth	Sample Type	^{14}C Age (uncalibrated yr BP)	Error (yrs)	Calibrated Age Range (2σ) (yr BP)	δ^{13}C (‰)
EI-D-01-15	18.5	Macrofossil	Modern			-26.61
EI-D-01-15	23	Macrofossil	410	15	467 - 509	Not Reported
EI-D-01-15	30	Macrofossil	1145	15	980 - 1172	Not Reported
EI-D-01-15	34	Macrofossil	1055	35	924 - 1054	Not Reported
EI-D-01-15	39.5	Macrofossil	3030	20	3167 - 3333	-27.52
EI-D-01-15	40.2	Macrofossil	8110	45	8815 – 9251	Not Reported
EI-P-01-15	43.86	Macrofossil	3915	20	4260 – 4421	Not Reported
EI-D-01-15	57	Macrofossil	2450	15	2364 – 2697	-26.96
EI-P-01-15	60.36	Macrofossil	2330	20	2331 – 2357	-26.61
EI-D-01-15	82	Macrofossil	3300	15	3479 – 3568	Not Reported
EI-P-01-15	96.16	Macrofossil	2945	15	3010 – 3167	Not Reported
EI-P-01-15	138.26	Macrofossil	3595	15	3844 – 3964	Not Reported
EI-P-01-15	138.86	Tephra (Helka-Selsund)	N/A	-	3750	N/A
EI-P-01-15	156.86	Tephra (Helka 4)	N/A	-	4260	N/A
EI-P-01-15	164.46	Macrofossil	4100	30	4453 – 4810	Not Reported
EI-P-01-15	174.96	Macrofossil	4310	15	4842 – 4870	Not Reported
EI-P-01-15	263.46	Macrofossil	7290	30	8026 – 8170	-25.7
EI-P-01-15	278.46	Macrofossil	7925	20	8636 - 8170	Not Reported
EI-P-01-15	301.46	Tephra (Saksunarvatn)	N/A	-	10397	N/A

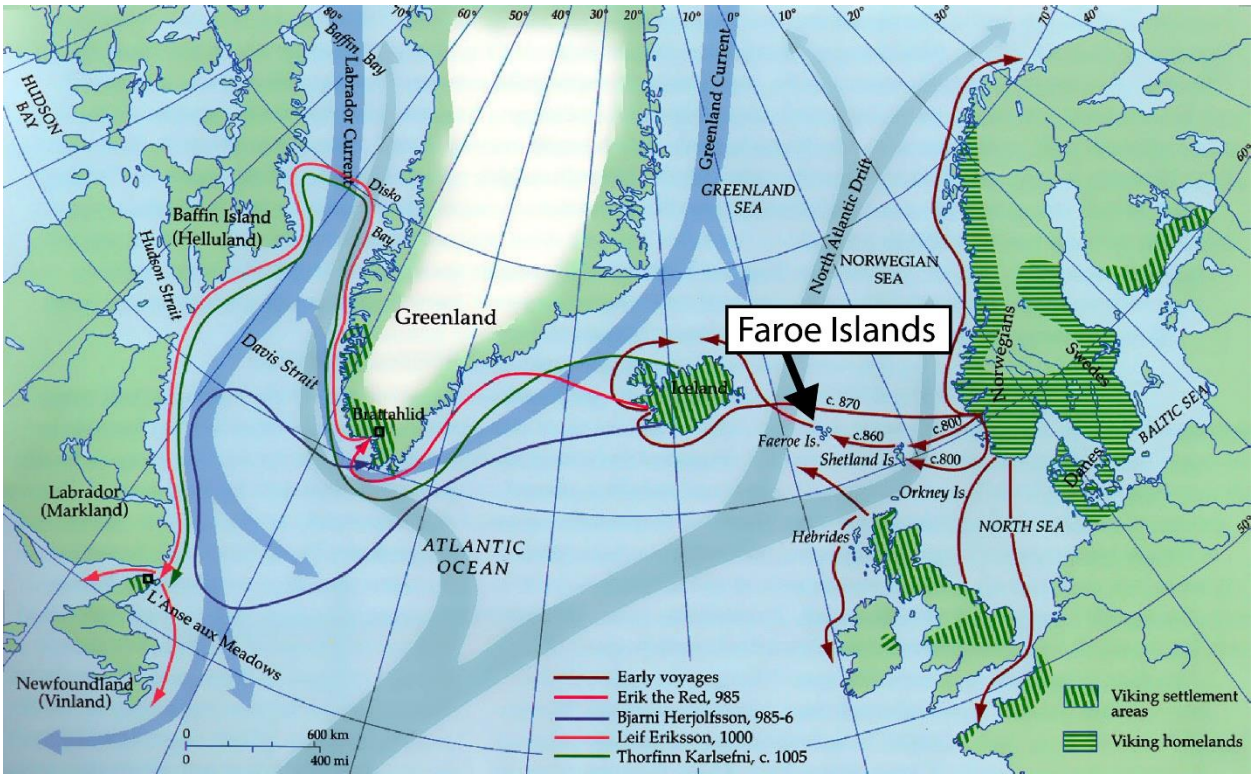

Figure 3.1- Map of the North Atlantic depicting Norse expansion during the late 1st millennium AD with the Faroe Islands labeled (modified from: vinland-map.brandeis.edu/assets/images/lightbox/Viking_voyage.jpeg)

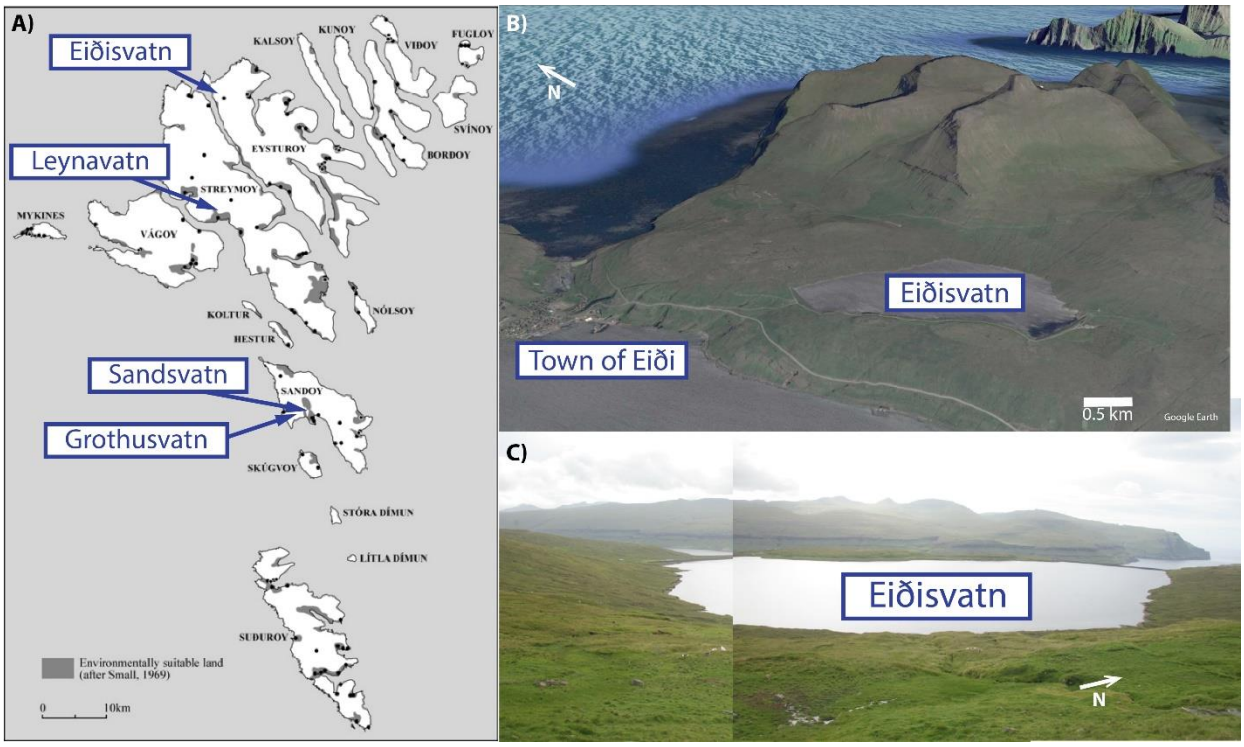

Figure 3.2 - A): Map of the Faroe Islands with lakes cored in the summer of 2015 labeled. Gray shaded area represents suitable land for farming activities (modified from Arge et al., 2005). B): Oblique Google Earth image of Eiðisvatn and the nearby town of Eidi. C): Composite panorama image of Eiðisvatn taken during fieldwork in 2015.

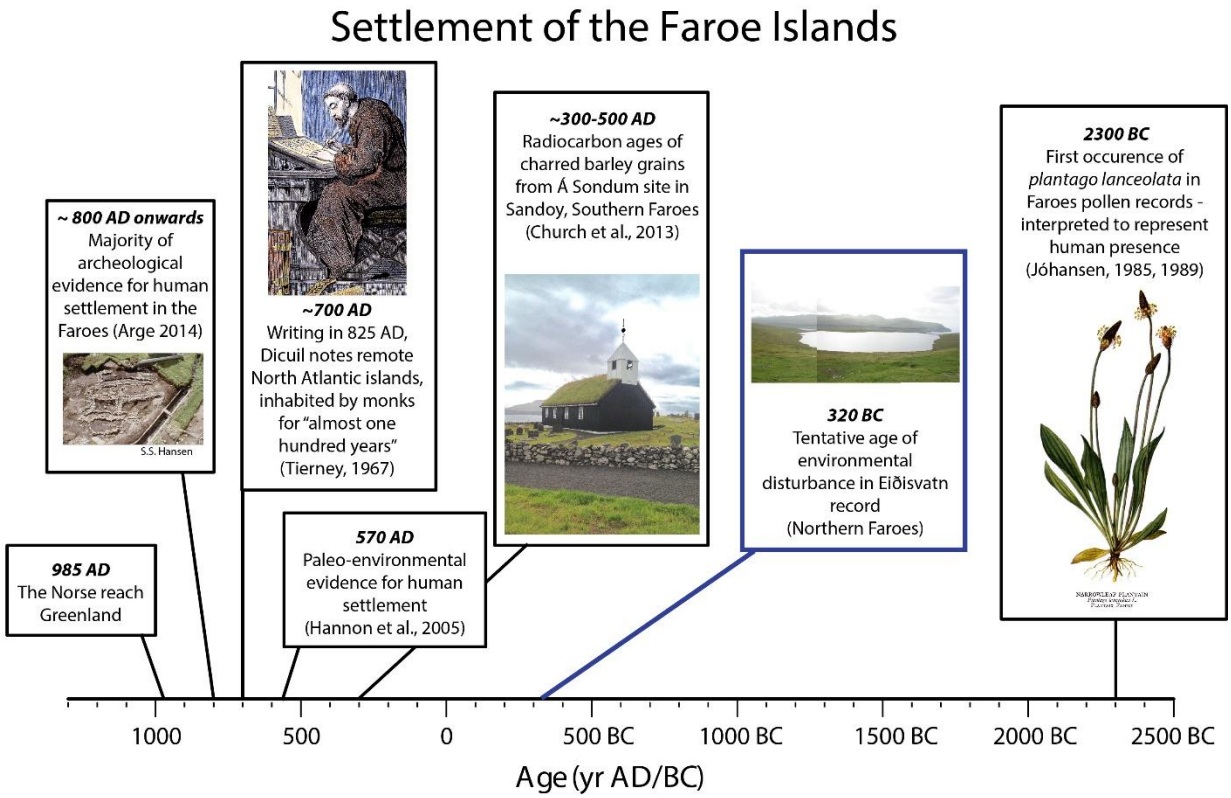

Figure 3.3 - Timeline depicting published evidence for settlement of the Faroes (black boxes) and date of possible anthropogenic disturbance in Eiðisvatn (blue) (this study).

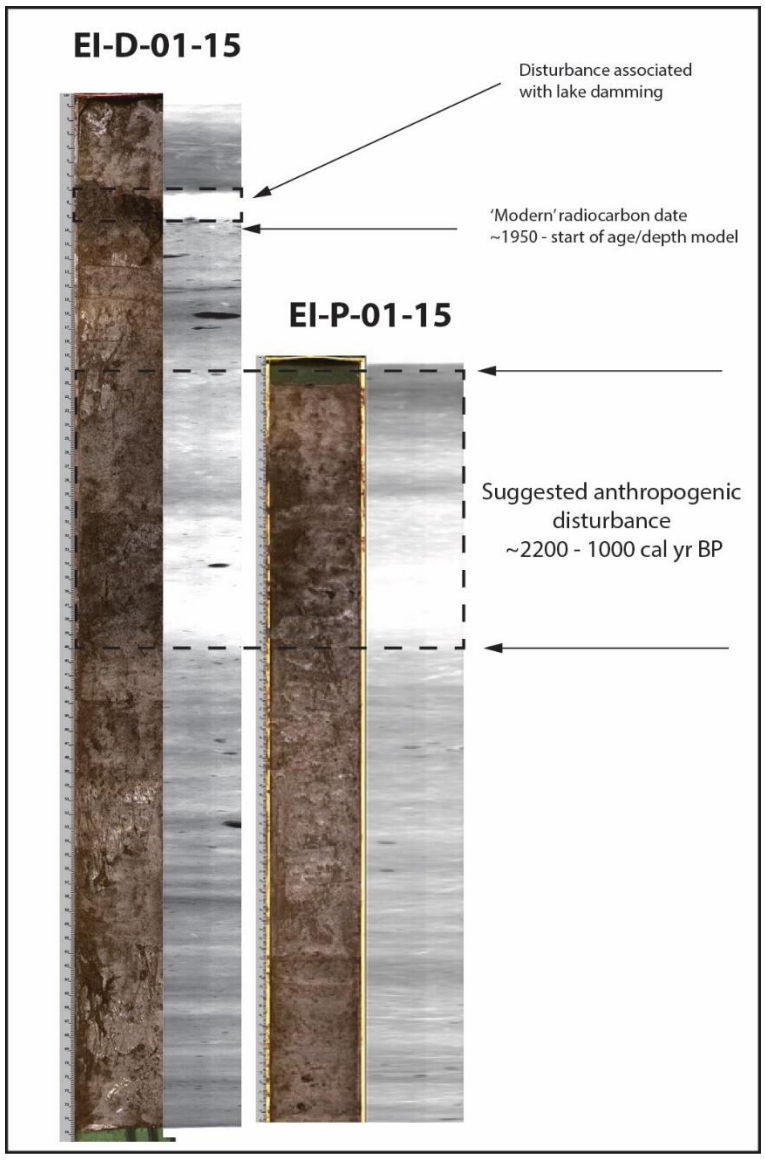

Figure 3.4 - Images and X-radiographs of EI-D-01-15 and EI-P-01-15. Both the disturbance associated with lake damming in the 1980s and the potential earlier settlement disturbance are outlined in dashed black lines.

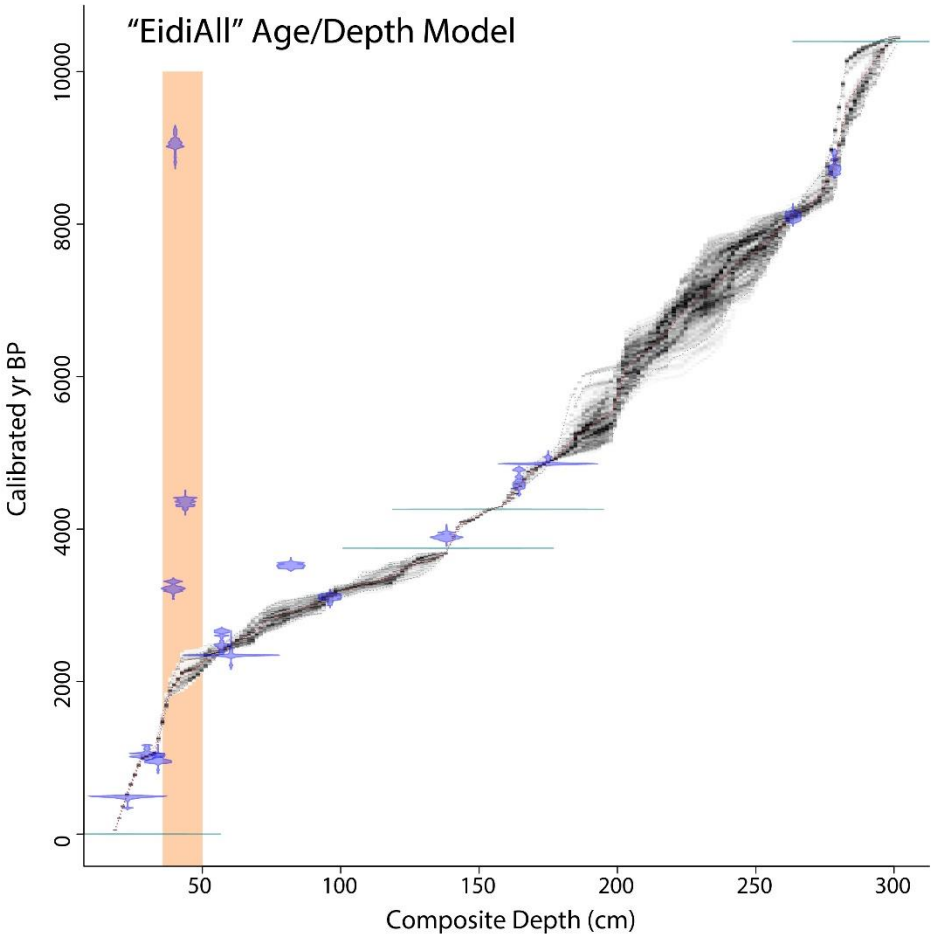

Figure 3.5 - "EidiAll" age model, created in Bacon using all available radiocarbon dates from Eiðisvatn (blue symbols) and 3 identified tephra layers (green lines). Disturbance interval is outlined in orange.

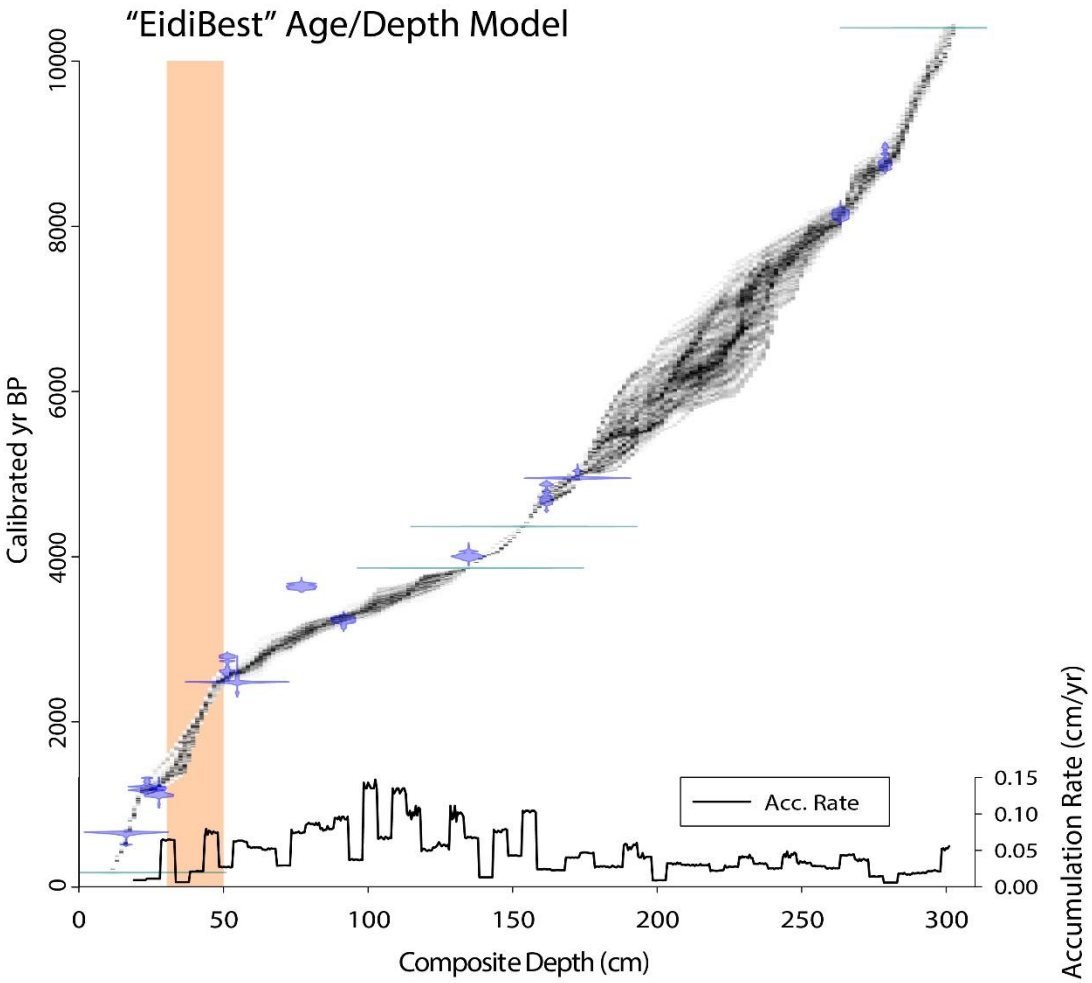

Figure 3.6 - "EidiBest" age model created without 3 stratigraphically old dates from disturbance interval, and sediment accumulation rates in cm/yr (bottom panel). Disturbance interval is outlined in orange.

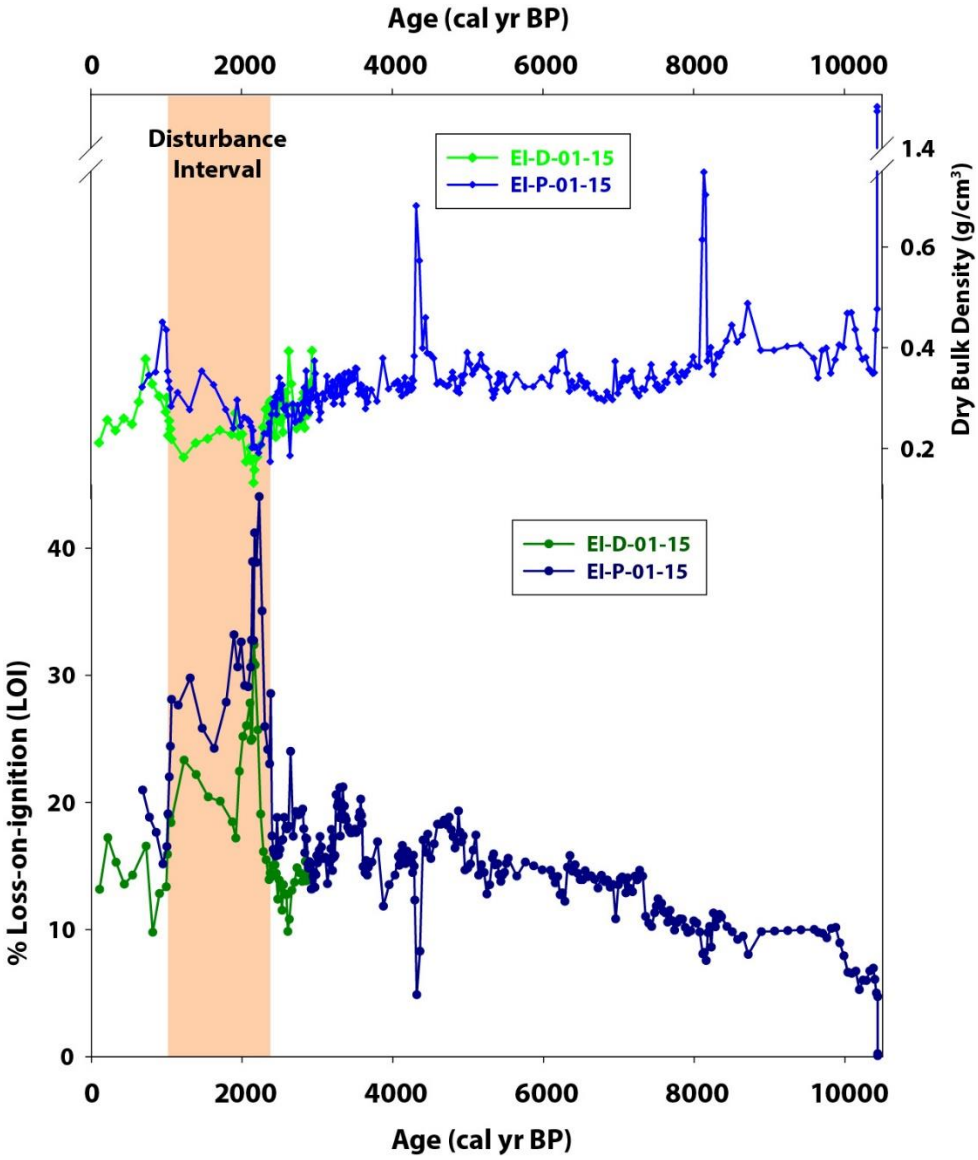

Figure 3.7 - % Loss-on-ignition (%LOI) and dry bulk density values (DBD) for both surface core EI-D-01-15 (green) and piston core EI-P-01-15 (blue). Note scale break in DBD y-axis. Disturbance interval is outlined in orange.

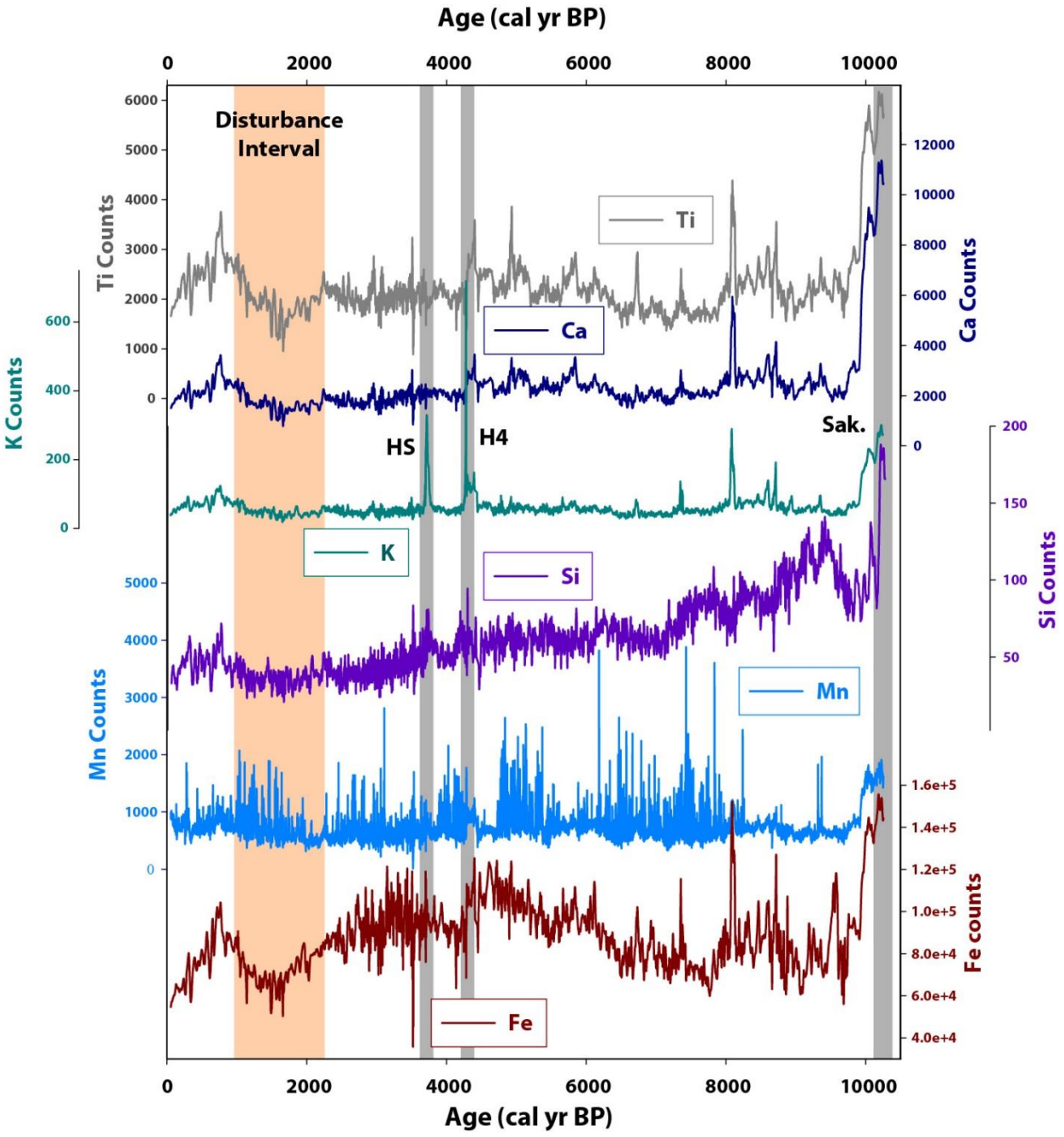

Figure 3.8 - Selected elemental counts from Itrax XRF core scanning for composite Eiðisvatn record. Disturbance interval is outlined in orange.

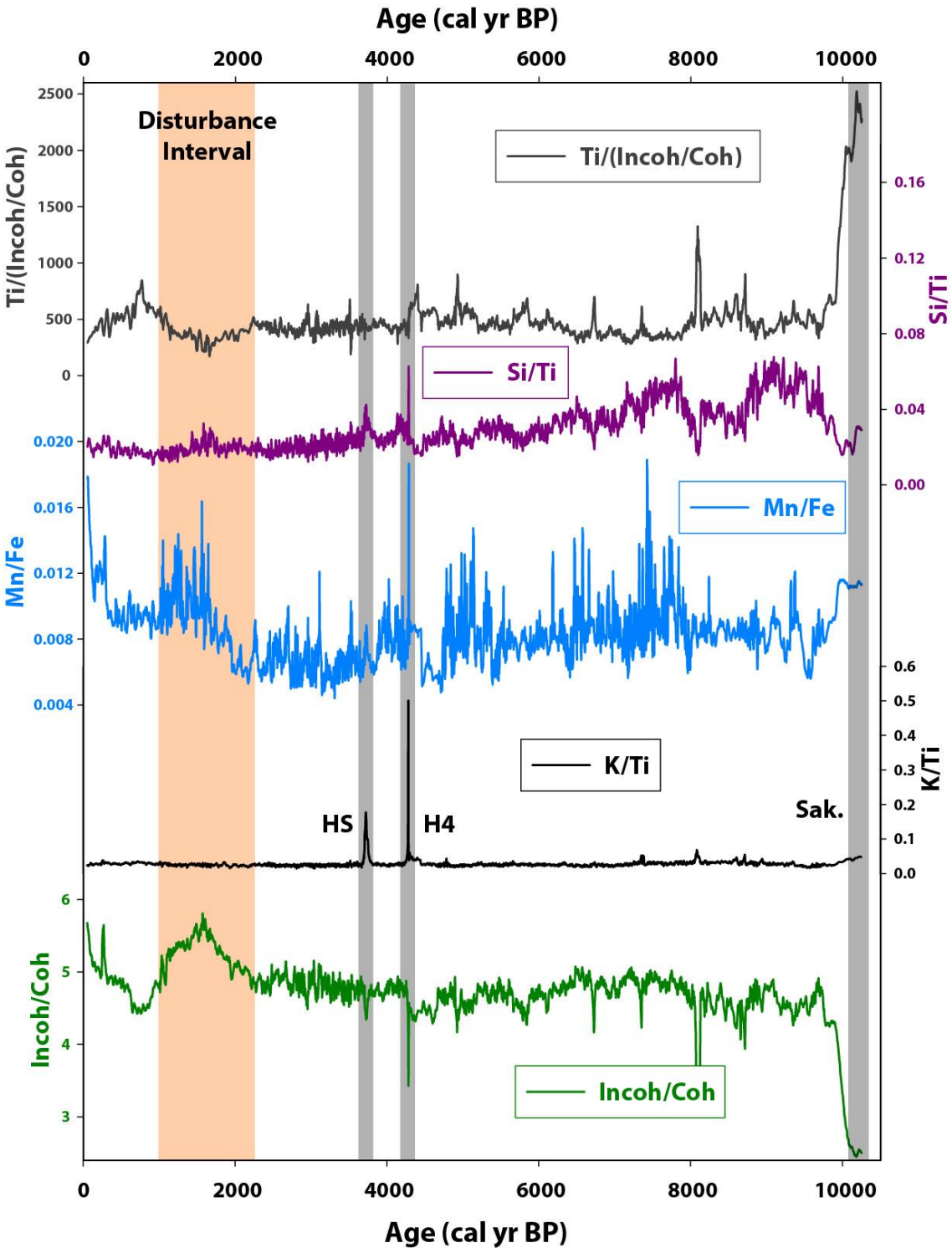

Figure 3.9 - Selected elemental ratios from Itrax XRF core scanning for composite Eiðisvatn record.

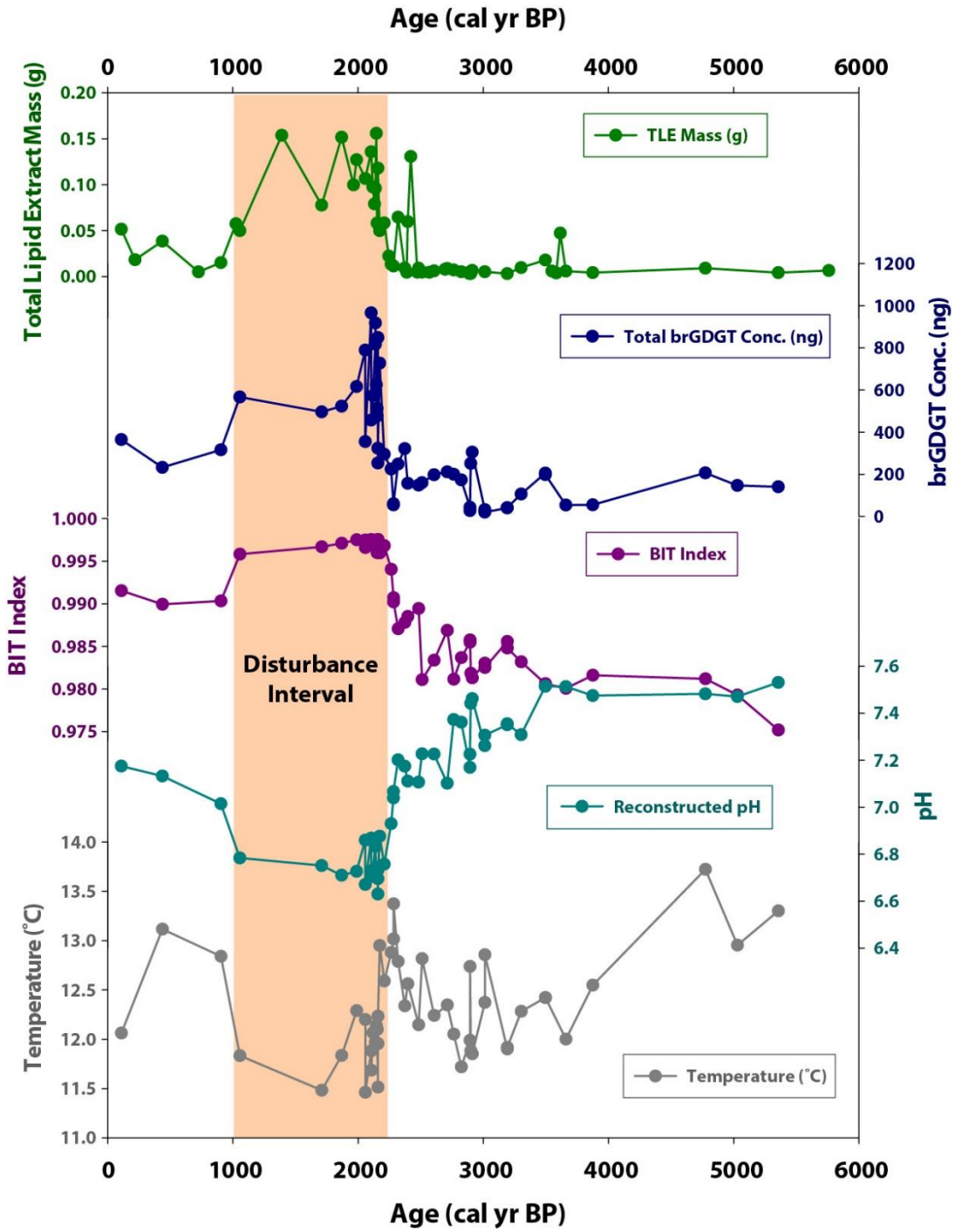

Figure 3.10 - brGDGT results from Eiðisvatn. Disturbance interval is outlined in orange.

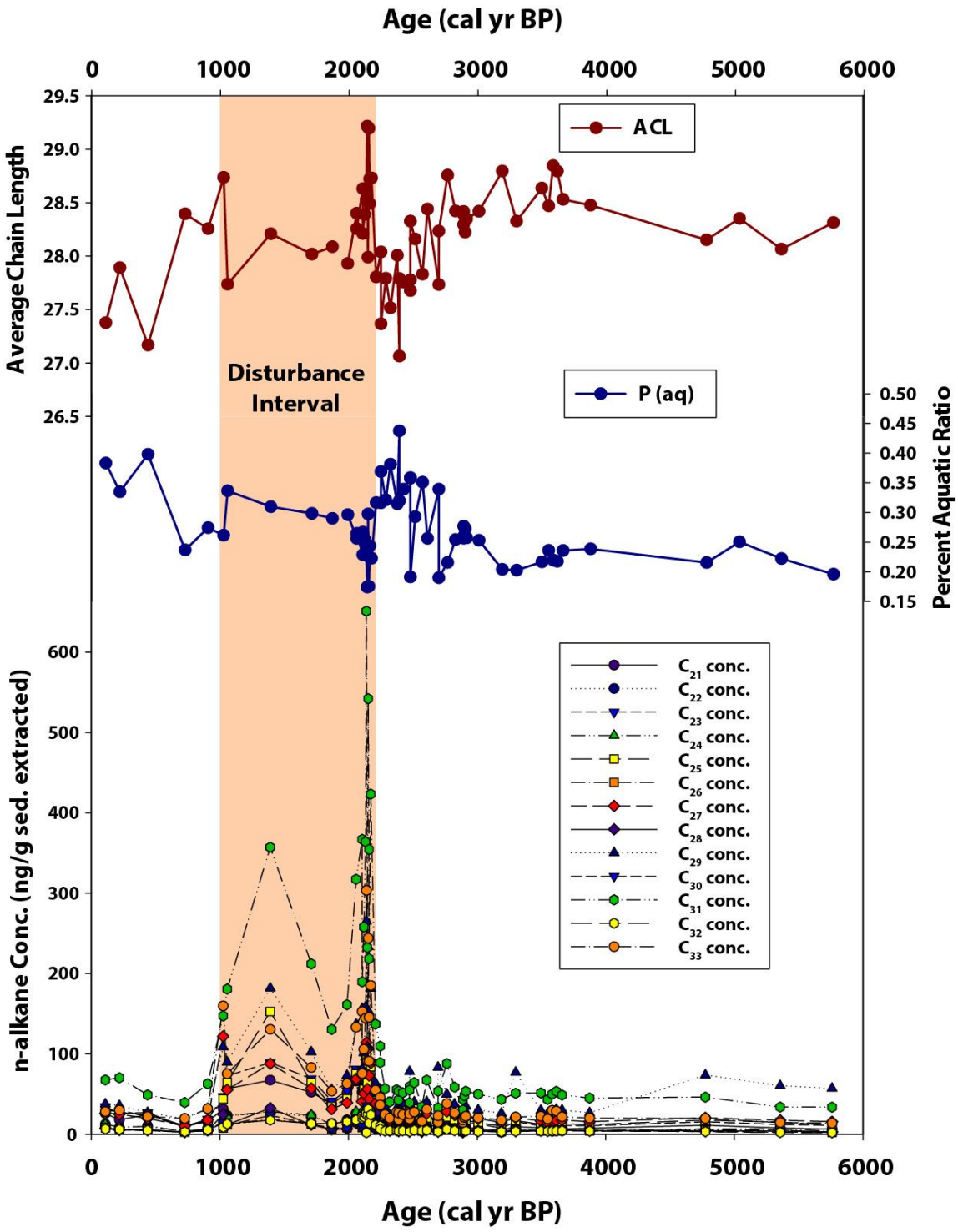

Figure 3.11 - Leaf wax n-alkane results from Eiðisvatn. Disturbance interval is outlined in orange.

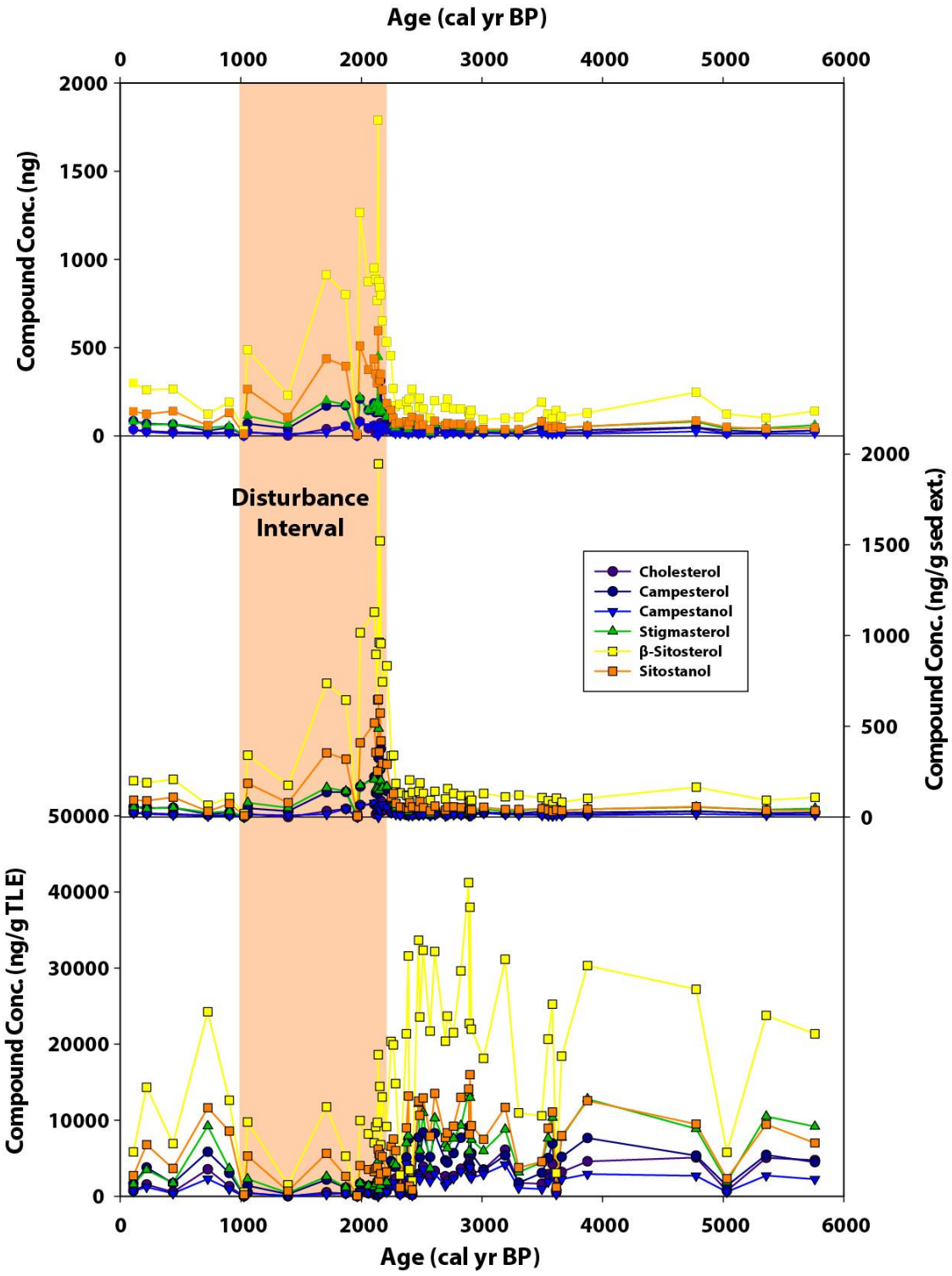

Figure 3.12 - Concentrations of primary productivity biomarkers in Eiðisvatn. Disturbance interval is outlined in orange.

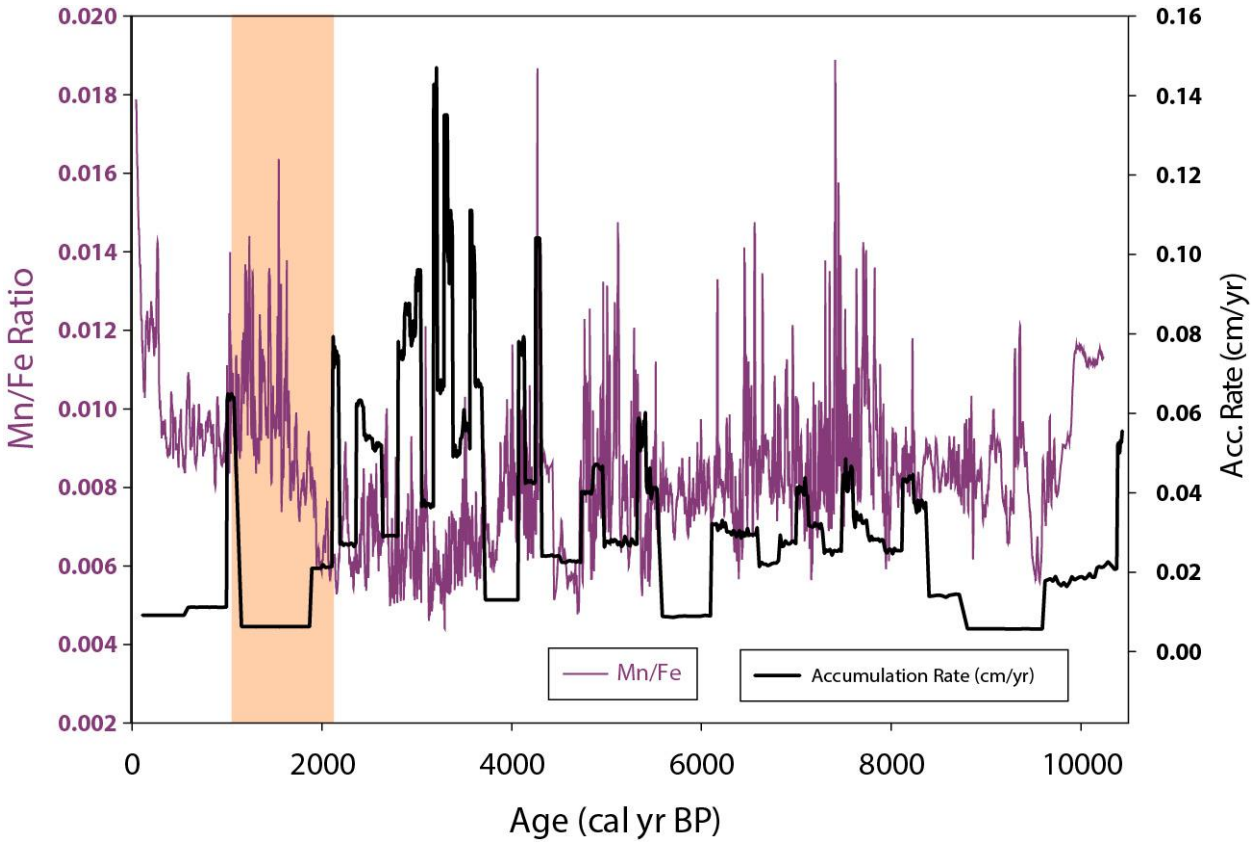

Figure 3.13 - Mn/Fe ratio (purple) from XRF core-scanning and accumulation rate (black) from Eiðisvatn over the Holocene. The ratio of Mn/Fe is indicative of bottom water oxygen levels (Naeher et al., 2013), and high values during the disturbance interval suggest relatively higher levels of oxygenation during that time.

CHAPTER 4

RECONSTRUCTION OF ENVIRONMENTAL CONDITIONS AND HUMAN OCCUPANCY IN SW GREENLAND

4.1 Introduction

From ~1000-1450 A.D. Norse colonists thrived in extensive settlements in SW Greenland. During the 15th century however, this society collapsed. Their demise has frequently been attributed to a deteriorating climate and the onset of Little Ice Age cooling, but others have argued instead that the Norse Greenlanders were undone by cultural and socio-economic factors, "large-scale historic processes and vulnerabilities created by their successful prior response to climate change" (Dugmore et al., 2012). This debate, primarily within the archaeological community, has been hampered by a lack of local, continuous paleoclimate reconstructions from the settlement region. The overall goal of this project is to generate high resolution records of temperature, hydrology, and human occupancy from multiple sites within the Eastern Settlement of the Norse in southwest Greenland. This chapter represents the first steps towards that ultimate goal. Here we present preliminary data from Eriksvatnet lake, near the modern day village of Qassiarsuk in SW Greenland. This site was proximal to the Norse farm Brattahlid, a major homestead within the Norse "Eastern Settlement".

4.2 Background

The Norse colonization and settlement of southwestern Greenland has been the subject of numerous archaeological and paleo-environmental studies (e.g. Edwards et al., 2008; Schofield et al., 2008; Buckland et al., 2009; Massa et al., 2012; Perren et al., 2012; Bichet et al., 2013; Millet et al., 2014), yet significant uncertainties remain regarding the role of climate change in the collapse of the Norse population during the mid-15th century (Dugmore et al., 2007; Dugmore et

al., 2012). Their demise has frequently been attributed to a deteriorating climate and the onset of Little Ice Age cooling (Jones and McGhee, 1986; Berglund, 1986; Grove, 2001; Andersen et al., 2006), but recent research has argued instead that the Norse Greenlanders were undone by "large-scale historic processes and vulnerabilities created by their successful prior response to climate change" (Dugmore et al., 2012). Even within the bounds of the Little Ice Age hypothesis, debate exists on which aspect of climate change was the most damaging, with some researchers suggesting precipitation changes and drought conditions were more detrimental to farming than cold temperatures (Andersen et al., 2006). The theme of collapse in response to climate change has been used to describe the Norse Greenlanders by high-profile authors such as Jared Diamond, and this theme of societal fragility in the face of ecological crisis certainly continues to increase in relevance in light of our current actions. Yet, the physical evidence for this narrative in SW Greenland is currently lacking. Only one local paleotemperature reconstruction exists from the Norse region (Millet et al., 2014), and while a large number of archaeological investigations have been completed, none are continuous and/or allow for direct comparison with a climatic time-series.

This project attempts to increase our understanding of the role climate played in the demise of the Norse in Greenland by analyzing organic molecular proxies from lacustrine sediment cores throughout the settlement region. The focus is currently limited to the so called "Eastern Settlement", the largest in Greenland during the Norse period, with over 2500 inhabitants at its height (Lynnerup, 1996) (**Figure 4.1**).

4.3 Study Site

To better understand the relationship between climate and the Norse population of Southern Greenland we analyzed multiple lake records from the region (**Figure 4.1**). This thesis chapter focuses specifically on preliminary results from Lake Eriksvatnet (F**igure 4.2**). Eriksvatnet is approx. 10.9 m deep and has a surface area of ~0.1 km^2. Two sediment cores were

collected in the summer of 2014 using a Uwitec gravity coring device; Eriksvatnet A core (73cm long) and Eriksvatnet B core (180cm long). The majority of analyses have been carried out on the A core to date, and we focus on those results in this chapter.

4.4 Methods

4.4.1 Laboratory Analyses

Cores were split and imaged at the University of Massachusetts, Amherst prior to analysis. Eriksvatnet A was analyzed using an ITRAX X-ray fluorescence (XRF) core scanner to determine elemental abundances. Scans were carried out using a molybdenum (Mo) tube with a downcore resolution of 200 µm. The voltage and current were set to 30kV and 55mA respectively, with an XRF count time of 10 seconds. The Eriksvatnet A core was also scanned using a Geotek multi-sensor core logger (MSCL) (Geotek LTD. UK). The core was scanned at 0.5cm resolution. Magnetic susceptibility data was collected using a Bartington point magnetic susceptibility sensor, and a radioactive Cesium source was used to determine relative changes in gamma attenuation, which have been converted to sediment density.

Eriksvatnet A was sub-sampled at 1 cm intervals for weight loss-on-ignition (LOI), dry bulk density (DBD), and water content (WC) (n=335) (after Dean, 1974; Heiri et al., 2001). A syringe was used to ensure a constant 1 cm^3 of sediment was removed. Macrofossils and bulk sediment samples were selected for radiocarbon dating from the Eriksvatnet A sediment core. Analyses were carried out at the Woods Hole NOSAMS facility and the University of California, Irvine AMS facilities.

A total of 62 samples were chosen for biomarker extraction and analysis. Samples were collected every cm for the upper 62cm of the Eriskvatnet A core. The sediment was freeze-dried and homogenized before lipid extraction. A total lipid extract (TLE) was obtained using a Dionex accelerated solvent extractor (ASE 200). Samples were extracted with a dichloromethane

(DCM)/methanol (9:1, v/v) mixture at 100ºC. The TLE was then saponified to separate the lipid extract into a neutral and fatty acid fraction (after Birk et al., 2012). The neutral fraction was then further separated into three fractions, apolar (9:1 DCM:hexane, v/v), ketone (1:1 DCM:Hexane, v/v) and polar (1:1 DCM:methanol, v/v), using alumina oxide column chromatography.

One half of the polar fraction was filtered in 99:1 hexane:isopropanol using a 0.45μm PTFE syringe filter prior to analysis by high performance liquid chromatography (HPLC) to identify and quantify brGDGTs. A C_{46} GDGT internal standard was added to all polar fractions prior to analysis. BrGDGTs were identified and quantified via high performance liquid chromatography - mass spectrometry using an Agilent 1260 HPLC coupled to an Agilent 6120 MSD following the methods of Hopmans et al. (2000) with minor modifications (Schouten et al., 2007). For compound separation a Prevail Cyano column (150 x 2.1mm, 3 μm) was used. Two solvent mixtures were used as eluents: mixture A) 100% hexane; mixture B) 90% hexane, 10% isopropanol (v/v). Samples were eluted with 10% mixture B for 5 minutes, which was then linearly increased to 18% mixture B from minutes 5-39, and finally increased to 100% mixture B for one minute. Scanning was performed in selected ion monitoring (SIM) mode. Concentrations were calculated by comparing brGDGT HPLC-MS chromatogram peak areas with peak areas of a known concentration (C_{46} GDGT standard added to every sample run). These values were then normalized to the mass of sediment extracted.

The other half of the split polar fraction was derivatized using BSTFA before injection on either a gas chromatograph – mass spectrometer (for compound identification) or gas chromatograph – flame ionization detector (GC-FID), for compound quantification. Individual compound peaks were compared against published mass spectra. Compound peak areas were related to a squalene calibration curve of known concentrations run within two weeks of analysis. For plant leaf waxes (*n*-alkanes) analyses, apolar fractions were first injected on a Agilent 7890A dual gas chromatograph-flame ionization detector (GC-FID) with an Agilent 7693 autosampler equipped with a 5% phenyl methyl silox-ane column (HP-5, 60 m ×0.32 mm×0.25 μm). The oven

program ramped from 70°C to 130°C at a rate of 10°Cmin^{-1}, then from 130°C to 320°C at a rate of 4°Cmin^{-1}, and held the final temperature for 10 min. Quantification was achieved by an external calibration curve of squalane ranging in concentration from 1 ng/µl to 100 ng/µl. The *n*-alkanes, along with polar compounds of interest, were identified by a Hewlett Packard 6890 gas chromatograph coupled to an Agilent 5973 Mass Selec-tive Detector equipped with a 5% phenyl methyl siloxane column (HP-5MS, 60 m ×0.25 mm×0.25 µm), with an identical oven pro-gram to the GC-FID.

4.4.2 Paleoenvironmental Reconstructions

Paleotemperatures and paleo-pH were reconstructed from brGDGT distributions using two indices as originally defined by Weijers et al. (2007). The first is the cyclisation ratio of branched tetraethers (CBT) (Eq. 1). This index measures the relative amount of cyclopentyl moieties in the branched GDGTs, which Weijers et al. (2007) found to be correlated to pH. The second index, the Methylation of Branched Tetraethers (MBT), measures the presence of methyl branches at the C-5 and C-5' positions and was found to be positively correlated to MAAT, and to a lesser extent, negatively correlated to pH (Eq. 2). By combining these two indices, Weijers et al. (2007) were able to produce a robust paleotemperature proxy for soil-derived brGDGTs. In recent years this MBT/CBT relationship has been expanded to include lake sediment samples, yielding numerous lake specific calibrations (e.g. (Loomis et al., 2012; Pearson et al., 2011; Sun et al., 2011; Tierney et al., 2010). For this study the calibration of Sun et al. (2011) (Eq. 3) was applied to reconstruct temperature. In equations 1 and 2 the roman numerals and letters denote the different brGDGT structures as shown in Figure A1, Appendix A in Weijers et al. (2007).

Eq. 1: $\mathbf{CBT} = \frac{\mathbf{[Ib]+[IIb]}}{\mathbf{[I]+[II]}}$ (Weijers et al., 2007)

Eq. 2: $\mathbf{MBT} = \frac{\mathbf{[I+Ib+Ic]}}{\mathbf{[I+Ib+Ic]+[II+IIb+IIc]+[III+IIIb+IIIc]}}$ (Weijers et al., 2007)

Eq. 3: $\boldsymbol{T = 6.803 - 7.602 \times CBT + 37.090 \times MBT}$ (Sun et al., 2011)

Eq. 4: $$\boldsymbol{ACL} = \sum_{\boldsymbol{n=21}}^{\boldsymbol{33}} \boldsymbol{n} * \boldsymbol{f}(\boldsymbol{C_n})$$

4.5 Results

4.5.1 Chronology

At the time of writing, the chronology of Eriksvatnet sediment core A is based on 12 radiocarbon dates on macrofossils isolated from the sediments (**Table 4.1**).

The age/depth relationship for this core is still preliminary, and should not be treated as final at this stage. Proxy results discussed below are presented on an age/depth model created using the Bayesian framework calibration software code 'Bacon' (v. 2.2; Blauw and Christen, 2011), run in 'R' (v. 3.2.2). Radiocarbon ages are reportedly mainly in calibrated years before present (cal yr BP; BP = 1950) according to IntCal13 (Reimer et al., 2013). The preliminary age model used here is based on a "best case" radiocarbon chronology utilizing the 8 most stratigraphically coherent dates **(Figure 4.3).** According to this age model, the ~73cm Eriksvatnet A core has a basal age of 2325 cal years BP and the average sedimentation rate over the length of the record is 0.047 cm/yr.

4.5.2 Core-scanning results

Selected results from Itrax XRF core scanning are presented in **Figure 4.4.** For brevity only certain elemental counts (Ti, Ca, K, Fe, and Mn) are presented here. These elements were selected as they have been shown to indicative of certain meaningful environmental processes in lake sediments (e.g Bakke et al., 2013; Balascio et al., 2015). Ti counts are highly variable throughout the core, varying between 2000 and 4000 counts per second (cps), with a slight increasing trend apparent from ~1000 cal yr BP to ~730 cal yr BP. Ca counts are also highly variable, generally varying between 4000 and 6000 cps, with somewhat higher frequency

variability during the past 500 years. K counts are broadly higher (between 2-3000 cps) in the early part of the record (~2300 – 1000 cal yr BP). They mostly fluctuate between 1-2000 cps for the past 1000 years (**Figure 4.4**). Trends are slightly more apparent in the Fe data, with counts declining from ~180000 to ~111000 during the earliest part of the record (2300-2100 cal yr BP). Fe counts then rise to a relative maxima ~1950 cal yr BP (~240000 cps), before declining again to ~145000 by 1650 cal yr BP (**Figure 4.4**). From a relative maxima at ~1500 cal yr BP counts decline to a minima of ~108000 by ~1010 cal yr BP. Counts then increase broadly until ~500 cal yr BP (~248000 cps) before declining, with variability, to values ~113000 cps at the top of the core. Mn displays a generally increasing trend throughout the core, rising from ~2000 cps at 2300 cal yr BP to above 4000 near the surface (**Figure 4.4**).

In many cases the ratio of different elemental data from the Itrax has been shown to be more informative than the raw counts themselves (e.g. Kylander et al., 2012). Selected elemental ratios are presented in **Figure 4.5.** The ratio of Si/Ti, a proxy for diamtom productivity in some lakes (e.g. Kylander et al., 2011; Bringham-Grette et al., 2013; Liu et al., 2013), is broadly higher in the earlier and latest parts of the Eriksvatnet record, with an additional peak centered around 1000 cal yr BP. The ratio of incoherent/coherent scattering (Incoh/Coh) has been interpreted by numerous authors as a proxy for organic matter content (e.g. Guyard et al., 2007; Kylander et al., 2012; Chawchai et al., 2016). In Eriksvatnet, a relative maxima of the Incoh/Coh ratio is observed from ~2300-2000 cal yr BP, 1800-1600 cal yr BP, and ~1000-750 cal yr BP. The ratio of Ti/(Incoh/Coh) has been interpreted as a proxy for clastic input (Kylander et al., 2012). In Eriksvatnet, this ratio looks broadly similar to raw Ti counts, with significant variability throughout the record.

The ratio of Mn/Fe has been shown to be potentially indicate the redox state of the lake water and sediments (Koinig et al., 2003; Kylander et al., 2011; Loizeau et al., 2001; Naeher et al., 2013; Wennrich et al., 2014). In Eriksvatnet the Mn/Fe ratio is highly variable in the early part of the record and then slowly increases from ~2000 cal yr BP to ~825 cal yr BP (**Figure 4.5**).

It then declines slightly and is broadly stable until ~275 cal yr BP, when it increases to the highest values seen in the record. The ratio of K/Ti has been utilized in other lake settings to isolate tephra layers (see Chapter 3 above; Kylander et al., 2012). In Eriksvatnet, however, the ratio is highly variable with no discernable, well-defined peaks (**Figure 4.5**).

Results from Geotek core scanning are shown in **Figure 4.6.** Sediment density, inferred from attenuated gamma counts, broadly declines throughout the record, with a brief period of relatively more dense sediment from ~1950 – 1400 cal yr BP. Magnetic susceptibility is more variable, with relatively low values (~15 SI units) from the base of the core (2300 cal yr BP) until ~2160 cal yr BP. Values then increase to above 30 SI units from ~2100 to 1975 cal yr BP, decline to below 20 SI units by 1900 cal yr BP, and then increase again to above 40 SI units by 1700 cal yr BP. From this point magnetic susceptibility declines to a minimum of less than 10 SI units at approx. 1250 cal yr BP. MS from this point remains relatively low until ~345 cal yr BP, when it increases dramatically to a maximum of nearly 47 SI units at ~130 cal yr BP before declining towards the top of the core (**Figure 4.6**).

4.5.3 Laboratory Results

Percent loss-on-ignition (%LOI) and dry bulk density (DBD) values are plotted in **Figure 4.7.** LOI values range from a maximum of 49% to a minimum of ~20%. LOI values broadly decline from ~2300 cal yr BP to ~1400 cal yr BP (43% down to ~30%), before they increase rapidly to nearly 44% at 1400 cal yr BP (**Figure 4.7**). This spike is followed by a slow decline to ~32% LOI by 375 cal yr BP. An abrupt decline (represented by two data points) then occurs, with values declining to below 25% by ~250 cal yr BP. LOI values then rise up to nearly 50% over the remainder of the record. DBD follows an inverse pattern to LOI, with values ranging from ~0.11 g/cm^3 to above 0.28 g/cm^3.

4.5.4 Biomarker Results

Concentrations of specific biomarker groups are presented in **Figure 4.8**. Total lipid extract (TLE) concentrations are relatively low in the early part of the record (between 20-70 mg/g sediment extracted) until approx. 1550 cal yr BP, when they increase to more than 250 mg/g sed. ext.. Concentrations remain above 100 mg/g sed ext. until ~1120 cal yr BP. From this point until ~500 cal yr BP, concentrations are generally below 50 mg/g sed ext. Over the last 500 years TLE concentrations are more variable, with values from ~15 – 200 mg/g sed ext. (**Figure 4.8**). Concentrations of branched glycerol dialkyl glycerol tetraethers (brGDGTs) are highly variable throughout the record, with a maximum concentration of ~2.8 µg/g sed ext. ~1530 cal yr BP and a minimum of 1.2 µg/g sed ext. ~100 cal yr BP. Concentrations of 5B stanols (compounds generally related to plant primary productivity) show a slightly increase trend throughout the early part of the record, from ~2300 cal yr BP to ~990 cal yr BP. A slight decline is then recorded over the next ~100 years, and concentrations vary until ~400 years ago, when they increase dramatically to a maximum at ~60 cal yr BP. Concentrations of leaf wax *n*-alkanes are highly variable throughout the record and appear to display a relatively repeatable cyclicity, which is especially pronounced over the most recent ~800 years of the record (**Figure 4.8**).

4.5.5 brGDGT Results

brGDGT specific results are presented in **Figure 4.9**. The Methylation of branched tetraethers index (MBT) is broadly stable, with some variability, from ~2300 – 660 cal yr BP (avg. 0.28). From this point onwards MBT declines to ~0.22 by the top of the core. The cyclisation of branched tetraethers index (CBT) increases from ~0.77 in the earliest part of the record to 0.83 by 2080 cal yr BP. From ~2080 cal yr BP until ~ 660 cal yr BP CBT declines, with variability, from 0.83 to 0.75. CBT then increases up to 0.82 by ~320 cal yr BP before declining to a minimum of 0.70 by the top of the record (**Figure 4.9)**. Reconstructed pH varies from ~7.55 to 7.8 units throughout the record, with the most basic values recorded near the top of the core.

Reconstructed temperatures, based on the calibration of Sun et al. (2011), vary between ~12.5°C and 9.8°C. Temperatures decline rapidly in the earliest part of the core, falling from ~12.5°C to 11.3°C from 2300 – 2080 cal yr BP. Reconstructed temperatures are then broadly stable (with some short term variability) until ~1240 cal yr BP, when they increase from ~11.5°C to 12.3°C by 660 cal yr BP. From 660 cal yr BP temperatures decline through the top of the core to a minimum of 9.8°C by ~60 cal yr BP (**Figure 4.9**).

4.5.6 Leaf wax *n*-alkane data

Leaf wax *n*-alkanes are long chain carbon compounds that make up the waxy outer coating of plant leaves and stems. Though this relationship does not hold everywhere (e.g. Bush and McInerney, 2013), short chain lengths (e.g. C_{17}-C_{21}) are broadly characteristic of aquatic plants, while longer chain lengths (C_{27}-C_{33}) are generally sourced from terrestrial higher plants (Eglinton and Hamilton, 1967). *n*-alkane results from Eriksvatnet are presented in **Figure 4.10**. *n*-alkane concentrations display marked variability in the Eriksvatnet record, as noted above. The seemingly cyclical nature of these values will be investigated further. The percent aquatic ratio (P_{aq}) is meant to elucidate the relative contribution of aquatic vs. terrestrial organic matter (Ficken et al., 2000). The P_{aq} ratio is highest, from approx. 2100-1300 cal yr BP, with a relatively stable but slightly declining trend thereafter. The ratio reaches a minimum of ~0.60 by ~ 20 cal yr BP. Average chain length values are based on the equation of Poynter and Eglinton (1990) (**Eq 4.)** and display less variability than the concentration data. Average chain lengths decline in the early part of the record from ~27.0 to ~26.0 from 2300 – 1450 cal yr BP. ACL is broadly stable, with a slight increasing trend, from 1450 – approx. 430 cal yr BP (up to 26.4). The average chain length then increases near the top of the core to ~27 (**Figure 4.10**).

4.5.7 Primary productivity compounds

Sterol and stanol concentrations from Eriksvatnet are presented in **Figure 4.11**. Of the seven compounds identified here, only cholesterol and brassicasterol are not produced by plants. Campersterol, campestanol, stigmasterol, β-Sitosterol, and sitostanol are all plant phytosterols. They are structurally similar to cholesterol, with varying carbon side chains and number and location of double bonds. Brassicasterol is mainly produced by diatoms (Orcutt and Patterson, 1975). Concentrations of these compounds all generally follow a similar pattern. Concentrations generally increase from the base of the core up to ~1000 cal yr BP, when all compounds decline, with variability, until ~500 cal yr BP. The concentrations of all compounds then increase over the remaining part of the record, with maximum concentrations in all 7 concentrations occurring ~60 cal yr BP (**Figure 4.11**).

4.6 Discussion of Preliminary Results

The primary goal of this research is to attempt to reconstruct temperature during the period of Norse occupation of the Eastern Settlement, SW Greenland. While our MBT/CBT based paleotemperature reconstruction can be currently treated as a first step towards this goal, numerous caveats, both pertaining to the proxy and to the Eriksvatnet site, must be addressed before this record can be deemed reliable.

One of the most important issues relates to the calibration chosen for the temperature reconstruction. We have chosen to present our data using the calibration of Sun et al. (2011), as the reconstruction from the uppermost sample from the core yields a temperature (10.0°C) similar to modern mean summer (June, July, August) temperature (9.3°C), and mean July temperatures (10.2°C) (yr.no weather data for Narsarsuaq). Previous work on brGDGTs in Arctic lakes (Shanahan et al., 2013), suggests that the temperature signal recorded by these compounds represents the summer production season and not a mean annual temperature. At this stage we therefore interpret the record from Eriksvatnet as representing a summer temperature signal,

though ongoing research will elucidate this further (see below). Additionally, it should be noted that the absolute temperature values reported here are highly dependent on the calibration chosen, and numerous published calibrations are currently available (e.g. Tierney et al., 2010; Pearson et al., 2011; Sun et al., 2011; Loomis et al., 2012; Yang et al., 2014), including calibrations related to soil-derived brGDGTs (e.g. Weijers et al., 2007). Importantly, however, application of nearly all of these published calibrations results in similar *relative* changes in temperature in our record. With regard to the source of brGDGTs in our lake sediment record, preliminary data from lake sediment core-top samples and soils from around SW Greenland (**Figure 4.12**) suggests that the sediment brGDGT distributions are markedly different than the catchment soils, lending weight to the choice of a lake specific calibration. We are currently investigating this further with sediment trap and thermistor data from the lakes and catchment.

Further complicating robust conclusions based on our MBT/CBT temperature reconstruction is the ambiguity of our age model. Though eight of our radiocarbon dates broadly fit into a coherent stratigraphic framework, four of the dates are stratigraphically reversed. While this may be explained by the in-washing of older material preserved on the landscape, their presence necessitates a more robust approach. To this end we are currently analyzing cryptotephra from the Eriksvatnet record, with tephra grains identified in numerous intervals in the upper part of the record. Geochemical analysis of these grains is ongoing. ^{137}Cs and ^{210}Pb analysis is also underway, and will contribute to the age determination of the upper part of the record.

In light of the caveats discussed above, the data presented here should be treated as preliminary. Based on our current age model our temperature reconstruction (re-plotted on the BC/AD age scale in **Figure 4.13**) would suggest that the Norse did arrive in Greenland during a period of relatively warmer temperatures, and that temperatures were declining during the period of abandonment in the 15th century. Again however, our purely radiocarbon based age model is

somewhat suspect, and requires the incorporation of additional radiocarbon dates along with the utilization of other dating methods.

A further complication that would ideally be addressed is the identification of the Norse occupation of the site based on the proxy data from the lake record itself. To date, coprostanol, a dominant fecal sterol in human waste (e.g. (Bull et al., 2002; D'Anjou, 2012) has not been identified in Eriksvatnet. Concentrations of primary productivity biomarkers (**Figure 4.11**) seem to decline during the supposed interval of Norse occupation (again, subject to the age model), a somewhat surprising result. More research is needed to determine whether these reductions in concentration were driven by increases in other (potentially anthropogenic related) compounds or represent real reductions in organic matter primary production.

4.7 Ongoing Research

As noted above, additional research is needed on the Eriksvatnet record before robust conclusions can be made. The majority of this work is focused on improving the age model with additional radiocarbon dates along with identification of tephra horizons and near-surface dating techniques. We also plan to pursue additional biomarkers which may be indicative of human settlement, including polycyclic aromatic hydrocarbons (PAHs), which can be indicative of biomass burning (e.g. D'Anjou et al., 2012), and bile acids (e.g. Tyagi et al., 2007).

This work is part of a larger NSF funded project to create local calibrations for biomarker based paleotemperature reconstructions from the Eastern Settlement. In July of 2016 two Technicap interval sediment traps and three fixed sediment trap lines were deployed in lakes within the Norse Eastern Settlement region and recovered in July of 2017. Additional soil and vegetation samples were also collected, which will be analyzed for biomarkers (brGDGTs, *n*-alkanes, etc.) to aide in interpretation of the sediment record. In addition to Eriksvatnet, numerous other lakes in the region have been cored (**Figure 4.1**) to date, and the sediments will be analyzed at the University of Massachusetts, Amherst to create comparable records of temperature other

climate proxies. The preliminary data presented here from Eriksvatnet represents the first step towards the broader goal of quantitatively reconstructing temperature from the Eastern Settlement region during the period of Norse occupation.

Table 4.1: Radiocarbon dates on Eriksvatnet A core.

Depth of sample (cm)	Sample Material	^{14}C Age	Error +/- (1σ)	Calibrated Age ±2 sigma	$\Delta^{13}C$ ‰ VPDB
5	Plant Remains	195	15	-4 - 289	Not reported
13	Plant Remains	655	25	559-669	Not reported
15	Plant Remains	1790	20	1626-1812	-14.83
19.5	Plant Remains	1440	75	1190 - 1525	-20.06
25	Plant Remains	1140	30	970-1173	-28.25
25	Plant Remains	1700	25	1549 – 1694	-18.23
32	Plant Remains	1600	25	1414 - 1545	-21.92
33	Plant Remains	1425	45	1284 - 1397	Not Reported
39.5	Plant Remains	1960	20	1867 - 1970	-22.3
43.5	Bulk Sediment	1030	20	924 – 965	-26.15
50	Bulk Sediment	2100	20	2002 - 2128	-23.56
72.6	Plant Remains	1890	20	1742 - 1887	-28.32

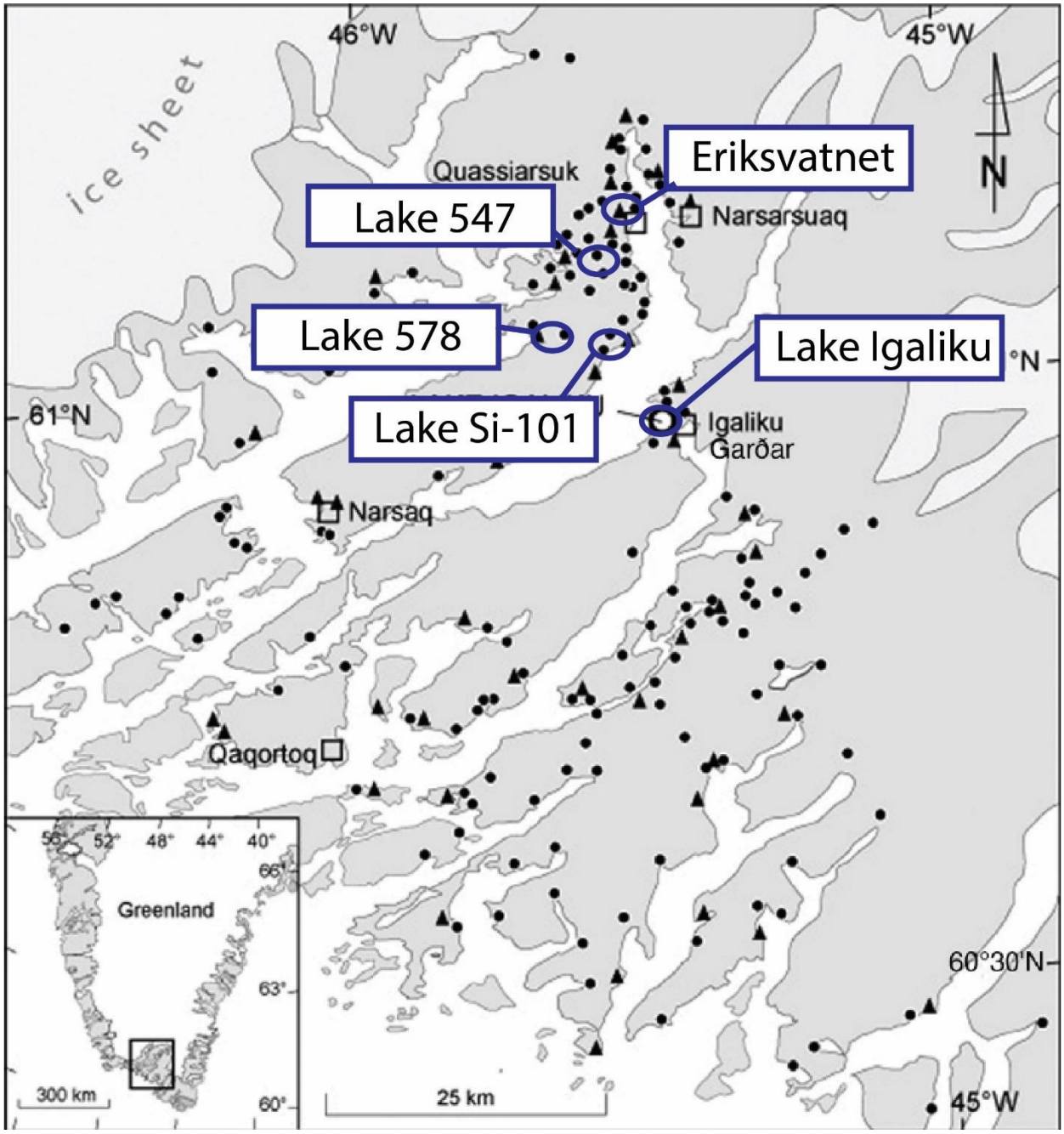

Figure 4.1 – Modified map of Norse Eastern Settlement region with known Norse sites marked (black circles) and the locations of studied lakes (modified from Bichet et al., 2013).

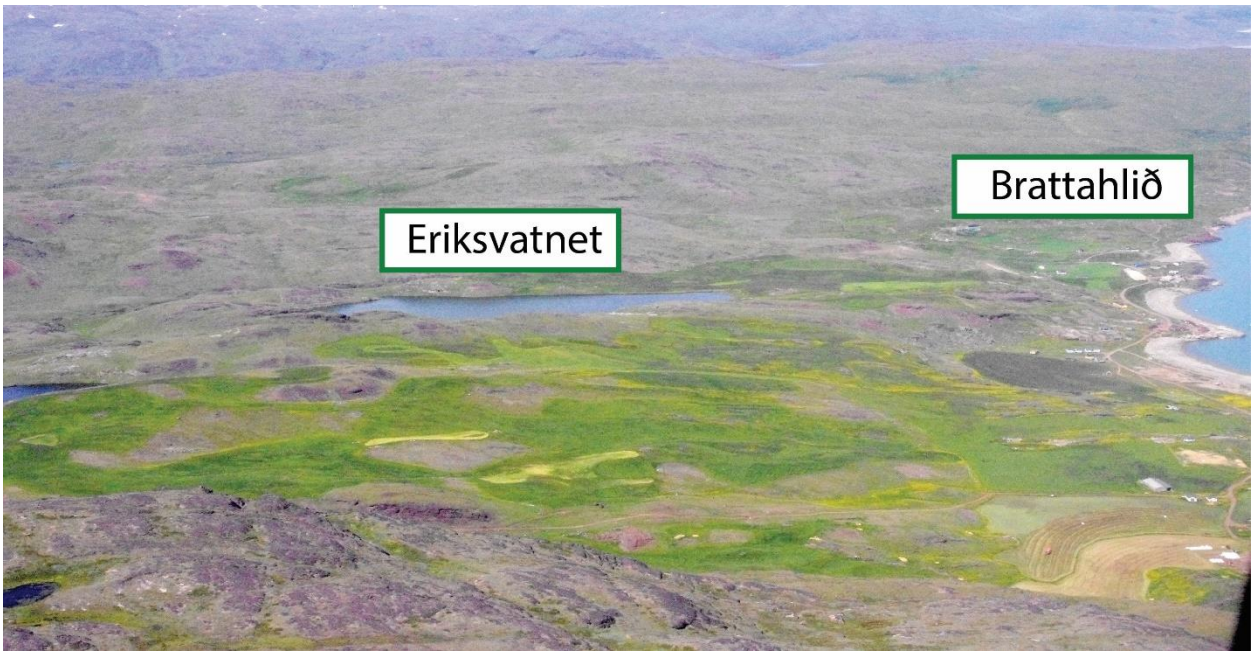

Figure 4.2 – Oblique air photograph of Eriksvatnet lake and nearby settlemtent of Brattahlíð (known as Qassiarsuk today).

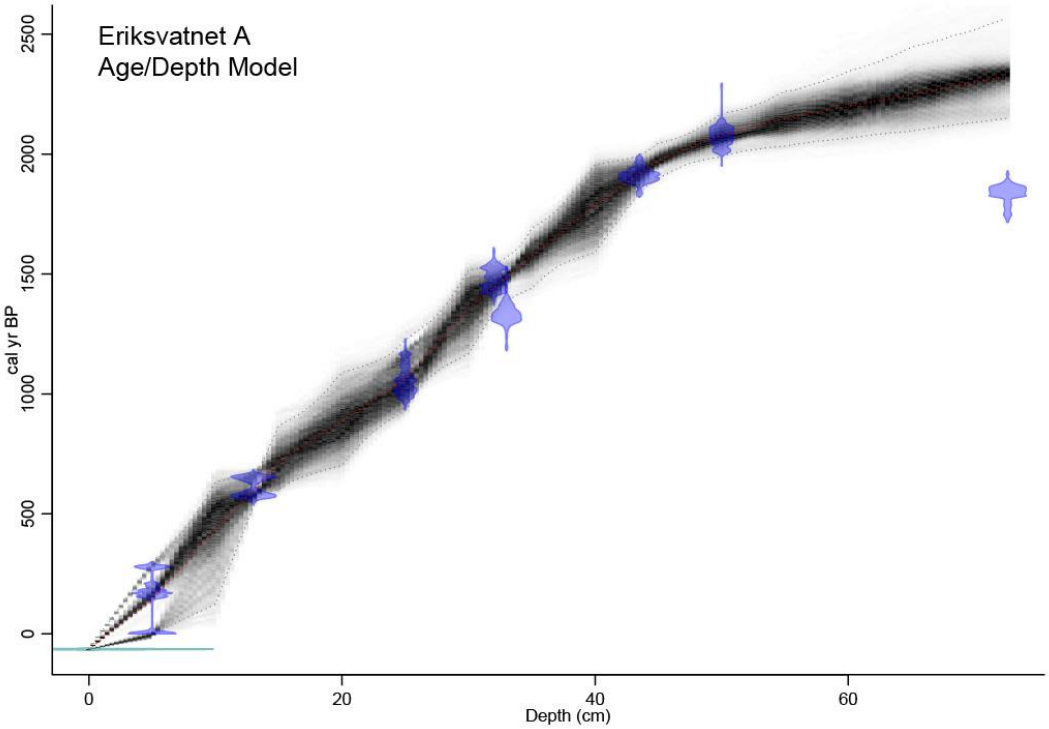

Figure 4.3 – Preliminary age/depth model for Eriksvatnet A core based on 8 radiocarbon dates.

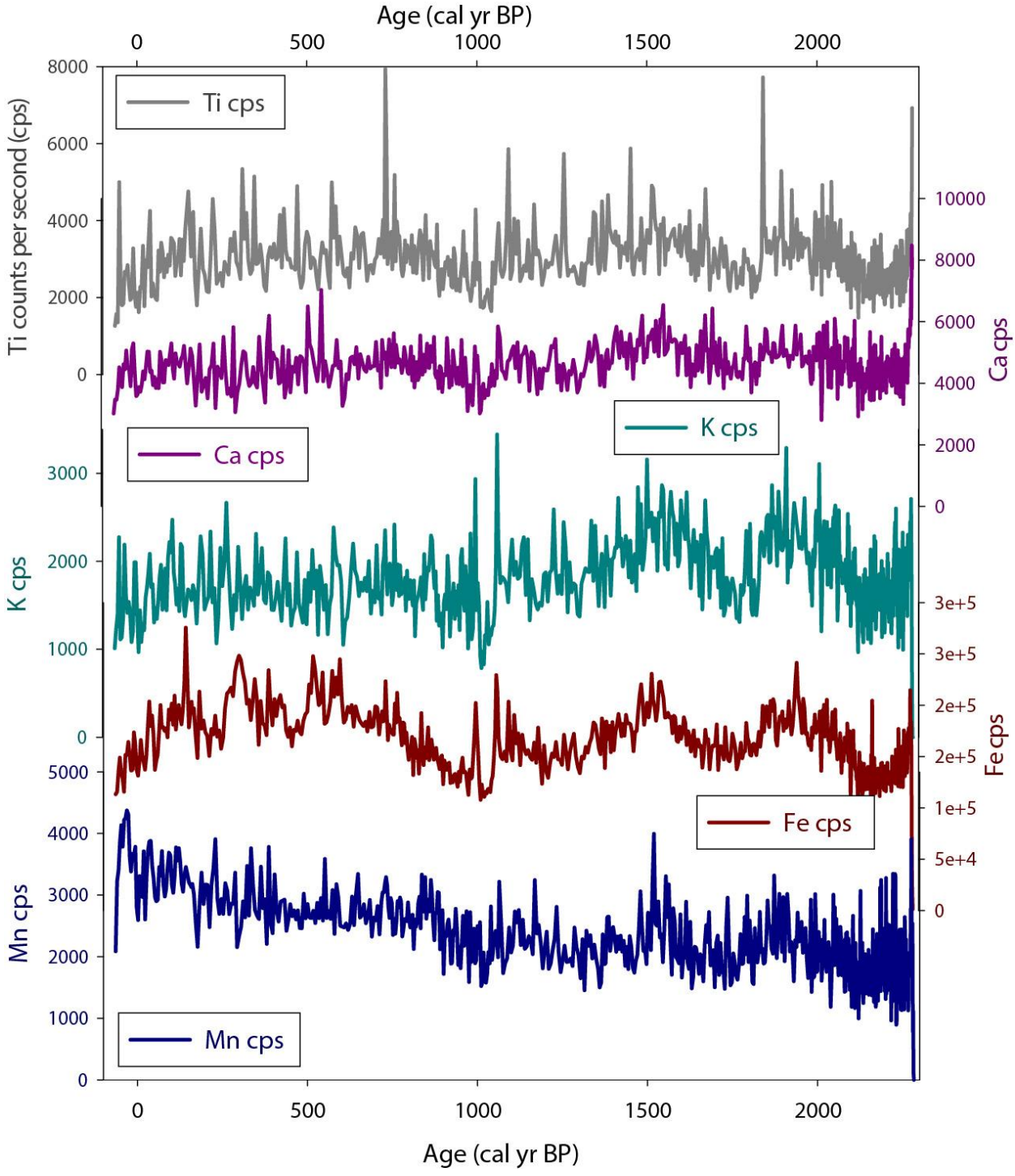

Figure 4.4 – Results from Itrax XRF core-scanning of Eriksvatnet A core.

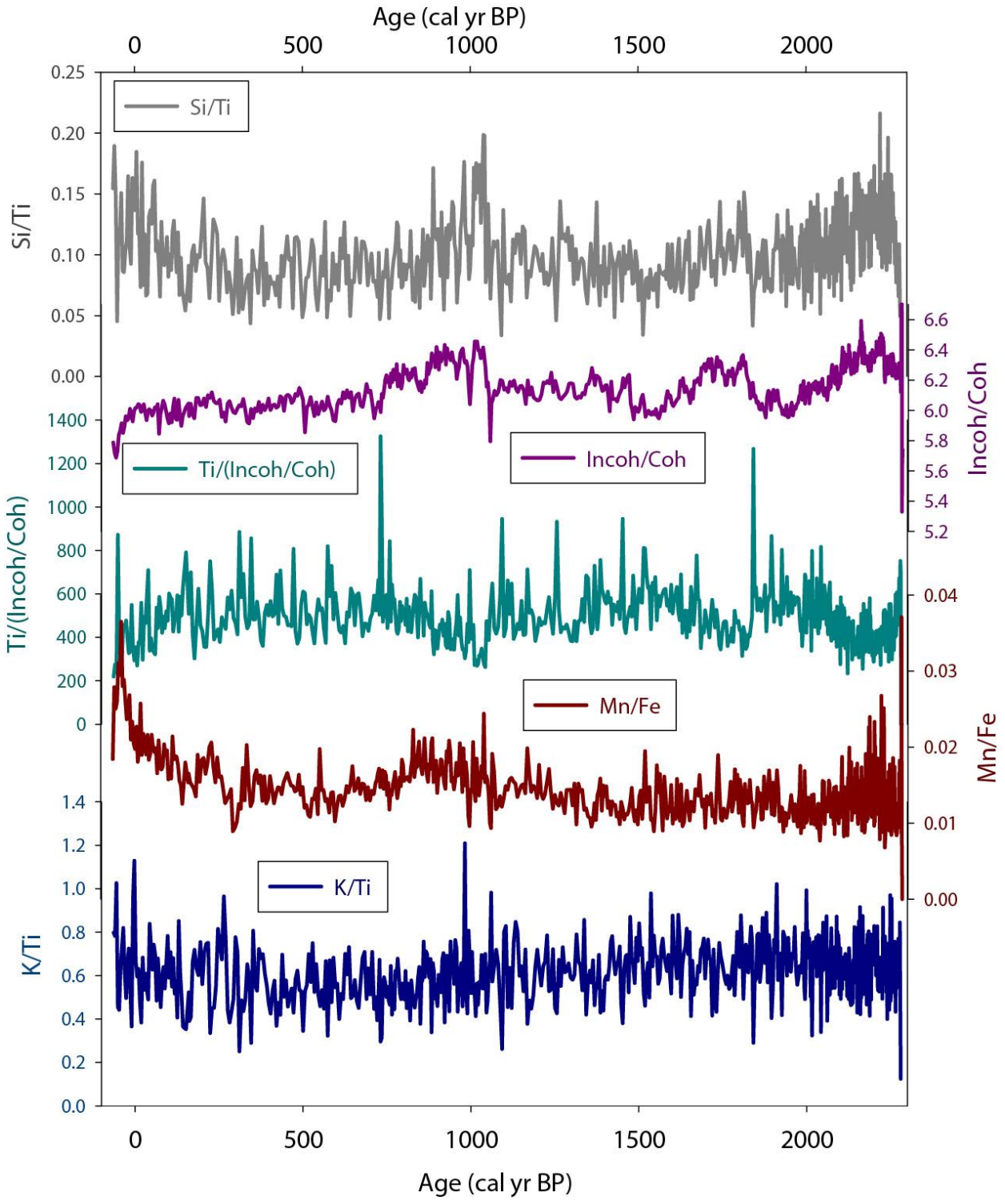

Figure 4.5 – Selected ratios of elemental data from Itrax XRF core-scanning from Eriksvatnet.

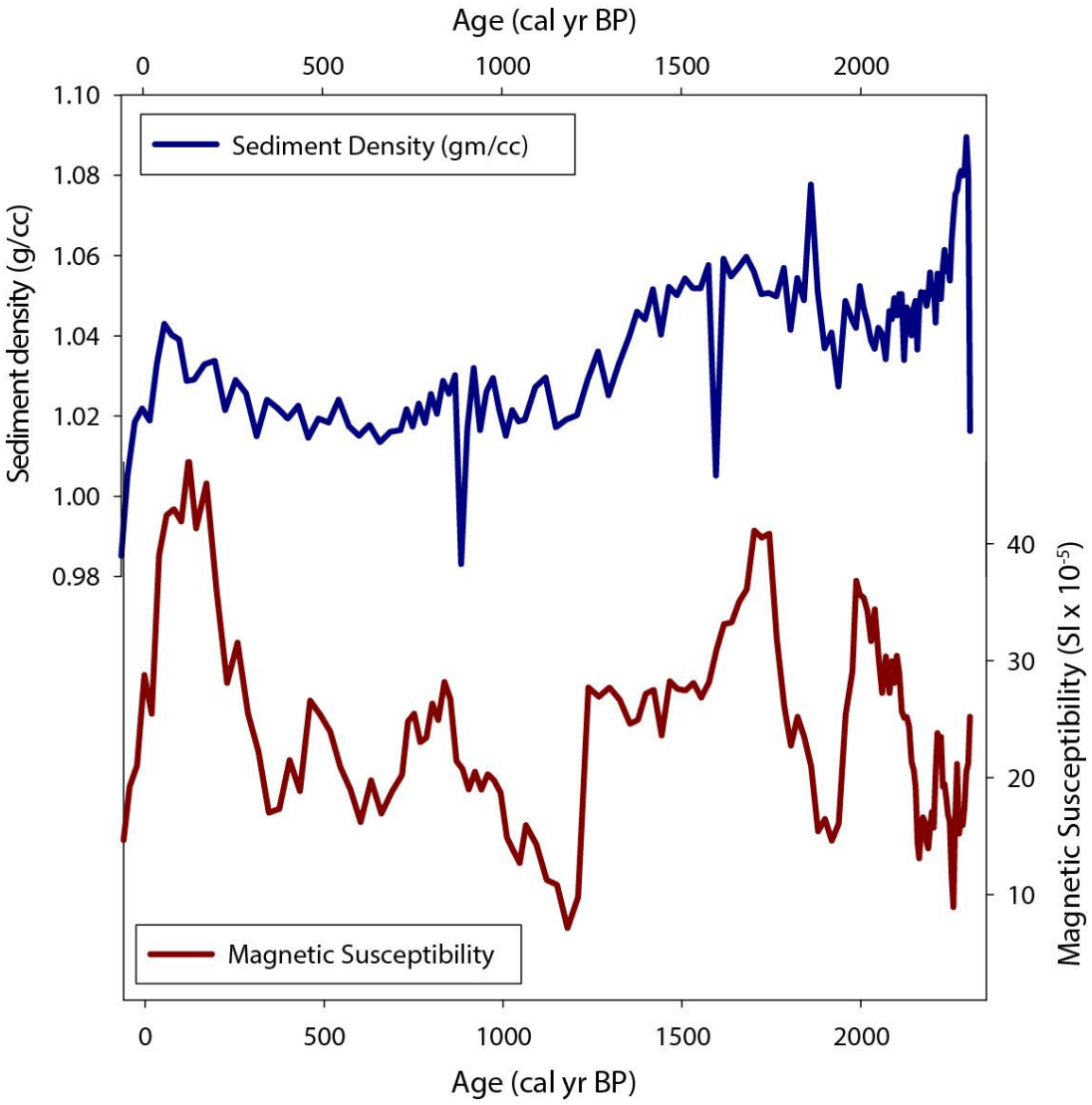

Figure 4.6 – Sediment density and magnetic susceptibility results from the Geotek MSCL core-logging system for the Eriksvatnet A core.

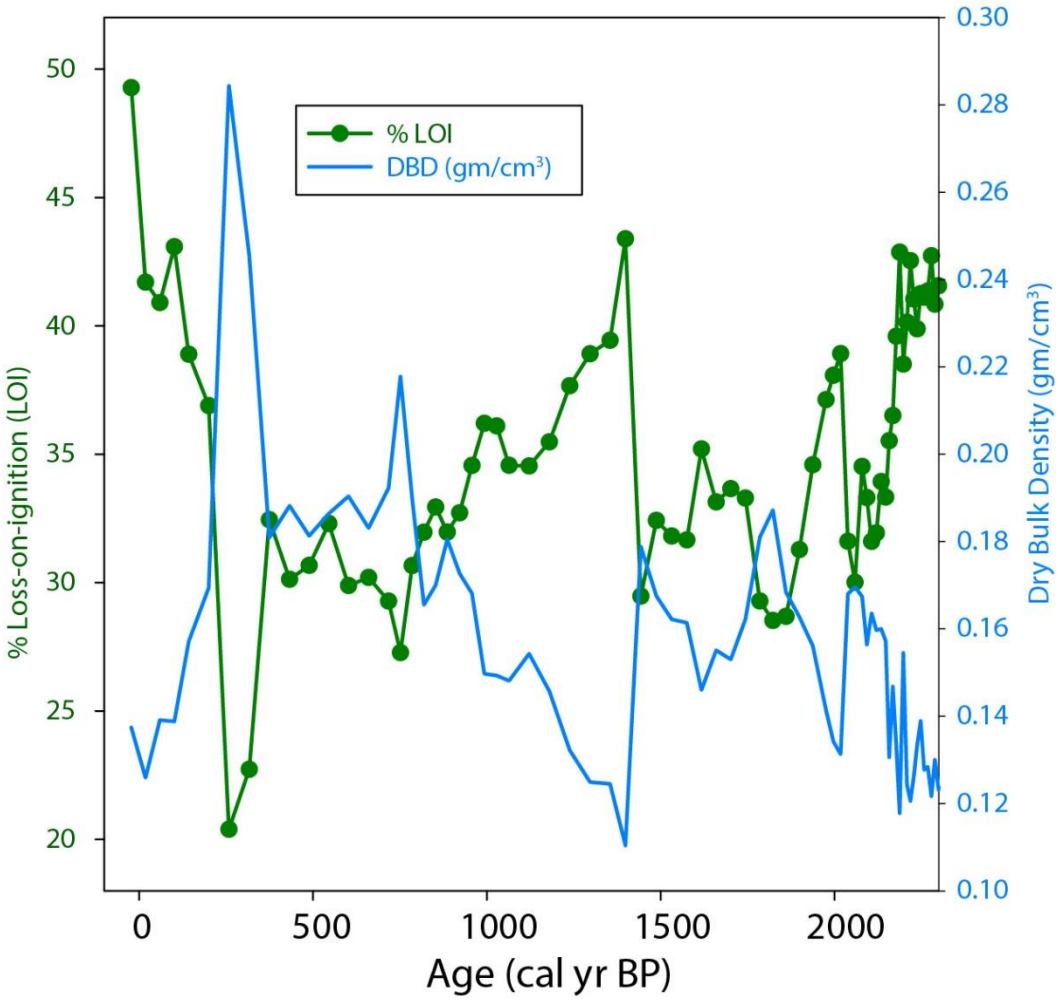

Figure 4.7 – Loss-on-ignition and dry bulk density results for the Eriksvatnet A core.

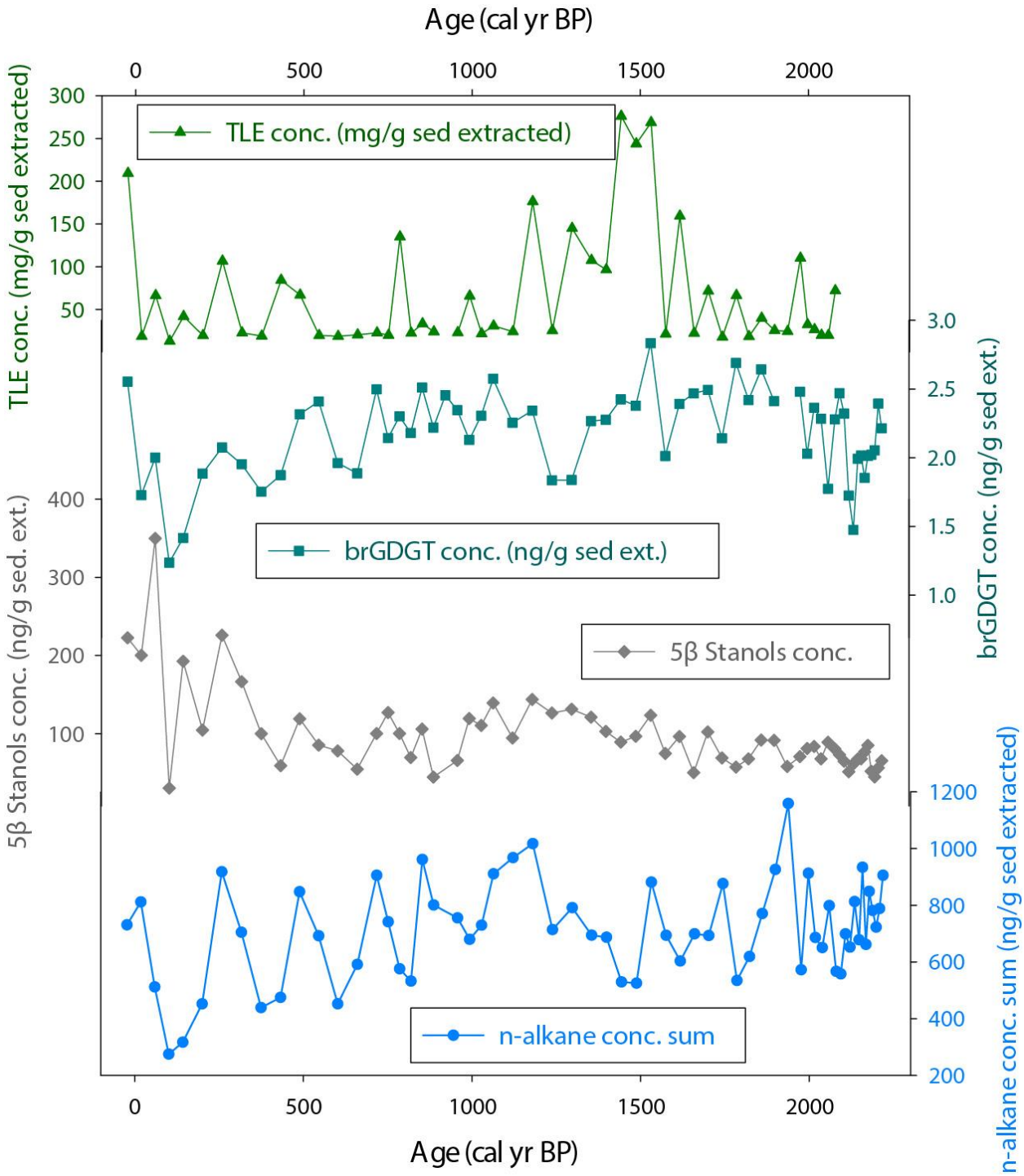

Figure 4.8 – Biomarker concentrations from Eriksvatn A core.

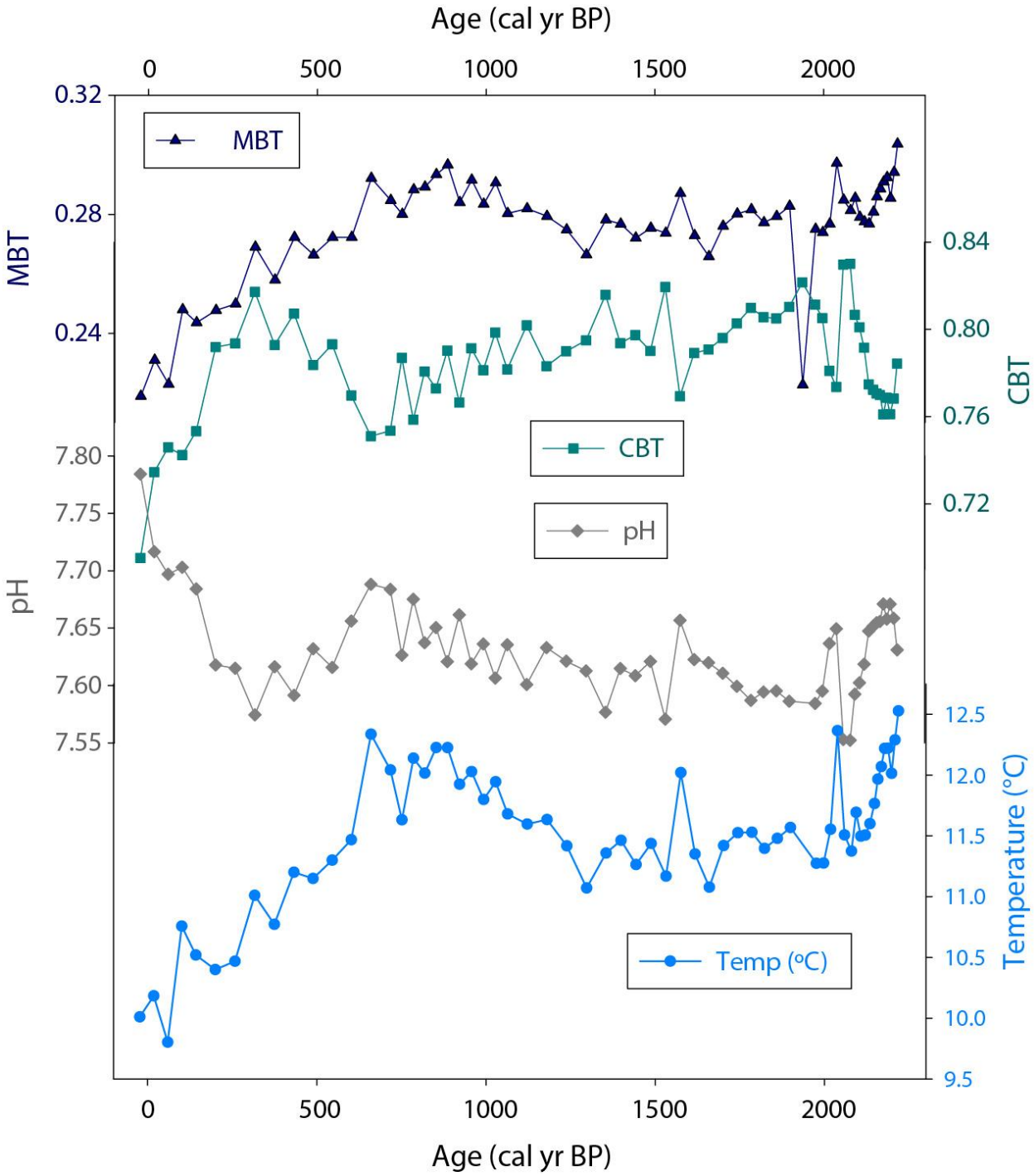

Figure 4.9 – brGDGT results from Eriksvatnet A core. pH and temperature were reconstructed using the equations of Sun et al., 2011.

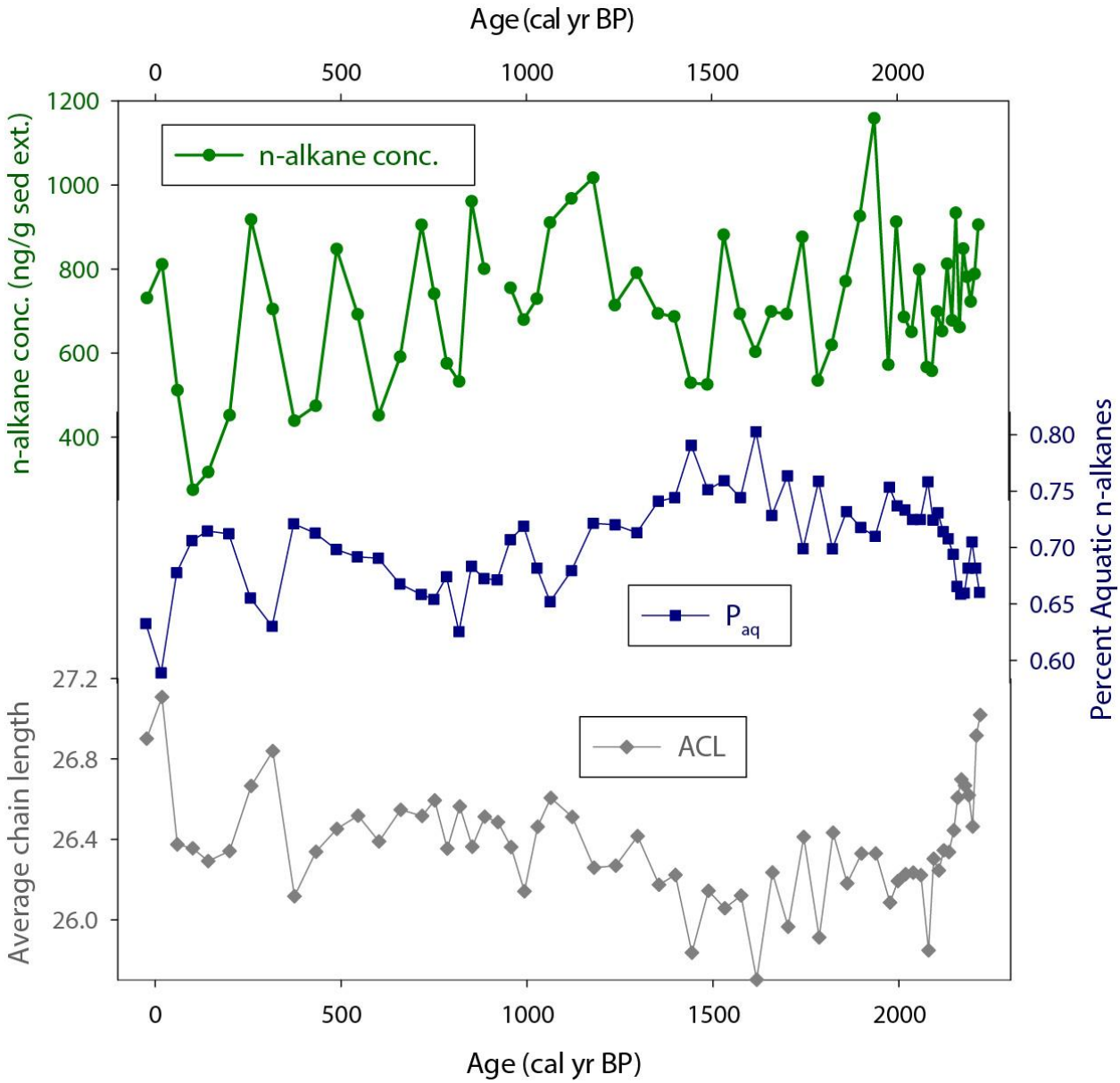

Figure 4.10 – Preliminary leaf wax *n*-alkane results from the Eriksvatnet A core.

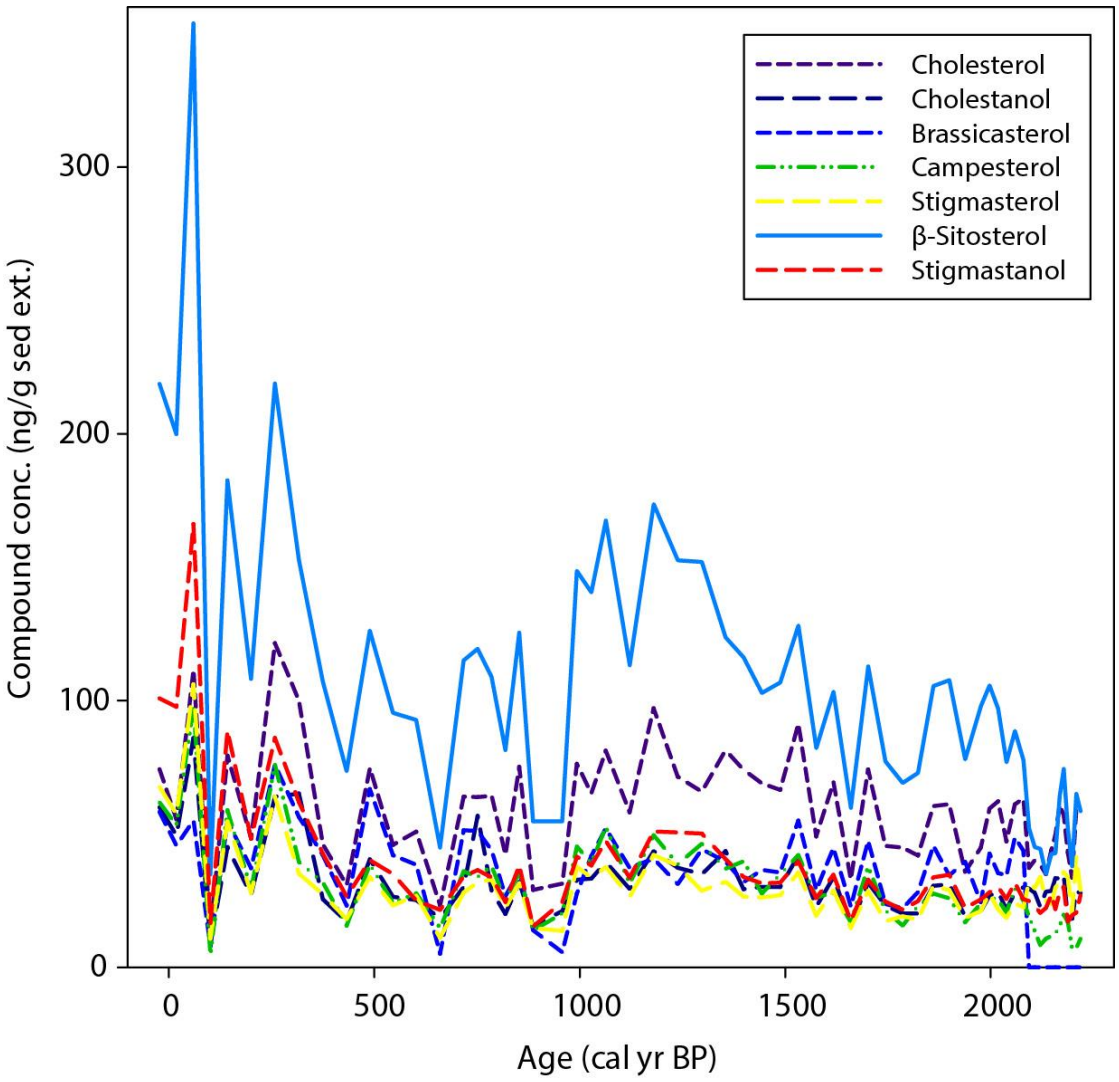

Figure 4.11 – Preliminary sterol and stanol biomarker concentration data from the Eriksvatnet A core.

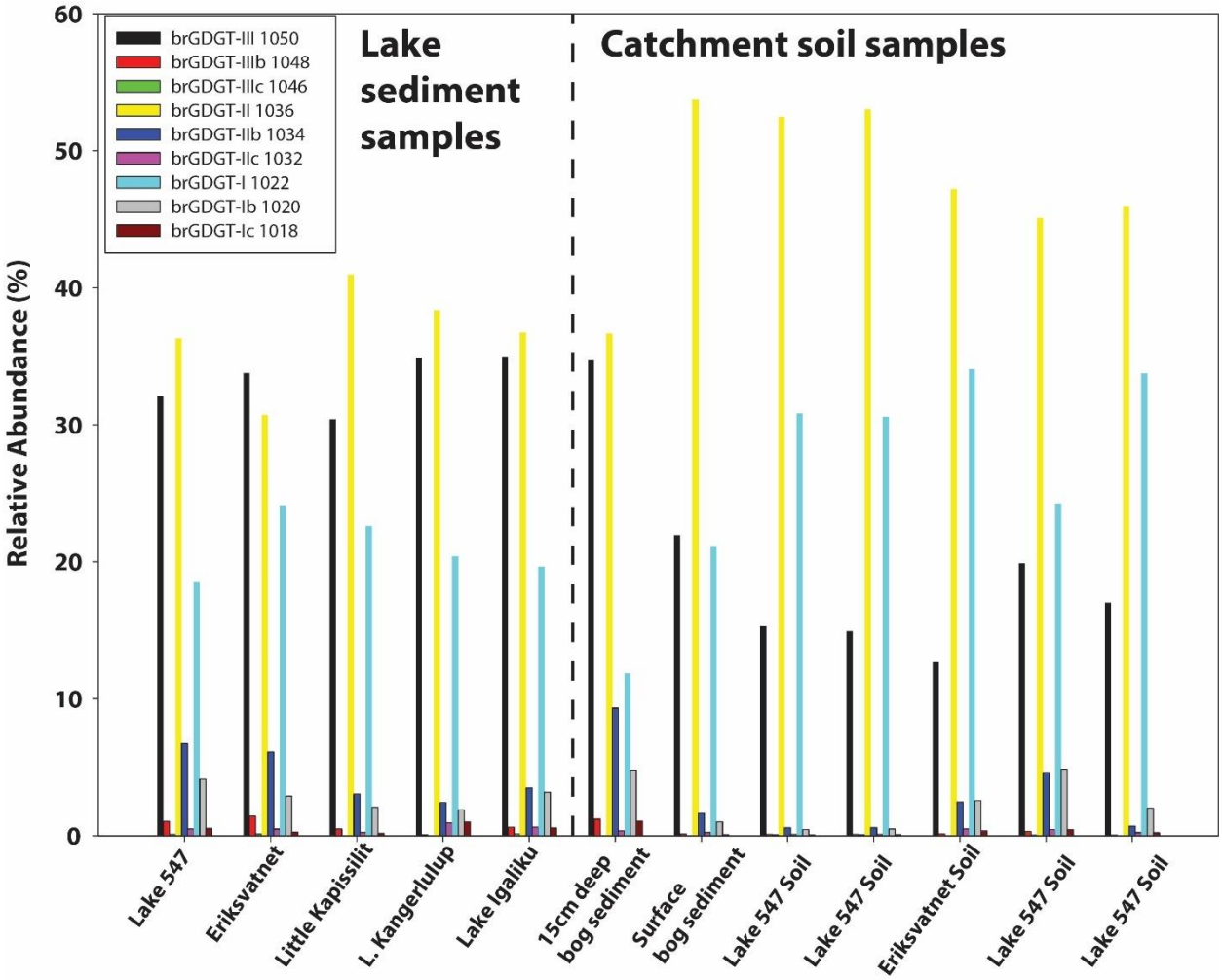

Figure 4.12 – Relative abundances of brGDGTs from both lake surface sediment samples (left panel) and soil samples (right panel) from throughout the Eastern Settlement region.

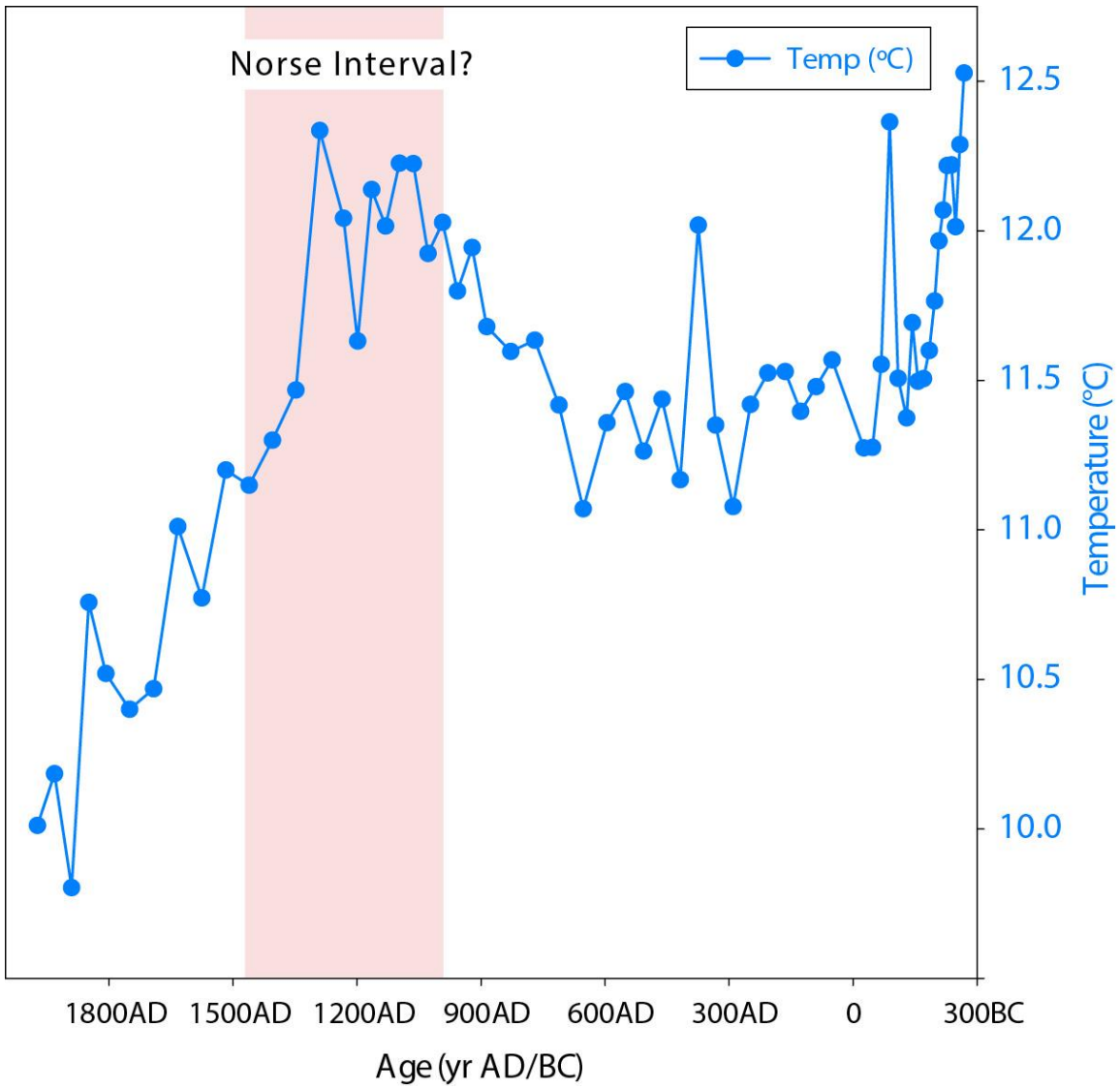

Figure 4.13 – Preliminary Eriksvatnet brGDGT based paleotemperatures on AD/BC age depth scale with approximate interval of Norse settlement outlined (red box).

CHAPTER 5

CONFIRMATION OF THE USE OF FTIR SPECTROSCOPY TO DETERMINE BIOGENIC SILICA AND ORGANIC MATTER CONTENT OF ARCTIC LAKE SEDIMENTS: A POWERFUL TOOL FOR HIGH-RESOLUTION PALEOCLIMATE RECONSTRUCTIONS

5.1 Introduction

In light of predicted climate change (IPCC, 2013), it is essential to understand how climate has changed in the past. While broad climate patterns in the Arctic over the Holocene are generally well understood, the identification of short-term fluctuations and/or rapid change requires high resolution paleoclimate reconstructions. Lake sediments can serve as excellent archives of environmental changes, and, in cases with high enough sedimentation rates, can record centennial to decadal scale climate information. Accessing this information however, can be hampered by numerous factors, including the amount of sediment required as well as expensive and time-consuming analytical procedures (Kaufman, 2012). Furthermore, lakes in particular are highly complex systems with multiple factors and sources contributing to the sediment eventually preserved in the lake bottom. To that end, robust paleoclimate reconstructions from a single lake sediment core increasingly utilize multiple proxies: in a recent compendium of 18 Arctic lake sediment records from the Holocene (Kaufman, 2012) researchers analyzed a total of 15 different parameters. One of the goals of the paleolimnological community is therefore to be able to produce high-resolution, high quality data at a low analytical cost.

Advances in instrumentation and analytical techniques have allowed some progress towards this goal. Multi-sensor core scanners can provide ultra-high resolution, non-destructive data, but climate interpretations from this data can be limited. Alternatively, biomolecular proxies such as the UK^{37} index (based on concentrations of alkenones), the TEX^{86} index (based on archaeal membrane lipid concentrations), and the MBT/CBT ratio (based on bacterial membrane lipid concentrations) can provide excellent climatic information but are expensive and time

consuming to analyze (Castañeda and Schouten, 2011). Furthermore, many of these techniques require large volumes of sediment for analysis, hampering their application. Traditionally, proxies such as total organic carbon (TOC) and biogenic silica (BSi) concentrations fall somewhere in the middle of the spectrum with regards to cost and time of analysis. Biogenic silica analysis using the traditional wet chemistry leaching method (Mortlock and Froelich, 1989), can be quite time consuming however, and running large numbers of samples on an elemental analyzer to determine TOC can be expensive. Here we present a regional calibration model confirming the independent application of Fourier Transform Infrared Spectroscopy (FTIRS) to accurately determine TOC and BSi concentrations downcore in a lake sediment record from SE Greenland spanning the past approximately ten thousand years.

FTIRS is a promising tool for high-resolution paleo-environmental reconstructions as it addresses many of the aforementioned issues of analytical costs and instrument time. Only a small amount of sediment is required for analysis (0.01g) and minimal pretreatment is required. Sample analysis is relatively fast (64 seconds/sample on the FTIRS). In addition, multiple parameters can be measured simultaneously (TOC, BSi, TIC, TN) (Rosèn et al., 2011). The method is based on the principle that vibrations in molecules containing covalent bonds are excited by infrared radiation (Vogel et al., 2008). Differences in the molecular structure and atomic composition of sediment lead to absorbance on IR radiation at specific wavelengths (Colthup et al., 1990), meaning that the absorption spectra of a sample is therefore indicative of its chemical composition. Calibration models based on traditionally measured proxies are then used to determine the concentration of the proxy of interest from the absorption spectra of a sample (or specific spectral peak areas). This method has been shown to accurately determine these variables on long timescales and from multiple regions throughout the world (e.g. Vogel et al., 2008; Rosen et al., 2010; Rosen et al., 2011; Meyer-Jacob et al., 2014).

Here we show that FTIRS based analysis of sediment from an Arctic lake accurately reconstructs both biogenic silica and total organic carbon concentrations downcore. Our

calibration models utilize Partial Least Squares (PLS) multivariate regression and are based on conventionally measured BSi and TOC. Our data suggest this method works well in Greenland lakes but acknowledge differences in data pre-processing and model configuration can affect reconstructed concentrations.

5.2 Study Area

The majority of the data used for this study are from a sediment record from Nanerersarpik Lake, in southeastern Greenland. Nanerersarpik Lake is located on the shore of Angmassalik Fjord in Southeast Greenland (66°54'47.58''N, 37°08'44.98''W) near the Innuit settlement of Kummiut approximately 45 kilometers from the coast (**Figure 5.1**). The lake itself is quite clear and has a surface area of 0.62 km^2 Cores were collected from the deepest part of the basin (54m water depth) in the southern half of the lake. A total of 841cm of sediment were recovered from the lake, of which 303cm were identified as mass movement deposits and removed from the paleoclimate reconstruction. An age model was created for the remaining 538cm using 7 AMS radiocarbon dates on organic macrofossils. FTIRS analysis was carried out at 5cm resolution for the older part of the record (past aprox. 6 thousand years (kyr BP)) and every centimeter for the most recent 4 kyr BP. Biogenic silica calibration samples (see below) were also included from nearby Lower Sermilik Lake (SE Greenland, **Figure 5.1**) and Fiskebol Lake (northern Norway).

5.3 Methods

5.3.1 Conventional biogenic silica measurements

Biogenic silica concentrations were determined for 33 samples using the conventional digestion method of Mortlock and Froelich (1989). 22 samples were analyzed from Nanerersarpik Lake, 8 from Lower Sermilik, and 3 from Fiskebol Lake in Norway. A further two samples of

pure washed quartz (used for calibration of the X-Ray Diffraction (XRD) instrument here at UMass, Amherst) were also included in the calibration dataset to represent 0% BSi, for a total of 35 conventional biogenic silica measurements. The range of measured BSi in our 3 lakes is 30.6% (high of 30.6%, low of 0%) (**Table 5.1**).

5.3.2 Conventional total organic carbon measurements

TOC concentrations were determined for 112 samples from Nanerersarpik Lake using a Costech ECS 4010 Elemental Analyzer at the University of Massachusetts, Amherst. Samples were freeze-dried and acidified with HCL to remove carbonate before analysis. The XRD calibration samples (0%TOC) mentioned above were also included in the calibration dataset. TOC concentrations in the Nanerersarpik samples ranged from ~5.2% to ~0.03% (**Table 5.2**).

5.3.3 Fourier Transform Infrared Spectroscopy analyses

290 freeze-dried samples from Nanerersarpik Lake were ground by hand using a mortar and pestle and weighed to a mass of 0.01g. The sediment was then mixed with 0.5g of oven-dried potassium bromide (KBr) to produce a sediment to KBr mass ratio of ~2%. KBr is spectrally neutral in the IR region and minimizes optical effects, such as distortion, that might influence the observed absorbance (Griffiths and De Haseth, 1986; Hahn et al., 2011; Rosén et al., 2011). The sediment/KBr mixture was then stored in a 60°C oven to prevent water saturation prior to analysis.

FTIRS analysis was carried out using a Bruker Vertex 70 FTIR spectrometer with a diffuse reflectance attachment (Harrick Inc., USA). Measurements were taken at a relatively constant room temperature (21°C). Samples were scanned a total of 64 times at a resolution of 2cm^{-1}, from wavenumbers 7,497 to 368cm^{-1}. For numerical analysis only the wavenumber range of 3750 to 400cm^{-1} was used as this portion of the spectrum contains the regions of interest

(Vogel et al., 2008; Rosén et al., 2010). This led to a total of 1,737 data points per sample. A background scan of pure KBr was carried out every ~10 samples to minimize instrument drift.

5.3.4 Numerical Analyses

Preliminary manipulation of collected spectral data was carried out using the OPUS spectroscopy software package provided by Bruker (http://www.bruker.com/products/infrared-near-infrared-and-raman-spectroscopy/opus-software/overview.html). Further analysis (including all PLS regressions) were carried using the Eigenvector Research PLS_Toolbox for Matlab (http://www.eigenvector.com/software/pls_toolbox.htm).

5.3.5 Normalization of spectral data

Multiple different baseline and scatter corrections were applied to normalize the spectral data prior to PLS analysis. The purpose of baseline/scatter corrections is to minimize variations caused by noise and intra-sample measurement variations (Rosén et al., 2010). A preliminary "rubber band" baseline correction was applied within the OPUS software package provided by Bruker. Once the data were imported into the Eigenvector PLS toolbox, 3 different types of baseline corrections and data normalization were applied (for more details see http://wiki.eigenvector.com/index.php?title=ModelBuilding_PreProcessingMethods):

1) *Specified points baseline correction*: This method simply sets two, user-specified, points on the spectrum equal to 0. For this study the region of 2200-2100 cm^{-1} and 3750cm^{-1} were used after Vogel et al., 2008 and Rosen et al., 2010.
2) *Specified points baseline correction, data mean centering (MC):* in addition to the specified points correction mentioned above, the spectral data are also mean centered where by the software "calculates the mean value of each column and subtracts that from the column".

3) Automatic weighted least squares baseline correction (AWLS), data mean centering (MC): AWLS uses an algorithm to determine which points are most likely due to a baseline offset. The net effect is a baseline correction that minimizes the creation of highly negative peaks.

5.3.6 Calibration models

Numerous calibration models (see Results) were created from conventionally measured BSi or TOC data to predict concentrations of these proxies downcore using either linear regression or partial least squares regression. The purpose of creating multiple calibration models is to assess the validity and reproducibility of each specific technique when applying FTIR spectroscopy.

A predictive model based on linear regression was created for biogenic silica based on the 35 conventionally analyzed samples. BSi concentrations were linearly regressed against measured peak areas for the spectral region from 1050-1280 and 775-830cm^{-1} (light blue boxes in **Figure 5.2**). Peak integrations were carried out after preliminary baseline correction within the OPUS software. These regions were chosen because they cover the main bands associated with amorphous silica; the 1050-1280cm^{-1} region contains the band associated with the bending modes of the SiO_4 tetrahedron while the band centered on 800cm^{-1} is related to an inter-tetrahedral Si-O-Si bending vibration (Rickert et al., 2002; Gendron-Badou et al., 2003; Vogel et al., 2008), and pure diatom valves show high absorbance in this part of the spectrum (Rosén et al., 2010; Rosén et al., 2011). Spectral analysis of diatomaceous earth and diatomaceous ooze also show high absorbance in these regions (**Figure 5.2**).

The linear regression model for TOC was created in a similar fashion, in this case using the spectral region from 2800-3000cm^{-1} (green box in **Figure 5.2**). These wavenumbers are correlated to vibrations between carbon and hydrogen in $–CH_3$, $-CH_2$, and –CH in organic compounds (Rosén et al., 2010). While there are other spectral regions associated with organic

matter use of these regions is complicated by the compounding interaction of other molecules, and so they were not used for this model (see Rosén et al., 2010 for details).

To compare with linear regression models, and in line with previous studies using FTIRS, partial least squares regression was also used to create predictive models for BSi and TOC. PLS is particularly well suited to spectroscopic analyses as there are a large number of potentially correlated predictor variables (collected spectral information) and a relatively small number of samples (Mevik and Wehrens, 2007). For both proxies two different types of PLS models were created; one using the entire mid-infrared spectrum (3750-400cm^{-1}), and another using only regions specific to the compound of interest (similar to the linear models described above). For the biogenic silica PLS models utilizing a specific part of the mid-IR spectrum (BSS), the region from 435-480 was included as well as 1050-1280 and 775-830cm^{-1} (**Figure 5.2**). This region is related to the bending vibration modes of the SiO_4 tetrahedron (Rosen et al., 2011). It was not included in the linear model as the integrated peak areas were to large to interpret linearly and decreased model performance.

To determine % organic carbon, the region from 2800-3000cm-1 was used (Figure 2.1) (Rosèn et al., 2010; Rosèn et al., 2011). Absorbance along these wavenumbers have been shown to relate to -CH, -CH_2, and -CH_3 aliphatic chains in lipids, proteins, and carbohydrates (Farmer, 1974; Hahn et al., 2011; Mecozzi et al., 2009; Liu et al., 2013). While there are other parts of the mid-IR spectrum that also show absorbance from organic matter, such as 1400-1750cm^{-1}, they also overlap with absorbance caused by other, non-organic substances and were therefore left out of the TOC specific model.

Cross validation was carried out using either Leave One Out (LOO) or Venetian Blinds techniques (Eigenvector Research). In most instances BSi and TOC concentrations were square root transformed prior to analysis after the methodology of Rosén et al. 2011 (see Results).

5.4 Results

5.4.1 Biogenic silica linear regression calibration model results

The linear model for biogenic silica was created by regressing measured peak areas related to BSi against conventionally measured BSi concentrations. The R^2 of the calibration model is 0.744 (**Table 5.3**). 74% of the calibration samples fall within the ±4.26% error of the traditional method (Conley, 1998), and the average offset from the traditionally measured values was 2.75% BSi (**gray bars in Figure 5.3**).

5.4.2 Biogenic silica calibration model results – All spectrum models

Models utilizing the entire mid-IR spectrum (**Figure 5.2**) are referenced with the prefix BAS (Biogenic silica All Spectrum) or TAS (Total organic carbon All Spectrum). All BSi PLS models were cross-validated using the Leave One Out (LOO) method. The best performing BAS model is presented below. All model results, including PLS models with different pre-processing and poorer performance, are summarized in **Table 5.3**.

BAS 14.2 utilized AWLS and MC preprocessing to produce a calibration model with an R^2 of 0.872 when compared to the calibration data. 89% of the predicted calibration samples were within the ±4.26% error of the traditional method (Conley, 1998), and the average offset from the traditionally measured values was 1.75% BSi (**Figure 5.3**).

5.4.3 Biogenic silica PLS calibration model results – Specific spectral region models

Models utilizing specific spectral regions associated with biogenic silica or organic carbon (Rosèn et al., 2011; Hahn et al., 2011; Meyer-Jacob et al., 2014) are referenced with the prefix BSS or TSS. For BSi analysis, the spectral regions from 435-480, 775-830, and 1050-1280 cm^{-1} were used. These regions were chosen as they have been shown to have a strong

correspondence with biologically produced Si-O bonds (Rosèn et al., 2011; Gendron Badou et al., 2003) (see Methods).

BSS 13.1 utilized AWLS baseline correction and data mean centering. This model produced an R^2 of 0.780 when compared to the calibration data. 86% of the calibration samples predicted BSi percentages were within the ±4.26% error of the traditional method (Conley, 1998), and the average offset from the traditionally measured values was 2.45% BSi (**Figure 5.3**).

5.4.4 BAS and BSS model predictions downcore from Nanerersarpik record

A total of 290 samples were analyzed on the FTIRS from the Nanerersarpik Lake record (including 22 from the calibration dataset). Each of the models described in **Table 5.3** were used to predict biogenic silica concentrations downcore. The results are summarized in **Table 5.4**. In general, models utilizing specified points baseline corrections as well as mean centering provide unrealistically high predictions (**Table 5.4, Figure 5.4**). Both models using only specified points pre-processing provide realistic results, but best model performance was achieved with BAS 14.2 and BSS 13.1 (AWLS, MC pre-processing). These models produce remarkably similar predictions (**Figure 5.5**), with average predicted percentages of 10.68 and 10.58% BSi respectively (**Table 5.4**) The highly variable nature of the reconstructions for all models is likely due to the nature of sedimentation in Nanerersarpik Lake, with large amounts of detrital material entering the lake from the steep-sided catchment and therefore periodically diluting the biogenic silica signal.

5.4.5 Total organic carbon linear regression calibration model results

The linear regression model for TOC was created by linearly regressing the spectral area from 2800-3000cm^{-1} against conventionally measured values (see Methods). This model

produced a calibration R^2 of 0.60, with the average offset from measured values of 0.81% TOC (**Table 5.5**, gray bars in **Figure 5.6**).

5.4.6 Total organic carbon calibration model results – All spectrum models

All TOC models incorporating the entire spectrum are referenced with the prefix TAS. The best performing TAS model is presented below, with information on models using other pre-processing given in **Table 5.5**. For organic carbon models, due to the large number of calibration samples (n = 112), a Venetian Blinds cross validation method was used as opposed to the Leave One Out approach used for BSi (Eigenvector Research). Measurement of organic carbon concentrations via an Elemental Analyzer also result in much smaller errors than associated with the traditional measurement of biogenic silica, so no "% within error" comparison was made.

TAS 10.1, utilizing just a specified points baseline correction, produced an R^2 of 0.80 when compared to the calibration data. The average offset from measured values was 0.58% TOC (light green bars in **Figure 5.6**).

5.4.7 Total organic carbon calibration model results – Specific spectral region models

Models utilizing specific spectral regions associated with organic carbon (Rosèn et al., 2011; Hahn et al., 2011; Meyer-Jacob et al., 2014) are referenced with the prefix TSS. To determine % organic carbon, the region from 2800-3000cm^{-1} was used (**Figure 5.2**) (Rosèn et al., 2010; Rosèn et al., 2011).

TSS 3.1 produced the highest R^2 of 0.81 of all organic carbon models. Pre-processing consisted of AWLS and data mean centering (**Table 5.5**). It also produced the lowest average offset from the traditionally measured values (0.47% TOC) (dark green bars in **Figure 5.6**)

5.4.8 TAS and TSS model predictions downcore from Nanerersarpik record

As with biogenic silica, the PLSR models were then applied to the 290 downcore samples from Nanerersarpik Lake (including the 112 used for the calibration). Similar to the BSi results, models using both the specified points baseline correction and mean centering produced unreasonably high TOC estimates (**Figure 5.7**) (**Table 5.6**). TOC models using the entire mid-IR spectrum, TAS 10.1, which utilized just a specified points baseline correction, produced the highest R^2 (0.80) and the smallest offset (0.59%TOC) (light green in **Figure 5.8**). The best performing model, however, was TSS 3.1, utilizing AWLS and MC pre-processing and the 2800-3000cm^{-1} spectral region (R^2 of 0.81, average offset of 0.47% TOC) (dark green in **Figure 5.8**).

5.5 Discussion

5.5.1 Biogenic silica estimates using FTIRS

Best predictions for biogenic silica concentrations downcore were achieved using the entire mid-infrared spectrum (BAS 14.2) as opposed to the specific regions known to be associated with Si-O bonds BSS 13.1, (435-480, 775-830, 1050-1280cm^{-1}). Similar studies have also found no difference between models using specific regions versus the entire spectrum for both BSi and TOC (Meyer-Jacobs et al., 2014; Pearson et al., 2014). The PLS loading plot for the first component of BAS 14.2 (54.76% of variance) (**Figure 5.9**) shows highest loading values for the spectral regions associated with biogenic silica (peaks at ~470, 785, and 1075 cm^{-1}), as would be expected. The 2nd component (22.57% of variance) however, shows a large area of positive loadings in the region ~2800-3700 cm^{-1}. Absorbance in this broad band is associated with OH vibrations in organic matter, and are not related to biogenic silica (Hahn et al., 2011; Kellner et al., 1998). Therefore the all spectrum PLS models for biogenic silica are placing at least some predictive importance on a region unrelated to silica bonded to oxygen. For this particular study it is not detrimental to the overall predictive capability of the model, likely do the relationship between organic matter and biogenic silica in the Nanerersarpik Lake record (R^2 of .5355)

(**Figure 5.10**) (see below). It is worth noting however, that the downcore predictions for BAS 14.2 and BSS 13.1 are remarkably similar in spite of the different spectral regions used (**Figure 5.5**, **Table 5.4**). Generally, FTIRS-based PLS models seem to be able to accurately predict biogenic silica concentrations downcore in the Nanerersarpik record. Absolute BSi concentrations are plausible and usually fall within errors associated with the conventional wet-chemistry technique.

5.5.2 Progressive addition of traditionally measured values to biogenic silica calibration dataset

To determine the effect of a greater number of calibration samples to the skill of the prediction model, a set of 3 models were created using progressively more biogenic silica calibration data (**Table 5.7**). All of these models utilized AWLS baseline correction and mean centering. The first, BAS 17.1 utilizes only the 22 samples measured conventionally from Nanerersarpik Lake. The second, BAS 17.2 includes a further 8 samples from nearby Lower Sermilik Lake, and finally BAS 14.2 includes all 35 measured samples (3 from Fiskebol Lake in Norway and two pure quartz samples). Both the RMSEC and RMSECV of the calibration model decrease as more samples are added (**Table 5.7**). Interestingly, the first model using only Nanerersarpik data generally produced the most conservative BSi estimates, the addition of Lower Sermilik samples leads to the highest BSi predictions, and finally the inclusion of Fiskebol and the pure quartz standards resulting in slightly smaller maximum predicted values, but the lowest predicted values of any of the three models (**Figure 5.11**). It is also worth noting that while all three of the models are generally similar for most of the record, there are major differences between BAS 17.2 and the other 2 models in the oldest part of the record (aprox. older than 8kyr) when we believe the catchment was directly influenced by glacial activity.

5.5.3 Total organic carbon concentration estimates using FTIRS

For organic carbon the best predictive model (TSS 3.1) utilized AWLS and mean centering pre-processing and the specific TOC spectral region (2800-3000cm^{-1}). Interestingly, the differences between the TSS and TAS models using the same AWLS and MC corrections are greater than for the two equivalent biogenic silica models (**Table 5.5**). Furthermore, for the all spectrum organic carbon models, the best prediction is achieved by TAS 10.1, which utilizes only specified points pre-processing (as opposed to AWLS, MC) . It is important to point out however, that the loadings for TAS 10.1 are similar to BAS 14.2, with peaks at ~460 and 1070cm^{-1} (not associated with organic carbon) (**Figure 5.12**). The 2800-3000cm^{-1} region does show up in the first component loadings but it overshadowed by aforementioned BSi-related peaks as well as the 3100-3600cm^{-1} region. Again, this is likely due to the positive relationship between BSi and TOC at Nanerersarpik. Reliance on the 3000-3700cm^{-1} region is not surprising, as it is related to OH vibrations in organic matter, but can also be influenced by other, non-organic components (Hahn et al., 2011). Due to these considerations, it seems that for this study, although both the TAS and TSS model predictions are similar, TSS 3.1 likely provides the most robust estimates of organic carbon downcore, by circumventing artificial predictive importance of BSi related regions.

5.5.4 Progressive addition of traditionally measured values to organic carbon calibration dataset

A similar approach as described in 5.5.2 was also carried out for organic carbon, with progressive addition of 10 more samples to the calibration dataset beginning with 35 and ending at 112 (**Table 5.8**). Here the results are somewhat less conclusive than with biogenic silica, with both the R^2 of the calibration data and the RMSEC and RMSECV following no distinct trends. The lowest RMSEC and RMSECV were achieved by model TAS 20.6, which included 85 of the potential 112 calibration samples. The highest R^2 was achieved by model TAS 20.7, which included 105 samples. It is worth noting, however, that all of these samples were from Nanerersarpik Lake, and therefore the inclusion of greater numbers of samples might not be

expected to change the model the same way as with biogenic silica (where added samples were from other lakes).

5.5.5 Applicability of created PLS models to other lacustrine systems

One of the most important outstanding questions regarding FTIRS techniques in relation to lake sediments is the applicability of a calibration model created using one lake to another, different system. While theoretically the spectral response of Si-O or C-H should be indifferent to source region, differences in sediment composition will effect the resulting absorbance spectra, certainly over the entire mid-IR range, and potentially even in regions that are thought to be specific for either TOC or BSi (Meyers-Jacobs et al., 2014; Liu et al., 2013). The majority of sediment analyzed in this study is from Nanerersarpik, and therefore we cannot fully answer the above question. Comparison between the TOC and BSi models is informative, however. The similarities between the loadings for BAS 14.2 and TAS 10.1 is likely due to the nature of sedimentation in Nanerersarpik and nearby Sermilik Lake. The composition of sediment in these Arctic lacustrine systems generally varies between minerogenic and organic dominated end-members. This leads to the positive relationship between BSi and TOC, as well as the similarity in loadings for the two respective PLS models. In different lake systems, where these proxies do not share this relationship, our all spectrum models would likely return poor predictions. It is possible that the specific spectral region models would return robust results, although this has not been attempted.

5.6 Conclusions

Fourier Transform Infrared Spectroscopy can be successfully applied to Greenland lake sediments to reconstruct both organic carbon and biogenic silica concentrations with reasonable accuracy. The use of Partial Least Squares regression is suggested for creation of calibration models, although for biogenic silica in particular, linear regression of measured peak areas

returned similar results. Reasonable predictions were attained using both models that incorporate the entire mid-IR spectrum (BAS, TAS), and regions specific to the proxy of interest (BSS, TSS). While some forms of data pre-processing return similar predictions (specified points, AWLS + mean centering), others (specified points + mean centering) over-predict proxy values. The similarity of the loading plots for both BAS and TAS models suggests that the related nature of biogenic silica and TOC in Nanerersarpik is affecting the all spectrum models. Similar predictions were achieved using the specific spectral region models however, suggesting the results are robust despite this relationship. FTIRS is a promising tool for paleolimnological studies that requires only a small amount of sediment, minimal pretreatment, and a fraction of the time required for traditional analyses.

Table 5.1: Results of conventional biogenic silica analyses used as calibration dataset for FTIRS BSi models

Lake	n	High (%)	Low (%)	Std. Dev
Nanerersarpik	22	30.6	4.1	.24 (two sets of triplicates)
L. Sermilik	8	19.9	5.0	1.8 (one set of duplicates)
Fiskebol	3	20.3	11.3	-
Calibration samples	2	-	0	-
Total	35	30.6	0	.77

Table 5.2: Results of conventional organic carbon measurements used as calibration dataset for FTIRS TOC models

Lake	N	High (%)	Low (%)
Nanerersarpik	112	5.26	0.019
Calibration Samples	2	-	0

Table 5.3: Calibration model results for BAS and BSS partial least squares regression models

Model Id	Portion of spectrum used (cm^{-1})	Model Pre-Processing	# of model components (% variance explained)	Cross validation method	Data square root transformed ?	Calibration model R^2	RMSEC	RMSECV	% within traditional method error	Average offset from traditional method (%BSi)
BAS 16.1	All	Specified points	5 (99.25)	LOO	No	0.723	3.8774	4.8238	80%	2.74% Bsi
BAS 13.1	All	Spc. pts, mean centering	3 (92.25)	LOO	Yes	0.815	.40712	.47264	86%	2.02% Bsi
BAS 14.2	All	AWLS, mean centering	6 (96.02)	LOO	Yes	0.872	0.33349	0.47724	89%	1.75% Bsi
BSS 16.1	1050-1280, 775-830, 435-480	Spc. pts	4 (99.92)	LOO	Yes	0.682	0.68179	0.81391	80%	2.96% Bsi
BSS 14.1	1050-1280, 775-830, 435-480	Spc. pts, mean centering	2 (99.02)	LOO	Yes	0.798	0.46515	0.51697	86%	2.07% BSi
BSS 13.1	1050-1280, 775-830, 435-480	AWLS, mean centering	2 (98.33)	LOO	Yes	0.78	0.49311	0.56355	86%	2.45% BSi
Linear	1050-1280, 775-830	Preliminary baseline correction*	-	-	-	0.744	-	-	74%	2.75% BSi

Table 5.4: Predicted biogenic silica downcore from BAS and BSS models

Model Id	Model Pre-Processing	Maximum predicted BSi	Minimum predicted BSi	Mean
BAS 16.1	Specified points	28.86	0.26	13.25
BAS 13.1	Spc. pts, mean centering	91.57	16.92	44.09
BAS 14.2	AWLS, mean centering	32.43	1.12	10.68
BSS 16.1	Spc. pts	31.93	0.005	10.85
BSS 14.1	Spc. pts, mean centering	82.94	16.38	38.57
BSS 13.1	AWLS, mean centering	33.78	1.73	10.58
Linear	Preliminary baseline correction*	28.39	0.33	10.24

Table 5.5: Calibration model results for TAS and TSS organic carbon PLS models

Model Name	Portion of spectrum used (cm^{-1})	Data Preprocessing	Cross Validation	Model Components (% variance explained)	R^2	RMSEC	RMSECV
Linear	2800-3000	Preliminary baseline correction	-	-	.5989	-	-
TAS 6.1	All	Baseline correction (AWLS), mean centering	Venetian blinds	8 (97.62%)	.932	.16471	.25006
TAS 7.3	All	Baseline correction (specified pts)	Venetian blinds	4 (99.12%)	.8009	.2747	.28527
TSS 3.1	2800-3000	Mean Center	Venetian blinds	3 (99.96%)	.812	.63948	.65799
TSS 4.1	2800-3000	Baseline correction (specified pts), mean centering	Venetian blinds	4 (99%)	.881	.21868	.2315
Rosén 1	All	Baseline correction, multiple scatter correction	10% CV	7	.98	-	1.2
Rosén 2	2800-3000	Unknown	Unknown	9	.97	-	1.8

Table 5.6: Predicted total organic carbon downcore from TAS and TSS models

Model Id	Model Pre-Processing	Maximum predicted TOC	Minimum predicted TOC	Mean
TAS 10.1	Specified points	6.05	0.0005	2.98
TAS 8.1	Spc. pts, mean centering	36.56	0.87	7.43
TAS 9.4	AWLS, mean centering	5.75	-0.79	2.6
TSS 8.1	Spc. pts	4.57	1.62	3.12
TSS 5.2	Spc. pts, mean centering	61.4	2.39	10.15
TSS 3.1	AWLS, mean centering	5.08	0.12	2.60
Linear	Preliminary baseline correction*	8.52	0.71	2.74

Table 5.7: Model information for BAS 17.1 (22 calibration samples), 17.2 (30 calibration samples), and 14.2 (35 calibration samples)

Model Id	N	Sample Locations	Max predicted BSi %	Min predicted BSi %	Average	RMSEC	RMSECV	R^2
BAS 17.1	22	Nanerersarpik	29.21	2.30	11.32	0.34901	0.57684	0.741
BAS 17.2	30	Nanerersarpik + Lower Sermilik	34.80	2.06	11.66	0.3342	0.512	0.745
BAS 14.2	35	Nan + LSRM + Fisk and calib samples	32.43	1.12	10.68	0.33349	0.47725	0.872

Table 5.8: Downcore model information for TAS models incorporating increasing numbers of calibration samples

Model Id	n	Calibration model R^2	RMSEC	RMSECV
TAS 20.1	35	0.807	0.71411	0.78877
TAS 20.2	45	0.776	0.68931	0.76097
TAS 20.3	55	0.835	0.46009	0.60368
TAS 20.4	65	0.775	0.49965	0.66767
TAS 20.5	75	0.798	0.52678	0.64456
TAS 20.6	85	0.801	0.50936	0.60321
TAS 20.7	95	0.796	0.57024	0.62244
TAS 20.8	105	0.84	0.54422	0.61164
TAS 20.9	112	0.814	0.54991	0.63882

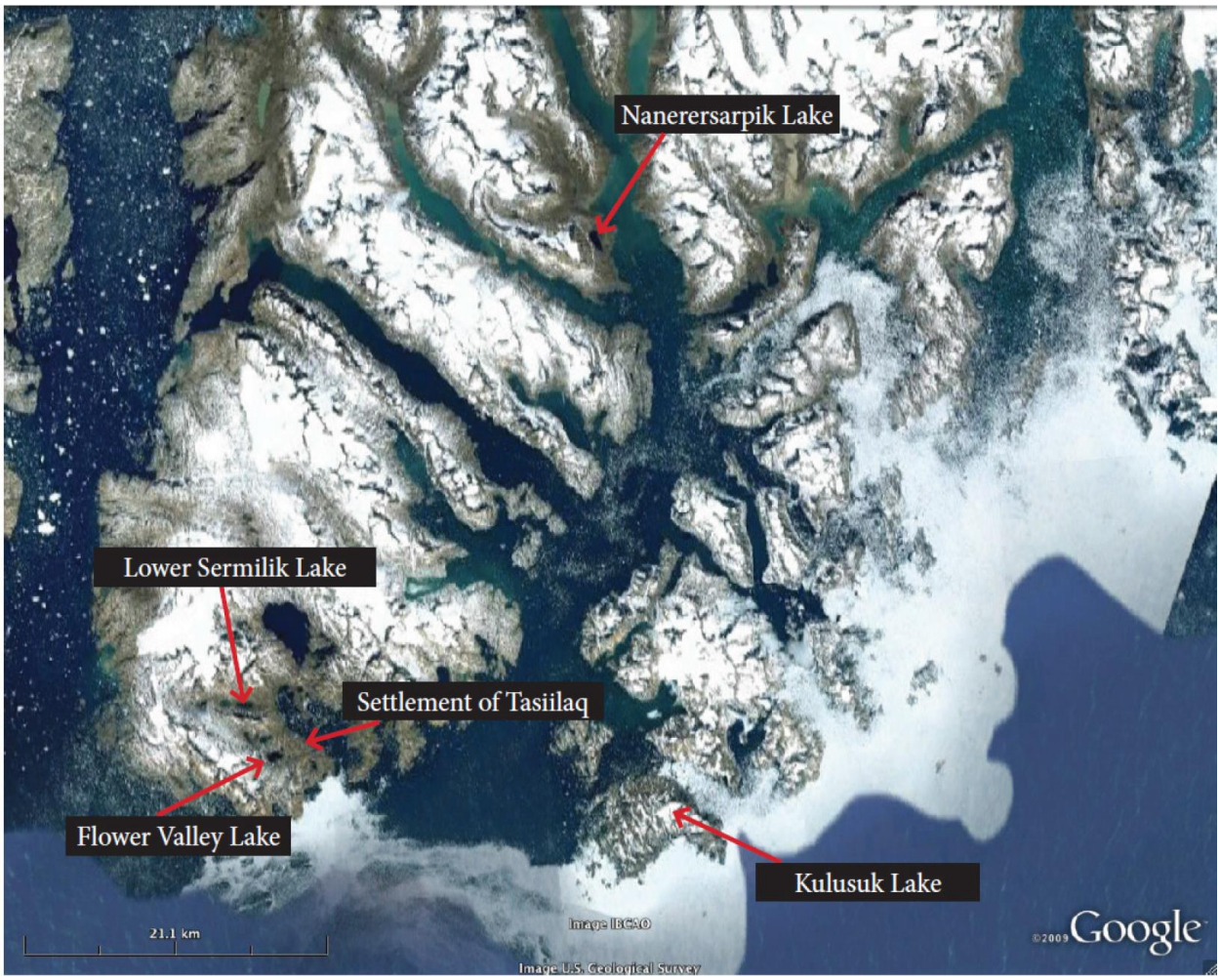

Figure 5.1 - Location of study area in SE Greenland (Nanerersarpik and Lower Sermilik used in this study).

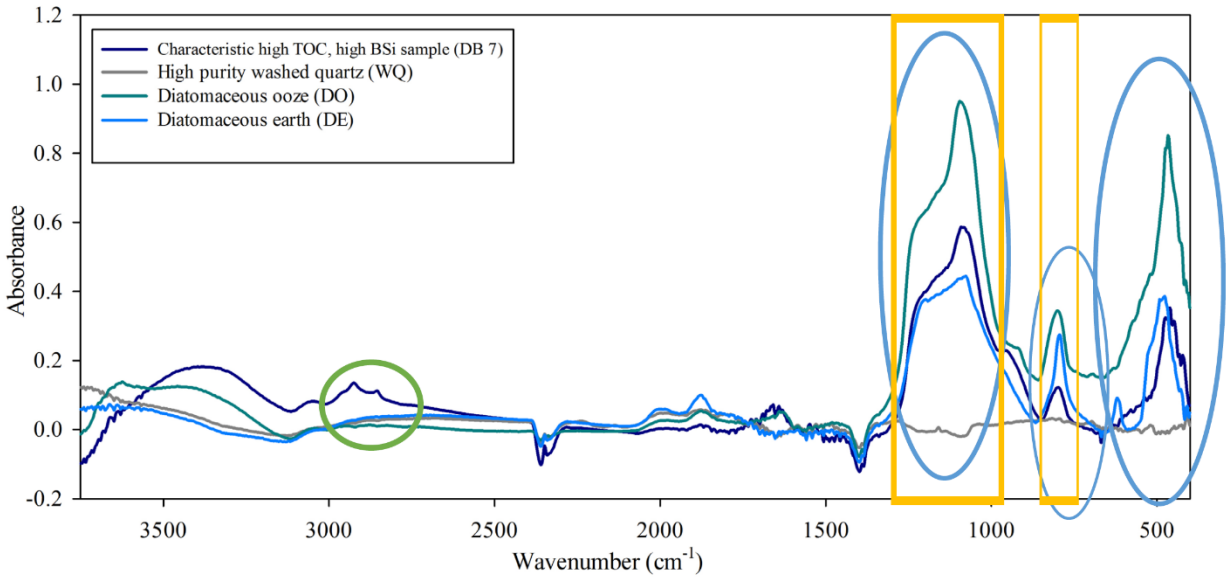

Figure 5.2 – Characteristic FTIRS absorbance spectra. Light blue circle denotes spectral region used for BSS models, light green circle for TSS models. Gold box outlines regions used in BSS linear regression model.

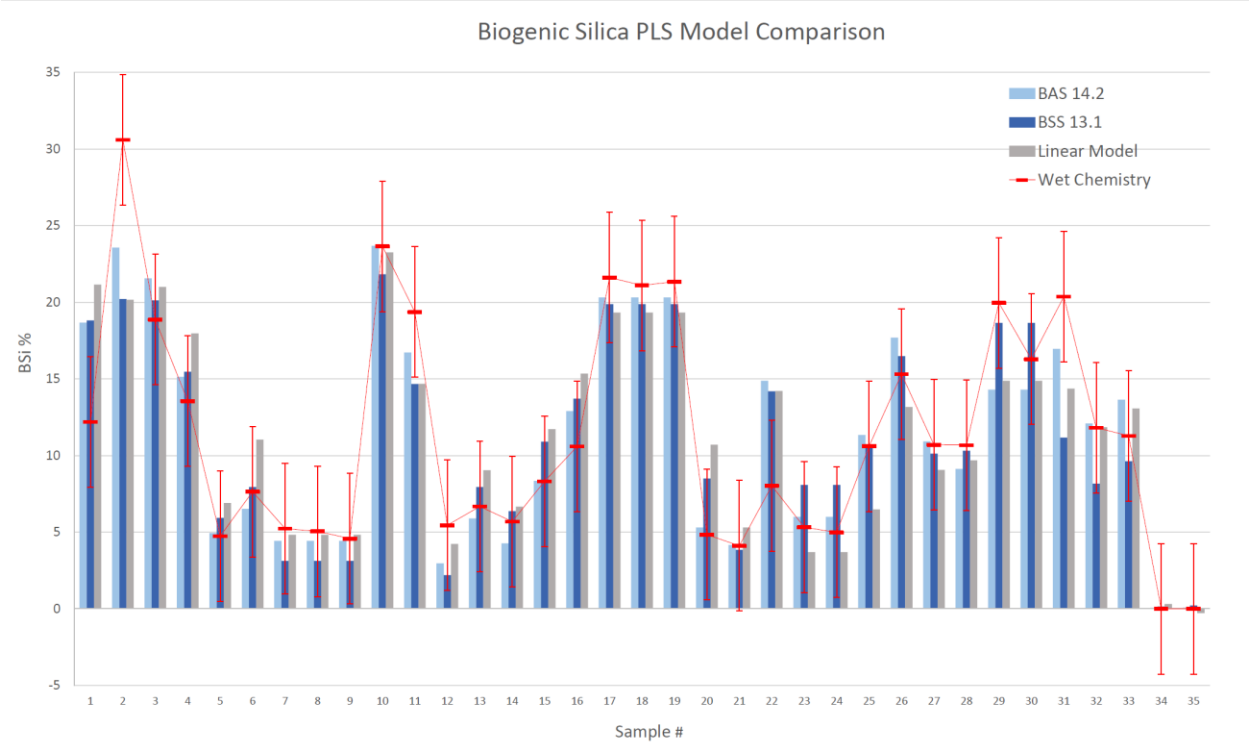

Figure 5.3 – BAS 14.2, BSS 13.1, linear regression calibrations model results compared against traditionally determined values (red rectangles). Error bars associated with wet chemistry values are inferred from Conley (1998).

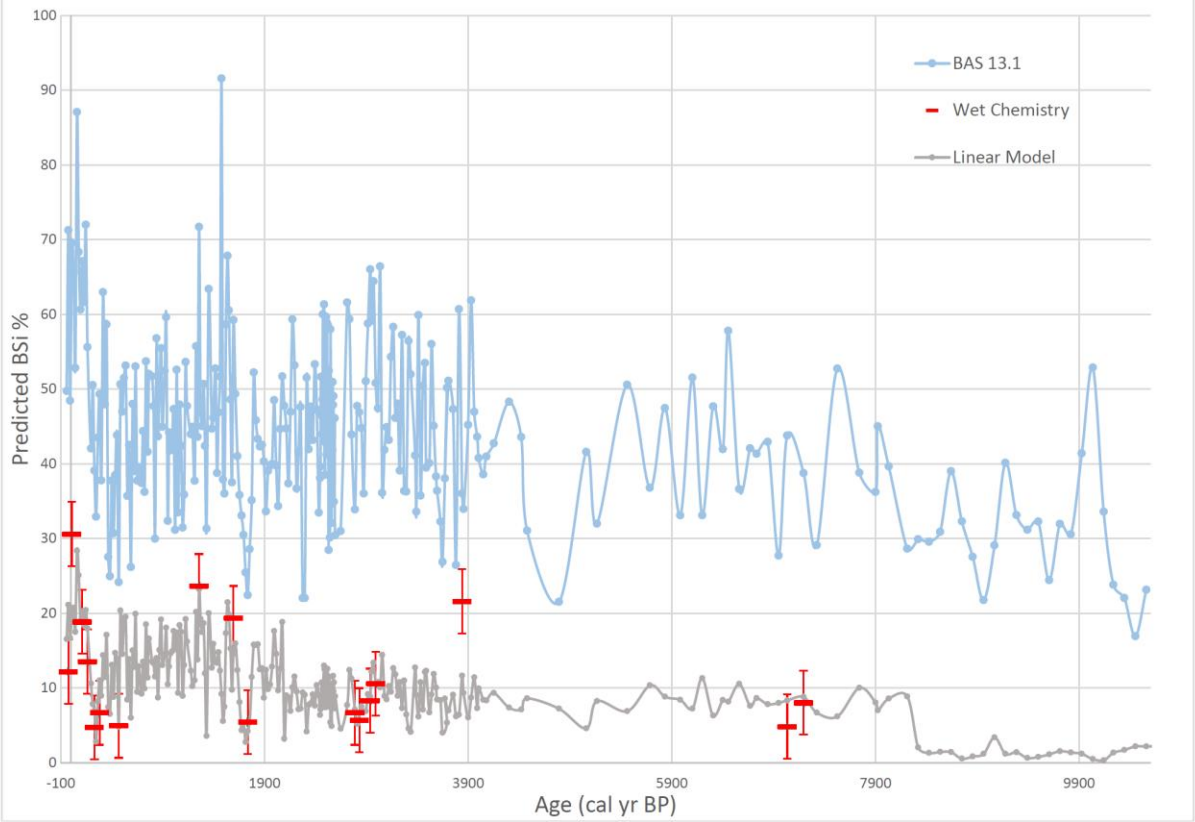

Figure 5.4 – Unrealistically high downcore predictions from BAS 13.1 (blue) compared to linear regression model (gray) and conventionally measured values (red).

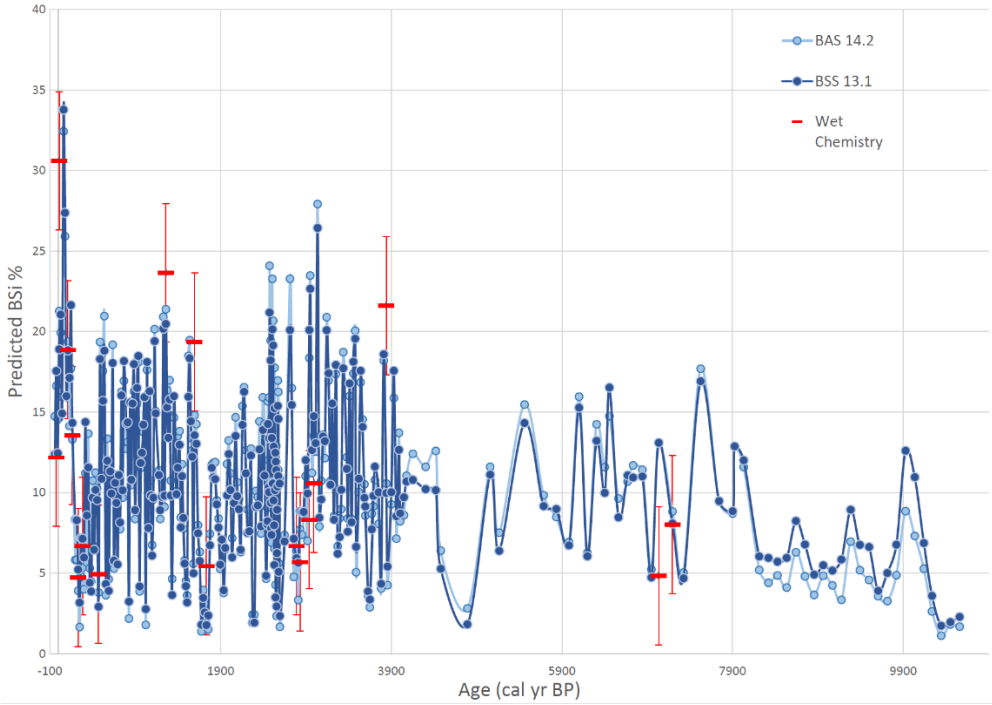

Figure 5.5 – Downcore BSi predictions from the best performing BAS model (14.2) and BSS model (13.1). Lower panel shows the most recent 4kyr of the record, where sampling resolution for FTIRS analysis was every centimeter.

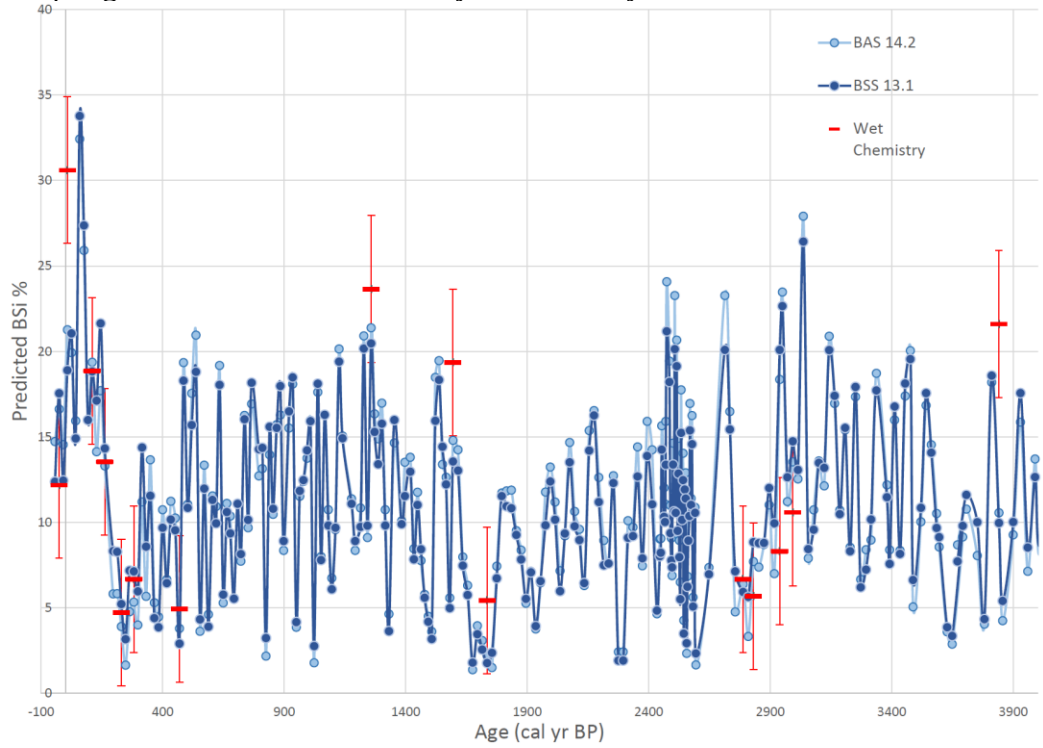

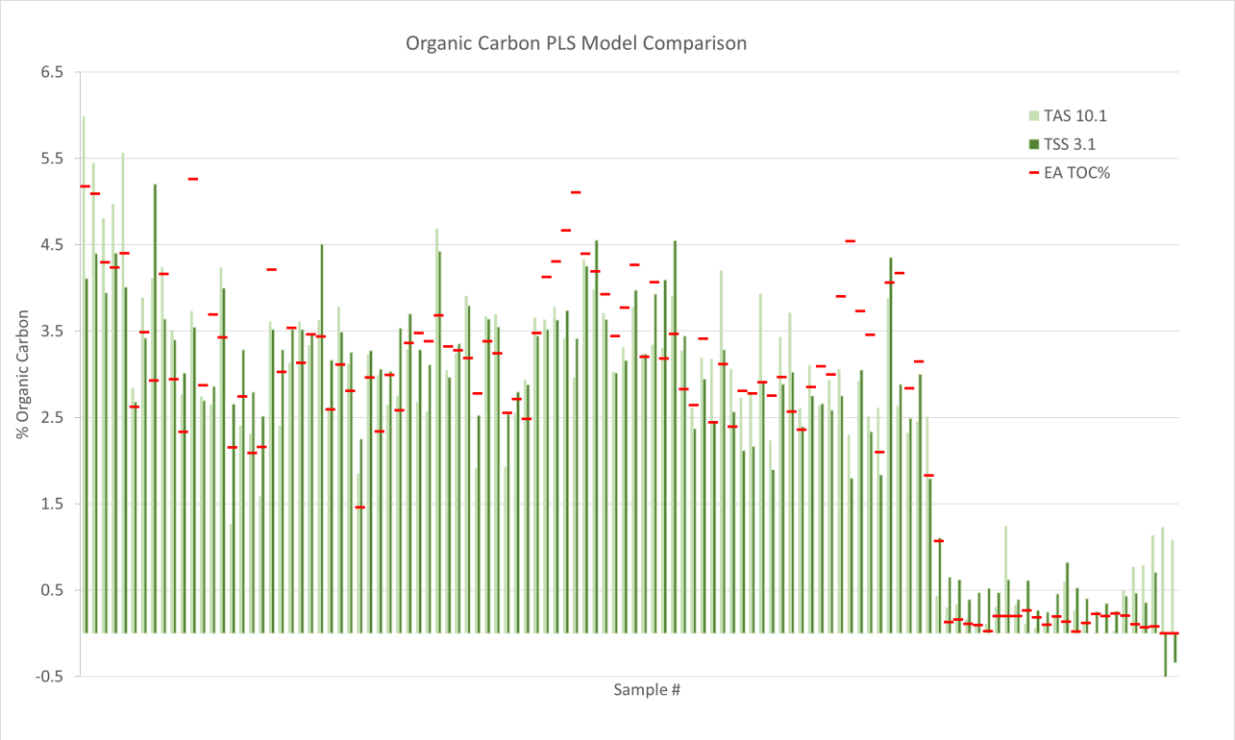

Figure 5.6 – TAS 10.1 and TSS 3.1 calibration model results compared against traditionally determined values (red rectangles).

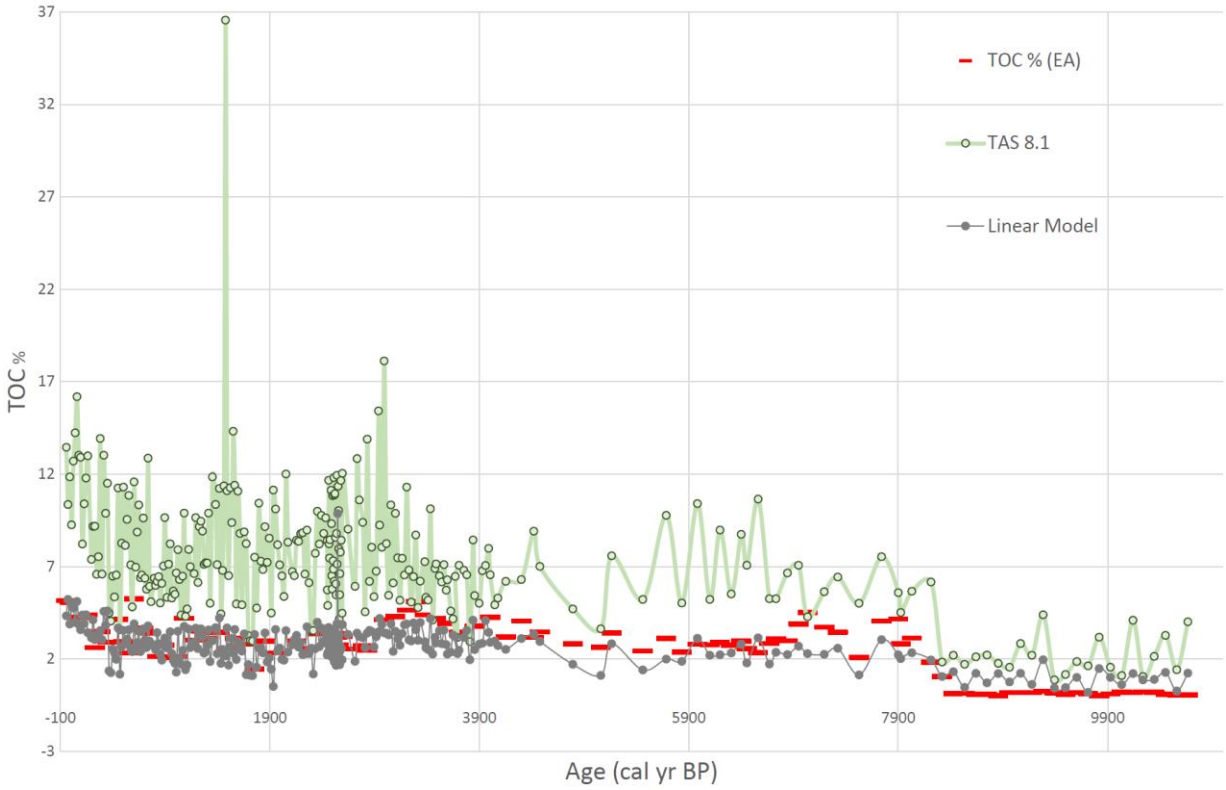

Figure 5.7 – Unrealistically high downcore predictions for PLS model TAS 8.1 (green) compared against predictions from linear regression model (gray) and traditionally measured values (red).

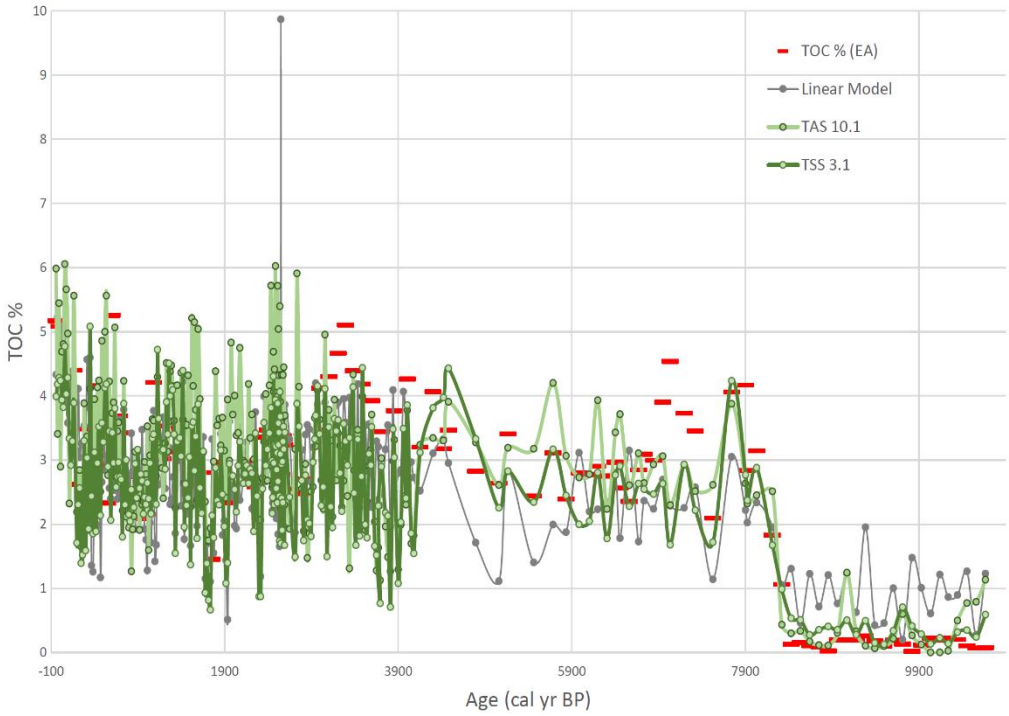

Figure 5.8 – Downcore TOC predictions from the best performing TAS model (10.1) and TSS model (3.1). Lower panel shows the most 4 kyr of the record, where sampling resolution for FTIRS analyses was every centimeter.

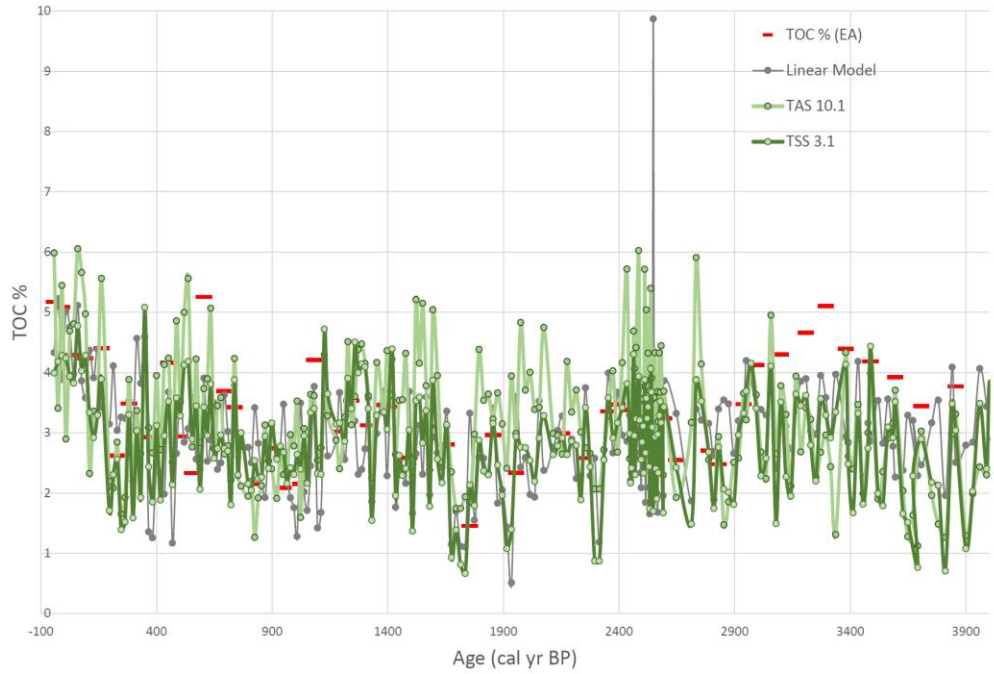

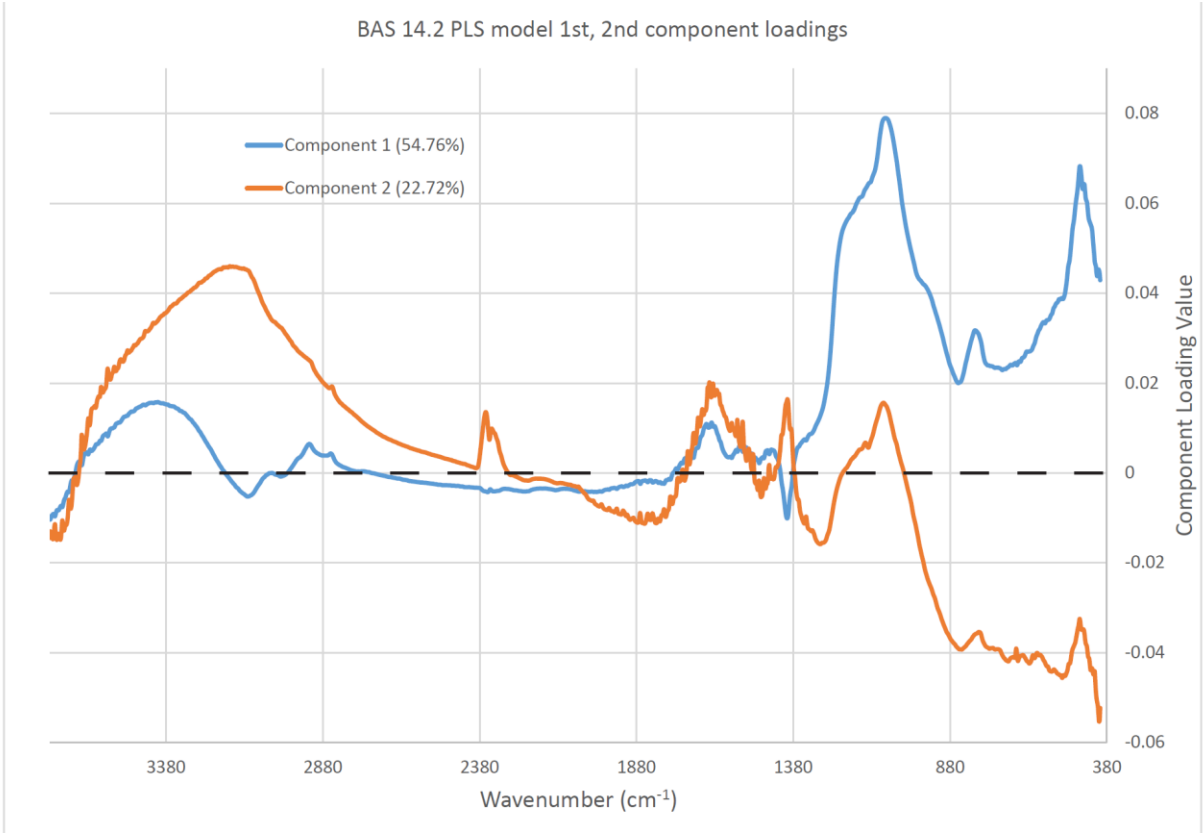

Figure 5.9 – PLS model loading plots for biogenic silica model BAS 14.2.

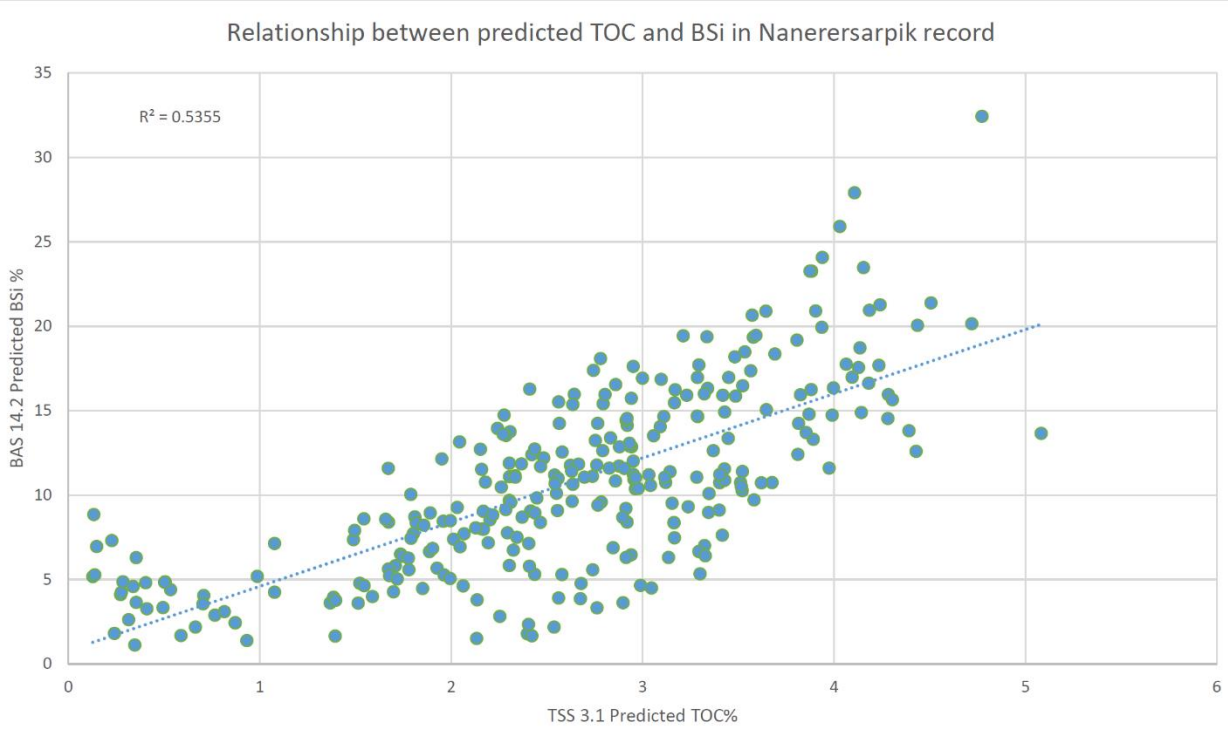

Figure 5.10 – Positive relationship between predicted total organic carbon (TOC) and biogenic silica (BSi) in Nanerersarpik record.

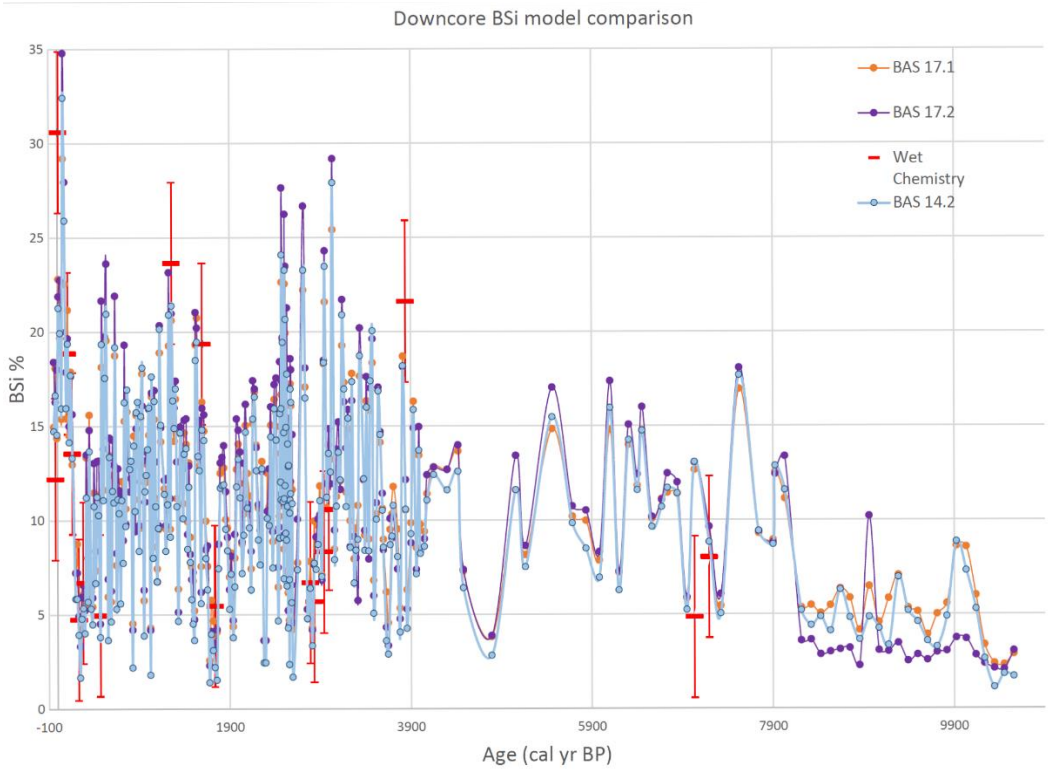

Figure 5.11 – Biogenic silica predictions downcore in Nanerersarpik record using best performing PLS models. Lower panel depicts past 4 kyr.

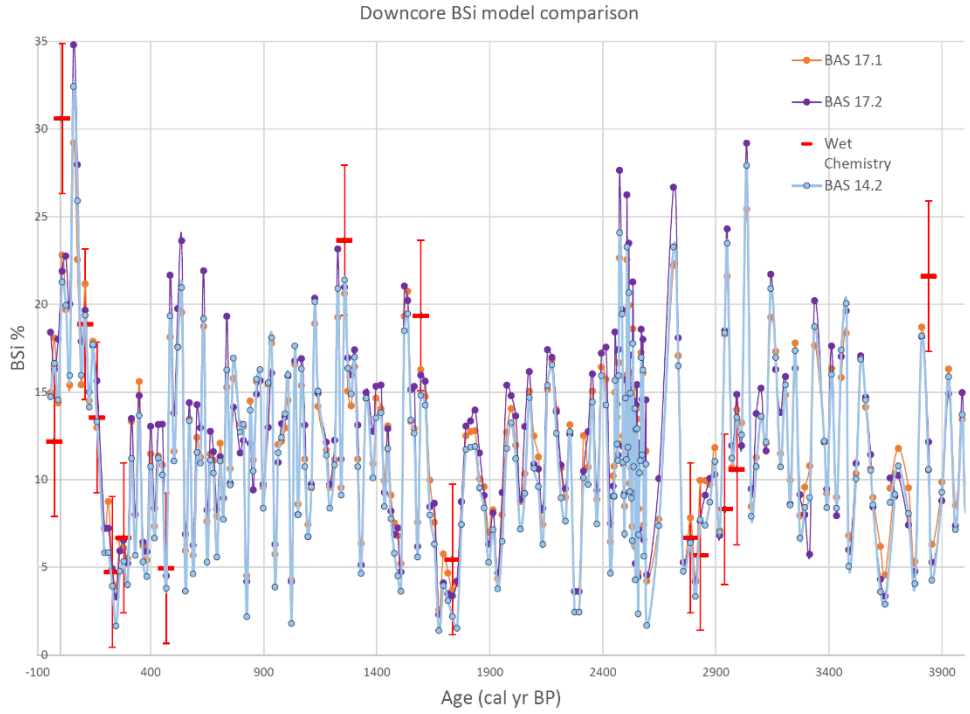

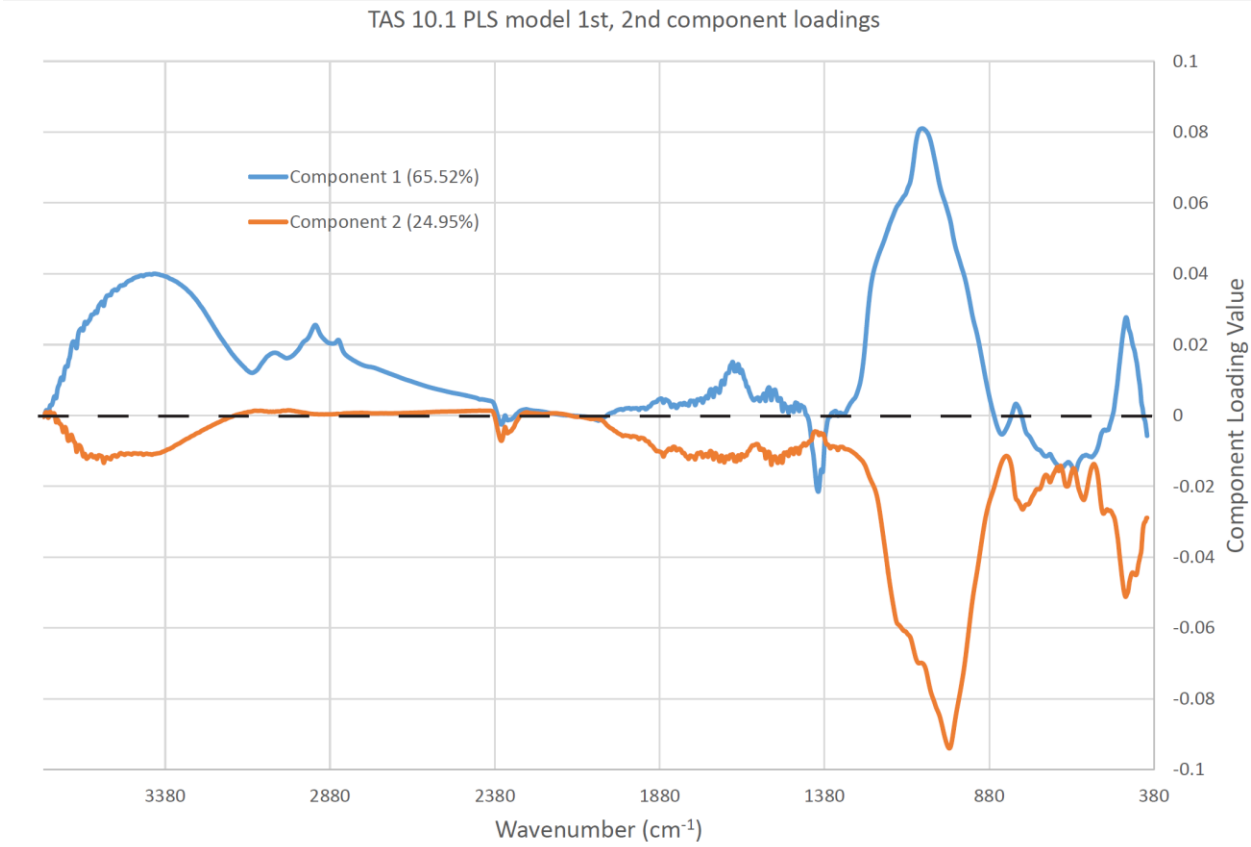

Figure 5.12 – PLS model loading plot for organic carbon PLS model TAS 10.1

REFERENCES

Aagaard-Sørensen, S., Husum, K., Hald, M., Marchitto, T., Godtliebsen, F., 2014. Sub sea surface temperatures in the Polar North Atlantic during the Holocene: Planktic foraminiferal Mg/Ca temperature reconstructions. The Holocene 24, 93–103.

Alley, R.B., Mayewski, P.A., Sowers, T., Stuiver, M., Taylor, K.C., Clark, P.U., 1997. Holocene climatic instability: A prominent, widespread event 8200 yr ago. Geology 25, 483. doi:10.1130/0091-7613(1997)025<0483:HCIAPW>2.3.CO;2

Andersen, K.K., Ditlevsen, P.D., Rasmussen, S.O., Clausen, H.B., Vinther, B.M., Johnsen, S.J., Steffensen, J.P., 2006. Retrieving a common accumulation record from Greenland ice cores for the past 1800 years. J. Geophys. Res. 111. doi:10.1029/2005JD006765

Andresen, C., Björck, S., Rundgren, M., Conley, D., Jessen, C., 2006. Rapid Holocene climate changes in the North Atlantic: evidence from lake sediments from the Faroe Islands. Boreas 35, 23–34. doi:10.1080/03009480500359228

Antoniades, D., 2008. Diatoms of North America: The freshwater floras of Prince Patrick, Ellef Ringnes and northern Ellesmere Islands from the Canadian Arctic Archipelago.

Arge, S.V., 2014. Viking Faroes: Settlement, Paleoeconomy, and Chronology. J. N. Atl. 7, 1–17. doi:10.3721/037.002.sp701

Arge, S.V., 1991. The landnám in the Faroes. Arct. Anthropol. 101–120.

Bakke, J., Trachsel, M., Kvisvik, B.C., Nesje, A., Lyså, A., 2013. Numerical analyses of a multi-proxy data set from a distal glacier-fed lake, Sørsendalsvatn, western Norway. Quat. Sci. Rev. 73, 182–195. doi:10.1016/j.quascirev.2013.05.003

Balascio, N.L., D'Andrea, W.J., Bradley, R.S., 2015. Glacier response to North Atlantic climate variability during the Holocene. Clim. Past 11, 1587–1598. doi:10.5194/cp-11-1587-2015

Belt, S.T., Massé, G., Rowland, S.J., Poulin, M., Michel, C., LeBlanc, B., 2007. A novel chemical fossil of palaeo sea ice: IP25. Org. Geochem. 38, 16–27. doi:10.1016/j.orggeochem.2006.09.013

Bennett, K.D., Boreham, S., Sharp, M.J., Switsur, V.R., 1992. Holocene History of Environment, Vegetation and Human Settlement on Catta Ness, Lunnasting, Shetland. J. Ecol. 80, 241. doi:10.2307/2261010

Berben, S.M.P., Husum, K., Cabedo-Sanz, P., Belt, S.T., 2014. Holocene sub-centennial evolution of Atlantic water inflow and sea ice distribution in the western Barents Sea. Clim. Past 10, 181–198. doi:10.5194/cp-10-181-2014

Berglund, J., 1986. The decline of the Norse settlements in Greenland. Arct. Anthropol. 109–135.

Bichet, V., Gauthier, E., Massa, C., Perren, B., Richard, H., Petit, C., Mathieu, O., 2013. The history and impacts of farming activities in south Greenland: an insight from lake deposits. Polar Rec. 49, 210–220. doi:10.1017/S0032247412000587

Birks, H.J.B., Jones, V.J., Rose, N.L., 2004. Recent environmental change and atmospheric contamination on Svalbard as recorded in lake sediments–synthesis and general conclusions. J. Paleolimnol. 31, 531–546.

Blaauw, M., 2010. Methods and code for "classical" age-modelling of radiocarbon sequences. Quat. Geochronol. 5, 512–518. doi:10.1016/j.quageo.2010.01.002

Blake, W., 2006. Occurrence of the Mytilus edulis complex on Nordaustlandet, Svalbard: radiocarbon ages and climatic implications. Polar Res. 25, 123–137.

Bond, G., 2001. Persistent Solar Influence on North Atlantic Climate During the Holocene. Science 294, 2130–2136. doi:10.1126/science.1065680

Brigham-Grette, J., Melles, M., Minyuk, P., Andreev, A., Tarasov, P., DeConto, R., Koenig, S., Nowaczyk, N., Wennrich, V., Rosen, P., Haltia, E., Cook, T., Gebhardt, C., Meyer-Jacob, C., Snyder, J., Herzschuh, U., 2013. Pliocene Warmth, Polar Amplification, and Stepped Pleistocene Cooling Recorded in NE Arctic Russia. Science 340, 1421–1427. doi:10.1126/science.1233137

Briner, J.P., McKay, N.P., Axford, Y., Bennike, O., Bradley, R.S., de Vernal, A., Fisher, D., Francus, P., Fréchette, B., Gajewski, K., Jennings, A., Kaufman, D.S., Miller, G., Rouston, C., Wagner, B., 2016. Holocene climate change in Arctic Canada and Greenland. Quat. Sci. Rev. 147, 340–364. doi:10.1016/j.quascirev.2016.02.010

Buckland, P.C., Edwards, K.J., Panagiotakopulu, E., Schofield, J.E., 2009. Palaeoecological and historical evidence for manuring and irrigation at Garthar (Igaliku), Norse Eastern Settlement, Greenland. The Holocene 19, 105–116. doi:10.1177/0959683608096602

Buckles, L.K., Weijers, J.W.H., Verschuren, D., Sinninghe Damsté, J.S., 2014. Sources of core and intact branched tetraether membrane lipids in the lacustrine environment: Anatomy of Lake Challa and its catchment, equatorial East Africa. Geochim. Cosmochim. Acta 140, 106–126. doi:10.1016/j.gca.2014.04.042

Bull, I.D., Lockheart, M.J., Elhmmali, M.M., Roberts, D.J., Evershed, R.P., 2002. The origin of faeces by means of biomarker detection. Environ. Int. 27, 647–654.

Bush, R.T., McInerney, F.A., 2013. Leaf wax n-alkane distributions in and across modern plants: Implications for paleoecology and chemotaxonomy. Geochim. Cosmochim. Acta 117, 161–179. doi:10.1016/j.gca.2013.04.016

Cabedo-Sanz, P., Belt, S.T., Jennings, A.E., Andrews, J.T., Geirsdóttir, Á., 2016. Variability in drift ice export from the Arctic Ocean to the North Icelandic Shelf over the last 8000 years: A multi-proxy evaluation. Quat. Sci. Rev. 146, 99–115. doi:10.1016/j.quascirev.2016.06.012

Callaghan, T.V., Bergholm, F., Christensen, T.R., Jonasson, C., Kokfelt, U., Johansson, M., 2010. A new climate era in the sub-Arctic: Accelerating climate changes and multiple impacts: CHANGING CLIMATE IN THE SUB-ARCTIC. Geophys. Res. Lett. 37, n/a-n/a. doi:10.1029/2009GL042064

Cappelen, J., Laursen, E.V., 1998. The Climate of the Faroe Islands: With Climatological Standard Normals, 1961-90. DMI.

Castañeda, I.S., Smith, L.M., Kristjánsdóttir, G.B., Andrews, J.T., 2004. Temporal changes in Holoceneδ18O records from the northwest and central North Iceland Shelf. J. Quat. Sci. 19, 321–334. doi:10.1002/jqs.841

Chawchai, S., Kylander, M.E., Chabangborn, A., Löwemark, L., Wohlfarth, B., 2016. Testing commonly used X-ray fluorescence core scanning-based proxies for organic-rich lake sediments and peat. Boreas 45, 180–189. doi:10.1111/bor.12145

Church, M.J., Arge, S.V., Brewington, S., McGovern, T.H., Woollett, J.M., Perdikaris, S., Lawson, I.T., Cook, G.T., Amundsen, C., Harrison, R., others, 2005. Puffins, pigs, cod and barley: palaeoeconomy at Undir Junkarinsfløtti, Sandoy, Faroe Islands. Environ. Archaeol. 10, 179–197.

Church, M.J., Arge, S.V., Edwards, K.J., Ascough, P.L., Bond, J.M., Cook, G.T., Dockrill, S.J., Dugmore, A.J., McGovern, T.H., Nesbitt, C., Simpson, I.A., 2013. The Vikings were not the first colonizers of the Faroe Islands. Quat. Sci. Rev. 77, 228–232. doi:10.1016/j.quascirev.2013.06.011

D'Andrea, W.J., Vaillencourt, D.A., Balascio, N.L., Werner, A., Roof, S.R., Retelle, M., Bradley, R.S., 2012. Mild Little Ice Age and unprecedented recent warmth in an 1800 year lake sediment record from Svalbard. Geology 40, 1007–1010. doi:10.1130/G33365.1

D'Anjou, R.M., 2012. Holocene Climate and Environmental Changes: Disentangling Natural and Anthropogenic Signals in the Sedimentary Record of Lake Lilandsvatnet (NW Norway).

De Jonge, C., Hopmans, E.C., Stadnitskaia, A., Rijpstra, W.I.C., Hofland, R., Tegelaar, E., Sinninghe Damsté, J.S., 2013. Identification of novel penta- and hexamethylated branched glycerol dialkyl glycerol tetraethers in peat using HPLC–MS2, GC–MS and GC–SMB-MS. Org. Geochem. 54, 78–82. doi:10.1016/j.orggeochem.2012.10.004

De Jonge, C., Hopmans, E.C., Zell, C.I., Kim, J.-H., Schouten, S., Sinninghe Damsté, J.S., 2014. Occurrence and abundance of 6-methyl branched glycerol dialkyl glycerol tetraethers in soils: Implications for palaeoclimate reconstruction. Geochim. Cosmochim. Acta 141, 97–112. doi:10.1016/j.gca.2014.06.013

DeConto, R.M., Pollard, D., Kowalewski, D., 2012. Modeling Antarctic ice sheet and climate variations during Marine Isotope Stage 31. Glob. Planet. Change 88–89, 45–52. doi:10.1016/j.gloplacha.2012.03.003

Dugmore, A.J., Keller, C., McGovern, T.H., 2007. Norse Greenland settlement: reflections on climate change, trade, and the contrasting fates of human settlements in the North Atlantic islands. Arct. Anthropol. 44, 12–36.

Dugmore, A.J., McGovern, T.H., Vésteinsson, O., Arneborg, J., Streeter, R., Keller, C., 2012. Cultural adaptation, compounding vulnerabilities and conjunctures in Norse Greenland. Proc. Natl. Acad. Sci. 109, 3658–3663.

Ebbesen, H., Hald, M., Eplet, T.H., 2007. Lateglacial and early Holocene climatic oscillations on the western Svalbard margin, European Arctic. Quat. Sci. Rev. 26, 1999–2011. doi:10.1016/j.quascirev.2006.07.020

Edwards, K.J., Schofield, J.E., Mauquoy, D., 2008. High resolution paleoenvironmental and chronological investigations of Norse landnám at Tasiusaq, Eastern Settlement, Greenland. Quat. Res. 69, 1–15. doi:10.1016/j.yqres.2007.10.010

Eglinton, G., Hamilton, R.J., 1967. Leaf epicuticular waxes. Science 156, 1322–1335.

Førland, E.J., Benestad, R., Hanssen-Bauer, I., Haugen, J.E., Skaugen, T.E., 2011. Temperature and Precipitation Development at Svalbard 1900–2100. Adv. Meteorol. 2011, 1–14. doi:10.1155/2011/893790

Forman, S.L., 1990. Post-glacial relative sea-level history of northwestern Spitsbergen, Svalbard. Geol. Soc. Am. Bull. 102, 1580–1590.

Forwick, M., Vorren, T.O., 2009. Late Weichselian and Holocene sedimentary environments and ice rafting in Isfjorden, Spitsbergen. Palaeogeogr. Palaeoclimatol. Palaeoecol. 280, 258–274. doi:10.1016/j.palaeo.2009.06.026

Fritz, S., 1989. Lake development and limnological response to prehistoric and historic land-use in Diss, Norfolk, UK. J. Ecol. 182–202.

Funder, S., Goosse, H., Jepsen, H., Kaas, E., Kjaer, K.H., Korsgaard, N.J., Larsen, N.K., Linderson, H., Lysa, A., Moller, P., Olsen, J., Willerslev, E., 2011. A 10,000-Year Record of Arctic Ocean Sea-Ice Variability--View from the Beach. Science 333, 747–750. doi:10.1126/science.1202760

Gathorne-Hardy, F.J., Lawson, I.T., Church, M.J., Brooks, S.J., Buckland, P.C., Edwards, K.J., 2007. The Chironomidae of Grothusvatn, Sandoy, Faroe Islands: climatic and lake-phosphorus reconstructions, and the impact of human settlement. The Holocene 17, 1259–1264. doi:10.1177/0959683607085133

Gjermundsen, E.F., Briner, J.P., Akçar, N., Salvigsen, O., Kubik, P., Gantert, N., Hormes, A., 2013. Late Weichselian local ice dome configuration and chronology in Northwestern Svalbard: early thinning, late retreat. Quat. Sci. Rev. 72, 112–127. doi:10.1016/j.quascirev.2013.04.006

Grove, J.M., 2001. The onset of the Little Ice Age. Springer.

Guyard, H., Chapron, E., St-Onge, G., Anselmetti, F.S., Arnaud, F., Magand, O., Francus, P., Mélières, M.-A., 2007. High-altitude varve records of abrupt environmental changes and mining activity over the last 4000 years in the Western French Alps (Lake Bramant, Grandes Rousses Massif). Quat. Sci. Rev. 26, 2644–2660. doi:10.1016/j.quascirev.2007.07.007

Hald, M., Andersson, C., Ebbesen, H., Jansen, E., Klitgaard-Kristensen, D., Risebrobakken, B., Salomonsen, G.R., Sarnthein, M., Sejrup, H.P., Telford, R.J., 2007. Variations in temperature and extent of Atlantic Water in the northern North Atlantic during the Holocene. Quat. Sci. Rev. 26, 3423–3440. doi:10.1016/j.quascirev.2007.10.005

Hald, M., Ebbesen, H., Forwick, M., Godtliebsen, F., Khomenko, L., Korsun, S., Ringstad Olsen, L., Vorren, T.O., 2004. Holocene paleoceanography and glacial history of the West Spitsbergen area, Euro-Arctic margin. Quat. Sci. Rev. 23, 2075–2088. doi:10.1016/j.quascirev.2004.08.006

Hall, I.R., McCave, I.N., Shackleton, N.J., Weedon, G.P., Harris, S.E., 2001. Intensified deep Pacific inflow and ventilation in Pleistocene glacial times. Nature 412, 809–812.

Haltia, E.M., Nowaczyk, N.R., 2014. Magnetostratigraphy of sediments from Lake El'gygytgyn ICDP Site 5011-1: paleomagnetic age constraints for the longest paleoclimate record from the continental Arctic. Clim. Past 10, 623–642. doi:10.5194/cp-10-623-2014

Hammarlund, D., 1993. A distinct δ13C decline in organic lake sediments at the Pleistocene-Holocene transition in southern Sweden. Boreas 22, 236–243.

Hannon, G., Hermanns-Auoardottir, M., Wastegård, S., 1998. Human impact at Tjørnuvík in the Faroe Islands. FróDskaparrit 46, 215–228.

Hannon, G.E., Bradshaw, R.H.W., 2000. Impacts and Timing of the First Human Settlement on Vegetation of the Faroe Islands. Quat. Res. 54, 404–413. doi:10.1006/qres.2000.2171

Hannon, G.E., Bradshaw, R.H.W., Bradshaw, E.G., Snowball, I., Wastegård, S., 2005. Climate change and human settlement as drivers of late-Holocene vegetational change in the Faroe Islands. The Holocene 15, 639–647. doi:10.1191/0959683605hl840rp

Hannon, G.E., Rundgren, M., Jessen, C.A., 2010. Dynamic early Holocene vegetation development on the Faroe Islands inferred from high-resolution plant macrofossil and pollen data. Quat. Res. 73, 163–172. doi:10.1016/j.yqres.2009.11.003

Hao, Q., Wang, L., Oldfield, F., Guo, Z., 2015. Extra-long interglacial in Northern Hemisphere during MISs 15-13 arising from limited extent of Arctic ice sheets in glacial MIS 14. Sci. Rep. 5, 12103. doi:10.1038/srep12103

Haug, G.H., Sigman, D.M., Tiedemann, R., Pedersen, T.F., Sarnthein, M., 1999. Onset of permanent stratification in the subarctic Pacific Ocean. Nature 401, 779–782.

Heiri, O., Lotter, A.F., Lemcke, G., 2001. Loss on ignition as a method for estimating organic and carbonate content in sediments: reproducibility and comparability of results. J. Paleolimnol. 25, 101–110.

Herbert, T.D., Peterson, L.C., Lawrence, K.T., Liu, Z., 2010. Tropical Ocean Temperatures Over the Past 3.5 Million Years. Science 328, 1530–1534. doi:10.1126/science.1185435

Honisch, B., Hemming, N.G., Archer, D., Siddall, M., McManus, J.F., 2009. Atmospheric Carbon Dioxide Concentration Across the Mid-Pleistocene Transition. Science 324, 1551–1554. doi:10.1126/science.1171477

Hoogakker, B.A.A., Chapman, M.R., McCave, I.N., Hillaire-Marcel, C., Ellison, C.R.W., Hall, I.R., Telford, R.J., 2011. Dynamics of North Atlantic Deep Water masses during the Holocene: HOLOCENE N ATLANTIC DEEP WATER DYNAMICS. Paleoceanography 26. doi:10.1029/2011PA002155

Hopmans, E.C., Schouten, S., Pancost, R.D., van der Meer, M.T., Sinninghe Damsté, J.S., 2000. Analysis of intact tetraether lipids in archaeal cell material and sediments by high performance liquid chromatography/atmospheric pressure chemical ionization mass spectrometry. Rapid Commun. Mass Spectrom. 14, 585–589.

Hopmans, E.C., Weijers, J.W.., Schefuß, E., Herfort, L., Sinninghe Damsté, J.S., Schouten, S., 2004. A novel proxy for terrestrial organic matter in sediments based on branched and isoprenoid tetraether lipids. Earth Planet. Sci. Lett. 224, 107–116. doi:10.1016/j.epsl.2004.05.012

Hormes, A., Gjermundsen, E.F., Rasmussen, T.L., 2013. From mountain top to the deep sea – Deglaciation in 4D of the northwestern Barents Sea ice sheet. Quat. Sci. Rev. 75, 78–99. doi:10.1016/j.quascirev.2013.04.009

Humlum, O., Christiansen, H.H., 1998. Late Holocene climatic forcing of geomorphic activity in the Faroe Islands. Frödskaparrit.

Humlum, O., Christiansen, H.H., Svensson, H., Mortensen, L.E., 1996. Moraine systems in the Faroe islands: glaciological and climatological implications. Geogr. Tidsskr.-Dan. J. Geogr. 96, 21–31.

Humlum, O., Elberling, B., Hormes, A., Fjordheim, K., Hansen, O.H., Heinemeier, J., 2005. Late-Holocene glacier growth in Svalbard, documented by subglacial relict vegetation and living soil microbes. The Holocene 15, 396–407.

Ingólfsson, Ó., Landvik, J.Y., 2013. The Svalbard–Barents Sea ice-sheet – Historical, current and future perspectives. Quat. Sci. Rev. 64, 33–60. doi:10.1016/j.quascirev.2012.11.034

Jessen, C.A., Rundgren, M., Bjorck, S., Andresen, C.S., Conley, D.J., 2008. Variability and seasonality of North Atlantic climate during the early Holocene: evidence from Faroe Island lake sediments. The Holocene 18, 851–860. doi:10.1177/0959683608093521

Jóhansen, J., 1989. Plantago lanceolota in the Faroe Islands and its significance as an indicator of prehistoric settlement. Fróðskaparrit34-35 68–75.

Jóhansen, J., 1985. Studies in the vegetational history of the Faroe and Shetland Islands. Føroya fróðskaparfelag.

Johnsen, S.J., Dahl-Jensen, D., Gundestrup, N., Steffensen, J.P., Clausen, H.B., Miller, H., Masson-Delmotte, V., Sveinbjørnsdottir, A.E., White, J., 2001. Oxygen isotope and palaeotemperature records from six Greenland ice-core stations: Camp Century, Dye-3, GRIP, GISP2, Renland and NorthGRIP. J. Quat. Sci. 16, 299–307. doi:10.1002/jqs.622

Jones, G., McGhee, R., 1986. The Norse Atlantic saga: being the Norse voyages of discovery and settlement to Iceland, Greenland, and North America. Oxford University Press New York.

Kaplan, M.R., Wolfe, A.P., 2006. Spatial and temporal variability of Holocene temperature in the North Atlantic region. Quat. Res. 65, 223–231. doi:10.1016/j.yqres.2005.08.020

Kaufman, D.S., Ager, T.A., Anderson, N.J., Anderson, P.M., Andrews, J.T., Bartlein, P.J., Brubaker, L.B., Coats, L.L., Cwynar, L.C., Duvall, M.L., others, 2004. Holocene thermal maximum in the western Arctic (0–180 W). Quat. Sci. Rev. 23, 529–560.

Khursevich, G.K., Prokopenko, A.A., Fedenya, S.A., Tkachenko, L.I., Williams, D.F., 2005. Diatom biostratigraphy of Lake Baikal during the past 1.25Ma: new results from BDP-96-2 and BDP-99 drill cores. Quat. Int. 136, 95–104. doi:10.1016/j.quaint.2004.11.011

Knudsen, K.., Jiang, H., Jansen, E., Eiríksson, J., Heinemeier, J., Seidenkrantz, M.-S., 2004. Environmental changes off North Iceland during the deglaciation and the Holocene: foraminifera, diatoms and stable isotopes. Mar. Micropaleontol. 50, 273–305. doi:10.1016/S0377-8398(03)00075-6

Koinig, K.A., Shotyk, W., Lotter, A.F., Ohlendorf, C., Sturm, M., 2003. 9000 years of geochemical evolution of lithogenic major and trace elements in the sediment of an alpine lake–the role of climate, vegetation, and land-use history. J. Paleolimnol. 30, 307–320.

Kubischta, F., Knudsen, K.L., Ojala, A.E., SALONEN, V.-P., 2011. HOLOCENE BENTHIC FORAMINIFERAL RECORD FROM A HIGH-ARCTIC FJORD, NORDAUSTLANDET, SVALBARD. Geogr. Ann. Ser. Phys. Geogr. 93, 227–242.

Kylander, M.E., Ampel, L., Wohlfarth, B., Veres, D., 2011. High-resolution X-ray fluorescence core scanning analysis of Les Echets (France) sedimentary sequence: new insights from chemical proxies. J. Quat. Sci. 26, 109–117. doi:10.1002/jqs.1438

Kylander, M.E., Lind, E.M., Wasteg\a ard, S., Löwemark, L., 2012. Recommendations for using XRF core scanning as a tool in tephrochronology. The Holocene 22, 371–375.

Landvik, J.Y., Bondevik, S., Elverhøi, A., Fjeldskaar, W., Mangerud, J., Salvigsen, O., Siegert, M.J., Svendsen, J.-I., Vorren, T.O., 1998. The last glacial maximum of Svalbard and the Barents Sea area: ice sheet extent and configuration. Quat. Sci. Rev. 17, 43–75.

Landvik, J.Y., Brook, E.J., Gualtieri, L., Raisbeck, G., Salvigsen, O., Yiou, F., 2003. Northwest Svalbard during the last glaciation: Ice-free areas existed. Geology 31, 905–908.

Laskar, J., Robutel, P., Joutel, F., Gastineau, M., Correia, A.C.M., Levrard, B., others, 2004. A long-term numerical solution for the insolation quantities of the Earth. Astron. Astrophys. 428, 261–285.

Lawson, I.T., Church, M.J., Edwards, K.J., Cook, G.T., Dugmore, A.J., 2007a. Peat initiation in the Faroe Islands: climate change, pedogenesis or human impact? Earth Environ. Sci. Trans. R. Soc. Edinb. 98, 15–28. doi:10.1017/S1755691007000035

Lawson, I.T., Church, M.J., McGovern, T.H., Arge, S.V., Woollet, J., Edwards, K.J., Gathorne-Hardy, F.J., Dugmore, A.J., Cook, G., Mairs, K.-A., Thomson, A.M., Sveinbjarnardótti, G., 2005. Historical Ecology on Sandoy, Faroe Islands: Palaeoenvironmental and Archaeological Perspectives. Hum. Ecol. 33, 651–684. doi:10.1007/s10745-005-7681-1

Lawson, I.T., Edwards, K.J., Church, M.J., Newton, A.J., Cook, G.T., Gathorne-Hardy, F.J., Dugmore, A.J., 2007b. ORIGINAL ARTICLE: Human impact on an island ecosystem: pollen data from Sandoy, Faroe Islands: Pollen data from Sandoy, Faroe Islands. J. Biogeogr. 35, 1130–1152. doi:10.1111/j.1365-2699.2007.01838.x

Layer, P.W., 2000. Argon-40/argon-39 age of the El'gygytgyn impact event, Chukotka, Russia. Meteorit. Planet. Sci. 35, 591–599.

Lisiecki, L.E., Raymo, M.E., 2005. A Pliocene-Pleistocene stack of 57 globally distributed benthic δ^{18}O records: PLIOCENE-PLEISTOCENE BENTHIC STACK. Paleoceanography 20, n/a-n/a. doi:10.1029/2004PA001071

Liu, X., Colman, S.M., Brown, E.T., Minor, E.C., Li, H., 2013. Estimation of carbonate, total organic carbon, and biogenic silica content by FTIR and XRF techniques in lacustrine sediments. J. Paleolimnol. 50, 387–398. doi:10.1007/s10933-013-9733-7

Loizeau, J.-L., Span, D., Coppee, V., Dominik, J., 2001. Evolution of the trophic state of Lake Annecy (eastern France) since the last glaciation as indicated by iron, manganese and phosphorus speciation. J. Paleolimnol. 25, 205–214.

Loomis, S.E., Russell, J.M., Heureux, A.M., D'Andrea, W.J., Sinninghe Damsté, J.S., 2014. Seasonal variability of branched glycerol dialkyl glycerol tetraethers (brGDGTs) in a temperate lake system. Geochim. Cosmochim. Acta 144, 173–187. doi:10.1016/j.gca.2014.08.027

Loomis, S.E., Russell, J.M., Ladd, B., Street-Perrott, F.A., Sinninghe Damsté, J.S., 2012. Calibration and application of the branched GDGT temperature proxy on East African lake sediments. Earth Planet. Sci. Lett. 357–358, 277–288. doi:10.1016/j.epsl.2012.09.031

Lynnerup, N., 1996. Paleodemography of the Greenland Norse. Arct. Anthropol. 122–136.

Mahler, D.L., 2007. Sæteren ved Argisbrekka. Økonomiske forandringer på Færøerne i vikingetid og tidlig middelalder. Faroe University Press.

Mahler, D.L.D., 1991. Argisbrekka. New evidence of shielings in the Faroe Islands. Acta Archaeol. 61, 60–72.

Maiorano, P., Marino, M., Flores, J.-A., 2009. The warm interglacial Marine Isotope Stage 31: Evidences from the calcareous nannofossil assemblages at Site 1090 (Southern Ocean). Mar. Micropaleontol. 71, 166–175. doi:10.1016/j.marmicro.2009.03.002

Massa, C., Perren, B.B., Gauthier, É., Bichet, V., Petit, C., Richard, H., 2012. A multiproxy evaluation of Holocene environmental change from Lake Igaliku, South Greenland. J. Paleolimnol. 48, 241–258. doi:10.1007/s10933-012-9594-5

Matras, C., 1956. Gammelfærøsk ærgi, n., og dermed beslægtede ord. Namn Och Bygd 44, 51–67.

Mayewski, P.A., Rohling, E.E., Curt Stager, J., Karlén, W., Maasch, K.A., David Meeker, L., Meyerson, E.A., Gasse, F., van Kreveld, S., Holmgren, K., Lee-Thorp, J., Rosqvist, G., Rack, F., Staubwasser, M., Schneider, R.R., Steig, E.J., 2004. Holocene climate variability. Quat. Res. 62, 243–255. doi:10.1016/j.yqres.2004.07.001

McGowan, S., Grauert, M., Anderson, N.J., 2008. A Late Holocene record of landscape degradation from Heygsvatn, the Faroe Islands. Palaeogeogr. Palaeoclimatol. Palaeoecol. 264, 11–24. doi:10.1016/j.palaeo.2008.03.003

McKay, R., Naish, T., Powell, R., Barrett, P., Scherer, R., Talarico, F., Kyle, P., Monien, D., Kuhn, G., Jackolski, C., Williams, T., 2012. Pleistocene variability of Antarctic Ice Sheet extent in the Ross Embayment. Quat. Sci. Rev. 34, 93–112. doi:10.1016/j.quascirev.2011.12.012

Melles, M., Brigham-Grette, J., Minyuk, P.S., Nowaczyk, N.R., Wennrich, V., DeConto, R.M., Anderson, P.M., Andreev, A.A., Coletti, A., Cook, T.L., Haltia-Hovi, E., Kukkonen, M., Lozhkin, A.V., Rosen, P., Tarasov, P., Vogel, H., Wagner, B., 2012a. 2.8 Million Years of Arctic Climate Change from Lake El'gygytgyn, NE Russia. Science 337, 315–320. doi:10.1126/science.1222135

Melles, M., Brigham-Grette, J., Minyuk, P.S., Nowaczyk, N.R., Wennrich, V., DeConto, R.M., Anderson, P.M., Andreev, A.A., Coletti, A., Cook, T.L., Haltia-Hovi, E., Kukkonen, M., Lozhkin, A.V., Rosen, P., Tarasov, P., Vogel, H., Wagner, B., 2012b. 2.8 Million Years of Arctic Climate Change from Lake El'gygytgyn, NE Russia. Science 337, 315–320. doi:10.1126/science.1222135

Melton, N., Nicholson, R., 2004. The Mesolithic in the Northern Isles: the preliminary evaluation of an oyster midden at West Voe, Sumburgh, Shetland, UK. Antiquity 78.

Meyers, P.A., 1997. Organic geochemical proxies of paleoceanographic, paleolimnologic, and paleoclimatic processes. Org. Geochem. 27, 213–250.

Miller, G.H., Brigham-Grette, J., Alley, R.B., Anderson, L., Bauch, H.A., Douglas, M.S.V., Edwards, M.E., Elias, S.A., Finney, B.P., Fitzpatrick, J.J., Funder, S.V., Herbert, T.D., Hinzman, L.D., Kaufman, D.S., MacDonald, G.M., Polyak, L., Robock, A., Serreze, M.C., Smol, J.P., Spielhagen, R., White, J.W.C., Wolfe, A.P., Wolff, E.W., 2010. Temperature and precipitation history of the Arctic. Quat. Sci. Rev. 29, 1679–1715. doi:10.1016/j.quascirev.2010.03.001

Millet, L., Massa, C., Bichet, V., Frossard, V., Belle, S., Gauthier, E., 2014. Anthropogenic versus climatic control in a high-resolution 1500-year chironomid stratigraphy from a southwestern Greenland lake. Quat. Res. 81, 193–202. doi:10.1016/j.yqres.2014.01.004

Moossen, H., Bendle, J., Seki, O., Quillmann, U., Kawamura, K., 2015. North Atlantic Holocene climate evolution recorded by high-resolution terrestrial and marine biomarker records. Quat. Sci. Rev. 129, 111–127. doi:10.1016/j.quascirev.2015.10.013

Müller, J., Werner, K., Stein, R., Fahl, K., Moros, M., Jansen, E., 2012. Holocene cooling culminates in sea ice oscillations in Fram Strait. Quat. Sci. Rev. 47, 1–14. doi:10.1016/j.quascirev.2012.04.024

Naeher, S., Gilli, A., North, R.P., Hamann, Y., Schubert, C.J., 2013. Tracing bottom water oxygenation with sedimentary Mn/Fe ratios in Lake Zurich, Switzerland. Chem. Geol. 352, 125–133. doi:10.1016/j.chemgeo.2013.06.006

Naish, T., Powell, R., Levy, R., Wilson, G., Scherer, R., Talarico, F., Krissek, L., Niessen, F., Pompilio, M., Wilson, T., Carter, L., DeConto, R., Huybers, P., McKay, R., Pollard, D., Ross, J., Winter, D., Barrett, P., Browne, G., Cody, R., Cowan, E., Crampton, J., Dunbar, G., Dunbar, N., Florindo, F., Gebhardt, C., Graham, I., Hannah, M., Hansaraj, D., Harwood, D., Helling, D., Henrys, S., Hinnov, L., Kuhn, G., Kyle, P., Läufer, A., Maffioli, P., Magens, D., Mandernack, K., McIntosh, W., Millan, C., Morin, R., Ohneiser, C., Paulsen, T., Persico, D., Raine, I., Reed, J., Riesselman, C., Sagnotti, L., Schmitt, D., Sjunneskog, C., Strong, P., Taviani, M., Vogel, S., Wilch, T., Williams, T., 2009. Obliquity-paced Pliocene West Antarctic ice sheet oscillations. Nature 458, 322–328. doi:10.1038/nature07867

Nichols, J.E., Booth, R.K., Jackson, S.T., Pendall, E.G., Huang, Y., 2006. Paleohydrologic reconstruction based on n-alkane distributions in ombrotrophic peat. Org. Geochem. 37, 1505–1513. doi:10.1016/j.orggeochem.2006.06.020

Nolan, M., Brigham-Grette, J., 2006. Basic hydrology, limnology, and meteorology of modern Lake El'gygytgyn, Siberia. J. Paleolimnol. 37, 17–35. doi:10.1007/s10933-006-9020-y

Nott, C.J., Xie, S., Avsejs, L.A., Maddy, D., Chambers, F.M., Evershed, R.P., 2000. n-Alkane distributions in ombrotrophic mires as indicators of vegetation change related to climatic variation. Org. Geochem. 31, 231–235.

Nowaczyk, N.R., Haltia, E.M., Ulbricht, D., Wennrich, V., Sauerbrey, M.A., Rosén, P., Vogel, H., Francke, A., Meyer-Jacob, C., Andreev, A.A., Lozhkin, A.V., 2013. Chronology of Lake El'gygytgyn sediments. Clim. Past Discuss. 9, 3061–3102. doi:10.5194/cpd-9-3061-2013

Olsen, J., Björck, S., Leng, M.J., Gudmundsdóttir, E.R., Odgaard, B.V., Lutz, C.M., Kendrick, C.P., Andersen, T.J., Seidenkrantz, M.-S., 2010. Lacustrine evidence of Holocene environmental change from three Faroese lakes: a multiproxy XRF and stable isotope study. Quat. Sci. Rev. 29, 2764–2780. doi:10.1016/j.quascirev.2010.06.029

Orcutt, D., Patterson, G., 1975. Sterol, fatty acid and elemental composition of diatoms grown in chemically defined media. Comp. Biochem. Physiol. Part B Comp. Biochem. 50, 579–583.

Pearson, E.J., Juggins, S., Talbot, H.M., Weckström, J., Rosén, P., Ryves, D.B., Roberts, S.J., Schmidt, R., 2011. A lacustrine GDGT-temperature calibration from the Scandinavian Arctic to Antarctic: Renewed potential for the application of GDGT-paleothermometry in lakes. Geochim. Cosmochim. Acta 75, 6225–6238. doi:10.1016/j.gca.2011.07.042

Perren, B.B., Massa, C., Bichet, V., Gauthier, É., Mathieu, O., Petit, C., Richard, H., 2012. A paleoecological perspective on 1450 years of human impacts from a lake in southern Greenland. The Holocene 22, 1025–1034.

Pollard, D., DeConto, R.M., 2009. Modelling West Antarctic ice sheet growth and collapse through the past five million years. Nature 458, 329–332. doi:10.1038/nature07809

Rasmussen, J., Noe-Nygaard, A., Henderson, G., 1970. Geology of the Faeroe Islands:(pre-quaternary).

Rasmussen, T.L., Forwick, M., Mackensen, A., 2013. Reprint of: Reconstruction of inflow of Atlantic Water to Isfjorden, Svalbard during the Holocene: Correlation to climate and seasonality. Mar. Micropaleontol. 99, 18–28. doi:10.1016/j.marmicro.2013.03.011

Rasmussen, T.L., Thomsen, E., 2010. Holocene temperature and salinity variability of the Atlantic Water inflow to the Nordic seas. The Holocene 20, 1223–1234. doi:10.1177/0959683610371996

Rasmussen, T.L., Thomsen, E., Skirbekk, K., Ślubowska-Woldengen, M., Klitgaard Kristensen, D., Koç, N., 2014. Spatial and temporal distribution of Holocene temperature maxima in the northern Nordic seas: interplay of Atlantic-, Arctic- and polar water masses. Quat. Sci. Rev. 92, 280–291. doi:10.1016/j.quascirev.2013.10.034

Reimer, P.J., Bard, E., Bayliss, A., Beck, J.W., Blackwell, P.G., Ramsey, C.B., Buck, C.E., Cheng, H., Edwards, R.L., Friedrich, M., others, 2013. IntCal13 and Marine13 radiocarbon age calibration curves 0–50,000 years cal BP. Radiocarbon 55, 1869–1887.
Renberg, I., 1990. A procedure for preparing large sets of diatom slides from sediment cores. J. Paleolimnol. 4, 87–90.
Reusche, M., Winsor, K., Carlson, A.E., Marcott, S.A., Rood, D.H., Novak, A., Roof, S., Retelle, M., Werner, A., Caffee, M., Clark, P.U., 2014. 10Be surface exposure ages on the late-Pleistocene and Holocene history of Linnébreen on Svalbard. Quat. Sci. Rev. 89, 5–12. doi:10.1016/j.quascirev.2014.01.017
Risebrobakken, B., Dokken, T., Smedsrud, L.H., Andersson, C., Jansen, E., Moros, M., Ivanova, E.V., 2011. Early Holocene temperature variability in the Nordic Seas: The role of oceanic heat advection versus changes in orbital forcing: EARLY HOLOCENE ADVECTION VS. INSOLATION. Paleoceanography 26. doi:10.1029/2011PA002117
Rohling, E.J., Pälike, H., 2005. Centennial-scale climate cooling with a sudden cold event around 8,200 years ago. Nature 434, 975–979.
Roncaglia, L., 2004. Palynofacies analysis and organic-walled dinoflagellate cysts as indicators of palaeo-hydrographic changes: an example from Holocene sediments in Skálafjord, Faroe Islands. Mar. Micropaleontol. 50, 21–42. doi:10.1016/S0377-8398(03)00065-3
Røthe, T.O., Bakke, J., Vasskog, K., Gjerde, M., D'Andrea, W.J., Bradley, R.S., 2015. Arctic Holocene glacier fluctuations reconstructed from lake sediments at Mitrahalvøya, Spitsbergen. Quat. Sci. Rev. 109, 111–125. doi:10.1016/j.quascirev.2014.11.017
Salvigsen, O., 2002. Radiocarbon-dated *Mytilus edulis* and *Modiolus modiolus* from northern Svalbard: Climatic implications. Nor. Geogr. Tidsskr. - Nor. J. Geogr. 56, 56–61. doi:10.1080/002919502760056350
Salvigsen, O., Forman, S.L., Miller, G.H., 1992. Thermophilous molluscs on Svalbard during the Holocene and their paleoclimatic implications. Polar Res. 11, 1–10.
Sarnthein, M., Kreveld, S., Erlenkeuser, H., Grootes, P., Kucera, M., Pflaumann, U., Schulz, M., 2003. Centennial-to-millennial-scale periodicities of Holocene climate and sediment injections off the western Barents shelf, 75 N. Boreas 32, 447–461.
Scherer, R.P., Bohaty, S.M., Dunbar, R.B., Esper, O., Flores, J.-A., Gersonde, R., Harwood, D.M., Roberts, A.P., Taviani, M., 2008. Antarctic records of precession-paced insolation-driven warming during early Pleistocene Marine Isotope Stage 31. Geophys. Res. Lett. 35. doi:10.1029/2007GL032254
Schofield, J.E., Edwards, K.J., Christensen, C., 2008. Environmental impacts around the time of Norse landnám in the Qorlortoq valley, Eastern Settlement, Greenland. J. Archaeol. Sci. 35, 1643–1657. doi:10.1016/j.jas.2007.11.004
Schouten, S., Hopmans, E.C., Sinninghe Damsté, J.S., 2013. The organic geochemistry of glycerol dialkyl glycerol tetraether lipids: A review. Org. Geochem. 54, 19–61. doi:10.1016/j.orggeochem.2012.09.006
Schouten, S., Huguet, C., Hopmans, E.C., Kienhuis, M.V.M., Sinninghe Damsté, J.S., 2007. Analytical Methodology for TEX $_{86}$ Paleothermometry by High-Performance Liquid Chromatography/Atmospheric Pressure Chemical Ionization-Mass Spectrometry. Anal. Chem. 79, 2940–2944. doi:10.1021/ac062339v
Scully, N., Leavitt, P., Carpenter, S., 2000. Century-long effects of forest harvest on the physical structure and autotrophic community of a small temperate lake. Can. J. Fish. Aquat. Sci. 57, 50–59.
Sejrup, H.P., Seppä, H., McKay, N.P., Kaufman, D.S., Geirsdóttir, Á., de Vernal, A., Renssen, H., Husum, K., Jennings, A., Andrews, J.T., 2016. North Atlantic-Fennoscandian Holocene climate trends and mechanisms. Quat. Sci. Rev. 147, 365–378. doi:10.1016/j.quascirev.2016.06.005

Serreze, M.C., Barry, R.G., 2011. Processes and impacts of Arctic amplification: A research synthesis. Glob. Planet. Change 77, 85–96. doi:10.1016/j.gloplacha.2011.03.004
Shanahan, T.M., Hughen, K.A., Van Mooy, B.A.S., 2013. Temperature sensitivity of branched and isoprenoid GDGTs in Arctic lakes. Org. Geochem. 64, 119–128. doi:10.1016/j.orggeochem.2013.09.010
Skirbekk, K., Kristensen, D.K., Rasmussen, T.L., Koç, N., Forwick, M., 2010. Holocene climate variations at the entrance to a warm Arctic fjord: evidence from Kongsfjorden trough, Svalbard. Geol. Soc. Lond. Spec. Publ. 344, 289–304.
Ślubowska, M.A., Koç, N., Rasmussen, T.L., Klitgaard-Kristensen, D., 2005. Changes in the flow of Atlantic water into the Arctic Ocean since the last deglaciation: Evidence from the northern Svalbard continental margin, 80°N: ATLANTIC WATER INFLOW INTO ARCTIC OCEAN. Paleoceanography 20, n/a-n/a. doi:10.1029/2005PA001141
Snyder, J.A., Werner, A., Miller, G.H., 2000. Holocene cirque glacier activity in western Spitsbergen, Svalbard: sediment records from proglacial Linnévatnet. The Holocene 10, 555–563.
Spurk, M., Leuschner, H.H., Baillie, M.G.L., Briffa, K.R., Friedrich, M., 2002. Depositional frequency of German subfossil oaks: climatically and non-climatically induced fluctuations in the Holocene. The Holocene 12, 707–715. doi:10.1191/0959683602hl583rp
Stocker, T.F., Qin, D., Plattner, G.-K., Tignor, M., Allen, S.K., Boschung, J., Nauels, A., Xia, Y., Bex, V., Midgley, P.M., 2013. Climate change 2013: The physical science basis. Intergov. Panel Clim. Change Work. Group Contrib. IPCC Fifth Assess. Rep. AR5Cambridge Univ Press N. Y.
Sun, Q., Chu, G., Liu, M., Xie, M., Li, S., Ling, Y., Wang, X., Shi, L., Jia, G., Lü, H., 2011. Distributions and temperature dependence of branched glycerol dialkyl glycerol tetraethers in recent lacustrine sediments from China and Nepal. J. Geophys. Res. 116. doi:10.1029/2010JG001365
Sun, Y., An, Z., Clemens, S.C., Bloemendal, J., Vandenberghe, J., 2010. Seven million years of wind and precipitation variability on the Chinese Loess Plateau. Earth Planet. Sci. Lett. 297, 525–535. doi:10.1016/j.epsl.2010.07.004
Svendsen, J.I., Mangerud, J., 1997. Holocene glacial and climatic variations on Spitsbergen, Svalbard. The Holocene 7, 45–57.
Teitler, L., Florindo, F., Warnke, D.A., Filippelli, G.M., Kupp, G., Taylor, B., 2015. Antarctic Ice Sheet response to a long warm interval across Marine Isotope Stage 31: A cross-latitudinal study of iceberg-rafted debris. Earth Planet. Sci. Lett. 409, 109–119. doi:10.1016/j.epsl.2014.10.037
Thomas, E.R., Wolff, E.W., Mulvaney, R., Steffensen, J.P., Johnsen, S.J., Arrowsmith, C., White, J.W.C., Vaughn, B., Popp, T., 2007. The 8.2ka event from Greenland ice cores. Quat. Sci. Rev. 26, 70–81. doi:10.1016/j.quascirev.2006.07.017
Tierney, J.E., Russell, J.M., Eggermont, H., Hopmans, E.C., Verschuren, D., Sinninghe Damsté, J.S., 2010. Environmental controls on branched tetraether lipid distributions in tropical East African lake sediments. Geochim. Cosmochim. Acta 74, 4902–4918. doi:10.1016/j.gca.2010.06.002
Tripati, A.K., Roberts, C.D., Eagle, R.A., Li, G., 2011. A 20 million year record of planktic foraminiferal B/Ca ratios: Systematics and uncertainties in< i> p CO< sub> 2 reconstructions. Geochim. Cosmochim. Acta 75, 2582–2610.
van der Bilt, W.G.M., Bakke, J., Vasskog, K., D'Andrea, W.J., Bradley, R.S., Ólafsdóttir, S., 2015. Reconstruction of glacier variability from lake sediments reveals dynamic Holocene climate in Svalbard. Quat. Sci. Rev. 126, 201–218. doi:10.1016/j.quascirev.2015.09.003

van der Bilt, W.G.M., D'Andrea, W.J., Bakke, J., Balascio, N.L., Werner, J.P., Gjerde, M., Bradley, R.S., 2016. Alkenone-based reconstructions reveal four-phase Holocene temperature evolution for High Arctic Svalbard. Quat. Sci. Rev. doi:10.1016/j.quascirev.2016.10.006

Velle, G., Kongshavn, K., Birks, H.J.B., 2011. Minimizing the edge-effect in environmental reconstructions by trimming the calibration set: Chironomid-inferred temperatures from Spitsbergen. The Holocene 21, 417–430. doi:10.1177/0959683610385723

Villa, G., Lupi, C., Cobianchi, M., Florindo, F., Pekar, S.F., 2008. A Pleistocene warming event at 1 Ma in Prydz Bay, East Antarctica: Evidence from ODP Site 1165. Palaeogeogr. Palaeoclimatol. Palaeoecol. 260, 230–244. doi:10.1016/j.palaeo.2007.08.017

Villa, G., Persico, D., Wise, S.W., Gadaleta, A., 2012. Calcareous nannofossil evidence for Marine Isotope Stage 31 (1Ma) in Core AND-1B, ANDRILL McMurdo Ice Shelf Project (Antarctica). Glob. Planet. Change 96–97, 75–86. doi:10.1016/j.gloplacha.2009.12.003

Weijers, J.W.H., Schouten, S., van den Donker, J.C., Hopmans, E.C., Sinninghe Damsté, J.S., 2007. Environmental controls on bacterial tetraether membrane lipid distribution in soils. Geochim. Cosmochim. Acta 71, 703–713. doi:10.1016/j.gca.2006.10.003

Wennrich, V., Minyuk, P.S., Borkhodoev, V., Francke, A., Ritter, B., Nowaczyk, N.R., Sauerbrey, M.A., Brigham-Grette, J., Melles, M., 2014. Pliocene to Pleistocene climate and environmental history of Lake El'gygytgyn, Far East Russian Arctic, based on high-resolution inorganic geochemistry data. Clim Past 10, 1381–1399. doi:10.5194/cp-10-1381-2014

Werner, K., Müller, J., Husum, K., Spielhagen, R.F., Kandiano, E.S., Polyak, L., 2015. Holocene sea subsurface and surface water masses in the Fram Strait – Comparisons of temperature and sea-ice reconstructions. Quat. Sci. Rev. doi:10.1016/j.quascirev.2015.09.007

Werner, K., Spielhagen, R.F., Bauch, D., Hass, H.C., Kandiano, E., 2013. Atlantic Water advection versus sea-ice advances in the eastern Fram Strait during the last 9 ka: Multiproxy evidence for a two-phase Holocene: HOLOCENE IN EASTERN FRAM STRAIT. Paleoceanography 28, 283–295. doi:10.1002/palo.20028

Wojtal, A.Z., Ognjanova-Rumenova, N., Wetzel, C.E., Hinz, F., Piatek, J., Kapetanovic, T., Ector, L., Buczko, K., 2014. Diversity of the genus Genkalia (Bacillariophyta) in boreal and mountain lakes-taxonomy, distribution and ecology. Fottea 14, 225–239.

Yang, H., Pancost, R.D., Dang, X., Zhou, X., Evershed, R.P., Xiao, G., Tang, C., Gao, L., Guo, Z., Xie, S., 2014. Correlations between microbial tetraether lipids and environmental variables in Chinese soils: Optimizing the paleo-reconstructions in semi-arid and arid regions. Geochim. Cosmochim. Acta 126, 49–69. doi:10.1016/j.gca.2013.10.041